3-D ACOUSTIC DOPPLER VELOCIMETRY AND TURBULENCE IN OPEN-CHANNEL FLOW

THÈSE N° 2395 (2001)

PRÉSENTÉE AU DÉPARTEMENT DE GÉNIE CIVIL

ÉCOLE POLYTECHNIQUE FÉDÉRALE DE LAUSANNE

POUR L'OBTENTION DU GRADE DE DOCTEUR ÈS SCIENCES

PAR

David HURTHER

Dipl.-Ing., Elektrotechnik, Fachhochschule Offenburg, Allemagne
DEA en mécanique et ingénierie, Université Louis Pasteur, Strasbourg, France,
de nationalité française

acceptée sur proposition du jury:

Prof. W.-H. Graf, directeur de thèse
Dr. U. Lemmin, rapporteur
Prof. P. Monkewitz, rapporteur
Prof. O. Scrivener, rapporteur
Dr. H.-P. Vaterlaus, rapporteur

Lausanne, EPFL

2001

À mes parents

ACKNOWLEDGEMENTS

I wish to acknowledge my indebtedness to a number of persons and sources that contributed to the completion of this work at the *Laboratoire de Recherches Hydrauliques (LRH)* of the *Ecole Polytechnique Fédérale de Lausanne (EPFL).* This work was funded by Swiss National Science Fundation through the research grant numbered 2100.50739.97. The author is grateful for their support.

Special thanks are due to Prof. W. H. Graf, director of the LRH, for his encouraging support and his critical comments on the thesis.

I would like to express my profound appreciation to Dr. U. Lemmin whose guidance and fruitful advice throughout my PhD study have been invaluable.

Thanks go also to Prof. P. Monkewitz from the *Laboratoire de Mécanique des Fluides* at *EPFL*, to Prof. O. Scrivener from the *Institut de Mécanique des Fluides de Strasbourg*, and to Dr. H. P. Vaterlaus from *Rittmeyer AG* in *Zug* for serving on the doctoral committee, reading the manuscript carefully and providing useful suggestions on the study.

The author has profited from the great experience and the clarifying discussions of Prof. S. Thorpe from the *Southampton Oceanography Center*, Prof. M. H. Garcia from *the University of Illinois at Urbana-Champaign*.

The ideal research climate and the outstanding efficiency of the permanent staff at *LRH* were essential for the completion of this thesis. I wish to acknowledge the generous help of C. Perrinjaquet, P. Aviolat, Dr. M. Altinakar, R. Fontanellaz, E. Guidetti and B. Tinguely. The friendship with my colleagues Dr. C. Shen, Dr. R. Jiang, K. Blanckaert, Dr. M. Cellino, I. Fer, I. Istiarto, Z. Qu, Y. Guan, A. Kurniawan and I. Schoppe will always remain in good memory.

Without the encouragement of my parents, the present achievement would not have been possible.

ABSTRACT

Understanding the dynamical details of transport of momentum, energy and tracers in currents is essential in assessing the impact of pollutants and their effect on water quality, at a time when the resource, high quality water, is becoming progressively scarce. The thesis is a contribution to our understanding of turbulence related transport mechanism in currents as well as to advances in flow measurement techniques.

Particular attention has been given to the dynamics of coherent flow structures in clear water and sediment suspension flows. In clear water open-channel flows, the measured instantaneous velocity and shear stress fields in uniform flows over smooth and rough beds show coherent structures extending over a large portion of the boundary layer that are approximatively independent of bottom roughness. Good agreement is found between these qualitative observations and a statistical analysis of the measurements which clearly documents that processes of shear stress generation and turbulent energy production are highly intermittent. Based on the measurements of the statistical properties, the vertical flux of turbulent kinetic energy, normalized by the cube of the bed friction velocity, is found to be constant. The value is equal to 0.3 over a depth range exceeding the intermediate flow region, independent of the flow and bed roughness conditions investigated here. The existence of this wall similarity in highly turbulent boundary layers offers a new method of determining the mean bed friction velocity. This method is better adapted to field measurements than previous methods because the measurements can be taken at a single level far from the bed over an extended depth range where the gradient of the mean flow profile is weak. In particular, this avoids the difficulty of needing to know the precise bed reference level, a difficulty that has introduced large errors in classical calculations based on profile measurements.

In suspension, open-channel flow under capacity charge conditions, the particle entrainment ability of coherent flow structures is investigated by comparing higher order statistical properties of shear stress and of turbulent mass fluxes. The suspended particle transport capacity of coherent structures has been quantified. The proportion of the relative particle concentration profile (relative to near bed equilibrium concentration taken at z/h=0.05) and the time fraction were estimated as functions of the shear stress threshold level (delimiting the coherent structures in the instantaneous flow field). It has been shown quantitatively that coherent structures are important contributors to suspended particle transport. Strong structures which are only present 30% of the time carry nearly 50% of the vertical particle flux. This indicates that particle transport is highly intermittent and that particle concentration in the water column varies strongly.

Based on these results, a bursting scales dependent formulation of the near bed equilibrium concentration has been modified and validated. It is found that the near bed particle entrainment function can be related directly to normalized time and space scales of bursts in suspension flows with different particle diameters and varying Shields parameters. This approach reveals the importance of the dynamics of flow structures when transport assesment in highly turbulent boundary layers is needed. Predicting sediment transport only from mean shear stresses obviously lacks the insight into the underlying physical processes.

A high resolution Doppler sonar measuring 3D quasi-instantaneous velocities has been developed. The pulse-to-pulse coherent technique is used which can provide high spatial (O(3mm)) and temporal (O(30Hz)) resolutions as well as high velocity resolution (O(1mms^{-1})). Whereas currently, available commercial 3D Acoustic Doppler Velocitimeters (ADV) are limited to point measurements, the proposed instrument allows non-intrusive acoustic 3D profiling (ADVP) over an extended water column. Furthermore, a novel correction method for turbulence measurements with 3D ADVP is proposed. It consists of reducing the noise contributions in the Doppler signal by a combination of a hardware (1) and a signal treatment method (2).

(1) An ultrasonic constant beamwidth transducer system is used which is capable of generating an extended focal zone by electronically focusing the beam over the desired water depth range. A higher beam directivity and a reduction in side lobe levels are obtained which result in an increased final resolution.

(2) It relies on a noise spectrum reconstruction from cross-spectra evaluations of two simultaneous and independent measurements of the same quantity over the whole water depth. Noise spectra and the noise variances are calculated and removed from the three fluctuating velocity variances.

The high flexibility of the conceived instrument allows laboratory as well as field measurements in rivers and lakes.

RESUME

La compréhension des détails dynamiques du transport de quantité de mouvement, d'énergie et de traceurs dans les fluides en écoulement est essentielle pour l'évaluation de l'impact des polluants et de leurs effets sur la qualité de l'eau. Il s'agit d'une nécessité au moment où la resource en eau de haute qualité devient progressivement rare. Cette thèse est une contribution à la compréhension des mécanismes de transport dans les écoulements turbulents ainsi qu'à la métrologie physique en milieu fluide.

En eau claire, les mesures simultanées du champ de vitesse 3D quasi-instantané et des tensions de Reynolds quasi-instantanées dans écoulement turbulent développé uniforme sur fond rugueux en canal ouvert, démontrent la présence de structures cohérentes sur toute la profondeur de la couche limite. Les échelles caractéristiques adimensionnelles de ces structures sont indépendantes de la rugosité uniforme du fond et du nombre de Reynolds, sur une distance de la couche limite dépassant la zone intermédiaire ($0.15<z/h<0.8$). Une forte concordance est obtenue entre ces observations qualitatives et les résultats d'une approche statistique quantitative d'ordre élevée, ce qui met en évidence le caractère hautement intermittent du processus de production d'énergie turbulente. Basé sur les propriétés statistiques des tensions de Reynolds, on constate une valeur constante du flux vertical moyen d'énergie cinétique turbulente normalisé par la vitesse de frottement au cube. La valeur mesurée est égale à 0.3 et reste constante sur une région de la couche limite correspondant à celle où les échelles caractéristiques adimensionnelles des structures cohérentes sont indépendantes des conditions de l'écoulement. A partir du concept de similitude pariétale dans les couches limites développées fortement turbulentes, on propose une nouvelle méthodologie de détermination de la vitesse moyenne de frottement pariétal. Cette méthode est mieux adaptée aux situations naturelles que les méthodes traditionnelles puisque la mesure se fait à une hauteur ponctuelle sur un domaine étendu de la couche limite et éloignée du fond. La mesure se fait donc dans une région de l'écoulement où la mesure est précise puisque le gradient moyen de la vitesse longitudinale y est très faible. De plus, la connaissance de la localisation précise du fond (pris comme origine du repère dans la direction verticale) n'est pas nécessaire alors que cette difficulté engendre de grandes erreurs dans les méthodes communément utilisées et basées sur le profil de vitesse moyenne.

En milieu diphasique (écoulement à surface libre saturé en transport particulaire), la capacité d'entraînement des particules en suspension par les structures cohérentes est étudiée en comparant les propriétés statistiques des tensions turbulentes à celles des flux de particules. La capacité de transport (i.e. maintien des particules en suspension) particulaire des structures cohérentes ainsi que leurs caractéristiques temporelles sont quantifiées en fonction d'un seuil de tension tangentielle turbulente. Ce critère d'échantillonnage conditionnel permet de

sélectionner les structures cohérentes dans le champ cinématique instantané. Il a été démontré quantitativement que ces structures cohérentes macroscopiques contribuent fortement au maintien des particules en suspension. Typiquement, ces structures sont présentes pendant 30% du temps et portent près de 50% des particules en suspension. Par conséquent, le transport de particules en suspension est de nature hautement intermittente ce qui démontre la forte variabilité de la concentration particulaire dans la couche limite turbulente.

À partir des résultats précédents, un modèle physique de transport particulaire en suspension basé sur les échelles caractéristiques des structures cohérentes a été modifié et validé expérimentalement. Il est démontré que la fonction d'entraînement de particules en zone pariétale peut être directement reliée aux échelles adimensionnelles temporelles et spatiales des bursts. Cette formulation reste valable pour différentes tailles de particules en suspension et pour des paramètres de Shields variants. La validité et la consistance de ce modèle révèlent l'importance de la dynamique des structures cohérentes dans le mécanisme de transport en couche limite fortement turbulente. La prédiction du transport sédimentaire basée exclusivement sur des valeurs moyennes de tension tangentielle turbulente, limite notre connaissance des phénomènes physiques existants.

Un profileur vélocimétrique acoustique Doppler haute résolution capable de mesurer le champ de vitesse tridimensionnel quasi-instantané a été conçu et réalisé. La technique de démodulation cohérente en mode pulsé fournit une haute résolution spatiale (O(3mm)), temporelle (O(30Hz)) et de vitesse (O(1mms^{-1})). L'avantage de l'instrument sur les vélocimètres acoustiques 3D commerciaux, concerne son aptitude à mesurer de manière non-intrusive et simultanée des profils de vitesse tridimensionnelle sur toute la profondeur de la couche limite turbulente. Les instruments disponibles sur le marché ne permettent qu'une mesure ponctuelle ce qui nécessite l'introduction des transducteurs dans le liquide et provoque une perturbation de l'écoulement. Une méthode de correction systématique des mesures de turbulence a été développée. Elle consiste à réduire les contributions du bruit dans le signal Doppler en combinant l'utilisation d'un transducteur piézo-électrique particulier (1) avec une méthode de traitement des signaux (2).

(1) Un émetteur ultrasonore à phase décalée est employé afin de générer un faisceau acoustique de largeur constante sur toute la profondeur de la couche limite insonifiée. Le gain en directivité du faisceau et la réduction des lobes secondaires ultrasonores, résultent en une augmentation de la résolution finale du système.

(2) La méthode consiste à reconstruire le spectre de bruit à partir de la mesure simultanée, instantanée et indépendante de deux quantités bruités similaires sur toute la profondeur de la

couche limite turbulente. Par considérations géométriques, les spectres de bruit et les variances associées sont évalués puis retirés des mesures du champ cinématique turbulent.

La fléxibilité de l'appareil conçu, permet d'effectuer des mesures en laboratoire ainsi qu'en condition naturelle telle que dans les rivières ou les lacs.

CONTENTS

CHAPTER 1

INTRODUCTION

1.1 Research motivation

Quantitative predictions of the transport rates of mass, momentum and energy are needed in a variety of situations, such as in the design of outfalls, the control of sedimentation in estuarine and nearshore regions, the impact assessment of discharges into rivers, water resource planning and interaction with biological processes in rivers and the estimation of gas transfer at air-water interface in free surface currents. As is demonstrated in the literature, prediction results scatter over a wide range depending on which assumptions have been made. This situation is not satisfactory at a time when the demand for river water use increases and potential pollutants become ever more toxic. Water resource management will therefore require improvements in the quantitative prediction.

Improvements can be brought about when more is known about the dynamics of transport in open-channel flows. This, in turn, can be best obtained through direct turbulence measurements of which very little exist today. In the present project we propose to fill this gap by measuring profiles of all three velocity components with a resolution on turbulent scales.

Turbulence is found to be the primary mechanism of transport processes in most natural shear flows. However, turbulence remains an unsolved problem in the sense that a clear physical comprehension of the phenomenon does not exist. The local time averaged conservation equations of scalar and vectorial flow quantities are of major importance for the determination of the physical processes interacting in fluids. These equations emphasize the highly non-linear behavior of the coupled mechanisms linked to turbulence. Nevertheless, this equation system posseses high degrees of freedom even in relatively simple flow conditions such as a stationary fully developed current, two-dimensional in the mean and uniform in the streamwise direction. In most of these cases, the mathematical complexity hinders the analytical resolution of these equations. To overcome this difficulty, the analytical resolution is achieved by the introduction of closure schemes based on phenomenological or empirical concepts. Examples are the Boussinesq assumption the the turbulent stresses in the momentum equations, Fick's law used to estimate the turbulent mass fluxes in the diffusion equations or the eddy viscosity approximation of the turbulent kinetic energy diffusion term in the energy equations of the k-ε model.

The research results over the last decades have revealed that these models fail to explain a variety of observed turbulence related phenomena. For example when secondary currents driven by mean turbulent anisotropy near the banks lead to helical motion in straight or curved channel flows (i.e. turbulent energy is transformed into mean kinetic energy). If the flow occurs over a movable sediment bed, these secondary currents can generate longitudinal ridges extending over long stream distances and subsequently affect the mixing process. Another unexplained mechanism connected to turbulence in open-channel flows is concerned with the formation cycle of boils and the surrounding pairs of spiral eddies with opposite normal vorticities appearing at the free surface. These turbulent flow structures may play a crucial role in gas transfer phenomena at the air-water interface which in turn affect the global climate change. Whilst at present, these complex flow mechanisms are not taken into account in the commonly used closure models, engineers have no choice other than to apply these models to try to solve practical transport problems. Further research is therefore essential in order to develop new turbulence models which are more consistent with the diverse experimental observations.

The emergence of non-intrusive high resolution measurement techniques since the late sixties, has brought to light the intermittent spatio-temporal behavior of the turbulence generation process. For shear flows, this phenomenon is characterized by the quasi-periodic appearance in the wall region of a quasi-organized flow structure called burst. The events connected to the burst cycle dominate the turbulent transport of momentum through the entire boundary layer. Their contribution is intense during their very short lifetimes which emphasizes their intermittent nature. The statistical description of such a dynamical particularity is only possible by considering higher order moments of the flow quantities. These higher order statistical properties are not included in the commonly used closure schemes mentioned above. This in turn, affects the validity of quantitative predictions. The description of the physical phenomena at the macro-scale level has started in recent years and needs to be refined in order to improve the quantitative assessment. This appears to be crucial at a time when an impact control of human activities on our natural environment is required to allow the desired sustainable development.

Today, the lack of instruments suited for the quantitative study of these aspects limits the progress in experimental fluid mechanics. Three dimensional instantaneous velocity measurement in single- and / or multiphase flows under uncontrolled situations such as natural condition is among the most relevant challenges of this multidisciplinary science. In multiphase flows, the ability to distinguish the velocity fields of the different phases is of particular interest for the investigation of interaction mechanisms. The need of instruments able to validate the recent results obtained from DNS and LES is of great significance. At present, no measurement systems exist which permit a three-dimensional Lagrangian visualization of the velocity field in a finite volume unlike the numerical simulation methods. On the other hand, numerical flow simulations at the macro scale level are limited to simple flow situations with respect to the extreme conditions encountered in field conditions. These conditions concern high Reynolds numbers, non-uniform wall roughnesses, complex flow geometries and non-stationary boundary conditions.

1.2 Objectives of the study

The attention given to the bursting phenomenon during recent years has significantly contributed to our knowledge of turbulence. These studies were focused on the mechanisms occuring in the inner region of the turbulent boundary layer since this wall layer contains the main source of turbulent energy. The process of streak formation in the viscous sublayer as well as the quantitative description of the quasi-organized flow structures in the buffer layer have been analyzed in detail. A consequence of these results is the progress made in the field of active control of the boundary layer. However, less attention has been given to the outer region of the boundary layer. In this context our motivations to study coherent structures in clear water flow are the following:

- Identify the types of coherent structures appearing in the outer and free surface flow regions from direct three-dimensional, quasi-instantaneous velocity measurements.
- Estimate the dynamical interactions between the inner and the outer domains of the turbulent boundary layer.
- The dynamics of coherent structures and their relation to bottom shear stress and corresponding bed roughness.
- Determine the appropriate scaling variables for the temporal and spatial characteristics of the quasi-organized flow eddies.
- Determine the entrainment ability of the macroscopic structural features over the entire boundary layer depth.

Solid particle transport by a turbulent flow is still considered an unsolved problem. Most of the existing models rely on mean quantities which do not take into account the finescale physical phenomena occuring in the boundary layer. Almost all the studies on coherent structure are focused on their dynamical interactions in a clear water shear flow. Few investigations on the impact of the quasi-organized turbulent eddies on the particle movement are found in the literature. We will therefore investigate these aspects with the objective to provide quantitative results on the particle transport capacity of coherent structures in open-channel suspension flows. In addition to that, we will tackle the possibilities to develop suspended sediment transport models based on characteristic scales of quasi-organized structures.

The study of turbulent transport mechanisms in open-channel flows proposed here will only be possible with adequate flow measuring techniques and the corresponding field deployable instruments. Over the past decade, high resolution multistatic ultrasonic velocity profilers working with coherent demodulation of the backscattered Doppler phase have found an increasing interest in the fields of fluid dynamics, physical oceanography and more recently, sediment transport and river hydrodynamics. They have shown their advantage particularly in field applications where the presence of particulate matter often does not allow measurements by other techniques. More recently, oceanic research has focused increasingly upon boundary layer studies in nearshore and coastal environments and in benthic boundary layers. In these applications, the depth range of interest is relatively short (about 1 m). Due to limitations inherent in “noncoherent” sonars, such instruments can no longer be used efficiently. Point measurement techniques have been applied in this environment. However, acoustic profiling using the “pulse-to-pulse” coherent technique offers an attractive alternative because it can cover the total depth range of interest in the boundary layer, and it is non-intrusive. Its suitability for river and oceanic studies is now established.

In this context, the objectives regarding the device development are the following:

- Develop a non-intrusive three-dimensional profiler of the quasi-instantaneous velocity field over the entire boundary layer height.

- Increase the velocity, spatial and time resolutions of the sonar to O(1 mm/s), O(1 mm) and O(10 ms) in order to undertake a quantitative study of the scales of coherent flow structures.

- Conceive a field deployable instrument adapted to shallow depth river measurements.

1.3 Thesis outline

The research study presented in this thesis is composed of two parts. The first part is concerned with the hydrodynamics of turbulent open-channel flows. The second part presents an acoustic measuring technique and the corresponding instrument which can profile the turbulent flow field.

Part one deals with the following subjects: Chapter 2 introduces the theoretical mean flow conservation equations for a subcritical, uniform and highly turbulent open-channel flow. Chapter 3 investigates the importance of coherent structures on turbulent transport processes in clear water as well as particle laden open-channel flows. Two conditional sampling methods are described in order to estimate the dynamics of coherent structures. Chapter 4 analyses the higher order statistical properties of coherent structures and their relation to the mean turbulent energy budget in clear water conditions. The wall similarity concept is discussed and validated in terms of its relation to statistical characteristics of quasi-organized eddies. Based on these results, a methodology for mean bed friction velocity determination is proposed. Chapter 5 analyses the particle entrainment ability of coherent structures in saturated suspension flows. Higher order statistical properties of mass flux and shear stress are estimated. The transport capacity of coherent structures is evaluated over the entire boundary layer height. Chapter 6 is a discussion of a recently developed sediment transport model based on characteristic scales of coherent structures. The model relates the near bed equilibrium concentration in suspension flows to temporal and spatial scales of coherent structures.

Part two deals with following topics: Chapter 1 presents the development and realization of the 3-D Acoustic Doppler Velocity Profiler (ADVP). The theoretical description of the ultrasonic Doppler signal is given. A detailed signal analysis is provided in order to identify the noise sources. The selected signal treatment algorithms are described. The hardware and software realizations are reported. Chapter 8 is concerned with the presentation of a constant beamwidth piezoelectrical transducer used as an emitter for the ADVP. Chapter 9 proposes a correction method of the ADVP Doppler signal in turbulent medium. Chapter 10 summarizes the main results of this work.

PART I

HYDRODYNAMICS OF OPEN-CHANNEL FLOW

CHAPTER 2

UNIFORM OPEN-CHANNEL FLOWS OVER SMOOTH AND ROUGH BEDS

2.1 Introduction

This chapter is devoted to the write-up of the mathematical framework for the experimental studies undertaken in this thesis. A detailed analysis of the equations, essentially based on the literature results, will be presented out here.

The hydrodynamic of incompressible flows is governed by the fundamental conservation equations of mass and momentum. These equations as well as the Reynolds stress and the energy budget equations (which are derived from the momentum equation) will be reported in the first paragraph for the case of a *uniform, subcritical, highly turbulent, clear water, open-channel flow*. The channel is straight, *prismatic*, with a rectangular cross section according to the conditions of the experiments conducted in the laboratory. The last two sentences contain statements which define the type of the studied flows. Their definition and mathematical implications are given here :

- A *clear water open-channel flow* is a natural or constructed channelized free surface water flow where the gravitational accelaration appears to be the fluid's motion driving force per unit mass of fluid. Consequently, a non-zero bed slope value is necessary for the initiation of fluid motion. Clear water means that the medium is monophasic, i.e. that no phase other than water is taking into account in the theoretical expressions. The presence of the free surface plays a crucial role in terms of the boundary layer's height. Indeed, since it is equal to 99% of the total water depth, the flow regions subdividing the boundary layer have dimensions specific to open-channel flows (see paragraph 2.3.1).

- Two hydrodynamic regimes known as subcritical flow and supercritical flow, exist dependent on the value of the bed slope. The physical criterium taken to determine whether the flow is *subcritical* or supercritical, is called the Froude number $\mathrm{Fr} = \mathrm{U} / \sqrt{\mathrm{gh_n}}$. U, g and $\mathrm{h_n}$ are the flow velocity averaged over the cross-section, the gravitational acceleration and the water depth in uniform flow conditions, respectively. It is defined as the ratio between the mean inertia force and the gravity force which in all the cases studied herein, is lower than unity ($0.3 \le \mathrm{Fr} \le 0.8$). Hence, subcritical flows are investigated.

- All experiments are carried out under *uniform* flow conditions. Regarding the flow equations, this assumption implies the elimination of all partial derivatives $\partial/\partial x$ in the main direction of the flow (Graf and Altinakar, 1998). Furthermore, all mean flow quantities, including the higher order mean turbulence characteristics, do not vary along the main flow axis. This condition leads to important simplification of the flow equations.

- A highly turbulent flow is characterized by a Reynolds number $Re = Uh_n/\nu$ significantly higher than the critical Reynolds number value Re_c (O(1000)). ν represents the kinematic viscosity. In the present study, all the investigated flows have Reynolds numbers as large as (O(10000)) and hence, satisfy the fully developed turbulence condition. The corresponding physical interpretation denotes that the mean inertia force acting on a finite volume of the fluid is O(10000) times higher than the friction forces due to molecular viscosity. Thus, when the Navier-Stokes equations are written in dimensionless form such that the Reynolds number is brought to the fore (Ryhming, 1985), the fully developed turbulence condition allows to neglect the terms which are proportional to the inverse Reynolds number. Nevertheless, in shear flows such as open-channel flows, this simplification is not valid very close to the bed in the so-called viscous sublayer where effects of molecular viscosity prevail.

- In a *prismatic* channel, the bed slope and roughness do not vary in the main flow direction.

In the second part of this chapter the characteristics of the flows corresponding to these conditions will be discussed and interpretated on the basis of well accepted literature data. Particular attention will be given to the effects of bed roughness. Experimental results as well as numerical results will be presented. However, their validity, reliability or accuracy will not be examined. The purpose is to discuss the flow characteristics in relation to the theoretical expressions given in the first part.

Eulerian variables are considered for all equations in this chapter. The instantaneous velocity vector is defined as $\vec{V} = u\,\vec{i} + v\,\vec{j} + w\,\vec{k}$, where u, v, w are the instantaneous velocity components in the main flow direction, transverse direction, vertical direction, respectively. The vectors $\vec{i}, \vec{j}, \vec{k}$, are the unity vectors of the Cartesian coordinate system with its origin located at the channel's bed and center. The directions of the $\vec{i}, \vec{j}, \vec{k}$, unity vectors are colinear to the constant bed slope, perpendicular to the main flow direction and perpendicular to the bed plane, respectively. The positive directions on the x, y, z, axes are taken in the flow direction, from the center to the left bank of the channel and from the bed to the free surface, respectively. The following Reynolds decomposition is adopted:

$$\begin{cases} u(t) = \overline{u} + u'(t) \\ v(t) = \overline{v} + v'(t) \\ w(t) = \overline{w} + w'(t) \end{cases} \quad \text{with} \quad \begin{cases} \overline{u} = \int_0^T u(t)\,dt \\ \overline{v} = \int_0^T v(t)\,dt \\ \overline{w} = \int_0^T w(t)\,dt \end{cases} \quad \text{and} \quad \begin{cases} \int_0^T u'(t)\,dt = 0 \\ \int_0^T v'(t)\,dt = 0 \\ \int_0^T w'(t)\,dt = 0 \end{cases} \tag{2.1}$$

where t is the time variable, the prime and the overbar denote the time fluctuating and time averaged components, respectively. The time interval T has to be large enough in order to obtain statistical stationarity for all estimated statistical moments. At some locations in the following text, Einstein's notation convention will be used for writing a general form of an equation.

2.2 Two-dimensional mean flow equations

Although three dimensional analysis of the flow quantities has brought to light many recent results regarding the structure of turbulence (see Chapter 3), the classical theory of two-dimensional mean flows using the statistical theory of turbulence, remains a fundamental base for the investigation of more complex phenomena. A two-dimensional approach of an open-channel flow leads to a simplified form of the investigated flow equations because it suggests that the velocity field is written as follows:

$$\overline{\vec{V}} = \overline{\vec{V}}(\overline{u},0,0) \quad \text{with} \quad \overline{u} = \overline{u}(z);\ \overline{v} = 0;\ \overline{w} = 0 \tag{2.2}$$

As pointed out by Nezu and Nakagawa (1984), a two-dimensional, open-channel flow approximation is valid at the center of wide channels with aspect ratios values B/h greater than 6. This geometrical condition implies that the effects of the helical secondary currents with mean longitudinal vorticity can be neglected. This secondary motion (also called secondary currents of Prandtl's second kind) is induced by the turbulence anisotropy near the banks of a channel. For narrow channels (B/h<6), the helical flow patterns symmetrical to the centerline can generate a velocity dip phenomena at the center implying that the flow can no longer be considered as two-dimensional in the mean. As will be demonstrated later, the aspect ratios of the flows analyzed herein always exceed the critical value of 6.

2.2.1 Equation of mass conservation

The differential form of the principle of mass conservation (also called the continuity principle) is written as follows :

$$\frac{D\rho}{Dt} = \frac{\partial \rho}{\partial t} + \vec{\nabla} \cdot \rho \vec{V} = 0 \quad \text{with} \quad \vec{\nabla} = \partial/_{\partial x} \cdot \vec{i} + \partial/_{\partial y} \cdot \vec{j} + \partial/_{\partial w} \cdot \vec{k} \tag{2.3}$$

where ρ is the fluid density, D/Dt represents the total derivative, $\vec{\nabla}$ is called the "nabla" operator. For incompressible flows (i.e. ρ is constant), one-directional flow in mean ($\overline{\vec{V}}(\bar{u},0,0)$), uniform and stationary conditions (i.e. no time variation of any statistical moment), Eq. (2.3) becomes:

$$\vec{\nabla} \cdot \vec{V} = 0 \qquad \text{with} \qquad \begin{cases} \vec{\nabla} \cdot \overline{\vec{V}} = \dfrac{\partial \bar{u}}{\partial x} = 0 \\ \vec{\nabla} \cdot \vec{V}' = \dfrac{\partial u'}{\partial x} + \dfrac{\partial v'}{\partial y} + \dfrac{\partial w'}{\partial z} = 0 \end{cases} \tag{2.4}$$

2.2.2 Equation of momentum conservation

The differential form of the principle of momentum conservation yields:

$$\frac{D}{Dt} \rho \vec{V} - \vec{\nabla} \overline{\overline{\sigma}} = \rho \vec{f} \tag{2.5}$$

where $\overline{\overline{\sigma}} = \overline{\overline{\tau}} - p\overline{\overline{I}}$ is called the stress tensor. $\overline{\overline{\tau}}$ is the stress tensor due to molecular viscosity of the fluid which in the case of highly developed turbulence conditions and for an incompressible flow, can be neglected. $\overline{\overline{I}}$ is equal to the two-dimensional identity tensor. p is the local pressure. Hence:

$$\frac{\partial}{\partial t} \rho \vec{V} + \vec{\nabla}\left(\rho \vec{V} \vec{V}\right) = -\overrightarrow{\mathrm{grad}}\; p + \rho \vec{f} \tag{2.6}$$

Eq. (2.6) reveals that the temporal variation rate of momentum (first term of the left hand side part) is driven by the convective transport (second term on the left hand side) as well as by the two source terms on the right hand side (corresponding to the surface and volume forces per unit volume). Under this so-called conservative form of the momentum equation, the analogy with the continuity equation becomes obvious. Two-dimensionality of the flow implies that:

$$\begin{cases} \frac{\partial}{\partial t}\rho u + \frac{\partial}{\partial x}\rho u^2 + \frac{\partial}{\partial z}\rho uw = -\frac{\partial p}{\partial x} + \rho g \sin\alpha \\ \frac{\partial}{\partial t}\rho w + \frac{\partial}{\partial x}\rho uw + \frac{\partial}{\partial z}\rho w^2 = -\frac{\partial p}{\partial z} + \rho g \cos\alpha \end{cases} \tag{2.7}$$

The last term of the right hand side of the first equation in Eq. (2.7) is the driving force per unit volume which characterizes free surface open-channel flows. It is equal to the projection on the x-axis of the gravitational acceleration. Consequently, its amplitude is dependent on the bed slope S_0 which in the case of a small angle α between the bed plane and the horizontal plane, can be approximated by $S_0 = \tan\alpha \cong \sin\alpha$. As mentioned previously, the small bed slope hypothesis is related to the subcritical flow regime.

Inserting Eq. (2.1) in Eq. (2.7) and assuming stationarity, uniformity and one-directional mean flow $\vec{V}(\bar{u},0,0)$, results in:

$$\begin{cases} \frac{\partial}{\partial t}\rho u' + \frac{\partial}{\partial x}\rho u'^2 + \frac{\partial}{\partial z}\rho(\bar{u}+u')w' = -\frac{\partial p'}{\partial x} + \rho g S_0 \\ \frac{\partial}{\partial t}\rho w' + \bar{u}\frac{\partial}{\partial x}\rho w' + \frac{\partial}{\partial x}\rho u'w' + \frac{\partial}{\partial z}\rho w'^2 = -\frac{\partial}{\partial z}(\bar{p}+p') + \rho g \cos\alpha \end{cases} \tag{2.8}$$

Taking the time average of Eq. (2.8) and taking into account the third statement in Eq. (2.1), gives:

$$\begin{cases} \rho\frac{\partial}{\partial z}\overline{u'w'} = \rho g S_0 \\ \rho\frac{\partial}{\partial z}\overline{w'^2} = -\frac{\partial}{\partial z}\bar{p} + \rho g \cos\alpha \end{cases} \tag{2.9}$$

Eq. (2.9) represents the momentum equation for a two-dimensional in the mean, stationary, uniform, highly turbulent open-channel flow. The mean shear stress τ_{zx} and modified hydrostatic pressure profiles are obtained by integrating Eq. (2.9) over the flow depth :

$$\begin{cases} \tau_{zx} = \rho u_*^2\left(1-\dfrac{z}{h}\right) \\ \overline{p} = \rho g\cos\alpha(h-z) - \rho\overline{w'^2} \end{cases} \tag{2.10}$$

where $u_* = \sqrt{\tau_0/\rho}$ represents the mean bed friction velocity at the center of the channel and τ_0 is the shear stress at the bed. h is the flow depth in uniform flow conditions. The first expression of Eq. (2.10) indicates that the shear stress profile is linear over the depth. The second indicates that the hydrostatic pressure distribution is modified by the normal stress term due to turbulence.

2.2.3 Equation of Reynolds stress conservation

In order to derive the Reynolds stress equation for an incompressible flow, the general form of the momentum equation (Eq. (2.6)) is considered as follows:

$$\begin{cases} \dfrac{\partial u}{\partial t} + \dfrac{\partial}{\partial x}u^2 + \dfrac{\partial}{\partial y}uv + \dfrac{\partial}{\partial z}uw = -\dfrac{1}{\rho}\dfrac{\partial p}{\partial x} + \nu\nabla^2 u + gS_0 \\ \dfrac{\partial v}{\partial t} + \dfrac{\partial}{\partial x}vu + \dfrac{\partial}{\partial y}v^2 + \dfrac{\partial}{\partial z}vw = -\dfrac{1}{\rho}\dfrac{\partial p}{\partial x} + \nu\nabla^2 v \\ \dfrac{\partial w}{\partial t} + \dfrac{\partial}{\partial x}wu + \dfrac{\partial}{\partial y}wv + \dfrac{\partial}{\partial z}w^2 = -\dfrac{1}{\rho}\dfrac{\partial p}{\partial x} + \nu\nabla^2 w + g\cos\alpha \end{cases} \tag{2.11}$$

where ν is the kinematic viscosity of water meaning that the stress terms due to molecular effects are taken into account. $\nabla^2 = \partial^2/\partial x^2 + \partial^2/\partial y^2 + \partial^2/\partial z^2$ represents the Laplacian operator. Applying the continuity equation, Eq. (2.4), yields:

$$\begin{cases} \dfrac{\partial u}{\partial t} + u\dfrac{\partial u}{\partial x} + v\dfrac{\partial u}{\partial y} + w\dfrac{\partial u}{\partial z} = -\dfrac{1}{\rho}\dfrac{\partial p}{\partial x} + \nu\nabla^2 u + gS_0 \\ \dfrac{\partial u}{\partial t} + u\dfrac{\partial v}{\partial x} + v\dfrac{\partial v}{\partial y} + w\dfrac{\partial v}{\partial z} = -\dfrac{1}{\rho}\dfrac{\partial p}{\partial y} + \nu\nabla^2 v \\ \dfrac{\partial u}{\partial t} + u\dfrac{\partial w}{\partial x} + v\dfrac{\partial w}{\partial y} + w\dfrac{\partial w}{\partial z} = -\dfrac{1}{\rho}\dfrac{\partial p}{\partial z} + \nu\nabla^2 w + g\cos\alpha \end{cases} \tag{2.12}$$

The time-averaged components of Eq. (2.12) are then substracted from the corresponding time-dependent component of Eq. (2.12). To obtain the dynamic equation of the Reynolds stress term $\rho u_i' u_j'$, the resulting equation of the component i is then multiplied with the component v' and added to the j-component multiplied by u'. Finally, time averaging results in the following $\rho\overline{u_i'u_j'}$-equations (see Hinze, 1975 for details):

$$\begin{aligned}\frac{\partial}{\partial t}\overline{u'^2} &= -\frac{\partial}{\partial z}\overline{u'^2 w'} + \nu\frac{\partial^2}{\partial z^2}\overline{u'^2}\\ &\quad -2\nu\overline{\left(\frac{\partial u'}{\partial x}\right)^2+\left(\frac{\partial u'}{\partial y}\right)^2+\left(\frac{\partial u'}{\partial z}\right)^2}\\ &\quad +\frac{2}{\rho}\overline{p'\frac{\partial u'}{\partial x}}\\ &\quad -2\overline{u'w'}\frac{\partial\bar{u}}{\partial z}\end{aligned} \tag{2.13}$$

$$\begin{aligned}\frac{\partial}{\partial t}\overline{v'^2} &= -\frac{\partial}{\partial z}\overline{v'^2 w'} + \nu\frac{\partial^2}{\partial z^2}\overline{v'^2}\\ &\quad -2\nu\overline{\left(\frac{\partial v'}{\partial x}\right)^2+\left(\frac{\partial v'}{\partial y}\right)^2+\left(\frac{\partial v'}{\partial z}\right)^2}\\ &\quad +\frac{2}{\rho}\overline{p'\frac{\partial v'}{\partial y}}\end{aligned} \tag{2.14}$$

$$\begin{aligned}\frac{\partial}{\partial t}\overline{w'^2} &= -\frac{\partial}{\partial z}\overline{w'^3} - \frac{2}{\rho}\frac{\partial}{\partial z}\overline{p'w'} + \nu\frac{\partial^2}{\partial z^2}\overline{w'^2}\\ &\quad -2\nu\overline{\left(\frac{\partial w'}{\partial x}\right)^2+\left(\frac{\partial w'}{\partial y}\right)^2+\left(\frac{\partial w'}{\partial z}\right)^2}\\ &\quad +\frac{2}{\rho}\overline{p'\frac{\partial w'}{\partial z}}\end{aligned} \tag{2.15}$$

$$\begin{aligned}\frac{\partial}{\partial t}\overline{u'w'} &= -\frac{\partial}{\partial z}\overline{u'\left(w'^2+\frac{p'}{\rho}\right)} + \nu\frac{\partial^2}{\partial z^2}\overline{u'w'}\\ &\quad -2\nu\overline{\frac{\partial u'}{\partial x}\frac{\partial w'}{\partial x}} - 2\nu\overline{\frac{\partial u'}{\partial y}\frac{\partial w'}{\partial y}} - 2\nu\overline{\frac{\partial u'}{\partial z}\frac{\partial w'}{\partial z}}\\ &\quad +\overline{\frac{p'}{\rho}\left(\frac{\partial w'}{\partial x}+\frac{\partial u'}{\partial z}\right)}\\ &\quad -\overline{w'^2}\frac{\partial\bar{u}}{\partial z}\end{aligned} \tag{2.16}$$

In Eqs. (2.13) to (2.16) the left hand side is the total rate of change of the corresponding stress term including the local temporal and convective rates of change. Although these terms can be omitted in the case of uniform and steady flow conditions, they are maintained here for a general interpretation of the expressions.

The first lines of the right hand side contain the diffusive transport terms related to the non-homogeneous flow field in the vertical direction. The diffusive transport terms due to viscous effects are proportional to the kinematical viscosity ν which in the case of fully developed turbulence conditions are negligibly small compared to the turbulent diffusion terms. The viscous dissipation, pressure-strain and turbulent energy production terms are represented in the second, third and last lines, respectively. The signs of these terms will reveal whether these local mechanisms contribute or not to energy loss.

As mentioned above, the total rate of change of the Reynolds stress terms are equal to zero for the flow conditions investigated herein. Hence, local equilibrium for each stress component is observed by the contribution of production, dissipation, diffusive transport and pressure strain processes.

Two-different production terms can be found in the fourth lines of Eq. (2.13) and Eq. (2.16). Subsequently, the production mechanism appears to only act on the longitudinal normal stress term as well as on the shear stress term in a non-isotropical way since the vertical and transverse normal stress terms are not affected by direct production mechanisms. Furthermore, based on the flow characteristics reported in the literature, it will be discussed in section 2.3.2 whether these terms make positive or negative contributions and their relative role in a global turbulence concept.

The production mechanism of turbulent energy in shear flows such as in open-channel flows, is by definition non-isotropic. Therefore, the pressure strain terms are responsible for the redistribution of turbulent energy towards isotropy between the different Reynolds stress components. These quantities are essential parameters in turbulence related transport phenomena. Very little is known so far on their quantitative contribution.

The viscous dissipation is responsible for the conversion of the turbulent energy into heat contained in the small scale structures or vice versa and therefore results in a direct loss or gain of kinetic energy.

2.2.4 Equation of energy conservation

The differential form of the principle of energy conservation yields:

$$\frac{D}{Dt}\rho(e+E)+\vec{\nabla}\cdot\vec{Q}+\vec{\nabla}\cdot\left(\overline{\overline{\sigma}}\cdot\vec{V}\right)=\rho\vec{f}\cdot\vec{V} \tag{2.17}$$

where e and E correspond to the internal and kinetic energy of the fluid, respectively. The term $\vec{\nabla}\cdot\vec{Q}$ is the total energy variation per unit time and volume of the total energy related to thermal conductivity. The conservation principle of the internal energy, which can be separated from the conservation principle of the kinetic energy of the fluid, leads to the first law of thermodynamics. Since in this thesis, the study is restricted to incompressible and highly turbulent flows with constant properties, only the balance of the local rate of change of the kinetic energy E is of interest. Thus, Eq. (2.18) becomes

$$\rho\frac{D}{Dt}E-\vec{\nabla}\cdot\left(\overline{\overline{\sigma}}\cdot\vec{V}\right)=\rho\vec{f}\cdot\vec{V} \tag{2.18}$$

Or,

$$\frac{\partial}{\partial t}E+\left(\vec{\nabla}\cdot\vec{V}\right)E=-\frac{1}{\rho}\vec{V}\cdot\overrightarrow{\text{grad}}\,p-\chi+\vec{g}\cdot\vec{V} \tag{2.19}$$

The left hand side of Eq. (2.19) accounts for the local temporal and advective variation of the total kinetic energy. The first term of the right hand side represents the work due to the pressure gradient, χ is the direct conversion of the total kinetic energy E and the last term of the right hand side is the work done by the gravity force. The work done by the viscous stresses are neglected in this equation since fully developed turbulence conditions are assumed. The total mean kinetic energy can written as follows:

$$\begin{aligned}
&E=\frac{1}{2}\left[\left(\bar{u}+u'\right)^2+\left(\bar{v}+v'\right)^2+\left(\bar{w}+w'\right)^2\right]=\overline{K}+\bar{u}u'+\bar{v}v'+\bar{w}w'+\frac{1}{2}k^2\\
&\overline{E}=\frac{1}{2}\left[\overline{\left(\bar{u}+u'\right)^2+\left(\bar{v}+v'\right)^2+\left(\bar{w}+w'\right)^2}\right]=\overline{K}+\frac{1}{2}\overline{k^2}\\
&\text{with}\quad \overline{K}=\frac{1}{2}\left(\bar{u}^2+\bar{v}^2+\bar{w}^2\right)\quad\text{and}\quad \overline{k^2}=\overline{u'^2}+\overline{v'^2}+\overline{w'^2}
\end{aligned} \tag{2.20}$$

where $\overline{K}$ and $(1/2)\overline{k^2}$ are the kinetic energy of the mean motion and the mean turbulent kinetic energy of the fluid, respectively.

For two-dimensional mean flow, the conservation equation of energy for the mean motion $\overline{K}$ is obtained by multiplying the x-component of Eq. (2.9) with the mean longitudinal velocity $\overline{u}$:

$$\frac{\partial \overline{K}}{\partial t} = -\overline{u}\frac{\partial}{\partial z}\overline{u'w'} + \overline{u}gS_0 = \overline{u'w'}\frac{\partial \overline{u}}{\partial z} - \frac{\partial}{\partial z}\overline{u}\,\overline{u'w'} + \overline{u}gS_0 \tag{2.21}$$

Stationary and uniform flow conditions imply that the left hand side of Eq. (2.21) is equal to zero. The direct conversion term $\nu(\partial\overline{u}/\partial z)^2$ of the mean motion energy is not taken into account in Eq. (2.21) since viscous effects were neglected in the momentum conservation equations for high Reynolds number conditions.

The equation of conservation of the mean turbulent kinetic energy is derived by taking the trace of the Reynolds stress tensor multiplied by the factor 1/2. Therefore, combining Eq. (2.13) with Eq. (2.14) and Eq. (2.15) yields:

$$\frac{1}{2}\frac{\partial}{\partial t}\overline{k^2} = -\overline{u'w'}\frac{\partial \overline{u}}{\partial z} - \frac{\partial}{\partial z}\overline{w'\left(\frac{p'}{\rho} + \frac{1}{2}k^2\right)} - \varepsilon \tag{2.22}$$

where the vertical diffusive transport due to molecular effects has been neglected compared to the vertical diffusive transport due to turbulence. Eq. (2.22) can also be derived directly from the substraction of Eq. (2.21) from Eq. (2.19) in which the Reynolds decomposition (Eq. (2.1)) and subsequent averaging with respect to time have been applied.

Stationary flow conditions imply that the left hand side of the last equation is equal to zero. The first term of the left hand side is the work done by the turbulent stress in the mean flow deformation over the flow depth per unit of time. This term originates from the normal turbulent stress in x-direction (Eq. (2.13)) and appears with opposite sign in the conservation equation of energy for the mean motion Eq. (2.21). Consequently, depending on the sign of the two terms which compose the production term, energy is lost or gained by the mean motion and thus, gained or lost by the turbulent flow field, respectively.

The last term of Eq. (2.22) represents the total mean dissipation into heat of turbulent kinetic energy or vice versa if the sign of ε would be negative.

An important feature of Eq. (2.22) concerns the absence of the pressure strain terms due to the assumption of incompressibility. Although these terms enter in the Reynolds stress balance for each component, no local effect exist on the turbulent kinetic energy budget. Hence, the role of the pressure strain in terms of turbulent energy redistribution over the normal stress components appears to be relevant.

2.3 Flow charateristics in smooth and rough bed conditions

The present section is concerned with the interpretation of the previously derived theoretical flow equations on the basis of flow characteristics reported in the literature. A detailed analysis of the relative order of magnitude and the sign of each term involved in the above differential equations is necessary. In order to present a general description of the investigated dynamical flow process, even though the quantitative results are still rather meager because of the lack of data, a qualitative modelization allows, at least, to distinguish to what extent turbulence related transport phenomena are complex and unsolved. Subsequently, a meaningful research topic relative to the state of the art of turbulence research, can be developed.

2.3.1 Mean velocity field and repartion of the flow field

Mean velocity field

Since Eq. (2.9) can not be integrated directly, the phenomenological mixing length concept of Prandtl (1925) can be used in order to obtain the mean velocity profile. It is based on two assumptions:

- The shear stress is constant over the entire flow depth and is equal to its value τ_0 at the wall.
- The mixing length is proportional to the coordinate z (i.e. the distance from the wall) in the wall region ($z/h < 0.2$). The proportionality factor corresponds to the universal von Karman constant κ.

These assumptions lead to:

$$d\bar{u} = \frac{\sqrt{\tau_0/\rho}}{\kappa\, z}\, dz \tag{2.23}$$

which, after integration, results in:

$$\frac{\bar{u}}{u_*} = \frac{1}{\kappa}\left[\ln(z) - \ln(z_0)\right] \tag{2.24}$$

The mean velocity $\bar{u}$ is assumed to be equal to zero at depth z_0. As suggested by the two hypothesis, this formulation is valid only for $z/h < 0.2$. Nevertheless, Eq. (2.24) is often applied to the entire flow depth for a first approximation of the mean velocity distribution. Based on a large number of experiments (Cardoso et al., 1989; Kironoto and Graf, 1993), the following constants have been obtained:

$$\frac{\bar{u}}{u_*} = \frac{1}{\kappa}\left[\ln(zu_*/\nu) + B_S\right] \quad \text{with } B_S = 5\,(\pm\,25\%) \tag{2.25}$$

$$\frac{\bar{u}}{u_*} = \frac{1}{\kappa}\left[\ln(z/k_S) + B_R\right] \quad \text{with } B_R = 8.5\,(\pm\,15\%) \tag{2.26}$$

Eq. (2.25) accounts for flows over smooth beds whereas Eq. (2.26) is used for flows with uniform bed roughness. k_S is the equivalent sand roughness defined by Nikuradse. He showed that in the case of pipe flows with wall roughness composed of uniform sand grains, the mean diameter d_{50} (taken at 50% of the granulometric curve) is a good approximation of the roughness height k_S. The equivalent roughness for most of uniformly distributed roughnesses is deduced from the friction law. The relative roughness number $k_S^+ = k_S u_*/\nu$ is generally accepted as the criteria used to distinguish three roughness situations known as:

- Smooth bed conditions: $k_S^+ < 5$
- Incompletely rough bed conditions: $5 \le k_S^+ \le 70$
- Completely rough bed conditions: $k_S^+ > 5$

As mentioned before, the log-law is only valid in the wall region of the flow. In the outer region of the flow, a deviation of the mean velocity from the log-law has been observed experimentally. Coles (1956) proposed to estimate the mean velocity distribution over the whole water depth (except in the viscous sublayer, i.e. for $z/h \le 0.05$) with the following velocity defect law:

$$\frac{\bar{u}_{max} - u}{u_*} = \frac{1}{\kappa}\ln\left(\frac{h}{z}\right) + \frac{2\Pi}{\kappa}\cos^2\left(\frac{\pi z}{2h}\right) \tag{2.27}$$

where Π is the so-called Cole's wake strength parameter dependent on the mean longitudinal pressure gradient (here the gradient is exceptionally defined relative to the horizontal plane). Kironoto and Graf (1993) have shown that for weak bed slopes $-0.1 \le \Pi \le 0.3$ independent of the bed roughness conditions.

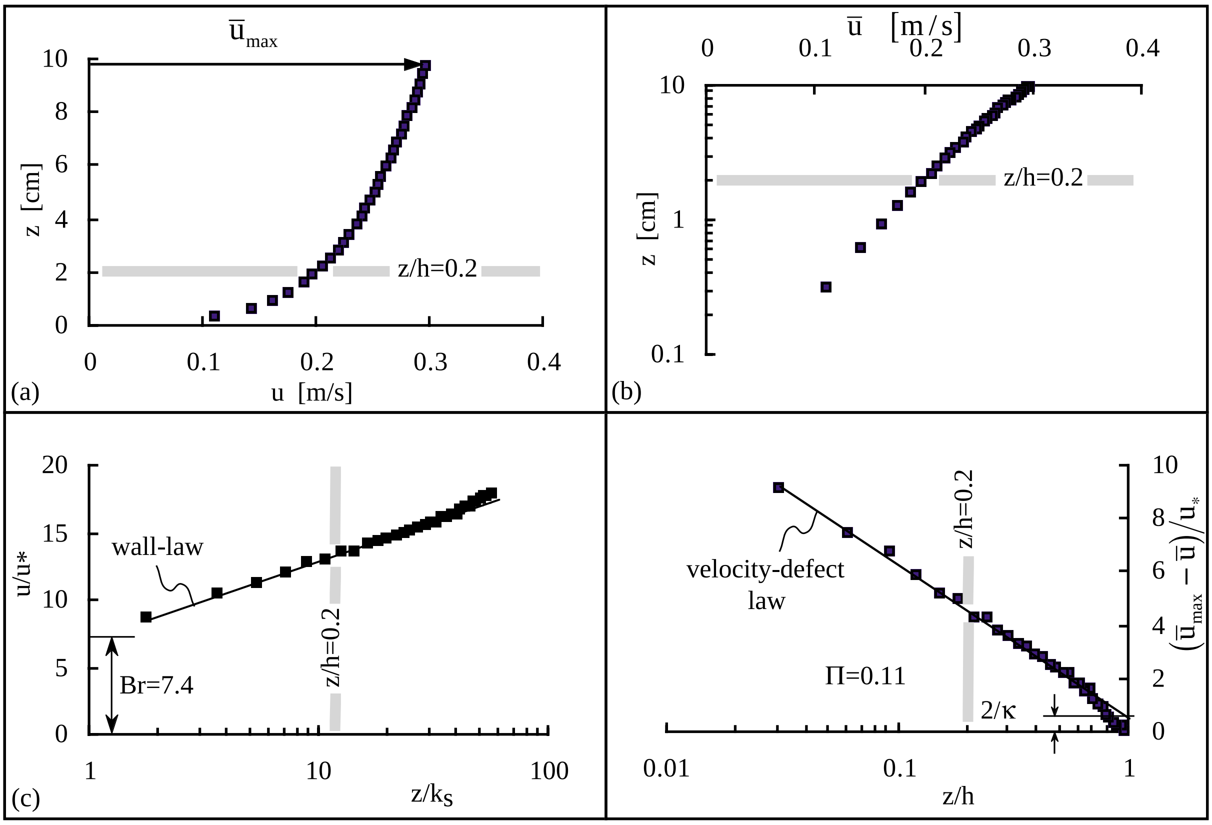

Fig. 2.1 Mean velocity measurements in an open-channel flow. (a) Mean longitudinal velocity profile. (b) Universal logarithmic velocity profile. (c) Wall-law validation in the inner flow region and evaluation of the constant B_R of the logarithmic profile. (d) Velocity-defect law validation and Π-factor evaluation of Cole's wake function.

Fig. 2.1a shows the mean longitudinal velocity profile taken at the center of a uniform open-channel flow over an incompletely rough bed with a value $k_S^+ \cong 36$ (Hurther and Lemmin, 2001). Fig. 2.1b represents the same measurements with a logarithmic scaling for the vertical distance z. Fig. 2.1c clearly demonstrates the validity of the logarithmic velocity distribution in the wall region. The deviation from the wall-law near to the water surface becomes obvious. A value of 0.11 has been obtained for the Π-factor of Cole's wake function (Fig. 2.1d) which agrees well with the results reported in Kironoto and Graf (1993).

Subdivision of the flow field

The total height of the boundary layer of an open-channel flow is defined by the vertical position of the velocity maximum $\bar{u}_{max}$. Usually, this height is equal to 99% of the flow depth although the presence of secondary currents in narrow channels (typically for channels with an aspect ratio smaller than 6) can reduce the vertical position of this velocity maximum. The local range of the flow scales found in the boundary layer changes as a function of the flow depth. These scales are used as characteristic scales for the normalization of the local statistical flow quantities. Three flow regions can be defined:

• In the inner region or wall region ($z/h < 0.2$) composed of

-the viscous sublayer ($zu_*/\nu \le 5$)

-the buffer layer, $5 \le zu_*/\nu \le 30$, where the bursting phenomenon and the associated maximal turbulent energy production take place

-the logarithmic region $30 < zu_*/\nu \le 500$.

The law of the wall is generally valid over the buffer layer and the logarithmic region. The characteristic scales, calculated from inner flow variables, of the phenomena occuring in this layer are of the order of magnitude of the viscous length $O(\nu/u_*)$. Many research efforts in the field of fluid dynamics are devoted to the understanding of the mechanisms found in this layer since it contains the initiation of the instability of turbulence.

• The outer region of the boundary layer is composed of the intermediate ($0.2 < z/h \le 0.6$) and the free surface flow regions ($0.6 < z/h \le 1$). In the intermediate flow layer, the characteristic scale is hardly affected by the wall effects (effects of molecular viscosity) or by free-surface effects. It is therefore difficult to determine whether inner, outer or combined flow variables are the adequate normalization parameters of the flow quantities. The scales present in the free-surface zone are defined by outer flow variables such as the flow depth or the maximal mean flow velocity for the length or velocity scales, respectively. Over the past decade, studies have dealt with the interaction mechanisms between wall turbulence and free-surface instabilities (Kumar et al., 1998; Smith et al., 1999) such as the one generated by additional wind-shear at the water surface, by the critical flow regime transition or by the combination of the two. An important number of structural flow features typical for free-surface flows are analyzed in minute detail. Among these are spiral eddies at the water-surface with normal vorticity component, boils, upwellings, downwellings. They are found to be relevant contributors in the gas transfer process at the air-water interface at a time when quantitative predictions of gas absorption by geophysical flows are needed in a variety of situations including global climate change or re-oxygenation of polluted rivers (Kumar et al., 1998).

It is noteworthy that no precise subdivision of the flow field is possible since several transport phenomena can occur over the full water depth and can subsequently result in a convection of the local flow structures towards other flow regions. Nevertheless, it is important to keep in mind that zones of the turbulent boundary layer where no mean turbulent transport processes occur but where mixing processes prevail, are well suited to determine some universal similarities, such as the wall similarity concept reported in Chapter 4.

2.3.2 Reynolds stresses and kinetic energy

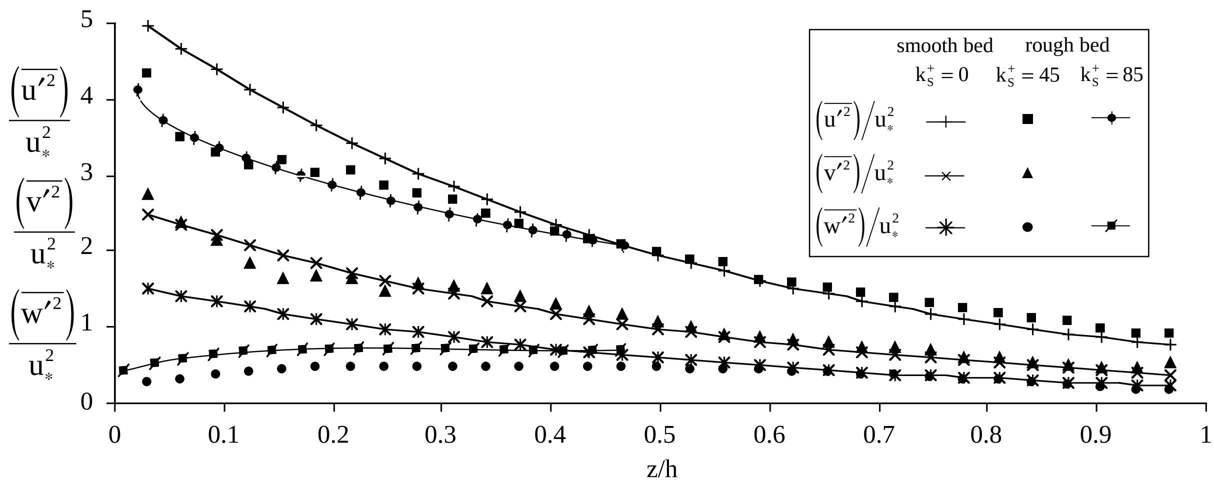

Fig. 2.2 Profiles of normal Reynolds stresses relative to the squared bed friction velocity, for smooth and rough bed conditions. (Hurther and Lemmin 2001)

As shown in section 2.2.2, the shear stress profile is derived directly from the momentum equation without any supplementary closure relation, whereas the previously presented equations do not allow a direct theoretical derivation of the normal stress profiles. Despite this fact, many experimental investigations (Kumar et al., 1998; Kironoto and Graf, 1993) have demonstrated the universal behaviour of the relative normal Reynolds stress profile and the relative turbulent kinetic energy profile (relative to the squared mean bed friction velocity). Universality is understood here in the sense of the independence of the Reynolds and Froude numbers of the flows. Fig. 2.2 presents the profiles of the relative normal stress over the flow depth, in the case of smooth and rough bed conditions. The relative turbulent kinetic energy and the relative shear stress profiles are shown in Fig. 2.3. For the smooth bed case ($k_S^+ = 0$), the following empirical formulations have been given by Nakagawa et al., (1975):

$$\begin{cases} \overline{u'^2}/u_*^2 = 5.29\exp(-2z/h) \\ \overline{v'^2}/u_*^2 = 2.65\exp(-2z/h) \\ \overline{w'^2}/u_*^2 = 1.61\exp(-2z/h) \\ \overline{k^2}/\left(2u_*^2\right) = 4.78\exp(-2z/h) \end{cases} \tag{2.28}$$

These curves are drawn in Fig. 2.2. For the rough bed case, measurements for different bed roughness conditions are shown. Grass (1971) measured the fluctuating velocity field in a free surface flume over a completely rough bed ($k_S^+ = 85$ meaning that the mean roughness height was greater than the height of the viscous sublayer) using a hydrogen bubble flow visualization technique. Data of Hurther and Lemmin (2001), collected in a flow over an incomplete rough channel bed ($k_S^+ = 45$), are also included in Fig. 2.2. Independently of the bed roughness conditions, the greatest amplitudes of all three components are found in the wall region where the production of turbulent kinetic energy is maximal. For the smooth case, the longitudinal stress is found to be 2 times and 3.28 times larger than the transverse and vertical stresses, respectively, over the entire flow depth. This observation can also be deduced qualitatively from the presence of the term $-\overline{u'w'}\partial\bar{u}/\partial z$ in the Reynolds stress equation for the $\overline{u'^2}$ component (Eq. (2.13)). From Fig. 2.1 and Fig. 2.3, the sign of $-\overline{u'w'}\partial\bar{u}/\partial z$ appears to be positive, implying that turbulent energy is produced only in form of normal stress $\overline{u'^2}$. Hence, the strong anisotropical behaviour of turbulence in shear flow becomes evident. From the data presented in Fig. 2.2 the following question arise: how can the existence of the components $\overline{v'^2}$ and $\overline{w'^2}$ be explained if turbulent energy is generated in form of normal stress $\overline{u'^2}$? In other words, by which process is the $\overline{u'^2}$ energy redistributed over the vertical and transverse normal stresses?

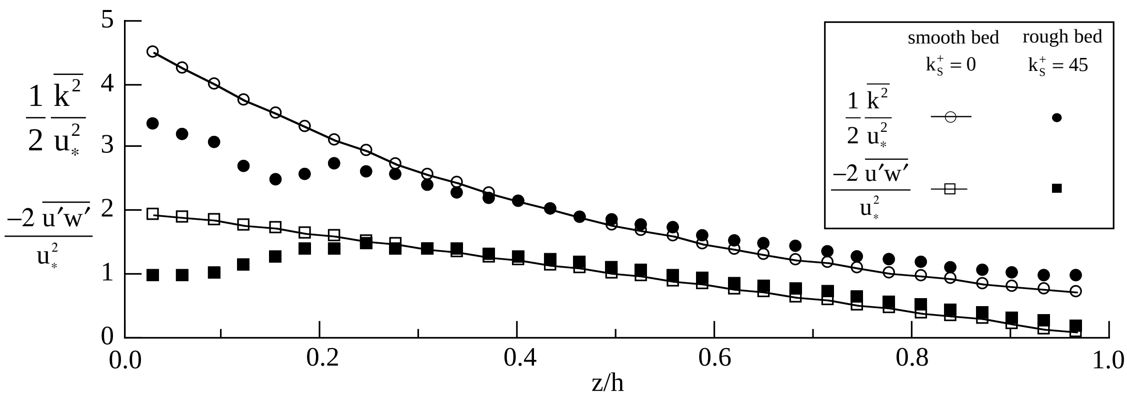

Fig. 2.3 Shear stress and turbulent kinetic energy profiles in open-channel flow over smooth and rough beds.

As mentioned in section 2.2.3, the pressure-strain terms are responsible for that mechanism. Since no direct measurement of these quantities can be found in the literature, the following conceptual model prevails: when a decceleration of the longitudinal velocity occurs, the term $\partial u'/\partial x$ becomes negative, thus we assume that the local fluctuating pressure p' is positive. Owing to the continuity equation Eq. (2.4), it follows that $\overline{p'(\partial v'/\partial y + \partial w'/\partial z)}$ is positive. Furthermore, since $\overline{u'^2} > 1/2\left(\overline{v'^2} + \overline{w'^2}\right)$ and no direct turbulent energy production term can be found in the Reynolds stress equations for the $\overline{v'^2}$ and $\overline{w'^2}$ components, it is assumed that on the average, $\overline{p'(\partial u'/\partial x)} < 0$, $\overline{p'(\partial v'/\partial y)} > 0$, and $\overline{p'(\partial w'/\partial z)} > 0$. It can be stated that the pressure strain term $\overline{p'(\partial u'/\partial x)}$ represents an energy loss for the $\overline{u'^2}$ component whereas the terms $\overline{p'(\partial v'/\partial y)}$ and $\overline{p'(\partial w'/\partial z)}$ contribute to an energy increase for the $\overline{v'^2}$ and $\overline{w'^2}$ components.

With similar reasoning, it can easely be demonstrated that the pressure strain term $\overline{p'(\partial w'/\partial x + \partial u'/\partial z)}$ in Eq. (2.16) acts as an energy loss for the $\overline{u'w'}$ component. Fig. 2.1 and Fig. 2.2 permit to recognize the positive sign of the term $\overline{w'^2}\,\partial\bar{u}/\partial z$ which implies that energy is produced since $\overline{u'w'} < 0$.

The above results concerning the normal stress profiles can be summarized as follows: the pressure-strain terms tend to reduce the local anisotropy generated by the shear stress term in such a way that the produced $\overline{u'^2}$ stress is transfered to the $\overline{v'^2}$ and $\overline{w'^2}$ normal stress components. On the other hand, the production of shear stress term $\overline{u'w'}$ is also dependent on $\overline{w'^2}$ which exhibits the highly non-linear behaviour of turbulence phenomena in open-channel flows. It clearly appears from the above qualitative results that these terms play a crucial role in turbulent transport processes. Unfortunately, direct measurements of local pressure-velocity correlations with high accuracy are extremely difficult. Consequently, linear pressure-strain correlation model have only been applied so far for numerical simulation by Launder et al. (1975), Naot and Rodi (1982). Some of their results will be used in paragraph 8.7 in order to compare them to direct Reynolds stress measurements.

While the profiles of relative normal stresses over smooth beds exhibits a universal distribution over the entire boundary layer, the relative normal stress distribution deviate from the curves given by Eq. (2.28) in the flow region $0 \le z/h \le 0.35$. One can observe from Fig. 2.3 that the mean relative shear stress profile on a rough bed is lower than the one over smooth beds. If we combine this information with the observed lower relative $\overline{u'^2}$ stress component in Fig. 2.2, it can be deduced that turbulent energy in uniform open-channel flow over rough beds is produced in a more isotropical form than over smooth channel beds.

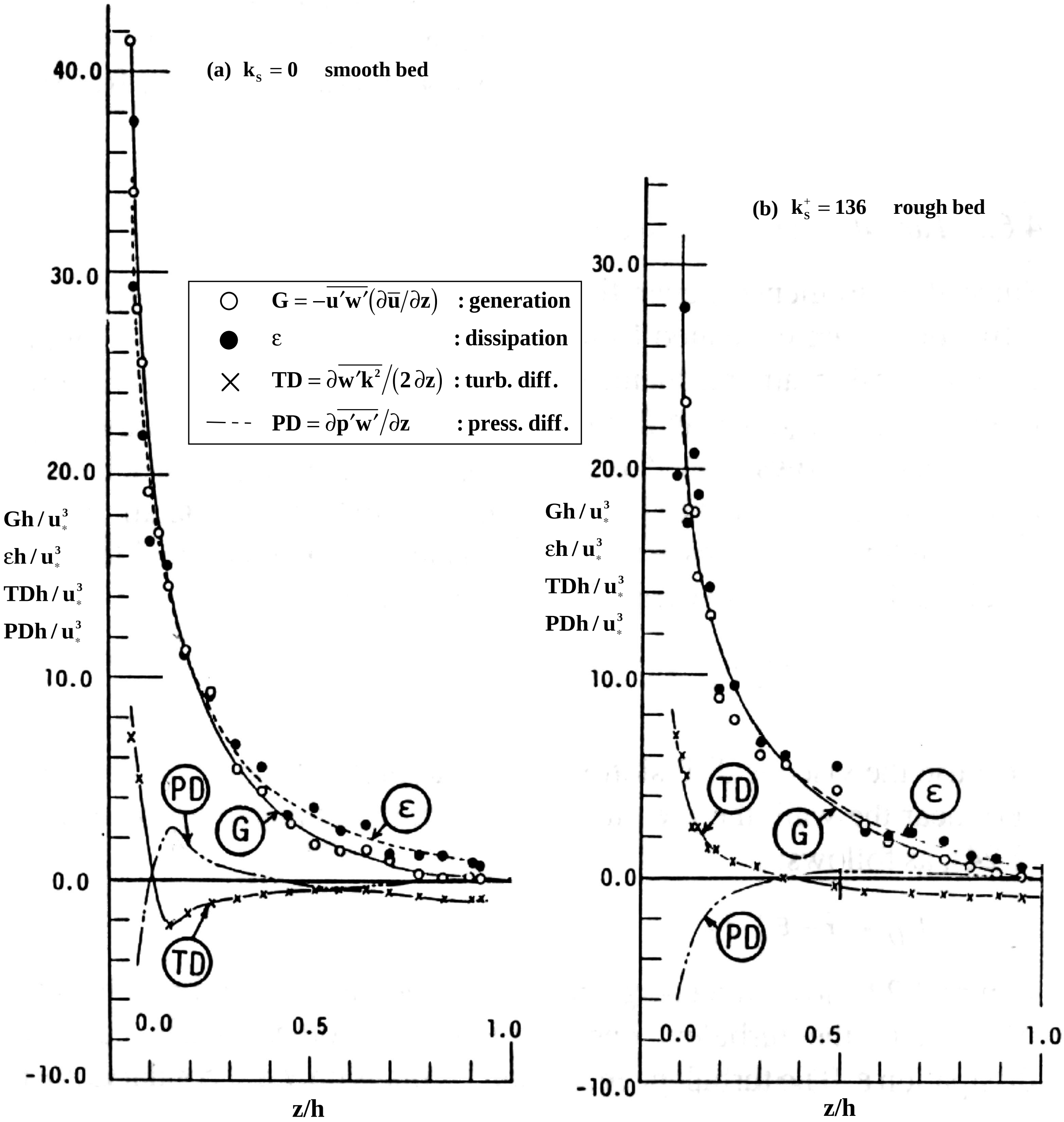

Fig. 2.4 Turbulent energy budget of 2D-mean open-channel flow over smooth and rough channel beds from Nezu and Nakagawa (1993).

In Fig. 2.4, the profiles of Nezu and Nakagawa (1993) represent the terms of the turbulent energy budget Eq. (2.22) with the following notation:

$$\frac{1}{2}\frac{\partial}{\partial t}\overline{k^2} = -\overline{u'w'}\frac{\partial\overline{u}}{\partial z} - \frac{\partial}{\partial z}\overline{w'\left(\frac{p'}{\rho} + \frac{1}{2}k^2\right)} - \varepsilon = G - PD - TD - \varepsilon \tag{2.29}$$

It can be seen from Fig. 2.4a ($k_S^+ = 0$) that the terms G and ε are positive, corresponding to an energy production and dissipation, respectively. Subsequently, the term -G in Eq. (2.21) indicates an energy loss or extraction from the mean flow. Additionally, the dissipation term is smaller than the production term for $z/h < 0.15$ and higher for $z/h \geq 0.15$. Consequently, since only transport processes in the vertical direction (turbulent diffusion and pressure diffusion terms) are present in addition to the production and dissipation processes, the local difference between the last two originates from transport over the vertical direction of the flow by turbulent diffusion processes. Hence, the energy excess resulting from production, dissipation and pressure diffusion in the inner flow region (for the smooth bed case) is transported from the wall towards the surface by the term TD. In the intermediate and free surface flow regions, the two transport terms provoke an energy gain which has been produced in the wall region.

For the rough bed case (Fig. 2.4b), one can observe that the transport of turbulent energy from the inner to the outer flow domain is again caused by the turbulent diffusion term TD in a monotonic form.

As described in Nezu and Nakagawa (1993), the term PD is deduced from the measurement of all the other terms, as follows: $PD = G - TD - \varepsilon$. The validity of the profile of the term PD will therefore be affected by the summation of the inaccuracies in the estimation of the terms. Unfortunately, very few experimental data which allow a check of the above quantities, are reported in the literature.

Finally, as has been shown by Raupach (1981), López and Garcia (1999), the second order moment of the fluctuating velocity field are affected by the roughness layer over an extended flow region nearly corresponding to the inner layer $(z/h < 0.2)$ of the turbulent boundary layer. A universal experimental characterization of the flow over rough beds in that flow domain has not been found so far.

Quantitative numerical predictions are not reliable either because of: the uncertainty on the boundary conditions, the high degree of coupling between the different components (i.e. non-linearity), the accuracy needed for the evaluation of the different terms (very small discrepancies between the terms are relevant in these transport mechanisms).

As will be shown in Chapter 4, a novel wall similarity concept has been developed in this thesis. It is based on higher order statistical properties of the flow field and the existence of an universal equilibrium region suggested by Townsend (1956). An extension of this concept to highly turbulent uniform open-channel flows with varying bed roughness is found.

2.3.3 Spectral characteristics of the flow field

All flow equations presented above contain time averaged quantities which do not allow to recognize what flow scales are involved in the different turbulence related processes. A description of the spectral distributions and related characteristic scales is given in the present paragraph in order to describe the theory of the turbulent energy cascade from larger to smaller flow scales at which the conversion of the turbulent kinetic energy into heat occurs due to molecular effects.

The well accepted statistical turbulence theory of Kolmogoroff (1941) demonstrates the existence of the turbulent energy cascade process. It states that turbulent energy is generated at low wavenumbers in the production range, cascades at a rate proportional to the wavenumber in the inertial subrange and is dissipated into heat by viscous effects in the dissipation range. The energy cascade is characterized by a universal -5/3 power law in the inertial subrange of the fluctuating velocity spectrum. It is expressed as follows:

$$S(K_x) = C\varepsilon^{2/3}K_x^{-5/3} \tag{2.30}$$

where Kolmogoroff's universal constant C is equal to 0.5. K_x is the wave-number in the streamwise direction and $S(K_x)$ corresponds to the wave-number spectrum (power density with the unity $m^3.s^{-2}$) of the longitudinal velocity component given by:

$$S(K_x) = \int_0^\infty \Psi(\xi)\cos(K_x\,\xi)d\xi = \int_0^\infty \Psi(\xi)\cos\left(\frac{2\pi f}{\bar{u}}\,\xi\right)d\xi \tag{2.31}$$

$\Psi(\xi)$ represents the spatial autocorrelation function, ξ is the space shift:

$$\Psi_x(\xi) = \frac{1}{X}\int_0^X u'(x)\,u'(x+\xi)\,d\xi \tag{2.32}$$

Fig. 2.5 presents the frequency spectra of the three fluctuating velocity components and their different spectral ranges. These data are obtained from flow measurements with the high resolution ultrasonic instrument described in Chapter 1. The -5/3 law can be distinguished in the inertial subrange where the tendency towards isotropy is observed in its higher range. The spectrum in the low frequency region is called the production range and is characterized by a -1 power law which has been explained recently by Nikora (1999).

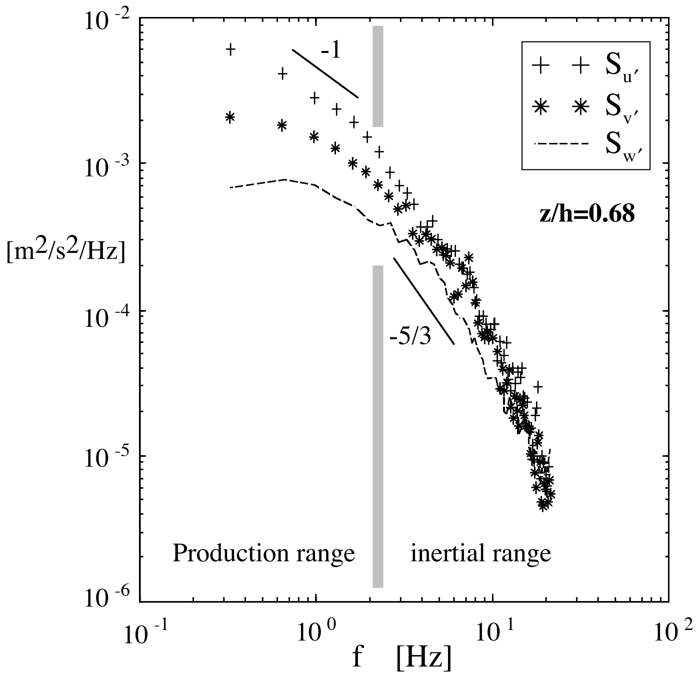

Fig. 2.5 Spectra of fluctuating velocity components.

The eddies observed in the turbulent flow field are characterized by mean macro- as well as mean micro-scales. The integral macroscale is defined as:

$$L_x = \frac{1}{\overline{u'^2}} \int_0^\infty \Psi_x(\xi) d\xi \tag{2.33}$$

It stands for the mean size of the macro flow structures involved in the turbulent energy production process. Coherent structures and bursts are found to be typical macro-scale processes inducing high shear stress and contributing mostly to the production term $\overline{u'w'}\partial\bar{u}/\partial z$ (see Chapter 3). Two micro-scales are commonly used to describe the mean size of the high wave-number flow structures in the inertial subrange. The Taylor micro-scale λ is equal to:

$$\frac{1}{\lambda^2} = \frac{1}{(2\pi)^3} \int_0^\infty K_x^2 S(K_x) dK_x \tag{2.34}$$

where $K_x^2\, S(K_x)$ represents the dissipation spectrum since:

$$\frac{1}{\lambda^2} = \frac{1}{\overline{u'^2}(2\pi)^3}\int_0^\infty K_x^2 S(K_x)dK_x = -\frac{\partial^2}{\partial\xi^2}\Psi_x(\xi)\bigg|_{\xi=0} = \frac{1}{\overline{u'^2}}\overline{\left(\frac{\partial u'}{\partial x}\right)^2} = \frac{\varepsilon}{\overline{u'^2}15\nu} \tag{2.35}$$

Although this scale provides information on the mean size of small turbulent eddies, it is less suited for universal characterization of the high wave number range of the velocity spectra than the Kolmogoroff micro-scale. This is due to the presence of the velocity variance $\overline{u'^2}$ in Eq. (2.35) which is dependent on outer flow conditions. Instead, the Kolmogoroff scale only contains inner flow parameters, as follows:

$$\vartheta = \left(\frac{\nu^3}{\varepsilon}\right)^{0.25} \tag{2.36}$$

This scale quantifies the size of the smallest isotropic eddies found in the inertial subrange and therefore, determines the beginning of the viscous dissipation range expressed as follows:

$$S(K_x) = \frac{1}{6}C^{-3}\left(\varepsilon\nu^{-2}\right)^2 K^{-7} \tag{2.37}$$

The -7 power law of the dissipation range is observed to be universal for eddy sizes smaller than ϑ. The conversion into heat of the cascading energy appears as a turbulent energy sink in Eq (2.29).

Fig. 2.6 shows the spectrum of the dissipation term ε in Eq. (2.34). It illustrates the turbulent energy cascade process from low frequencies to high frequencies where the maximal dissipation can be distinguished in the inertial sub-range. These measurements are made with the herein developed instrument which reveals that it is well adapted for turbulence analysis in open-channel flows.

Furthermore, the spectra in Fig. 2.5 show that the turbulence can be considered as isotropic at the frequency of maximal dissipation (equal to $\cong$4 Hz from Fig. 2.6). Estimations of the dissipation rate ε from the inertial subranges of the velocity spectra measured with the ultrasonic device (see Chapter 1) are therefore considered as highly reliable (an estimation of the measurement accuracy is undertaken in Chapter 9).

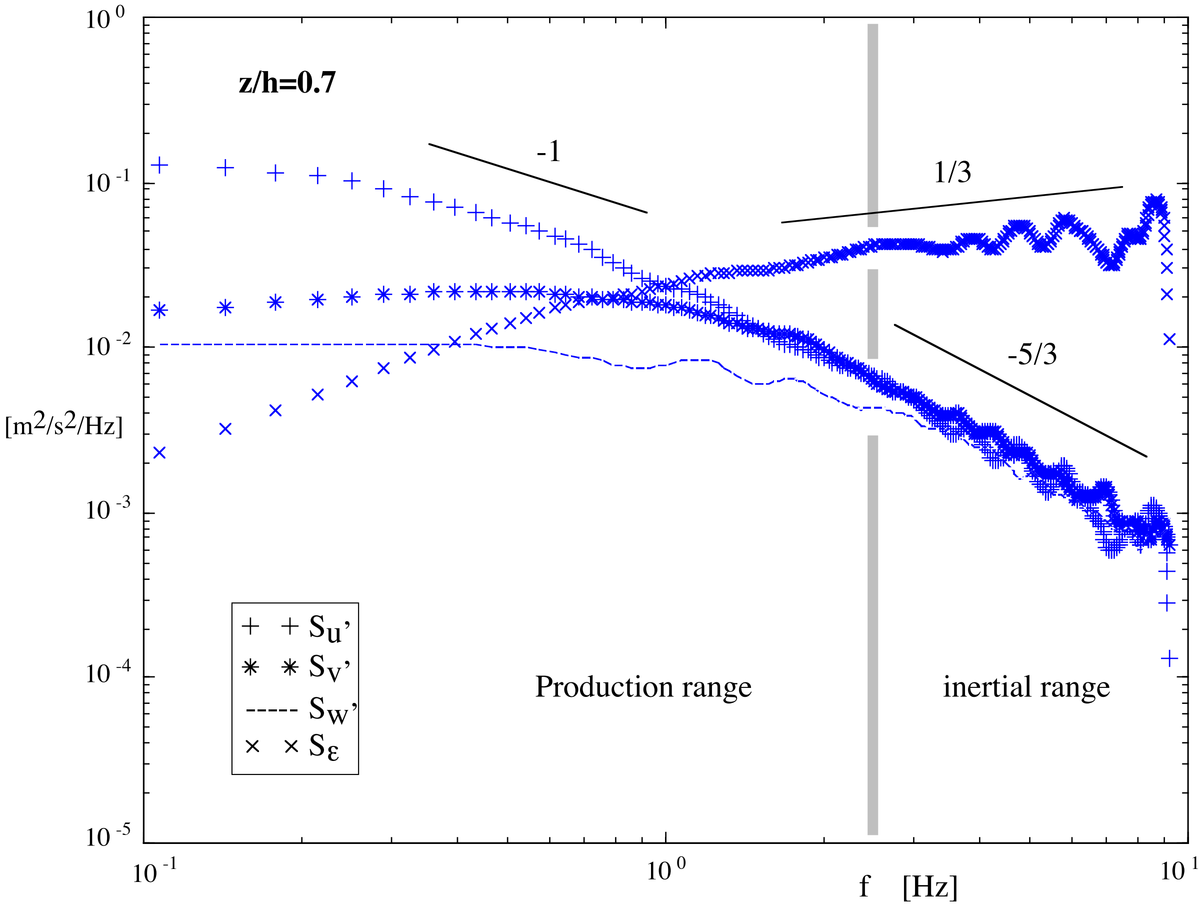

Fig. 2.6 Spectrum of dissipation term ε and velocity spectra (calculated from measurements in Hurther and Lemmin 2001).

2.4 Conclusion

This chapter analyzed the mean conservation equations for 2D mean, highly turbulent, subcritical, and uniform open-channel flow over smooth and rough bed conditions, to be used in the following of the thesis. Mean characteristics of free surface flow as well as the turbulent energy cascade and its corresponding spectral properties have been outlined. These theoretical considerations provide a solid base for the investigation of the complex turbulence related transport mechanism in open-channel flows.

2.5 References

Cardoso A. H., Graf W. H., Gust G. (1989). Uniform flow in a smooth open-channel. J. Hydr. Res., 27(5), 45-57.

Coles, D. (1956). The law of the wake in the turbulent boundary layer. J. Fluid Mech., 1, 191-226.

Graf, W. H. and Altinakar, M. (1998). Fluvial Hydraulics. Wiley & Sons Ltd, 781 pp.

Grass, A. J. (1971). Structural features of turbulent flow over smooth and rough boundaries. J. of Fluid Mech., 50(2), 233-255.

Hinze, J. O. (1975). Turbulence. McGraw-Hill, 790 pp.

Hurther, D. and Lemmin, U. (2001). A correction method for turbulence measurements with a 3-D Acoustic Doppler Velocity Profiler. J. of Atm. and Oceanic Techn., 18(3), 446-458.

Kironoto, B. and Graf, W. H. (1993). Turbulence characteristics in rough uniform open-channel flow, Instn Civ. Engrs, Wat., Marit. et Energy, GB.

Kolmogoroff, A. N. (1941). The local structure of turbulence in incompressible viscous fluid for very large Reynolds numbers. C. R. Acd. Sci. U.R.S.S., 30(301).

Kumar, S., Gupta, R. and Banerjee, S. (1998). An experimental investigation of the characteristics of the free surface turbulence in channel flow. Phys. of Fluids, 10(2), 437-456.

Launder, B. E., Reece, G. J. and Rodi, W. (1975). Progress in the development of a Reynolds stress turbulence closure. J. Fluid Mech., 68, 537-566.

López, F. and Garcia, M. H. (1999). Wall similarity in turbulent open-channel flow. J. of Eng. Mech., 125(7), 789-796.

Nakagawa, H., Nezu, I. and Ueda, H. (1975). Turbulence of open-channel flow over smooth and rough beds. Proc. of Japan Soc. Civil Engrs., pp. 155-168.

Naot, D. and Rodi, W. (1982). Calculation of secondary currents in channel flow. J. Hydraulics Div., 108, 948-968.

Nezu, I. and Nakagawa, H. (1984). Cellular secondary currents in straight conduit. J. Hydraulic Eng., 110, 173-193.

Nezu, I. and Nakagawa, H. (Editors), 1993. Turbulence in open-channel flows. AIHR Monograph series. Balkema, 281 pp.

Nikora, V. (1999). Origin of the -1 spectral law in wall bounded turbulence. Phys. Rev. Letters, 83(4), 734-736.

Prandtl, L. (1925). Uber die ausgebildete Turbulenz. ZAMM.

Raupach, M. R. (1981). Conditional statistics of Reynolds stress in rough wall and smooth wall turbulent boundary layers. J. Fluid Mech., 108, 363-382.

Ryhming, I. L. (1985). Dynamique des fluides. PPUR, 462 pp.

Smith, W. A. M. N., Thorpe, S. A. and Graham, A. (1999). Surface effects of bottom-generated turbulence in a shallow tidal sea. Nature, 400(6741), 251 - 254.

Townsend, A. A. (1956). The properties of equilibrium boundary layers. J. Fluid Mech., 1, 561-573.

CHAPTER 3

COHERENT STRUCTURES IN OPEN-CHANNEL FLOW

3.1 Introduction

In Chapter 2, the fundamental mathematical framework for turbulent open-channel flow has been reported through the derivation of the conservation equations of scalar and vectorial flow quantities, such as mass, momentum and energy. The exact balance equations allow for a general understanding of turbulence in open-channel flows. Unfortunately, very few of these mathematical relations can be applied directly owing to their high degree of complexity and the corresponding inability to resolve them analytically. As a result, closure schemes such as the eddy viscosity concept or Fick's diffusion law, are imposed for the modelization of the second order moments (turbulent momentum flux, turbulent kinetic energy fluxes). These physical assumptions rely on phenomenological aspects which fail to describe many experimental flow observations. Assessing turbulence phenomena only from mean flow quantities obviously lacks insight into the underlying physical processes.

In that context, coherent flow structures are ignored in the statistical models of the flow presented in Chapter 2 although they are found to play the essential role in the turbulence generation mechanism. A coherent structure can be defined as a three-dimensional domain in the flow field in which one or more flow quantities such as the velocity and/ or the pressure are correlated with itself and/ or another quantity over a given time period and/ or space. Its highly spatio-temporal evolution exhibits a life cycle that can not be captured when a long-time average of the flow variables is executed. Nevertheless, a certain short term organized motion can be deduced from the time-averaged equations. In shear flows such as open-channel flows, a portion of the mean flow energy is converted into turbulent fluctuations through the work done by the turbulent stresses $-\rho\overline{u'w'}$ in the mean flow deformation $\partial\bar{u}/\partial z$. This mechanism is found to be self-sustaining (see Eq. (2.22)) because a certain amount of turbulent energy per unit mass and time is produced and dissipated in a steady state. The existence of the mean covariance term $\overline{u'w'}$ associated with the fact that $\overline{u'} = 0$ and $\overline{w'} = 0$, is a proof in itself that a phase persistency over a limited time period does exist between the fluctuating velocity components. Hence, the fluctuating velocity variables cannot be considered as random variables following a Gaussian probability distributions. Instead, higher order moments such as the skewness and flatness factors corresponding respectively to the third and fourth order moments, have to be considered in the probability density functions for a statistical modelization reflecting the complex dynamical processes in a turbulent boundary layer.

3.1.1 General description of coherent motion in the boundary layer

Over the last decades, the major contribution to our knowledge of turbulence relates to the attention given to the so-called bursting phenomenon and the related coherent flow motion. The existence of coherent structures have been revealed by flow visualization techniques employing hydrogen bubbles, dye or smoke in the sixties (Runstadler et al., 1963; Kline et al., 1967; Corino and Brodkey, 1969; Grass, 1971; Kim et al., 1971). A brief presentation of a conceptual model describing the near wall mechanism of coherent motions, proposed by Hinze (1975) is given here. Fig. 3.1 is a sketch of the birth of a hairpin vortex emerging from the edge of a decelerated streak found in the viscous sublayer. The formation of the vortex originates from a local convective instability mechanism occuring at the top of the streak pattern. The dimensionless sizes of a streak are equal to $x^+_{burst} \cong 40$ and $y^+_{burst} \cong 25$, and less than 10 viscous lengths in height. The index + denotes that the distances are normalized by the viscous length ν/u_*. As can be observed in Fig. 3.1, mainly transverse vorticity appears in the initial phase which is gradually converted into longitudinal vorticity when the legs of the hairpin vortex arise at the two sides of the original streak pattern. When the head of the horseshoe vortex reaches the buffer layer at $z^+_{burst} \cong 80-100$, a violent burst event characterized by an internal shear layer, occurs. Sequences of ejection and sweep events are found to surround the detached head. An ejection event is delimited by an instantaneous velocity field composed of negative fluctuating streamwise velocity component and positive vertical velocity component. A sweep event has a velocity field with opposite sign compared to an ejection. The maximal turbulent energy production located in the buffer layer is associated with this process. Fig. 3.1 also represents the effect on the instantaneous longitudinal velocity profile during a complete cycle of a burst event. Important inflection is illustrated at the fourth and fifth steps of the cycle when the angle between the wall and the hairpin structure reaches a maximum value of 45°. Hinze (1975) indicates that the transverse spacing between the streaks in the viscous sublayer and the streamwise spacing between one cycle is equal to $y^+_{spacing} \cong 100$ and $x^+_{spacing} \cong 500-1000$, respectively. It should be noted that this conceptual model describes the bursting process in the inner region.

Interaction mechanisms of coherent flow motions between the inner and the outer flow domains have been considered in the conceptual model of Pratury and Brodkey (1978). Fig. 3.2 reveals the presence of shear layers scaling with the total depth of the boundary layer, located at the fronts which separate the instantaneously accelerated and decelerated fluid. Tilted transverse vortex patterns arise from the wall to the intermediate flow regions along these shear layers while being convected by the mean motion. These separated vortex heads may originate from the bursting phenomenon occuring in the near wall flow region.

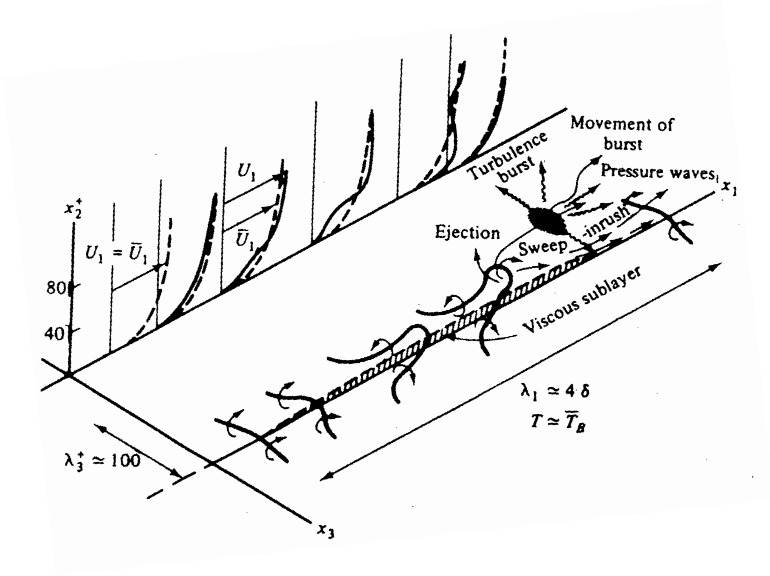

Fig. 3.1 Conceptual model of bursting phenomenon in the inner region of the boundary layer (Hinze, 1975).

Two of these vortex heads can be distinguished in the instantaneous velocity sample shown in Fig. 3.5a (measured with the instrument developed in the present thesis) at x=0.1 m, z/h=0.4 and x=0.26 m, z/h=0.6. We will demonstrate in Chapter 4 that these flow visualization data are in good agreement with the conceptual model of Pratury and Brodkey (1978) and the observations given by Grass et al. (1993). The intrusion of the vortex core into the outer layer entrains high-speed fluid from the free-surface flow domain towards the inner region through the intermediate region. The inflow pattern generates a growing inflexion on the boundary line between the inner and the outer domain and exhibits a critical state at which a maximal tail is observed. As in the previous conceptual model valid in the near wall region, this process is repeated with a quasi-periodicity scaling with outer flow variables.

These two conceptual models are idealized qualitative representations of the mechanism underlying the experimental observations undertaken in turbulent boundary layers. Only two of them have been described briefly above although many others are documented in the literature (Theodorsen, 1952; Willmarth and Tu, 1967; Kline and Kline, 1974; Tardu, 1995). The diversity of the existing models results mainly from the variety of measurement and signal treatment techniques used by the different research groups. Each of these techniques gives a uncomplete view of the flow field such as a local Eulerian vision of the measured flow quantities or a limited Lagrangian vision of the flow. Consequently, the diversity of the existing models originates partially from the difficulty to interpret spatio-temporal flow structures from the obtained measurements.

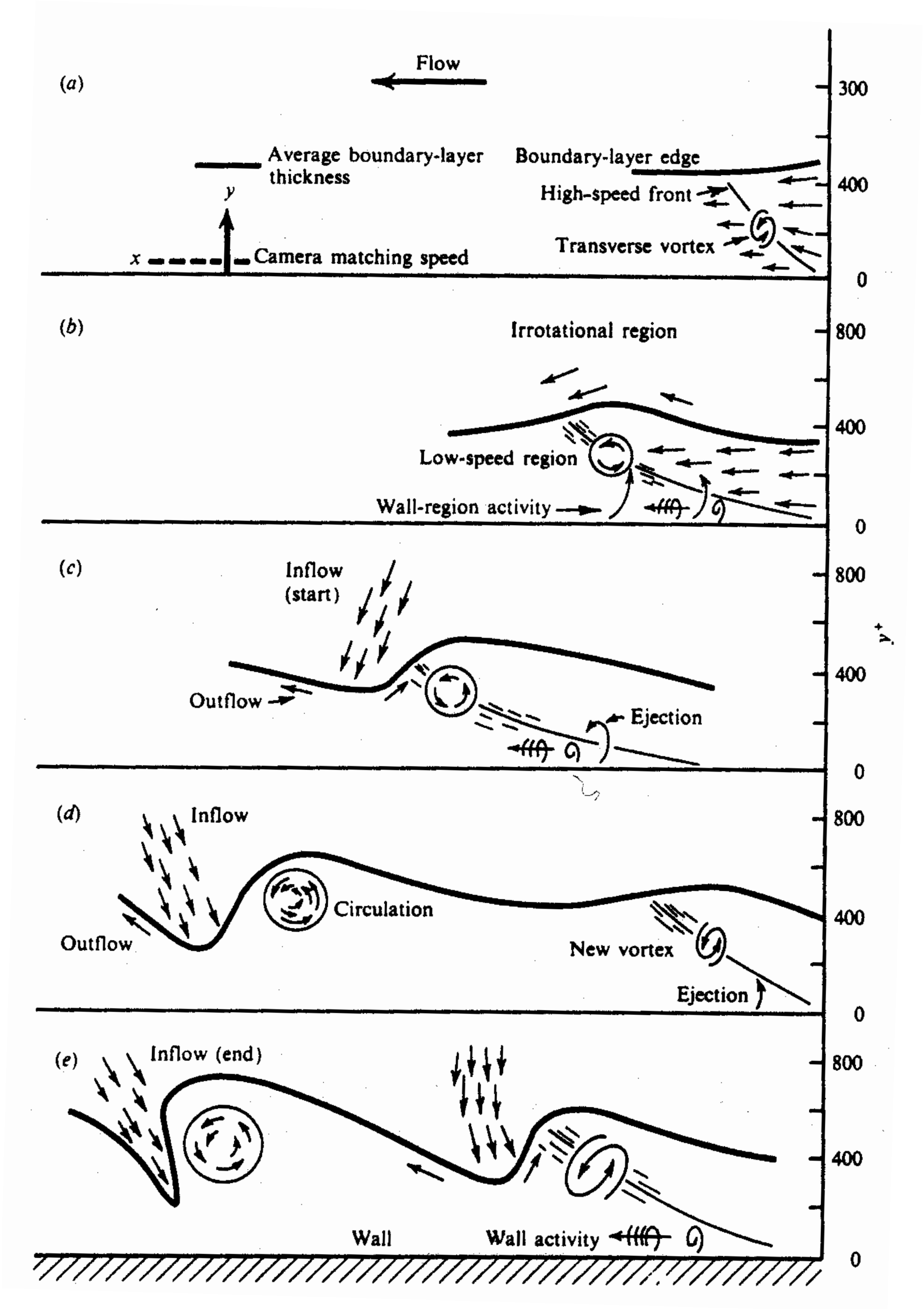

Fig. 3.2 Conceptual model of coherent motions interactions between the inner and outer layers (Pratury and Brodkey, 1978).

To this extent, the Lagrangian flow overview in an entire volume, permitted by large eddy simulations and direct numerical simulations (Kim et al., 1987; Spalart, 1988) have brought to light many aspects concerning the three-dimensional structural flow features found in turbulent boundary layers. Two examples illustrate these results: Fig. 3.3 represent two instantaneous snapshots of the laminar to turbulent transition of a uniform flow over a flat plate. Fig. 3.4 is an example of data resulting from a direct numerical simulation of a fully developed turbulent boundary layer with zero pressure gradient over a flat plate (Chong et al., 1998). The contours exhibit quasi-organized flow structures found in the inner flow region. Simulation investigations are limited by the following requirements in terms of computational resources: the maximal Reynolds number of the simulated flow is O(1000) which is low compared to highly turbulent conditions encountered in geophysical flows O(10000)-O(100000). The numerical analysis of coherent motion is restricted to the inner layer of the boundary layer at a time when most scrutiny is given to the interactions between the inner and the outer flow domains as shown in Adrian et al. (2000). The simulated geometry is extremely simple compared to the cases in natural conditions such as bed roughness, step flow, spillways flows.

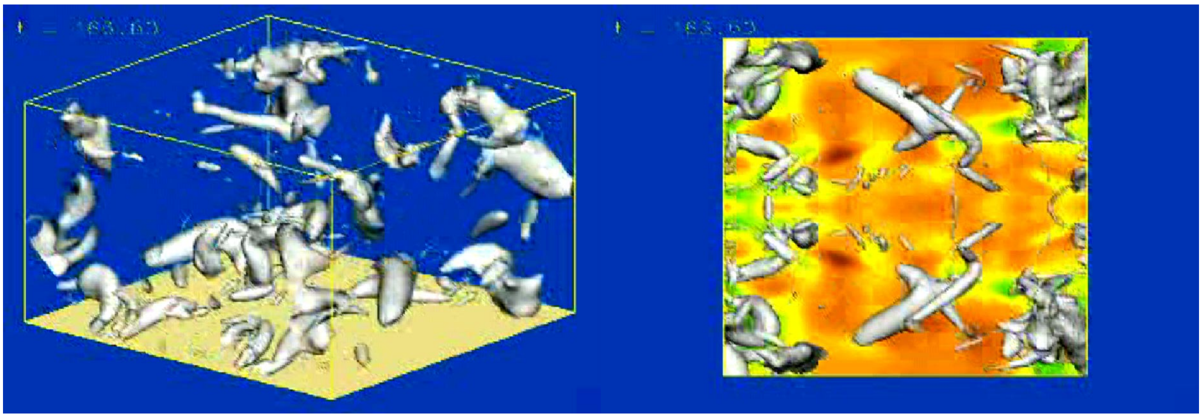

Fig. 3.3 DNS samples of quasi-organized flow structures at the late stages of laminar to turbulent transition of a flow over a flat plate (data from the German Aerospace Center). The picture on the right is the top view of the one on the left.

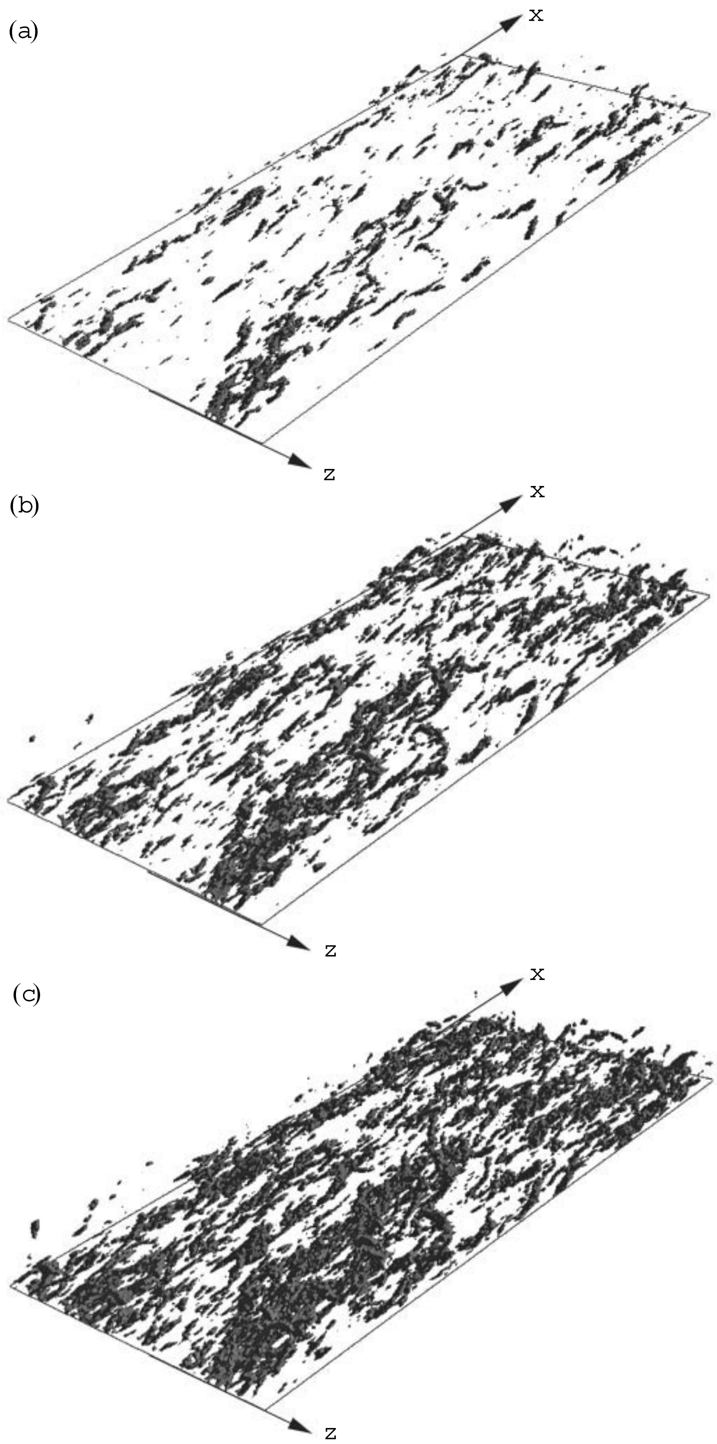

Fig. 3.4 Visualization of coherent flow structures from a DNS simulation of a fully developed turbulent flow with zero pressure gradient over a flat plate. The three pictures are taken at the same time and for three different values of the flow structure sampling criteria, decreasing from (a) to (c)(Chong et al., 1998).

3.1.2 Motivations and Objectives

The present thesis is concerned with flows presenting two particularities typical for geophysical flows. The first is the existence of the free surface (and the related free surface flow region, see section 2.3.1) and the second is the existence of a rough bed (see section 2.3.1). It implies that the link between the flow structures found in the wall region of turbulent boundary layers over a smooth wall and the turbulent structures observed in the open-channel flows is not straightforward. For that reason, the turbulence phenomena occurring in natural flows can not be explicitly deduced from studies undertaken in well-controlled, idealized laboratory flows. Most of the studies mentioned previously have been devoted to a detailed description of the flow organization in the inner region of the boundary layer. Particular attention was given to the following two processes:

- The near wall formation mechanism of the streak patterns in the viscous sublayer
- The burst cycle occuring in the buffer layer

Most research projects still focus on elucidating these fundamental turbulence producing phenomena. In order to obtain a model which can be used for quantitative predictions, no attempt is made in this thesis to contribute directly to that problem. Additionally, the adequate flow measuring technique would require a resolution of the order of magnitude of $O(z^{+})$ which is not reached with the device used herein (see Chapter 1).

The motivations to undertake an experimental analysis of coherent flow motion in the logarithmic and outer flow domains, emanate from the ability of the developed instrument to resolve the involved temporal and spatial scales with the following performances:

- 3-D quasi-instantaneous velocity field measurement
- Instantaneous profiling over the total boundary layer depth
- High order moments (up to the fourth) of the three velocity components are measured with a high accuracy

A major difference between the herein explored flow conditions compared to those of the existing studies concern the high order of magnitude O(10000) of the Reynolds numbers. Furthermore, the present analysis is directed to mass and momentum transfer from the inner to the outer layers as well as the mass and the momentum transfer from the outer to inner region in boundary layers under highly turbulent conditions. In that context, the objectives are the following:

- Interpretation of the visualized patterns in clear water conditions over smooth and rough walls.

- Determination of higher order statistical properties of momentum fluxes in clear water conditions.

- Identification the effects of bed roughness on these properties in clear water conditions.

- Physical interpretation of higher order statistical properties of coherent motion with respect to the conservation equations presented in Chapter 2.

- Interpretation of the visualized flow patterns in particle suspended open-channel flows.

- Determination of higher order statistical properties of particle fluxes in suspension flows.

- Characterization of the effects of instantaneous momentum fluxes on instantaneous particle fluxes.

- Quantification of the particle entrainment and transport capacity of coherent structures in suspension flows under various hydraulic conditions (with a particular focus on Reynolds number and Shields parameter dependency).

- Possibilities of a global physical model for sediment transport assessment based on scales of coherent structures.

3.1.3 Employed methods

A combination of three methods is applied for the analysis of the coherent motion dynamics:

- Flow visualization technique

- Conditional statistics of momentum fluxes

- Conditional sampling of momentum fluxes

The flow visualization technique consists in the representation of the three-dimensional quasi-instantaneous velocity profiles (i.e. instantaneously over the total boundary layer depth) as function of time or function of the main streamwise x-direction of the flow, if Taylor's hypothesis of frozen turbulence is used. An Eulerian signature of the instantaneous flow field is obtained at one vertical of the open-channel flow. For the investigation of two-dimensional mean flow quantities, the measure volume will therefore be located at the centerline of the channel. Since three-dimensional quasi-instantaneous velocity data are available over the whole water depth, the nine terms of the Reynolds stress tensor are estimated instantaneously.

This allows to superimpose the instantaneous shear stress information on the instantaneous velocity field information as shown in Fig. 3.5. Coherent flow structures such as ejections, sweeps, vortical eddies, upwellings as well as downwellings can be recognized from the visualization technique. A detailed discussion of the detected flow patterns is given in Chapter 4. Nevertheless, it may be noted that Eulerian signatures of the flow field as those used herein, are limited to the identification of coherent patterns passing through a fixed measure volume because they have a spatio-temporal evolution (Robinson et al., 1988). Since the tracking of the eddies is impossible, the description of their life cycle composed of several characteristical stages can only be suggested from comparison of the data with those documented in the literature.

Conditional statistics and conditional sampling permit to evaluate quantitative information concerning organized motion dynamics. They have been used extensively in order to detect coherent structures (Lu and Willmarth, 1973; Blackwelder and Kaplan, 1976; Nakagawa and Nezu, 1981) in turbulent boundary layers. The two methods rely on the treatment of the shear stress measurement which appears to be an optimal selection criteria from the flow visualization data. For example, ejections events as well as sweeps events in Fig. 3.5 are delimited by contours of high instantaneous values of relative shear stress term $-\rho\overline{u'w'}$. Furthermore, the choice of the turbulent shear stress quantity is obviously related to the fact that an open-channel flow is a shear flow implying that, as shown in Chapter 2, the work done by $-\rho\overline{u'w'}$ in the mean flow deformation $\partial\bar{u}/\partial z$ represents the production term of the turbulent kinetic energy (Eq. (2.22)). Since the bursting phenomenon is known to be the mechanism responsible for the turbulence generation, it is implicitly suggested that the instantaneous turbulent stress dynamics play a crucial role in the flow organization.

The conditional statistics and sampling of the turbulent stress terms mean that ensemble averages of the considered shear stresses are undertaken as function of two conditions: a condition on the sign of the fluctuating velocities (spatial condition) composing the considered covariance (i.e. the turbulent stress divided by $-\rho$) and a condition on the instantaneous amplitude of the considered covariance relative to its mean value. The areas delimited by the condition on the relative amplitude are represented in Fig. 3.5 by the isolines of instantaneous shear stress term $u'w'$ greater than four times the mean term $\overline{u'w'}$. The condition on the sign is represented by the direction of the instantaneous fluctuating two-dimensional velocity vector $\vec{V}'(u',w')$.

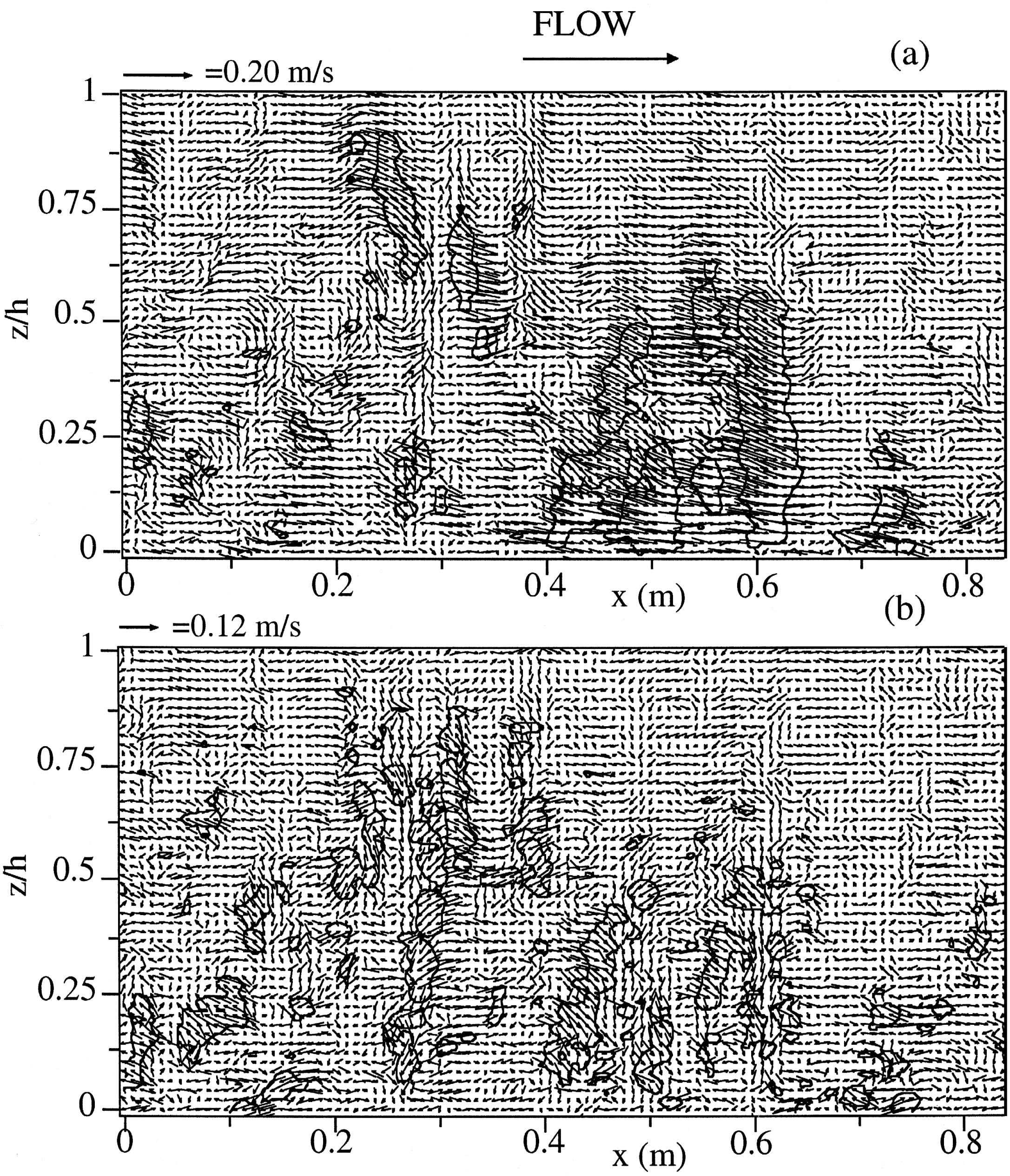

Fig. 3.5 Iso-contours of conditional sampled Reynolds stress and fluctuating velocity field at centerline of an open-chanel flow: (a) for **V**'(u',w') velocity vector, (b) for **V**'(v',w') velocity vector.

Although the same ensemble averages as function of the spatial and amplitude conditions are calculated from the conditional statistics and conditional sampling methods, they have different purposes. The conditional statistics considers a theoretical statistical model of the conditionally sampled shear stress dynamics whereas the conditional sampling technique is based on an experimental estimation of the shear stress dynamics. In other words, the ensemble averages of shear stress estimated with the first method need a theoretical model of the probability densities expressed as function of the moments. The ensemble averages of shear stress estimated with the second method are directly calculated from the measurements. The results obtained with the experimental method are therefore used to determine the quadrant dynamics of the shear stresses and to validate the results of the theoretical model. The theoretical model takes into account the moments of the velocity components which appear in the conservation equations of Chapter 2. The objective of the theoretical approach is to relate the characteristics of coherent structures to mean conservation relations through the properties of the moments.

In the following, a detailed description of the applied methods is given. The results are reported in Chapter 4, Chapter 5 and Chapter 6.

3.2 Conditional statistics for the study of coherent structure dynamics

3.2.1 Cumulant discarded expansions of shear stress probability density functions

The cumulant discard method has been used by several authors in order to predict quantitatively the Reynolds stress $u'w'$ term statistics for different wall roughness conditions in a zero pressure gradient turbulent boundary layer. Antonia and Atkinson (1973) estimated the higher order moments (skewness and flatness factors) of the shear stress fluctuations by using a fourth order approach and expressed the probability density distribution of the normalized $u'w'$ term from a Gram-Charlier type joint probability density function of u' and w'. They found good agreement between the skewness and flatness factors evaluated by the cumulant discard method (up to fourth order) and the corresponding experimental factors in the inner region of the flow whereas only a qualitatively similar tendency was observed in the outer intermittent region. Nakagawa and Nezu (1977; hereinafter NN77) developed the equations of the probability density for the relative covariance term $u'w'$ conditionally sampled over the four quadrants of the (u',w') plane. Therefore events with quadrant 1 $(u'>0, w'>0)$, quadrant 2 $(u'<0, w'>0)$, quadrant 3 $(u'<0, w'<0)$ and quadrant 4 $(u'>0, w'<0)$ orientation are respectively identified as outward interaction, ejection, inward interaction and sweep events. They showed that a third order Gram-Charlier distribution is sufficient to quantify the quadrant time fractions and quadrant covariance fractions in the wall region ($z/h \leq 0.2$) and in the equilibrium region ($0.2 < z/h \leq 0.6$) of the open-channel flow. Again, some weak discrepancies between the model results and experimental results were pointed out in the free surface ($z/h > 0.6$) domain where the flow becomes more intermittent. The authors suggested that errors may be introduced by neglecting higher order cumulants.

In this section we present the theoretical development of the equations for fractional covariance contributions from the different quadrants. We define the variables as follows: u', v', w' are the zero mean fluctuating longitudinal, transverse and vertical velocity components respectively. $\hat{u}, \hat{v}, \hat{w}$ are equal to $u'/\sqrt{\overline{u'^2}}, v'/\sqrt{\overline{v'^2}}, w'/\sqrt{\overline{w'^2}}$ where $\sqrt{\overline{u'^2}}, \sqrt{\overline{v'^2}}\ \sqrt{\overline{w'^2}}$ denote the root mean square values. As mentioned in the previous part, instantaneous 3-D velocity can be measured over the whole water depth. We shall quantify the contributions from the different planes of the relative shear stress for the covariance terms $\varepsilon_1 = u'w'/\overline{u'w'}$ and $\varepsilon_2 = v'w'/\overline{v'w'}$. The four quadrants for $u'w'$ events (see Fig. 3.6) are located in the longitudinal plane where quadrant I1, II1, III1 and IV1 correspond respectively to events with $(u' > 0, w' > 0), (u' < 0, w' > 0), (u' < 0, w' < 0)$ and $(u' > 0, w' < 0)$. The four quadrants for $v'w'$ events which take place in the transverse section of the flow are denoted as quadrant I2, II2, III2 and IV2 corresponding to $(v' > 0, w' > 0), (v' < 0, w' > 0), (v' < 0, w' < 0)$ and $(v' > 0, w' < 0)$ respectively. The statistical properties of the terms ε_1 and ε_2 will be treated separately ; therefore two characteristic functions $\phi_1(\hat{u}, \hat{w})$ and $\phi_2(\hat{v}, \hat{w})$, expressed as the Fourier transforms of joint probability density functions $p_1(\hat{u}, \hat{w})$ and $p_2(\hat{v}, \hat{w})$ respectively, can be written in the following form as indicated by Kendall (1948):

$$\phi_1(\alpha, \beta) = \iint_{\infty} p_1(\hat{u}, \hat{w}) e^{i(\hat{u}\alpha + \hat{w}\beta)} d\hat{u} d\hat{w} \tag{3.1}$$

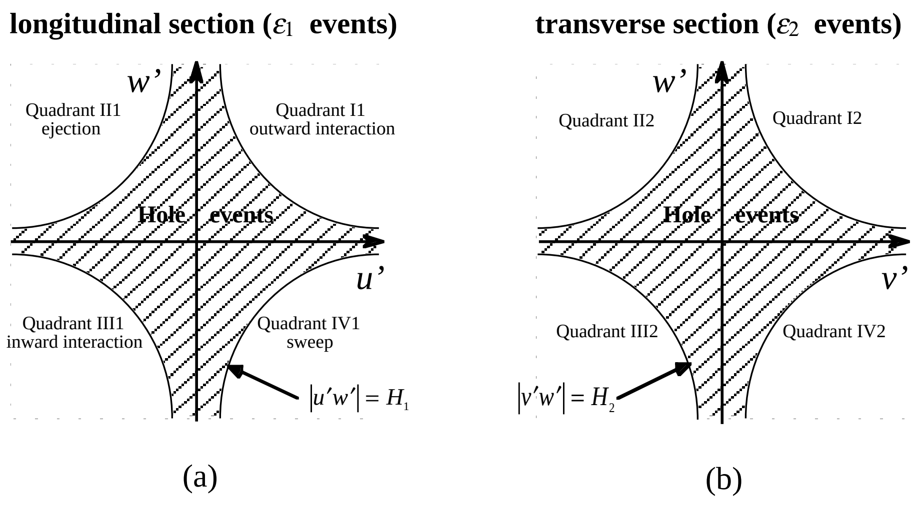

Fig. 3.6 Division of events in the longitudinal (a) and transverse (b) planes.

The characteristic functions,

$$\phi_1(\alpha,\beta) = \sum_{j,k=0}^{\infty} m_{1,jk} \frac{(i\alpha)^j (i\beta)^k}{j!\,k!} \tag{3.2}$$

where $m_{1,jk} = \overline{\hat{u}^j \hat{w}^k}$ and $m_{2,jk} = \overline{\hat{v}^j \hat{w}^k}$ denote the moments of (j+k)th order, are also called the moment generating functions. If the characteristic functions are written as

$$\ln\phi_1(\alpha,\beta) = \sum_{j,k=0}^{\infty} k_{1,jk} \frac{(i\alpha)^j (i\beta)^k}{j!\,k!} \tag{3.3}$$

they represent the cumulant generating functions with $k_{1,jk}$ and $k_{2,jk}$ corresponding to the cumulants. The relation between cumulants and moments (for j+k ≤ 4) are obtained by identifying the coefficients of the variables $(\alpha^j\beta^k)$ and $(\gamma^j\beta^k)$ of the same power in the corresponding Eq. (3.3) and the logarithm of Eq. (3.2). This leads to:

$$(j+k=0)\quad k_{1,00} = k_{2,00} = 1 \qquad (j+k=1)\quad k_{1,10} = k_{2,10} = k_{1,01} = k_{2,01} = 0$$

$$(j+k=2)\begin{cases} k_{1,20} = k_{2,20} = m_{1,20} = m_{2,20} = 1 \\ k_{1,02} = k_{2,02} = m_{1,02} = m_{2,02} = 1 \\ k_{1,11} = m_{1,11} = \overline{\hat{u}\hat{w}} = -r_1 \\ k_{2,11} = m_{2,11} = \overline{\hat{v}\hat{w}} = -r_2 \end{cases} \qquad (j+k=3)\begin{cases} k_{1,21} = m_{1,21} = \overline{\hat{u}^2\hat{w}} \\ k_{2,21} = m_{2,21} = \overline{\hat{v}^2\hat{w}} \\ k_{1,30} = m_{1,30} = \overline{\hat{u}^3} \\ k_{1,03} = m_{1,03} = \overline{\hat{w}^3} \end{cases} \tag{3.4}$$

$$(j+k=4)\begin{cases} k_{1,40} = m_{1,40} - 3 \\ k_{1,31} = m_{1,31} + 3r_1 \\ k_{1,22} = m_{1,22} - 2r_1^2 - 1 \\ k_{1,31} = m_{1,13} + 3r_1 \\ k_{1,04} = m_{1,04} - 3 \end{cases} \qquad (j+k=5)\begin{cases} k_{1,50} = m_{1,50} - 10m_{1,30} \\ k_{1,41} = m_{1,41} + 4m_{1,30}r_1 - 6m_{1,21} \\ k_{1,32} = m_{1,32} - m_{1,30} + 6m_{1,21}r_1 - m_{1,12} \\ k_{1,23} = m_{1,23} - m_{1,03} + 6m_{1,12}r_1 - m_{1,21} \\ k_{1,14} = m_{1,14} + 4m_{1,03}r_1 - 6m_{1,12} \\ k_{1,05} = m_{1,05} - 10m_{1,03} \end{cases} \tag{3.5}$$

where r_i are the correlation coefficients. For the relation of $k_{i,jk}$ (j<k) the indices j and k can be exchanged in the Eqs (3.4) and (3.5). Using the last two relations we can calculate the standard deviation, the skewness and flatness factors of random variables $\left(\varepsilon_i - \overline{\varepsilon_i}\right)$, for i = 1,2:

$$\sigma_i = \sqrt{\overline{\left(\varepsilon_i - \overline{\varepsilon_i}\right)^2}} = \frac{1}{m_{i,11}}\sqrt{m_{i,22} - m_{i,11}^2}$$

$$S_{\varepsilon_i} = \frac{\overline{\left(\varepsilon_i - \overline{\varepsilon_i}\right)^3}}{\sigma_i^3} = \frac{1}{\left(m_{i,22} - m_{i,11}^2\right)^{3/2}}[m_{i,30}m_{i,03} + 9m_{i,12}m_{i,21} + 3(m_{i,31} + m_{i,13})$$
$$- 2m_{i,11}(5m_{i,11}^2 - 3m_{i,22} + 9)] \qquad (3.6)$$
$$F_{\varepsilon_i} = \frac{\overline{\left(\varepsilon_i - \overline{\varepsilon_i}\right)^4}}{\sigma_i^2} = \frac{1}{\left(m_{i,22} - m_{i,11}^2\right)^2}\{m_{i,40} + m_{i,04} + 16m_{i,31}m_{i,13} + 24(m_{i,21}m_{i,03} + m_{i,12}m_{i,30})$$
$$+18\left[m_{i,22}^2 + 2(m_{i,21}^2 + m_{i,12}^2)\right] - 30m_{i,11}^2 m_{i,22}^2 - 3\left(m_{i,11}^4 + 24m_{i,11}^2 + 6\right)$$
$$-12r_i(m_{i,31} + m_{i,13} - 9m_{i,21}m_{i,12} - m_{i,30}m_{i,03})\}$$

The cumulant discard method used here takes into account the cumulants of order j+k=4. In this case, if $\hat{u}, \hat{v}, \hat{w}$ are weakly non-Gaussian, the magnitude of the cumulants of order 3 ≤ j+k < 5 gives a measure of the non-Gaussianity by making the assumption that cumulants of higher order are equal to zero. Antonia and Atkinson (1973) showed that in the outer part of the turbulent boundary layer the departure of $\hat{u}$ and $\hat{w}$ from Gaussianity are more important and that the cumulants of order up to the 6th should be inserted in the above expressions. However, measurements of orders higher than the 4th are difficult because they become unreliable. NN77 came to the same conclusion concerning the free surface region where the flow's intermittence increases.

The expression of the probability density function is given by the inverse Fourier transform of the Taylor series expanding the characteristic function about α = β = 0 for $\phi_1(\hat{u},\hat{w})$ and γ = β = 0 for $\phi_2(\hat{v},\hat{w})$, in which Eq. (3.2) has been introduced making use of Eq. (3.6):

$$\begin{cases} p_1(\hat{u},\hat{w}) = N_1(\hat{u},\hat{w})\left[1 + \sum_{j,k=3}^{4}(-1)^{j+k}\frac{k_{1,jk}}{j!k!}\frac{\partial^{j+k}N_1(\hat{u},\hat{w})}{\partial\hat{u}^j\partial\hat{w}^k}\right] \\ \qquad = N_1(\hat{u},\hat{w})\left[1 + \sum_{j,k=3}^{4}\frac{k_{1,jk}}{j!k!}H_{jk}(\hat{u},\hat{w})\right] \\ p_2(\hat{v},\hat{w}) = N_2(\hat{v},\hat{w})\left[1 + \sum_{j,k=3}^{4}(-1)^{j+k}\frac{k_{2,jk}}{j!k!}\frac{\partial^{j+k}N_2(\hat{v},\hat{w})}{\partial\hat{v}^j\partial\hat{w}^k}\right] \\ \qquad = N_2(\hat{v},\hat{w})\left[1 + \sum_{j,k=3}^{4}\frac{k_{2,jk}}{j!k!}H_{jk}(\hat{v},\hat{w})\right] \end{cases} \qquad (3.7)$$

where $N_1(\hat{u},\hat{w})$ and $N_2(\hat{v},\hat{w})$ represent the joint normal distributions of $(\hat{u},\hat{w})$ and $(\hat{v},\hat{w})$ respectively:

$$\begin{cases} N_1(\hat{u},\hat{w}) = \dfrac{1}{2\pi\left(1-r_1^2\right)^{1/2}} \exp\left(\dfrac{\hat{u}^2 + 2r_1\hat{u}\hat{w} + \hat{w}^2}{2\left(1-r_1^2\right)} \right) \\ N_2(\hat{v},\hat{w}) = \dfrac{1}{2\pi\left(1-r_2^2\right)^{1/2}} \exp\left(\dfrac{\hat{v}^2 + 2r_2\hat{v}\hat{w} + \hat{w}^2}{2\left(1-r_2^2\right)} \right) \end{cases} \tag{3.8}$$

3.2.2 Cumulant discarded Gram-Charlier functions and quadrant distribution

The rightmost terms in the second and fourth lines of Eq. (3.7) are called Gram-Charlier distributions of order 4 where $H_{jk}(x,y)$ is a Hermite polynomial of two variates. When $k_{ji,k}$=0 for 3≤j+k<5, the probability density function (3.7) takes the form of a joint normal (Gaussian) distribution of two dependant variates (Eq. (3.8)), with the cross cumulants being the criteria of dependence.

As indicated by Antonia and Atkinson (1973), the probability densities $p_1(\varepsilon_1)$ and $p_2(\varepsilon_2)$ are obtained by replacing the variable $\hat{w} = -r_1\varepsilon_1/\hat{u}$ and $\hat{w} = -r_2\varepsilon_2/\hat{v}$, respectively, and integrating the resulting function over $\hat{u}$ and $\hat{v}$ respectively from -∞ to +∞. NN77 expressed the conditionally sampled probability densities over the four quadrants of covariance event ε_1. Thereby the relation between the bursting process and the shear stress statistics becomes evident through the importance of the third order cumulants (connected with turbulent diffusion) which disappear due to the oddness of the Hermite polynomials for the odd orders when the general formulation of $p_1(\varepsilon_1)$ is calculated. The mathematical manipulation is completely described in NN77 who give the following equations:

$$\begin{array}{llll} p_{i,2}(\varepsilon_i) = p_{iN}(\varepsilon_i) + \varphi_i^-(\varepsilon_i) & p_{i,4}(\varepsilon_i) = p_{iN}(\varepsilon_i) - \varphi_i^-(\varepsilon_i) & (\varepsilon_i > 0) & i = 1,2 \\ p_{i,1}(\varepsilon_i) = p_{iN}(\varepsilon_i) + \varphi_i^+(\varepsilon_i) & p_{i,3}(\varepsilon_i) = p_{iN}(\varepsilon_i) - \varphi_i^+(\varepsilon_i) & (\varepsilon_i < 0) & \end{array} \tag{3.9}$$

where the index q in $p_{i,q}$ denotes the quadrant index in the i^{th} plane with planes 1 and 2 corresponding to the longitudinal and transverse planes respectively. The probability density $p_{iN}(\varepsilon_i)$ is directly developed from the normal distribution. The non-conditionally sampled probability function of shear stress is:

$$p_i(\varepsilon_i) = p_{i,1}(\varepsilon_i) + p_{i,2}(\varepsilon_i) + p_{i,3}(\varepsilon_i) + p_{i,4}(\varepsilon_i) = 2p_{i,N} \qquad i = 1,2 \tag{3.10}$$

with

$$\begin{cases} p_{iN}(\varepsilon_i) = \dfrac{r_i}{2\pi}\exp(r_i t_i)\dfrac{K_0(|t_i|)}{\left(1-r_i^2\right)^{1/2}} \\ \varphi_i^+(\varepsilon_i) = \dfrac{r_i}{2\pi}\exp(r_i t_i)K_{1/2}(|t_i|)\dfrac{|t_i|^{1/2}}{(1-r_i^2)}\left[(1+r_i)\left(\dfrac{S_i^+}{3}+D_i^+\right)|t_i| - \left(\dfrac{2-r_i}{3}S_i^+ + D_i^+\right)\right] \\ \varphi_i^-(\varepsilon_i) = \dfrac{r_i}{2\pi}\exp(r_i t_i)K_{1/2}(|t_i|)\dfrac{|t_i|^{1/2}}{(1+r_i^2)}\left[(1-r_i)\left(\dfrac{S_i^-}{3}+D_i^-\right)|t_i| - \left(\dfrac{2+r_i}{3}S_i^- + D_i^-\right)\right] \\ t_i = \dfrac{r_i\varepsilon_i}{\left(1-r_i^2\right)} \quad ; \quad S_i^\pm = \dfrac{1}{2}\left(k_{i,03} \pm k_{i,30}\right) \quad ; \quad D_i^\pm = \dfrac{1}{2}\left(k_{i,21} \pm k_{i,12}\right) \end{cases} \tag{3.11}$$

where, $K_0(t)$ is the 0-th order modified Bessel function of the second kind. The coefficients $S_i^\pm$ are related to the skewness of the two corresponding variates and the $D_i^\pm$ terms related to the diffusion term of the turbulent energy equation as will be indicated later. From Eqs. (3.10) we will calculate the first order moment of each conditional probability density distribution as function of the threshold levels H_i. These levels allows the selection of ε_i events defined as :

$$\varepsilon_i \geq H_i \tag{3.12}$$

Therefore, by taking into account only strong fractional Reynolds stress events by increasing H_i, their directional distribution over the different quadrants in the longitudinal and transverse sections can be investigated using the following expressions :

$$\begin{aligned} RS_{i,q}(H_i) &= \int_{H_i}^{\infty} \varepsilon_i p_{i,q}(\varepsilon_i)d\varepsilon_i \qquad H_i \geq 0 \qquad i = 1,2 \qquad q = 2,4 \\ RS_{i,q}(H_i) &= \int_{-\infty}^{H_i} \varepsilon_i p_{i,q}(\varepsilon_i)d\varepsilon_i \qquad H_i \leq 0 \qquad i = 1,2 \qquad q = 1,3 \end{aligned} \tag{3.13}$$

As mentioned in section 3.1.3, the relative shear stress contributions are therefore calculated as function of two conditions: a condition on the direction of the velocity field (quadrant repartition) and a condition on the amplitude of the instantaneous shear stress (threshold value H_i). Also, it is convenient to estimate the time fractions $T_{i,q}$ of these conditionally sampled events by using :

$$
\begin{aligned}
&T_{i,q}(H_i) = \int_{H_i}^{\infty} p_{i,q}(\varepsilon_i)d\varepsilon_i \qquad H_i \geq 0 \qquad i = 1,2 \qquad q = 2,4 \\
&T_{i,q}(H_i) = \int_{-\infty}^{H_i} p_{i,q}(\varepsilon_i)d\varepsilon_i \qquad H_i \leq 0 \qquad i = 1,2 \qquad q = 1,3
\end{aligned}
\tag{3.14}
$$

Consequently, the terms of the events having relative shear stress values lower than the defined thresholds are called the hole event terms $RS_{i,5}$ and $T_{i,5}$ and are given by :

$$
RS_{i,5}(H_i) = 1 - \sum_{q=1}^{4} RS_{i,q}(H_i) \qquad\qquad T_{i,5}(H_i) = 1 - \sum_{q=1}^{4} T_{i,q}(H_i) \tag{3.15}
$$

3.3 The uw-quadrant threshold technique

This technique has been developped by Lu and Willmarth (1973). The parameters $RS_{i,q}$ which are evaluated from the measurements of the instantaneous velocity field are the same than those obtained from the theoretical approach (section 3.2) considering the cumulant discard expressions of the probability density functions. The relative contribution of the covariance term ε_i in quadrant q, excluding the events with an amplitude smaller than H_i, is:

$$
RS_{i,q} = \frac{1}{T}\int_0^T \varepsilon_i(t) D_{i,q,H_i}\left[\varepsilon_i(t)\right]dt \tag{3.16}
$$

where $D_{i,q,H_i}\left[\varepsilon_i(t)\right]$ is called the detection function and yields:

$$
D_{i,q,H_i}\left[\varepsilon_i(t)\right] = \begin{cases} 1 & \text{if } \varepsilon_i \text{ is in quadrant q and } \varepsilon_i \geq H_i \\ 0 & \text{otherwise} \end{cases} \tag{3.17}
$$

The detection method based on this conditional sampling technique needs the determination of the adequate value of the threshold level H_i. The following question arises: what is the influence of this criteria on the validity of the detections?

Bogard and Tiedermann (1986) analyzed the influence of the threshold level H_i on the detection of bursts events. For that purpose, they compared the quandrant threshold results with those obtained from flow visualization. They introduced the following probabilities:

- P(Ej): the probability that an ejection event is detected

- P(Fail): the probability of a failure detection

A visualized ejection is considered as detected when the detection function $D_{i,q,H_i}\left[\varepsilon_i(t)\right]$ passed from zero to one during a visualized ejection event. The probability P(Ej) is equal to the ratio between the number of detected events with the algorithm and the number of visualized ejections. Correspondingly, a failure detection is counted when the detection function $D_{i,q,H_i}\left[\varepsilon_i(t)\right]$ passed to one whereas no ejection pattern could be recognized from the visualization. The probability P(Fail) is equal to the ratio between the number of fail detection and the number of visualized ejections.

The determination of the optimal detection level, i.e. the one resulting in P(Ej)=1 has interested an large number of researchers because the value of the sampling threshold will affect the ensemble averages and the deduced scales of the structures. It is evident that the threshold level has to be high enough to avoid fail detections. On the other hand a high threshold value will bias the ensemble averages of the mean lifetime of the selected structure.

Bogard and Tiedermann (1986) stated in their study that the optimal threshold value is obtained when the number of burst detections from the algorithm is equal to the number of visualized bursts. This condition is not obvious since too high threshold value can result in more algorithm detections during a single visualized detections. Compared to the well-known VITA-technique (variable-intervall-time-average) proposed by Blackwelder and Kaplan (1976) and a modified VITA-technique (including a supplementary condition on the sign of the instantaneous longitudinal gradient of the fluctuating velocity component), Bogard and Tiedermann (1986) obtained the highest P(Ej) value with the uw-quadrant technique confirming the efficiency of this sampling technique when coherent structure detection is desired.

It is worthwhile noting that the discussion undertaken here, whether the sampling parameter is detecting a burst structure or not, is not of major importance for the studies presented in this work. The attention is more focused on the variation of the relative shear stress contribution and the time fractions of events from the different quadrants as function of the selection criteria. The question of the validity of the detection algorithm is more relevant when no simultaneous flow visualization is available (for example when the velocity field is only measured at one level in the boundary layer) which is not the case here. Furthermore, a well-defined burst structure can only be found in the wall layer over a limited flow region and when the Reynolds number of the flow is much lower than the ones of the flows investigated herein. Since the objectives are devoted to momentum transfer between the inner and the outer flow regions where a diversity of organized structural flow features do exist, the finding of the optimal selection criteria value detecting one specific coherent eddy, is less relevant.

3.4 Effects of coherent flow structures on sediment transport in suspension flow

3.4.1 Introduction

Among the diverse physical processes in which turbulence is implicated, the turbulent transport process of mass, momentum, energy and heat is of major significance for engineering and geophysical problems. Over the past decades, intensive investigations based on fundamental theoretical approaches, have been devoted particularly to turbulent mixing and turbulent diffusion problems of neutrally buoyant contaminants and heat. However, as pointed out by Sumer and Deigaard (1981), sediment transport assessment in highly turbulent fluids can still be considered as an unsolved problem since the existing models depend on empirical assumptions which do not take into account the fine scale physical phenomena occurring in turbulent flows. Indeed, many sediment transport models (Yalin, 1972; Graf and Altinakar, 1998) rely on the concept of the mean critical shear stress condition for the initiation of the particles motion. This type of "simplified" model supposes that the lifting force is proportional to the drag force which is assumed to be proportional to the force $\tau_0 d_{50}^2$ where τ_0 represents the mean bed shear stress and d_{50} is the diameter of the particles. This force is then proportional to the immersed weight of the particle through a constant representing the critical threshold level.

Most of these formulations are expressed as function of mean flow quantities averaged over an infinite time length although the recent experimental results have revealed the highly pulsative and intermittent nature of the turbulent quantities in clear water flows. Therefore, the possibilities to develop sediment transport models based on characteristic scales of the intermittent turbulent stress events dominating the turbulence production process should be investigated.

The first part of this chapter described the techniques used to quantify the dynamics of coherent flow structures in highly turbulent, clear water open-channel flows. In this second part, we will describe the methods applied to investigate the impact of the organized flow motions on the suspended sediments.

Bedload transport and suspended sediment transport

Two types of sediment transports can be distinguished:

- The bedload transport of the sediments occurs in the inner region of the boundary layer. Two modes of particle movement are simultaneously present: the intermittent rolling or sliding of the particles on the bed and the saltation motion of the particle. The saltation motion is associated with the intermittent jumps of particles in the inner flow domain. Due to the presence of the bursting phenomenon in that region of the boundary layer, it is suggested that the saltation motion of the sediments can be initiated by the strong turbulent stress events such as ejection or sweep events.

- The suspended sediment transport theory considers the mechanisms causing the maintenance of the fine sediments at a certain height in the flow. Although most of these fine particles are not deposited on the bed, some of the heavier sediments can settle down to the bed before being re-entrained in the suspension. Therefore, since the sediment source in open-channel flow is located at the bed, the mechanisms of sediment resuspension and maintaining have to be analyzed in great detail. It is not yet clear if the two categories of suspended sediments originate from the same turbulent entrainment mechanism.

3.4.2 A brief review of the existing literature results

Particle-turbulence interactions: a review of the observed physical phenomena

Sumer and Deigaard (1981) have demonstrated that ejection events are responsible for the saltation movements of the particles in the inner flow region. The experimental study consists of the visualization of the trajectories of the particles under various bed roughness conditions (from smooth to completely rough beds). Particles with diverse sizes and densities are present in the flow. The following results are found: the mean suspended travel time of the particles with a density almost equal to the density of water, corresponds to the mean lifetime of ejection events. The mean longitudinal distance of the travel distance is in agreement with the characteristic wavelength of an ejection in clear water. The mean temporal and spatial characteristics of the trajectories of the heavier particles deviate from the characteristic scales of the ejections. These discrepancies result from the slip velocity between the fluid and the solid particles. Subsequently, the solid particle is released by the ejection before the end of the ejection cycle and settles down to the bed (see Fig. 3.7)

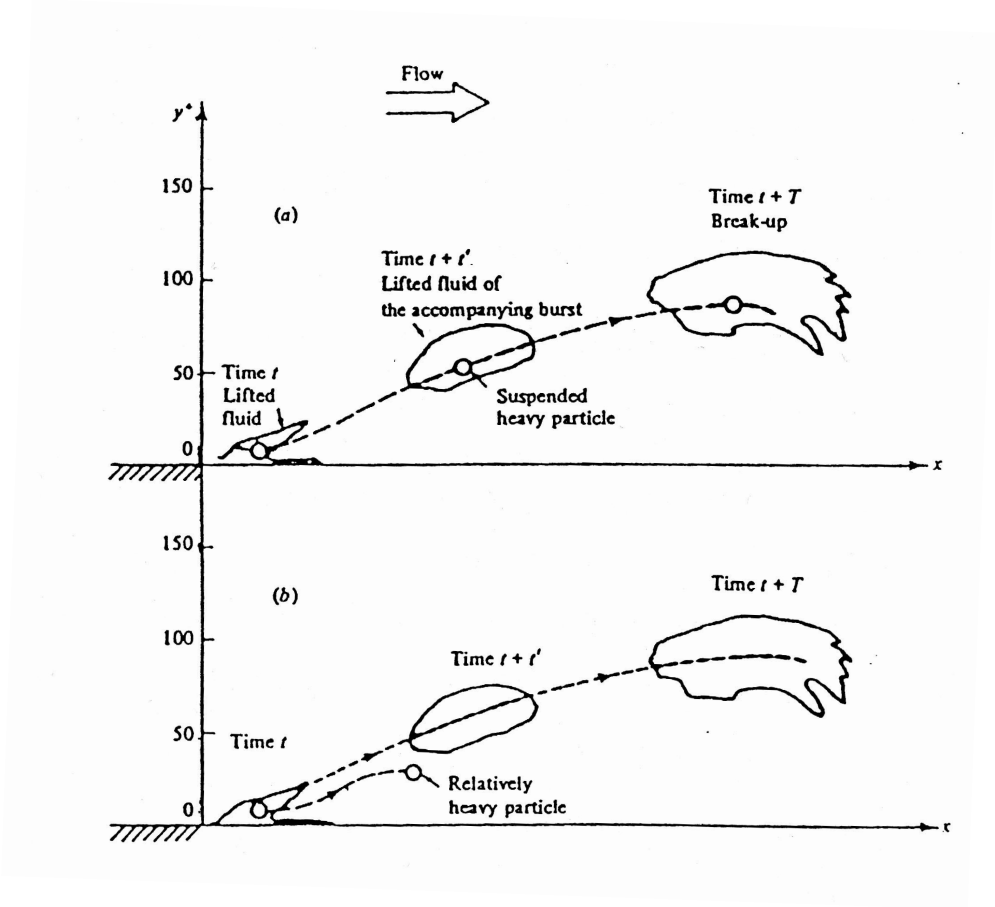

Fig. 3.7 Typical encountered trajectories of a particle entrained by an ejection event in the inner flow region (Sumer and Deigaard, 1981). (a) for a particle with a density almost equal to the density of water. (b) for a heavier particle.

Sumer and Deigaard observed that the deposited heavier particles are entrained by sweep events into decelerated streaks from where a new ejection event is arising.

A more detailed study on the particle-turbulence interactions in the near wall region has been undertaken by Nino and Garcia (1996). Flow visualization with a high-speed video system was used in an open-channel flow with two bed roughness conditions (smooth and transitionally rough beds). They found that in the case of smooth bed conditions, the particles that are immersed in the viscous sublayer are sorted along the low speed streaks. The formation of the low speed streaks is due to the presence of counter-rotating streamwise vortices appearing quasi-periodically in time and randomly along the bottom wall. The dimensions of the accumulated particle zones are in good agreement with the dimensions obtained by Hetsroni (1991). Although particles larger than the thickness of the viscous sublayer do not accumulate along the low speed streaks, the kinematical characteristics of the larger particles are observed to respond to the streaky structure of the wall region. In the transitionally rough bed condition, the particle sorting on the channel bed has not been visualized by the authors. The particle entraining flow structure appears to have the form of a shear layer similar to the one described by Pratury and Brodkey (1978) (see section 3.1.1). As shown in Fig. 3.8, an ejection event located downstream from the convected shear layer entrains particles into the core of the shear layer which extends from the inner to the outer flow regions. After the shear layer has lost its coherence, the entrained particles can be deposited directly on the bed or can be picked up by another ejection before touching the wall.

Furthermore, it is observed that another coherent structure occuring in the outer flow region is able to maintain the lifted particles. Another case where the particles are released from the shear layer before they lose their coherence occurs in a way similar to the one described by Sumer and Deigaard (1981) (see Fig. 3.8).

Nino and Garcia (1996) stated that this particle entrainment mechanism is also valid for small particles immersed in the viscous sublayer although this observation is in contradiction with the results of Yung et al. (1988). They found that these particles are not affected by the quasi-periodical bursting cycle. Furthermore, Nino and Garcia demonstrated that the visualized particle entrainment process is independent of the wall roughness. Finally, they determined that the ratio of the number of particles entrained by ejection events over the total number of ejection events increases with the Shields parameter of the flow.

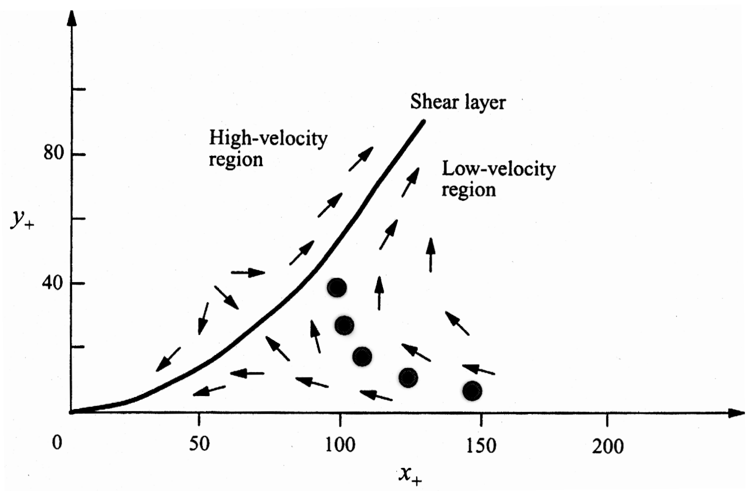

Fig. 3.8 Particle entrainment of an ejection event into a shear layer extending from the inner to the outer flow regions (Nino and Garcia, 1996)

Soulsby et al. (1994) have observed the turbulent structure of a suspension of sand ($d_{50} = 165\,\mu m$) in a tidal current. The instantaneous velocity as well as the instantaneous concentration were measured simultaneously at three locations above a sandwave having a wavelength of 25 m and a height of 75 cm. The spatio-temporal correlations of the instantaneous concentration data revealed the presence of an inclined sand cloud of length and extrapolated height roughly equal to 1 m and 1.30 m in mean, rescpectively. Fig. 3.9 shows the mean shape of such a cloud in a current of depth equal to 2.65 m and a near bed velocity equal to 1.16 m/s. When compared with the velocity data obtained, the authors showed that these high concentration patterns are strongly correlated with ejection events of identical spatial sizes. By applying a conditional sampling technique, they found that the ejection and sweep events account for 65 % of the vertical mass flux in only 23 % of time. From a comparison with literature results, these values are found to agree well with the shear stress contributions of to the ejections and sweep events related to the bursting phenomenon.

Furthermore, the authors have pointed out that the turbulent kinetic energy of the suspension flow has been reduced to a quarter of the clear water value. According to the authors, the ejections are the dominant mechanism for the sand resuspension and sweeps are responsible for the bedload movement of the particles in a tidal current. Supplementary field studies are needed to confirm these statements.

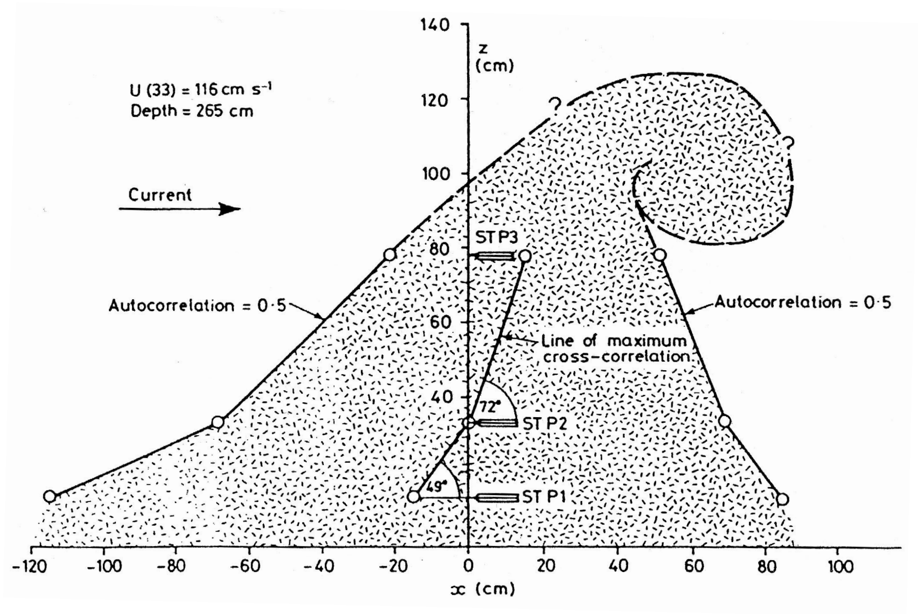

Fig. 3.9 Mean sand cloud entrained by ejection and sweep events in a tidal current (Soulsby et al., 1994).

Sediment transport models based on coherent structure characteristics

The majority of the sediment transport models based on coherent flow structures dynamics consider that the ejections events are the most relevant structures in the particle entrainment. They are observed to contribute essentially to the saltation and resuspension processes.

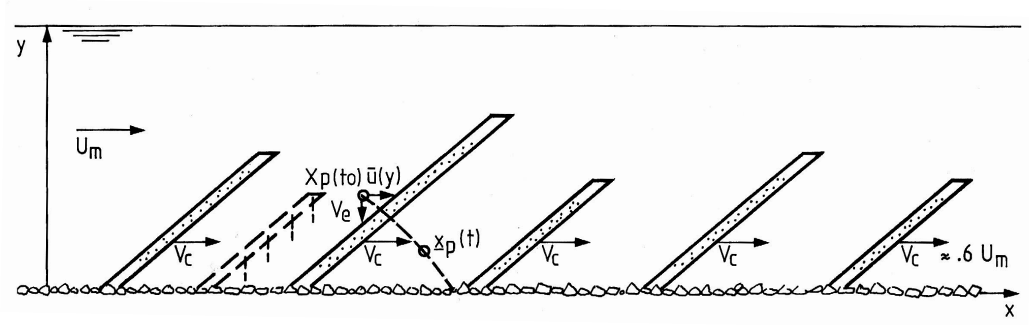

Fig. 3.10 Schematic representation of sediment transport by ejection events proposed by (Gyr, 1983)

Fig. 3.10 shows the principle of the conceptual sediment transport model proposed by Gyr (1983). The ejection event is seen as an inclined water column carrying particles of diverse sizes. The total amount of particles transported by the ejections is called the excited load. Saltation movements (i.e. bedload transport) as well as suspended sediments are contained in the excited load.

The principle of this model is based on geometrical and kinematical characteristics of the ejections. During the lifetime of the ejections, the excited load is suspended in the water column. When the ejection starts to loose its coherence, the particles are released and start to settle down towards the bed at a velocity depending on their size and density and the state of turbulence (corresponding to their settling velocity in still water). Considering the mean geometrical and kinematical characteristics of the ejection events, the probability that a released particle is resuspended by another ejection before it is deposited on the bed, can be determined. Gyr shows that this probability allows to distinguish the suspended sediments from the saltating sediments. For that purpose he introduces a threshold for the probability that a particle is resuspended by another ejection before it reaches the bed. In the case that the probability is lower than this critical probability, the considered particles are part of the bedload. The suspended sediments have a probability of resuspension that is higher than the critical probability. This conceptual model suggests that only ejections contribute to an entrainment of the sediments.

Cao (1999) has recently developed a novel formulation for the near bed equilibrium concentration of suspended sediments based on the characteristics of the bursting phenomenon. This model relies on the same general concept as the one suggested by Cleaver and Yates (1973). Compared to the commonly used empirical expression proposed by VanRijn (1984) Zyserman and Fredsoe (1994), Cao's relation relies on a physical concept which takes into account the dimensionless temporal as well as spatial scales of the organized motions found in the inner region of the turbulent boundary layer. The two characteristic scales needed for the evaluation of the near bed sediment entrainment function are:

- The dimensionless bursting period $T_B^+ = T_B U_\infty / h$, normalized with outer flow parameter. U_∞ is the mean flow velocity at the free surface and T_B is the bursting period defined at the half-value threshold level as proposed by Nakagawa and Nezu (1977).

- The bed surface fraction A_1 per unit of bed area of the bursts containing enough energy to lift up the sediments deposited at the bed is given by $A_1 = A_C(\theta - \theta_c)/\theta_c$. The parameter A_C corresponds to the surface fraction per unit of bed area of all bursts. This value is determined from the well-accepted measurements of Kline et al. (1967) and Kim et al. (1971). The variables θ and θ_c represent the Shields parameter and the critical Shields parameter for the initiation of particle motion, respectively.

The volumetric near bed equilibrium concentration proposed by Cao is then written as follows:

$$C_a \cong \frac{A_C}{T_B^+} \frac{C_0 d}{w_0 \theta_c} \frac{(\theta - \theta_c) U_\infty}{h} \tag{3.18}$$

where C_0, d and w_0 are the volumetric particle concentration at the bed, the mean size of the particles and the settling velocity of the considered particles in still water, respectively.

Eq. (3.18) reproduces the steady state equilibrium condition between the downward particle flux under the effect of gravity and the ascending particle flux generated by the quasi-periodic particle flux entrained by a turbulent burst. It has to be specified that the burst parameter T_B^+/A_C is obtained from a calibration procedure based on data from the literature since very few direct measurements of this parameter are available. Fig. 3.11a shows the parameter T_B^+/A_C as function of the dimensionless particle size $R_p = \sqrt{(\rho/\rho_p - 1) g d} \cdot d / \nu$ where ρ, ρ_p, g, d, and ν are the water density, the particle density, the gravitational acceleration, the mean particle diameter and the kinematical viscosity of water, respectively. For small particle sizes this parameter shows strong variations. Fig. 3.11b represents the near bed equilibrium concentration calculated from Eq. (3.18) versus the results from the literature. The good agreement between them reveals the validity of Cao's formulation over a wide range of Shields parameter and particle sizes. Chapter 6 of the thesis is devoted to a detailed discussion of this model.

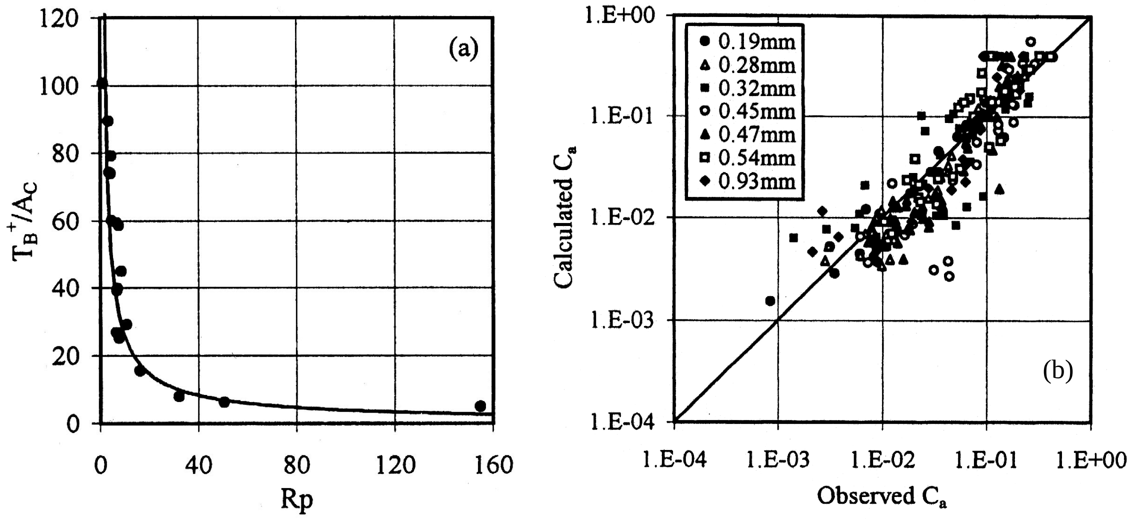

Fig. 3.11 (a) Burst parameter T_B^+/A_C as function of the dimensionless particle size. (b) Comparison of near bed equilibrium concentration calculated from Eq. (3.18) with results reported in the literature (Cao, 1999)

3.4.3 Application of the conditional statistics theory to particle flux and shear stress

Our motivation to undertake a detailed analysis of the role of the coherent flow structures in the suspended particle entrainment mechanisms is based on the unique flow and particle flux measurements provided by the Acoustic Particle Flux Profiler (APFP). The novel measurement principle and the corresponding instrument have been developed by Shen and Lemmin (1997). The novelty of the APFP resides in its ability to profile simultaneously over the entire flow depth, the quasi-instantaneous two-dimensional velocity field and the particle concentration. The high spatial and temporal resolutions of the device allow to determine the small scale organized motions as well as the small scale particle flux events (the characteristics of the instrument are reported in Chapter 5). Consequently, the instantaneous shear stress and the instantaneous particle mass flux can be evaluated simultaneously over the total boundary layer height as shown in Fig. 3.12 (the hydraulic flow conditions are described in Chapter 5). It represents a typical sample of the row data used for the present statistical study. The drawn contours are the isolines of instantaneous covariance term $u'w' = H_1 \overline{u'w'}$, the color patterns show the instantaneous vertical particle flux $c'w'$ where c' correspond to the local fluctuating particle concentration. It should be mentioned that unlike the 3-D-ADVP presented in Chapter 1, the APFP does not measure the transverse velocity component.

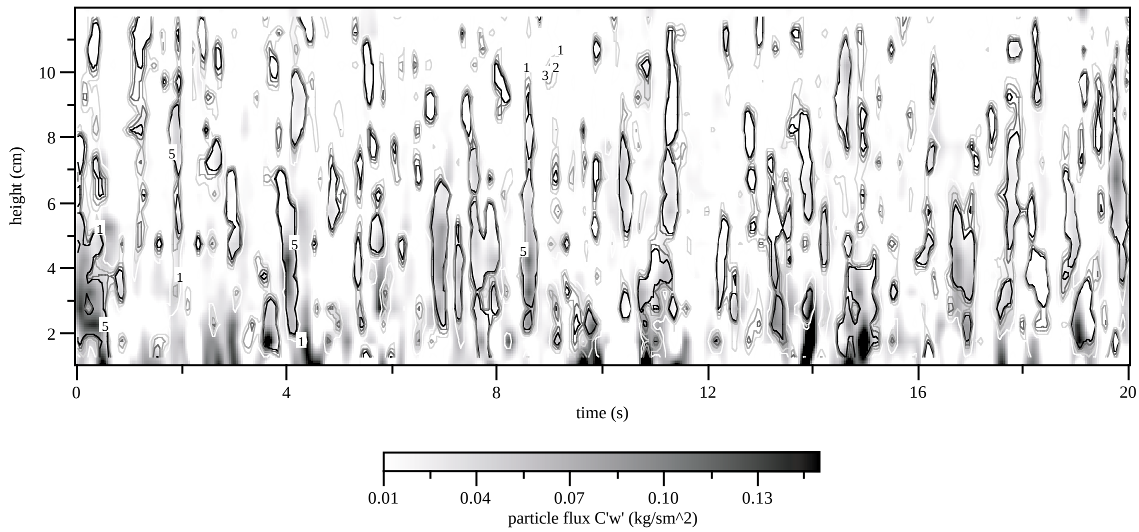

Fig. 3.12 Iso-contours of high shear stress events and vertical particle fluxes at the centerline of the open-channel flow. These measurements are obtained from the Acoustic Particle Flux Profiler (APFP) developed by (Shen and Lemmin, 1997a).

The objectives of this study are the following:

- Interpretation of the visualized flow patterns in particle suspended open-channel flows.
- Determination of the higher order statistical properties of particle fluxes in suspension flows.
- Comparison with the higher order statistical properties of the shear stress.
- Characterization of the impact of instantaneous momentum fluxes on instantaneous particle fluxes.
- Quantification of the particle entrainment and transport capacity of coherent structures in suspension flows under various hydraulic conditions (with particular focus on Reynolds number and Shields parameter dependency).

The theory of conditional statistics usually applied to the measured shear stress terms (see section 3.2) will be extended to the simultaneously measured vertical and horizontal particle fluxes and shear stress terms. It appears that this has never been done before and represents a powerful technique to assess quantitatively the particle entrainment by organized flow structures in suspension flows.

The derivation of the quadrant probability densities of the particle flux terms is, from a mathematical point of view, similar to the derivation described in section 3.2. Therefore, in order to avoid unnecessary repetitions, the reader is referred to Chapter 5 where the adaptation of the statistical theory to the mass flux terms is demonstrated in detail.

The proposed statistical theory will allow to quantitatively compare the quadrant repartition of the vertical and the horizontal mass fluxes with the one of the momentum fluxes. The momentum fluxes quadrant distribution in suspension flows will also be compared to the one in clear water flows. In the first step, the particle fluxes $\varepsilon_2 = c'u'/\overline{c'u'}$, $\varepsilon_3 = c'w'/\overline{c'w'}$ and the shear stress $\varepsilon_1 = u'w'/\overline{u'w'}$, will be treated as statistically independent. Fig. 5.1 shows the orientation of the quadrants in the respective planes. Subsequently, the relative quadrant contributions of each of the particle fluxes and the momentum flux can be estimated by evaluating the first order moment of the cumulant discarded quadrant probability density functions. Additionally, the time fractions of the three quantities in function of the corresponding threshold levels are calculated. Since the three quantities are treated independently, three corresponding threshold levels account for the selection of more or less strong instantaneous events (mass fluxes and shear stress).

The theoretical expressions of the quadrant density functions allow to identify the moments which are dominating the observed quadrant distribution of the relative shear stress and mass flux terms. These moments will be compared to the moments evaluated in clear water open-channel flows. The particle-turbulence interaction will therefore be interpretated in terms of the higher order statistical properties of the particle fluxes and momentum flux. Finally, some aspects of the turbulence modulation due to the presence of the particles will be analyzed.

3.4.4 Application of the quadrant threshold method to particle flux and shear stress

The validity of the quadrant repartitions resulting from the theoretical expressions will be examined by comparing them to the quadrant distributions estimated from the conditional sampling procedure. This method is identical to the uw-quadrant threshold method (see section 3.3) proposed by Lu and Willmarth (1973) but is extended here to the instantaneous longitudinal as well as vertical mass flux variables $\varepsilon_2 = c'u'/\overline{c'u'}$ and $\varepsilon_3 = c'w'/\overline{c'w'}$, respectively. Subsequently, the particle entrainment capability of the quasi-organized flow structures will be interpreted in view of their quadrant distributions.

A slightly modified sampling method will be used in Chapter 5. As mentioned previously, the quadrant dynamics of the momentum and mass fluxes are treated independently in the sense that their quadrant contributions are calculated as function of the corresponding threshold levels. A direct link between these results is therefore not obvious. Since the quasi-instantaneous momentum and mass fluxes are measured simultaneously, the modified sampling method consists in estimating the quadrant contributions of the mass fluxes in response to an instantaneous momentum flux event. For this purpose, the quadrant contributions of the mass fluxes are computed as function of the shear stress threshold and will be compared to the independently treated quadrant distributions of the mass fluxes and the shear stress.

3.5 Conclusions

The study in Chapter 4 is devoted to an analysis of the shear stress statistics in highly turbulent, clear water open-channel flow over beds with different roughness conditions. The experimental and theoretical statistical methods described in the sections 3.2 and 3.3 will be combined with flow visualization in order to determine the higher order statistical properties of the coherent structures. The quasi-instantaneous profiling ability of the ADVP allows to undertake the analysis over the entire flow depth, whereas mostly existing experimental studies are limited to point measurements mainly in the inner region of the turbulent boundary layer. Particular attention will therefore be given to the role of the quasi-organize flow structures in the momentum transfer mechanism between the inner and the outer layer regions. Another aspect concerns the effects of the relative roughness number on the statistical properties of the shear stresses. Are these effects restricted to a certain flow region? Is there a flow domain where a dynamical equilibrium between the turbulent momentum fluxes is dominated by the bursting phenomenon and can this property be interpreted in view of the time averaged conservation equations discussed in Chapter 2? Can this concept be generalized to any uniform open-channel flow over rough beds and to what application could this universal process be applied?

Chapter 5 deals with a study on shear stress and mass flux in suspension flows. The statistical procedures proposed in sections 3.4.3 and 3.4.4 are employed to determine the higher order statistical properties of the mass fluxes and to compare them with the properties of the shear stress in suspension as well as clear water flows. Can we quantify the impact of the strongly intermittent shear stress patterns on the suspended particle movements? Is the relative sediment transport capacity of coherent structures dependent on the Reynolds and / or the Shields parameter? Based on the results of the studies in these two chapters, Chapter 6 is concerned with a discussion of Cao's (1999) model described in section 3.4.2. A correction of the formulation relating the near bed equilibrium concentration in suspension flows to the characteristic scales of coherent motion is proposed. An extension of this approach to the concentration profile prediction would lead to a completely new model for the sediment transport assessment in suspension flows based on coherent structure characteristics.

3.6 References

Adrian, R. J., Meinhart, C. D. and Tomkins, C. D. (2000). Vortex organization in the outer region of the turbulent boundary layer. J. Fluid Mech., 422, 1-54.

Antonia, R. A. and Atkinson, J. D. (1973). High-order moments of Reynolds shear stress fluctuations in a turbulent boundary layer. J. Fluid Mech., 58(3), 581-593.

Blackwelder, R. F. and Kaplan, R. E. (1976). On the wall structure of the turbulent boundary layer. J. Fluid Mech., 76, 89-112.

Bogard, D. G. and Tiedermann, W. G. (1986). Burst detection with single-point velocity measurements. J. Fluid Mech., 162, 389-413.

Cao, Z. (1999). Equilibrium near-bed concentration of suspended sediment. J. Hydraulic Eng., 125(12), 1270-1278.

Chong, M., Soria, J., Perry, A. E., Chacin, J., Cantwell, B. J. and Y. Na (1998). Turbulence structures of wall-bounded shear flows found using DNS data. J. Fluid Mech., 357, 225-248.

Cleaver, J. W. and Yates, B. (1973). Mechanism of detachment of colloid particles from a flat substrate in turbulent flow. J Colloid Interface Sci., 44(464-473).

Corino, E. R. and Brodkey, R. S. (1969). A visual investigation of the wall region in turbulent flow. J. Fluid Mech., 37, 1-30.

Graf, W. H. and Altinakar, M. (1998). Fluvial Hydraulics. Wiley & Sons Ltd.

Grass, A. J. (1971). Structural features of turbulent flow over smooth and rough boundaries. J. of Fluid Mech., 50(2), 233-255.

Grass, A. J., R. J. Stuart and M. Mansour-Tehrani (1993): Common vortical structure of turbulent flows over smooth and rough boundaries. AIAA Journal 31(5): 837-847.

Gyr, A. (1983). For a better definition of the three types of sediment transport. J. Hydraulic Eng., 21(1), 1-14.

Hetsroni, G. (1991). The effect of particles on the turbulence in a boundary layer. Butterworth.

Hinze, J. O. (1975). Turbulence. McGraw-Hill, 790 pp.

Kendall, M. G. (1948). The advanced theory of statistics, I. Charles Griffin and Company, London, 457 pp.

Kim, H. T., Kline, S. J. and Reynolds, W. C. (1971). The production of turbulence near a smooth wall in a turbulent boundary layer. J. Fluid Mech., 50(133-160).

Kim, J., Moin, P. and Moser, R. (1987). Turbulence statistics in fully-developed channel flow at low Reynolds number. J. Fluid Mech., 177, 133-166.

Kline, G. R. and Kline, S. J. (1974). Combined dye-streak and hydrogen-bubble visual observation of a turbulent boundary layer. J. Fluid Mech., 62, 223-239.

Kline, S. J., Reynolds, W. C., Schraub, F. A. and Runstadler, P. W. (1967). The structure of turbulent boundary layers. J. Fluid Mech., 30(4), 741-773.

Lu, S. S. and Willmarth, W. W. (1973). Measurements of the structure of the Reynolds stess in a turbulent boundary layer. J. Fluid Mech., 60, 481-511.

Nakagawa, H. and Nezu, I. (1977). Prediction of the contribution to the Reynolds stress from bursting events in open-channel flows. J. Fluid Mech., 80(1), 99-128.

Nakagawa, H. and Nezu, I. (1981). Structure of space-time correlations of bursting phenomena in an open-channel flow. J. Fluid Mech., 104, 1-43.

Nino, Y. and Garcia, M. H. (1996). Experiments on particle-turbulence interactions in the near-wall region of an open-channel flow: implications for sediment transport. J. Fluid Mech., 326, 285-319.

Pratury, A. K. and Brodkey, R. S. (1978). A stereoscopic visual study of coherent structures in turbulent shear flows. J. Fluid Mech., 89, 251-272.

Robinson, S. K., Kline, S. J. and Spalart, P. R. (1988). Quasi-coherent structures in the turbulent boundary layer: Part II. Verification and new information from a numerically simulated flat-plate layer. In: S. J. Kline and N. H. Afgan (Editors), Near-wall turbulence, Zoran Zaric memorial conference. Hemisphere publishing corporation, Dubrovnik, Croatia, pp. 218-247.

Runstadler, P. G., Kline, S. J. and Spalart, P. R. (1963). An experimental investigation of flow structure of the turbulent boundary layer. No: MD-8, Stanford University, Paolo Alto.

Shen, C. and Lemmin, U. (1997). A two-dimensional acoustic sediment flux profiler. Meas. Sci. Technol., 8, 880-884.

Soulsby, R. L., Atkins, R. and Salkield, A. P. (1994). Observations of the turbulent structures of a suspension of sand in a tidal current. Cont. Shelf Res., 14(4), 429-435.

Spalart, P. R. (1988). Direct simulation of a turbulent boundary layer up to Re_θ=1410. J. Fluid Mech., 187, 61-98.

Sumer, B. M. and Deigaard, R. (1981). Particles motion near the bottom in turbulent flow in an open-channel. Part 2. J. Fluid Mech., 109, 311-337.

Tardu, F. S. (1995). Characteristics of single and clusters of bursting events in the inner layer. Exp. in Fluids, 30, 112-124.

Theodorsen, T. (1952). Mechanism of turbulence, Proc. Midwest Conf. Fluid Mech., 2nd, Columbus, Ohio, pp. 1-18.

VanRijn, L. C. (1984). Sediment transport, part II: Suspended load transport. J. Hydr. Engrg., ASCE, 11(110), 1613-1641.

Willmarth, W. W. and Tu, B. J. (1967). Structure of turbulence in the boundary layer near the wall. Phys. Fluids, 10, 134-137.

Yalin, M. S. (1972). Mechanics of sediment transport. Pergamon Press, Oxford GB.

Yung, B. P. K., Merry, H. and Bott, T. R. (1988). The role of turbulent bursts in particle re-entrainment in aqueous systems. Chem. Engng. Sci., 44, 873-882.

Zyserman, J. A. and Fredsoe, J. (1994). Data analysis of bed concentration of suspended load. J. Hydr. Engrg., ASCE, 9(120), 1021-1042.

CHAPTER 4

SHEAR STRESS STATISTICS AND WALL SIMILARITY ANALYSIS IN TURBULENT BOUNDARY LAYERS USING A HIGH RESOLUTION 3-D ADVP

Published in the IEEE Journal of Oceanic Engineering (2000) Vol. 25, No. 4, pp 446-457.

Special issue on current measurements.

4.1 Abstract

3-D quasi-instantaneous acoustic Doppler velocity profiles at the center of uniform, turbulent open-channel flow over smooth and rough beds have been analyzed for the dynamics of coherent structures. The qualitative aspects of simultaneously measured Eulerian velocity and shear stress signatures identify coherent structures in the water column. A cumulant discard method is applied to describe the statistical properties of the covariance terms $u'w'$ along the mean flow and $v'w'$ across the mean flow relative to their time means. Conditional statistics and conditional sampling are used to compare the theoretical and experimental relative covariance contributions from the four quadrants in the longitudinal and transverse planes. The results in the (u', w') plane show the dominance of ejections (quadrant 2; $u' < 0, w' > 0$) and sweeps (quadrant 4; $u' > 0, w' < 0$). In contrast, the distribution of fractional $v'w'$ events in the transverse plane is quasi uniform over the four quadrants. Based on these experimentally determined statistical properties of the covariance terms in different flow conditions, a simplified form of the vertical turbulent energy flux in the intermediate flow region is given and the concept of wall similarity in turbulent boundary layers is validated. Since the validity of the wall similarity concept over a wide range of bed roughness has been shown, it is proposed to determine the mean bed friction velocity from the evaluation of the vertical turbulent energy flux.

4.2 Introduction

Over the past decade, Doppler sonars have become powerful instruments for the measurement of oceanic current profiles. The type of instrument most often used applies the “noncoherent” technique (Pinkel, 1979). More recently, oceanic research has focused increasingly upon boundary layer studies in nearshore and coastal environments and in benthic boundary layers. In these applications, the depth range of interest is relatively short (O(1m)) and due to limitations inherent in “noncoherent” sonars, such instruments can no longer be used efficiently. Point measurement techniques have been applied in this environment. However, acoustic profiling using the “pulse-to-pulse” coherent technique (Lhermitte and Serafin, 1984; Lhermitte and Lemmin, 1994) offers an attractive alternative because it is possible to cover the total depth of the boundary layer, and it is non-intrusive.

Boundary layer flows are often characterized by strong vertical gradients. The pulse-to-pulse coherent technique can provide the high spatial (O(5 mm)) and temporal (O(15 Hz)) resolution as well as the high velocity resolution (O(3 mms^{-1})) required to study the details of boundary layer flow. By changing the acoustic frequency and the system geometry, the system can be adapted to the boundary layer dimensions encountered in the field.

The presence of high spatial and temporal variability in the boundary layer flow field has been documented in the literature. The streamwise velocity field in the near wall region of a boundary layer is known to be organized in alternating streaks of high and low velocity which are persistent in time. Related to this structure are intermittent, quasi-periodic events, consisting of outward ejections of low-speed fluid from the bed and inrushes of high-speed fluid towards the bed, called coherent structures. From studies of wall-bound turbulent shear flows, these organized motions (i.e., the bursting phenomena) are identified as a primary turbulence mechanism for the production of Reynolds stress and turbulence energy in the near bed region (Kline et al., 1967; Nagano and Tagawa, 1995). Little is known so far about the dynamics of coherent structures in the cross-stream plane.

Profiling the whole depth of the boundary layer in a single sweep is an ideal technique to study the dynamics of these coherent structures. They have been made evident using 2-D (Rolland and Lemmin, 1997) and 3-D (Hurther and Lemmin, 1998) acoustic Doppler velocity profilers in various flow conditions. Recently, we have also shown their relation to sediment resuspension and transport using an acoustic flux profiler (Shen and Lemmin, 1999; Hurther and Lemmin, 2000).

The cumulant discard method has been used by several authors, all of whom used point measurement techniques, in order to predict quantitatively the covariance $u'w'$ term statistics in the streamwise direction for different wall roughness conditions in zero pressure gradient boundary layers. Antonia and Atkinson (1973) estimated the skewness and flatness factors of the shear stress fluctuations by a fourth order approach and expressed the probability density distribution of the normalized $u'w'$ term from a Gram-Charlier type joint probability density function of u' and w'. In the inner region of the flow, they found good agreement between results of the cumulant discard method and the corresponding experimental factors. Only a qualitatively similar tendency was observed in the outer region where the flow was found to be more intermittent.

Nakagawa and Nezu (1977; hereinafter NN77) developed the equations of the probability density for the relative covariance term $u'w'$ conditionally sampled over the four quadrants of the (u',w') plane. Events with quadrant 1 $(u'>0, w'>0)$, quadrant 2 $(u'<0, w'>0)$, quadrant 3 $(u'<0, w'<0)$ and quadrant 4 $(u'>0, w'<0)$ orientation are respectively identified as outward interaction, ejection, inward interaction and sweep events. They showed that a third order Gram-Charlier distribution is sufficient to quantify the quadrant time fractions and quadrant covariance fractions in the wall region (z/h< 0.1, where h is the water depth) and in the equilibrium region (0.15 < z/h < 0.6) of open-channel flow.

Raupach (1981) applied a third order Gram-Charlier type distribution to quantify the covariance statistic parameters in rough-wall and smooth-wall turbulent wind tunnel boundary layers. These three studies agree on the effect of roughness on the dynamics of shear stress events $u'w'$: In the vicinity of the wall it is characterized by an increase of sweep event contribution, both with roughness and with proximity to the wall.

This paper reports on an experimental investigation of the conditionally sampled covariance events $u'w'$ in the streamwise direction and $v'w'$ in the across stream plane. In order to evaluate the dynamics under controlled conditions, experiments were carried out in turbulent open-channel flow over smooth and rough beds using a 3-D acoustic Doppler velocity profiler. An interpretation of the Eulerian signatures of the covariance and 3-D velocity fields over the whole depth will be presented.

To validate the effect of roughness on covariance dynamics, experimental results of fractional contribution to the corresponding shear from each quadrant of both covariance terms will be compared to results from a cumulant discard Gram-Charlier distribution, applied to both $u'w'$ and $v'w'$ terms.

From the observed linear relation of the third order moments in the equilibrium flow region of the boundary layer, a simplified form of the vertical turbulent energy flux is validated. Since a constant value of the normalized turbulent kinetic energy flux is found in the flow region (0.25< z/h <0.75), a method for the determination of the bed friction velocity is proposed which has certain advantages over commonly used methods.

4.3 Acoustic Doppler Velocity Profiler

A pulse-to-pulse coherent Acoustic Doppler Velocity Profiler (ADVP) is used to evaluate the three velocity components simultaneously over the entire investigated water depth. The system consists of a central narrow beam emitter and up to four wide-angle receiver transducers placed symmetrically around the center. The transducers are arranged in two perpendicular planes, each of which allows to resolve profiles of one horizontal and the vertical velocity component. The redundancy of the vertical component provides for a control of the quality of the geometrical alignment of the transducers. Since sound is emitted only from the central transducer, all velocity components are evaluated from phase information coming from the same scattering volume. Unlike commercially available profilers, the ADVP measures velocities along a single straight line of consecutive scattering volumes. This is the only way in which turbulence information and particularly a correlation between velocity components can correctly be evaluated without any specific requirements for the flow conditions. Quasi-instantaneous velocity components are estimated using the pulse-pair algorithm. The system is described in more detail in Lhermitte and Lemmin (1994), Rolland and Lemmin (1997) and Lemmin et al. (1999)

A combination of a hardware method (1) and a software method (2) is used here to reduce noise contributions in the turbulence measurements with the 3-D ADVP. A brief explanation of the two methods is given:

(1) An ultrasonic constant beamwidth transducer system is used which is capable of generating an extended focal zone by electronically focusing the beam over the desired water depth range (Hurther and Lemmin, 1998; Lemmin et al., 1999). Beam directivity measurements show that the higher beam directivity and the reduction in side lobe level lead to an increase of the signal-to-noise ratio by up to 15dB compared to a plane disc transducer. It also leads to significant reduction in spectral broadening effects, which in the case of plane disc transducers reduce the velocity resolution and interfere with correct data interpretation (Lhermitte and Lemmin, 1994).

(2) A direct Doppler signal treatment method is applied to the data (Hurther and Lemmin, 1999). The technique does not rely on any hypothesis concerning flow characteristics. No knowledge about supplementary device dependent parameters such as the sample volume size or the acoustic beam opening angle are needed. It is based on a noise spectrum reconstruction from cross-spectra evaluations of two simultaneous and independent measurements of the vertical velocity over the whole water depth. Correcting for the system geometry, the noise spectra and the noise variances are calculated and removed from the three fluctuating velocity components. The corrected turbulence spectra show a –5/3 slope over the whole inertial subrange delimited by the frequency band of the device.

The corrected profiles of turbulence intensities, turbulent kinetic energy, shear stress and turbulent energy balance equation terms such as production, transport and dissipation are in good agreement with different semi-theoretical formula and other measurements from the literature.

The combination of this correction method with the use of the constant beamwidth emitter allows turbulence measurements with a relative error under 10% in the intermediate and free surface flow regions ($0.15<z/h<1$) of the boundary layer. As indicated in Hurther and Lemmin (1999), deviations of the corrected mean turbulence measurements from semi-theoretical laws are observed in the wall region. Supplementary studies are needed to evaluate quantitatively the limits of sonar measurements in that flow domain. While we allocate the remaining variations to effects of the spatial averaging due to the strong profile gradients in this layer, effects of bottom roughness cannot be excluded either.

4.4 Experimental set-up

Experiments were carried out in two laboratory open-channels under uniform flow conditions: the first one (29m long, 2.45m wide, 75cm deep) has a rough bed and the second one (43m long, 2m wide, 1m deep) has a smooth bed. For experiments over rough beds (experiments B, C and D in Table 4.1), a sand bed with a mean grain size of d_{50}=1.7mm (estimated at 50% of the granulometric curve) was used. The measurement sections are placed 13m and 16m downstream from the entrances for rough and smooth bed conditions, respectively, where the turbulent flow is well developed. All velocity data presented here were taken in the center of the channels. The hydraulic parameters are given in Table 4.1. These indicate subcritical highly turbulent flows for all experiments with varying Reynolds, Froude numbers and bed friction velocities. The uncertainties on discharges, water depths and discharge velocities estimations shown in Table 4.1 are less than 5% and less than 10% for the bed shear velocity estimations.

Exp.	Q (m^3/s)	h (cm)	U (cm/s)	u_* (cm/s)	$u_{*,S}$ (cm/s)	$u_{*,log}$ (cm/s)	S ($\times10^{-4}$)	Re_h ($\times10^3$)	Fr_h	B/h	k_S^+	Π
A	0.115	19.1	32	2.1	2.3	2.3	2.8	61	0.23	10.5	≈0	0.4
B	0.069	10.6	25.5	2.0	2.3	2.0	5	27	0.25	23	34	0.1
C	0.122	16	31	2.5	2.8	2.7	5	49.6	0.25	15.3	45	0.1
D	0.200	17.3	47.5	2.9	2.9	3.0	5	82.2	0.36	14.2	50	0.3

Table 4.1 Hydraulic parameters for experiments

The variables u_* $u_{*,S}$ and $u_{*,log}$ represent the friction velocities obtained from linear extrapolation of the mean Reynolds stress at the wall, from the energy line slope formula for uniform flow and from the log law, respectively. The relative errors (relative to $u_{*,log}$) are less than 10% which shows that conditions of uniform flow are satisfied. The standard roughnesses k_S^+ are normalized with the corresponding viscous lengths and are smaller than 70, for all experiments, corresponding to incompletely rough beds found in oceanic boundary layers. A Manning-Strickler formula is used to estimate the physical grain size from the uniform flow conditions in the cases of rough beds (experiments B to D in Table 4.1). We obtain values between 3mm and 5mm for the mean particle diameter d_{50}. The difference between the calculated values and the true value (1.7mm) indicates the difficulty to determine realistic results from profile extrapolations for rough bed bottoms where the position of the profile origin is poorly defined. The Π factor of Coles wake function (Table 4.1) is extracted from the velocity defect law (Graf and Altinakar, 1998) with κ equal to 0.4 and varies between 0.1 and 0.4.

The experiments were conducted under clear water conditions where particles do not contribute significantly to backscattering. Shen and Lemmin (1997) identified the ultrasonic targets as being concentration microstructures originating from clusters of fine air bubbles. Since these structures have a very small size, they are able to follow the turbulent motion without inertial lag over the investigated frequency band. All measurements presented here are extracted from data sets acquired over 600 second intervals. The spatial and temporal resolutions are dependent on the settings of the instrument and are equal to ≅3mm and 0.024s, respectively in the present case.

4.5 Observations of common structural flow features over smooth and rough beds

Eulerian signatures are limited for the identification of the different types of coherent structures passing through a fixed measurement volume because they have a high spatio-temporal evolution (Robinson et al., 1988). In order to compare our data qualitatively to simultaneous velocity measurements over an entire cross section presented in Grass et al. (1993), a Lagrangian flow field was computed by applying Taylor's hypothesis for the mean flow direction. As in Grass et al. (1993), a convection velocity, U_d, equal to the depth-averaged mean velocity was chosen in order to compare the measurements. Fig. 4.1 shows four sequences (of our data) where the covariance and fluctuating velocity patterns are superimposed. Fig. 4.1a presents the fluctuating 2-D velocity vectors $\mathbf{V}(u\text{-}U_d,w')$ and covariance iso-contourlines in the longitudinal flow plane in rough (experiment A) and Fig. 4.1b in smooth (experiment D) bed conditions. Figs. 1c and 1d give the same information in the transverse flow plane for rough (experiment D) and smooth (experiment A) bed conditions, respectively.

The diagrams in Fig. 4.1 show flow structures similar to those observed by Grass et al. (1993). Flow patterns such as vortex cross-sections, internal shear layers, ejections, sweeps, upwellings, downwellings over a smooth bed are identical to those over a rough bed. For example, internal high-shear layers are observed in Fig. 4.1a at x=0.8m, z/h=0.25, corresponding to a sweep event (quadrant 4 direction) and in Fig. 4.1b at x=1.1m, z/h=0.125, corresponding to an ejection event (quadrant 2 direction). Vortex cross-sections can be seen in the longitudinal (Fig. 4.1a at x=0.36m, z/h=0.42 and Fig. 4.1b at x=0.1m, z/h=0.45) and transverse (Figs. 1c at x=0.68m, z/h=0.375 and Fig. 4.1d at x=1.23m, z/h=0.8) flow fields indicating the three dimensionality of the vortical structures. Vortex cross-sections associated with an underlying high shear layer such as an ejection event can be observed at x=1.49m, z/h=0.25 in Fig. 4.1a.

Numerical boundary layer simulation results of Robinson et al. (1988) show similar structures where the vortex core is identified as the head of a horseshoe vortex located above an ejection event. In the free surface flow region, upwellings and downwellings can be seen at several locations in the flow fields (in Fig. 4.1a at x=1.06m, z/h=0.85 and in Fig. 4.1b at x=1.32m, z/h=0.88). As shown by Kumar et al. (1998) by instantaneous Lagrangian flow visualization, these time persistent free-surface structures (especially upwellings) were observed to generate one or more pairs of spiral eddies at the water surface with opposite normal vorticities. They suggested that this sequence of events might be typical for the generation process of water surface structures such as boils in turbulent free surface flows.

Previous (Lemmin and Rolland, 1997 and Shen and Lemmin, 1999) and present observations of different kinds of coherent structures give support to the existence of flow patterns common to both smooth and rough beds. Furthermore, the matching of these flow patterns with the patterns shown in Grass et al. (1993) confirms the presence of horseshoe vortical structures although they could not be visualized spatially with our measurement technique. In the longitudinal flow plane, ejection and sweep events seem to be predominant. No dominant patterns can be distinguished in the transverse shear stress structures (Fig. 4.1c and Fig. 4.1d). This observation will be confirmed below by quantifying the 3-D statistical properties of the longitudinal and transverse relative covariance terms.

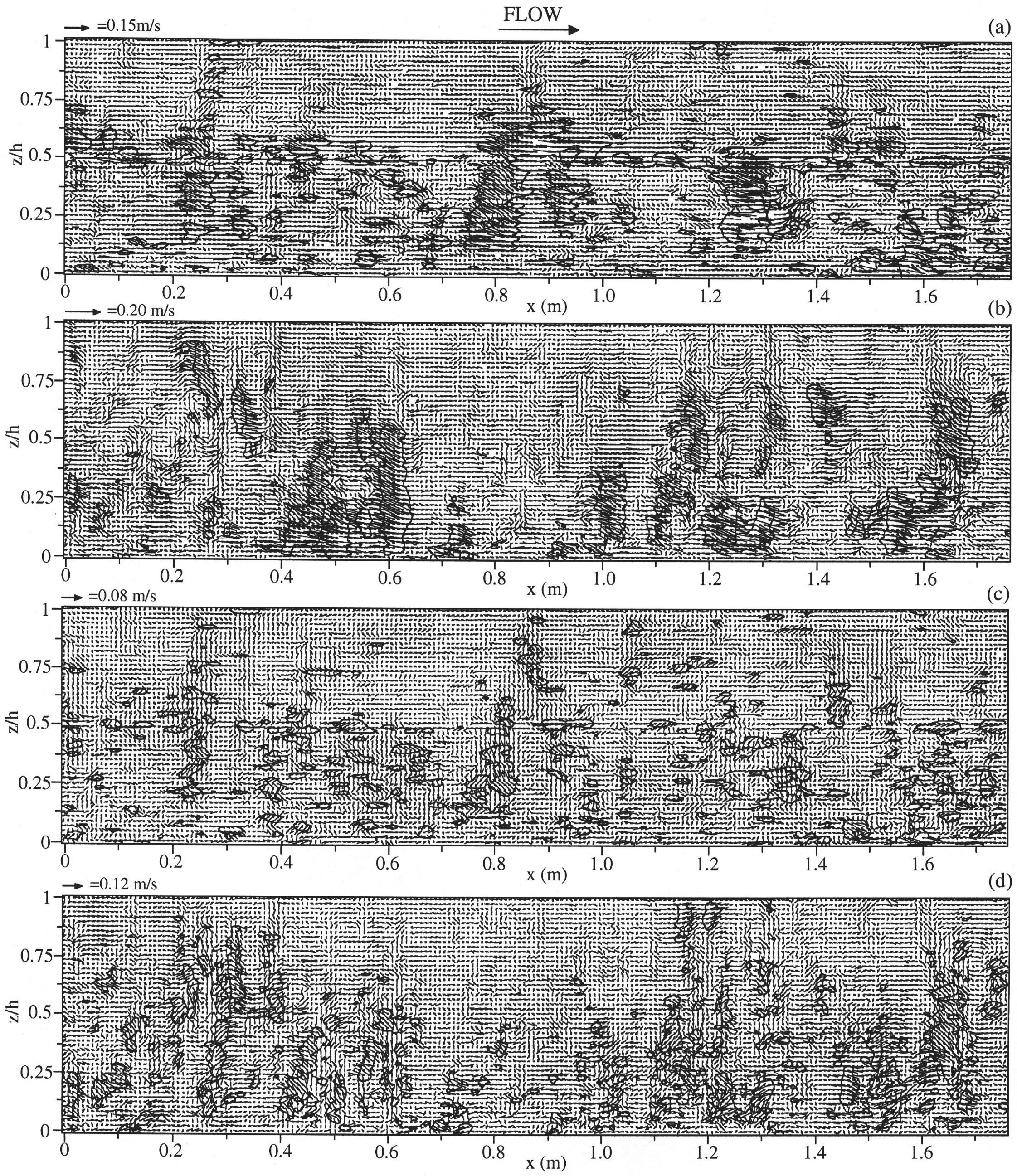

Fig. 4.1 Iso-contours of high shear patterns and fluctuating velocity field at centerline of the channel: (a) for **V**'(u',w') velocity vector (in Exp. A), (b) for **V**'(u',w') velocity vector (in Exp. D), (c) for **V**'(v',w') velocity vector (in Exp. A), (d) for **V**'(v',w') velocity vector (in Exp. D).

4.6 Conditional statistics of relative covariances

4.6.1 Theoretical aspects

This section is refered to section 3.2

4.6.2 Results and discussion

Fig. 4.2 presents the theoretical and experimental quadrant fractional contributions of the relative covariance term ε_1 calculated from Eq. (3.13) using the $u'w'$-quadrant technique for experiment C. A comparison of the results at four different depths confirms the ejection-sweep dominance in ε_1 contributions. Good agreement is seen between the theoretical and the experimental distributions for a threshold level $H_1 < 10$. Above that value, deviations between the theoretical and the experimental curves point to the limitation of the third order model because the covariance generation process becomes more intermittent with increasing H_1. However, the value of $T_{1,5}$ in Fig. 4.2 indicates that less than 10% of all events still contribute in that case.

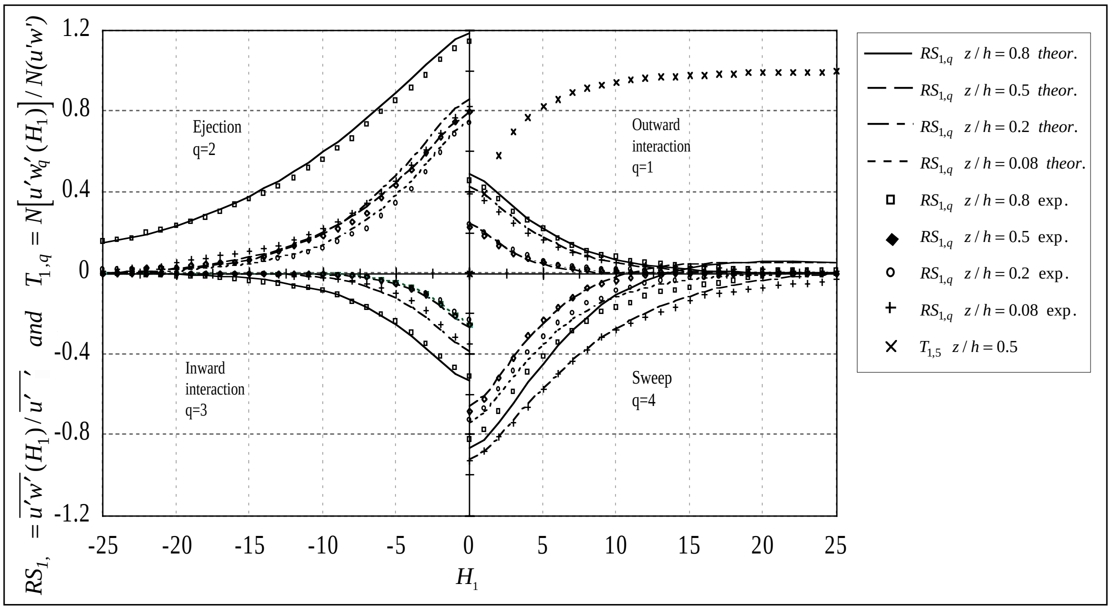

Fig. 4.2 Fractional contribution of relative covariance ε_1 versus threshold level at four flow depths and time fraction of hole event $T_{1,5}$(z/h=0.5, H_1) , for Experiment C. The notation N[x] represents the number of x values.

In the outer region of the boundary layer (z/h>0.2), ejections contribute more than sweeps. In the inner region, the sweep contribution increases and reaches the same level as the ejections. This was also observed by Grass (1971) who stated that sweep events become larger in the vicinity of the bed. The contributions of inward (quadrant 3) and outward (quadrant 1) interactions are much lower, remaining nearly constant over the entire boundary layer depth.

The time fraction of the hole events $T_{1,5}$ at depth z/h=0.5 is also indicated in the Fig. 4.2. The variation of $T_{1,5}$ with depth was found to be weak. A given H_1 value indicates the time fraction of those events which do not contribute to the $RS_{i,q}(H_1)$ level. For example for $H_1 = 10$, the time fraction of the hole events is more than 90%. Thus, less than 10% still contribute to the event generation. In that case (for z/h=0.08) $RS_{1,1} = 0.05$, $RS_{1,3} = -0.02$,

$RS_{1,4} = -0.28$, $RS_{1,2} = 0.2$, which characterize the turbulence generation process as a short duration, high magnitude event. This quantitative calculation confirms the qualitative observation in Figs. 1a and 1b. Coherent structures such as ejections and sweeps are obviously related to the generation of important covariance events and as a result, also act as the main turbulent energy producers. The results in Fig. 4.2 agree well with those previously described by several authors using hot film or LDA measurements.

In Fig. 4.3 the same quantities as in Fig. 4.2 are presented for the covariance events ε_2, in the transverse plane of the boundary layer. The curves fall off more slowly, stretching to much larger values of the threshold level H_2, thus denoting larger ε_2 variations from their temporal mean and low mean covariance $\overline{v'w'}$. It is particularly striking that the ε_2 covariance generation is nearly equal for all quadrants, independent of the threshold level H_2 and depth z/h. This quantitative calculation confirms the qualitative observation in Figs. 1c and 1d.

In order to compare quantitatively the $RS_{i,q}$ and $T_{i,q}$ values of the different quadrants and planes, Fig. 4.4 represents their profiles over the depth for two-different threshold levels $H_1 = H_2$ and two bed roughness conditions (Experiments A and D). As indicated above, $RS_{1,2}$ and $RS_{1,4}$ contribute significantly to covariance events ε_1, $RS_{1,2}$ becoming larger than $RS_{1,4}$ towards the free surface independent of bed roughness. The effect of roughness is evident from an increase towards the bed of the ejection contribution in the rough bed case compared to the smooth bed case (at z/h≈0.3). In the wall region the ejection contribution becomes lower than the sweep contribution at z/h≈0.12, whereas the ejection contribution remains greater than the sweep contribution in the smooth case. This tendency is independent of the parameter H_1.

We can observe from the $T_{i,q}$ profiles that even with very low time fraction of quadrant 2 and 4 events, their contribution remains important for high threshold values (for $H_1 = 8$ we find depth averaged values of $T_{1,2} \approx T_{1,4} \approx 0.04$ and $RS_{1,2} = 0.4$ $RS_{1,4} = 0.15$). The time fraction evolution with H_1 indicates a rapid decrease of $T_{1,1}$ and $T_{1,3}$ reaching a zero value at $H_1 = 4$ (not shown in Fig. 4.4) whereas $T_{1,2}$ and $T_{1,4}$ remain nearly equal except for $H_1 = 0$. NN77 had previously given profiles for ε_1 events, but only for $H_1 = 0$. The presented results correspond well with theirs.

In Fig. 4.4, the fractional ε_2 covariance magnitudes $RS_{2,q}$ are normalized by $\sqrt{\overline{v'^2}\,\overline{w'^2}}$ because the low values of the term $\overline{v'w'}$ induces very high $RS_{2,q}$ values. As mentioned before, the contributions from the different quadrants are nearly the same and independent of z/h and H_2. It can be seen that the time fractions only slightly vary with depth remaining close to 0.25 for $H_2 = 0$ over the whole depth. From Figs. 4 and 5 we can confirm that no apparent quadrant related bursting process is observed for the covariance term ε_2 in the transverse flow plane.

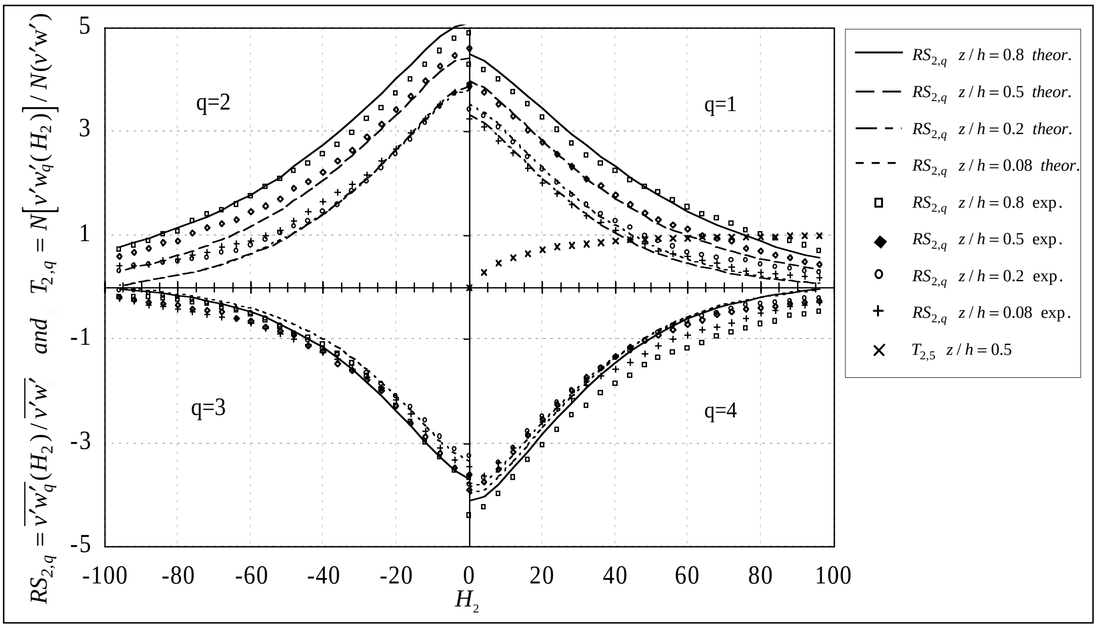

Fig. 4.3 Fractional contribution of relative covariance ε_2 versus threshold level H_2 at four flow depths and time fraction of hole event $T_{2,5}$(z/h=0.5, H_2), for Experiment C. The notation N[x] represents the number of x values.

The third order cumulants (crossed and non-crossed) determine the repartition of the relative covariance contributions over the different quadrants. In Eq. (3.11) the terms S_1^-, D_1^-, S_2^+, S_2^- only depend on third order cumulants. Therefore, a comparison of these moments for the different flow conditions gives information about the shear stress dynamics.

Fig. 4.5 shows all third order moments needed to evaluate the factors S_i^+ and S_i^- in Eq. (3.11) for experiment C. As previously observed by NN77 and Raupach (1981) the $m_{1,jk}$ profiles are symmetrical over an extended range roughly corresponding to $0.2 \le z/h \le 0.8$. The relation between all four moments can be assumed to be linear (Raupach, 1981). NN77 considered that $m_{1,30}$ and $m_{1,21}$ are the reflections of $m_{1,03}$ and $m_{1,12}$ respectively on the zero axis but did not relate the crossed moments to the skewness factors. In our study, 3-D velocity data are available from the ADVP measurements and the crossed third order moment $m_{2,21}$ can be calculated whereas this term had to be approximated in the previous studies. In our case a linear combination of these third order moments yields:

$$m_{1,30} = -0.94 m_{1,03} = -1.78 m_{1,21} = 1.43 m_{1,12} = -2.27 m_{2,21} \qquad \text{for} \quad 0.25 \le z/h \le 0.75 \qquad (4.1)$$

where the coefficients have been estimated by applying a least square fit to data included in the interval $0.25 \le z/h \le 0.75$. The mean correlation coefficients (averaged over the four experiments) are $R_{c_{1,03}} = 0.82$, $R_{c_{1,12}} = 0.81$, $R_{c_{1,21}} = 0.87$, $R_{c_{2,21}} = 0.51$.

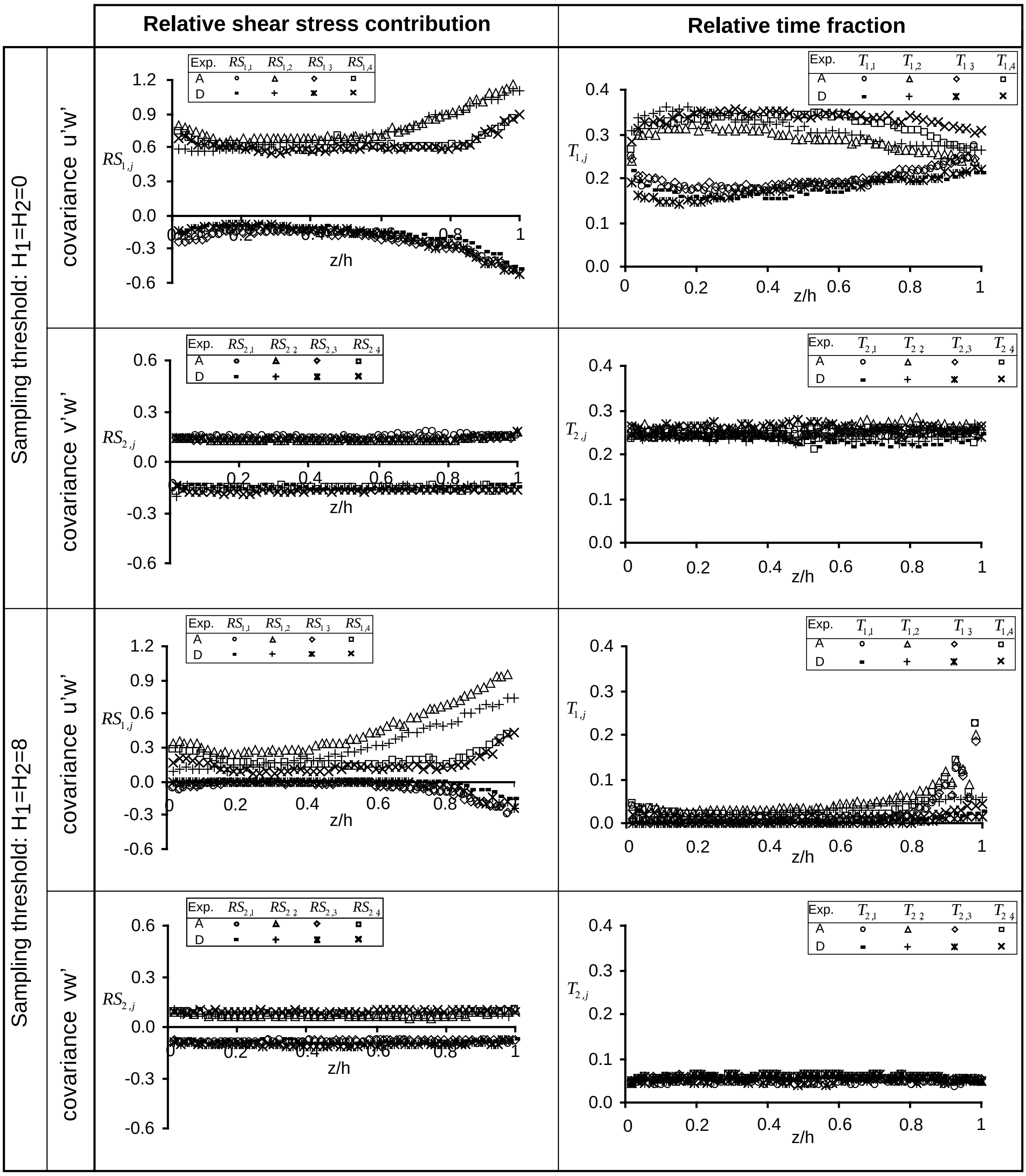

Fig. 4.4 Comparison of fractional covariance and time fractions of ε_1 and ε_2 versus flow depth at two $H_1= H_2$ threshold levels for experiment A (smooth) and experiment D (rough bed)

In order to determine whether these numerical values of the coefficients linking the different third order moments are constant and independent of Reynolds, Froude numbers and bed roughness, Eq. (4.1) is presented for all experiments in Fig. 4.6. For $0.25 \le z/h \le 0.75$, the values of the different coefficients in Eq. (4.1) are found to be nearly equal for all investigated flow conditions. Slight deviations are observed in the wall and free surface flow regions.

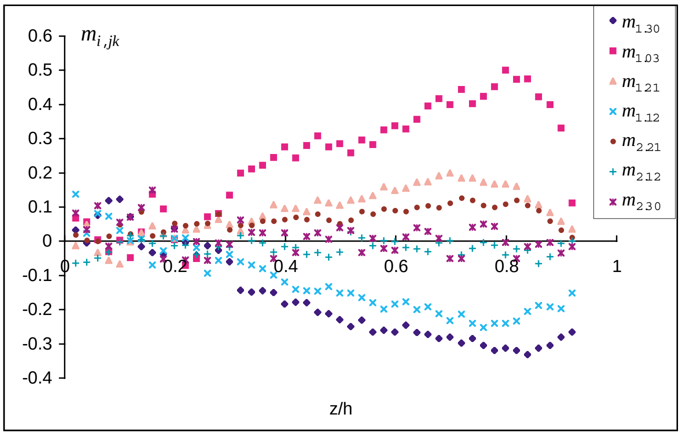

Fig. 4.5 Representation of third order moments (experiment C)

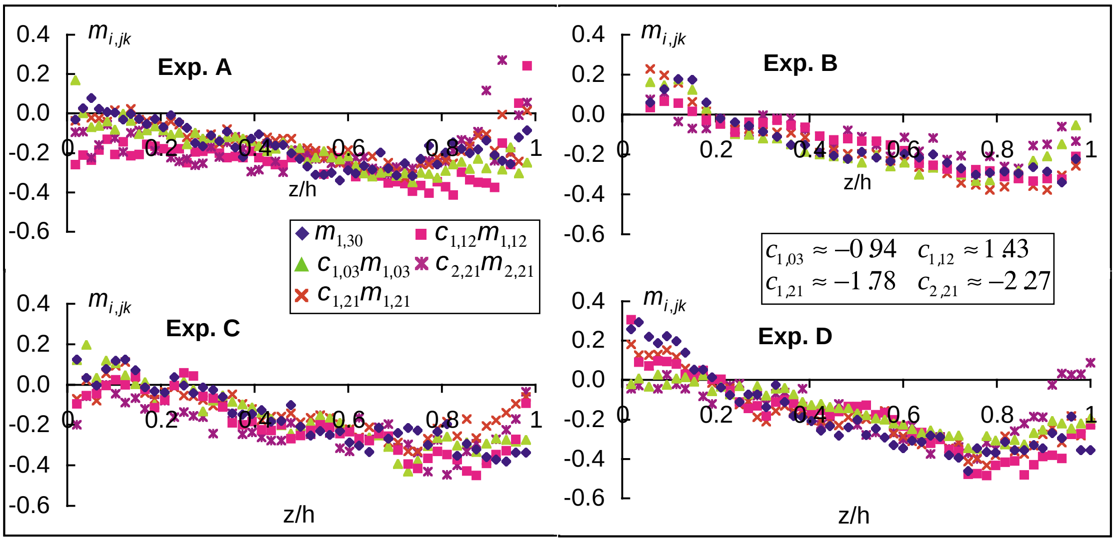

Fig. 4.6 Observed constant relationship between third order moments for experiments A, B, C and D.

4.7 Wall similarity in turbulent boundary layers

The wall similarity concept in turbulent boundary layer flow under uniform flow conditions is based on the existence of an extended region in depth where the turbulent energy production and dissipation terms are in equilibrium and the diffusion terms are negligible. The two-diffusion terms (fluctuating pressure and turbulent kinetic energy diffusion) not only compensate each other but are nearly equal to zero (Nezu and Nakagawa, 1993). Therefore, the similarity concept implies that in uniform flows with high Reynolds numbers, a similar equilibrium flow region exists, independent of the flow conditions and bed roughness conditions. This concept can be described by the turbulent energy budget equation:

$$\underbrace{\frac{\partial}{\partial t}\frac{\overline{k^2}}{2}+\bar{u}_k\frac{\partial}{\partial x_k}\frac{\overline{k^2}}{2}}_{\text{TRANSPORT}}+\underbrace{\overline{u_i'u_k'}\frac{\partial \bar{u}_i}{\partial x_k}}_{\text{PRODUCTION}}=\underbrace{-\frac{\partial}{\partial x_k}\overline{\left(\frac{p'}{\rho}+\frac{k^2}{2}\right)u_k'}}_{\text{TURBULENT DIFFUSION}}+\underbrace{\nu\frac{\partial^2}{(\partial x_l)^2}\frac{\overline{k^2}}{2}}_{\text{VISCOUS DIFFUSION}}\underbrace{-\nu\overline{\frac{\partial u_i'}{\partial x_l}\frac{\partial u_i'}{\partial x_l}}}_{\text{DISSIPATION}} \tag{4.2}$$

in which Einstein's notation convention is employed (i.e. $\overline{k^2}/2=\overline{u_i'^2}/2$ is the turbulent kinetic energy). Fig. 4.7 shows the normalized shear stress profiles for all investigated experiments. The observed linear variations over the relative flow depth confirm that the flow is uniform and in the mean two-dimensional at high Reynolds number (see Table 4.1). Hence, the last equation yields:

$$\underbrace{-\overline{u'w'}\frac{\partial \bar{u}}{\partial z}}_{\text{PRODUCTION}}=\underbrace{\frac{\partial}{\partial z}\left[\frac{1}{2}\overline{(u'^2+v'^2+w'^2)w'}+\overline{p'w'}\right]}_{\text{TURBULENT DIFUSION}}+\underbrace{\varepsilon}_{\text{DISSIPATION}} \tag{4.3}$$

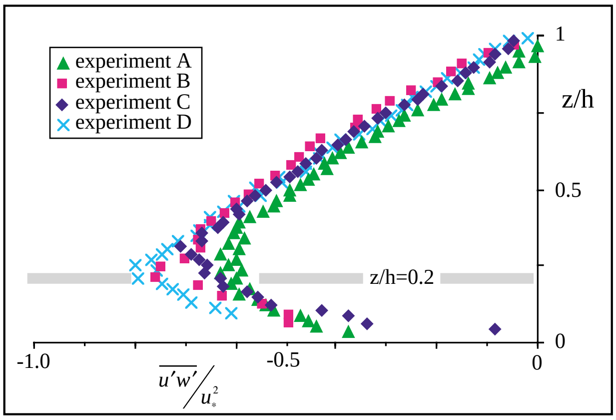

Fig. 4.7 Shear stress profiles for all experiments.

The equilibrium concept is expressed as follows:

$$-\overline{u'w'}\frac{\partial \bar{u}}{\partial z}\cong\varepsilon \qquad \text{with} \qquad \frac{1}{2}\overline{(u'^2+v'^2+w'^2)w'}\cong \text{const.} \quad \text{for} \quad 0.15\le z/h\le 0.6 \tag{4.4}$$

The relation of the third order moments, discussed in section 4.6, to the normalized vertical flux of turbulent kinetic energy is given by (the normalization variable will be discussed later):

$$F_k = \frac{1}{2u_*^3}\overline{(u'^2 + v'^2 + w'^2)w'} = \frac{\sqrt{\overline{w'^2}}}{2u_*^3}\left(\overline{u'^2}m_{1,21} + \overline{v'^2}m_{2,21} + \overline{w'^2}m_{1,03}\right) \tag{4.5}$$

This equation indicates a direct connection between the turbulent energy flux and the dynamics of the shear stress events through the third order moments. As shown previously, these statistical parameters determine the distribution of the relative covariance terms over the different quadrants. Furthermore, the statistical analysis has shown that the relation between the different third order moments is linear over a flow region exceeding the intermediate flow region (Eq. (4.1)). This is represented by the following expression:

$$\begin{cases} m_{1,30} = c_{1,03}m_{1,03} \\ m_{1,30} = c_{1,21}m_{1,21} \\ m_{1,30} = c_{1,12}m_{1,12} \\ m_{1,30} = c_{2,21}m_{2,21} \end{cases} \tag{4.6}$$

If the relations between the different turbulence intensities are used, i.e.:

$$\sqrt{\frac{\overline{v'^2}}{\overline{u'^2}}} = C_1 \qquad \sqrt{\frac{\overline{w'^2}}{\overline{u'^2}}} = C_2 \tag{4.7}$$

Eq. (4.5) can be rewritten as a function of only one third order moment as follows:

$$F_k = S\,\frac{\overline{u'^3}}{u_*^3} \quad \text{with} \quad S = \frac{C_2}{2}\left(\frac{1}{c_{1,21}} + \frac{C_1^2}{c_{2,21}} + \frac{C_2^2}{c_{1,03}}\right) \quad \text{for } 0.25 \le z/h \le 0.75 \tag{4.8}$$

NN77 derived the following expression for Eq. (4.5):

$$F_k \cong \frac{1}{2}\left(\frac{\sigma_w}{\sigma_u}\right)\left(\frac{\sigma_u}{u_*}\right)^3\left[m_{1,21} + 2\left(\frac{\sigma_w}{\sigma_u}\right)^2 m_{1,03}\right] \qquad \text{with} \qquad \sigma_i = \sqrt{\overline{u_i'^2}} \tag{4.9}$$

by considering that $m_{1,30}$ and $m_{1,21}$ are the reflections of $m_{1,03}$ and $m_{1,12}$ respectively on the zero axis. They did not relate the crossed moments to the skewness factors. Since they did not have 3-D measurements, they approximated the crossed third order moment $m_{2,21}$ in Eq. (4.5).

We evaluated Eqs. (4.5), (4.8) and (4.9) using our data. The results are plotted in Fig. 4.8. The three curves coincide except in the inner flow region. Some of the differences between them might be due to the use of Eqs. (4.7) which are only valid over the whole depth if the bed is smooth. In the presence of roughness elements, the turbulence intensity profiles deviate considerably from Eqs. (4.7) in the wall region (Nezu and Nakagawa, 1993).

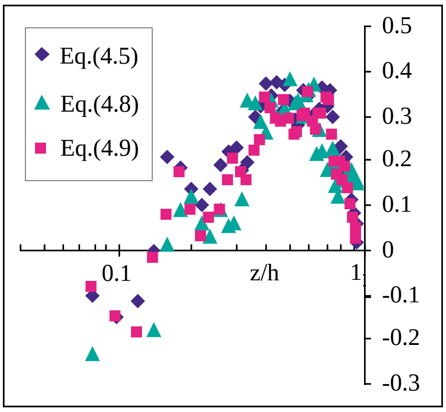

Fig. 4.8 Validation of simplified relation of Fk (data of experiment C)

4.8 Bottom shear velocity in turbulent boundary layers

The statistical analysis (section 4.6.2, Fig. 4.6) has shown that the factors relating the third order moments are independent of Reynolds number, Froude number and bed roughness over a depth range corresponding to roughly $0.25 \leq z/h \leq 0.75$. Therefore, when properly normalized, the vertical flux of turbulent kinetic energy should be constant over that range of depths. We normalized it by the cube of the bed friction velocity, which takes into account the bed roughness effect through the energy slope and boundary layer depth. Fig. 4.9 Normalized flux of turbulent kinetic energy (for experiments A, B, C and D) presents the normalized flux for all our experiments. In all cases we found a nearly constant flux for $0.25 \leq z/h \leq 0.75$ with values varying between 0.28 to 0.35. In a recent study using point measurements, López and Garcia (1999) found a value of 0.33 over a smaller range of depths but a wider range of bottom roughness. They concluded that a constant value of 0.3 may be universal, which is in good agreement with the present results.

The observed similarity provides another method for determining the mean bed friction velocity, since Eq. (4.8) requires knowledge of only one instantaneous velocity component (in comparison with Eqs. (4.5) or (4.9) in which the crossed third order moments are estimated from 3-D or 2-D velocities measurements, respectively). Taking C_1=0.75 and C_2=0.35, we found $S \cong -0.35$ from our data. Using the value of F_k from Fig. 4.9 Normalized flux of turbulent kinetic energy (for experiments A, B, C and D) in Eq. (4.8), the mean bottom friction velocity can then be determined. Due to the one-third power relationship, this method of calculation is not very sensitive to even large errors in the determination of the energy flux.

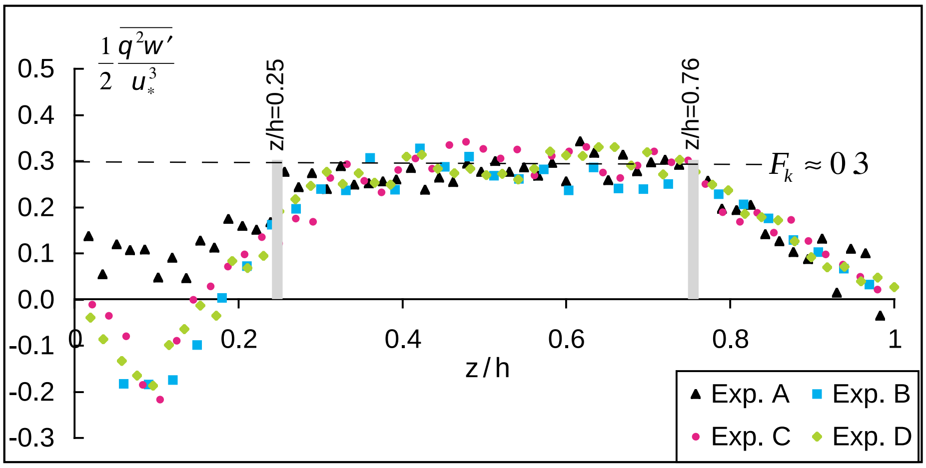

Fig. 4.9 Normalized flux of turbulent kinetic energy (for experiments A, B, C and D)

Difficulties and advantages of different methods for the determination of the mean bottom friction velocity are discussed in Lopez and Garcia (1999). In field studies they suffer either from the lack of knowledge of the precise location of the bed reference level, or the restricted range of validity of the underlying assumptions. In the present study we found the similarity concept to be valid over a wide depth range for bottom roughnesses which are typical of oceanic boundary layers. The precision of the determination of the measurement position within that range, and thus the bed reference level, is therefore not critical. Furthermore, this range is well above the bed where the gradient of the mean velocity is weak. Measurement techniques with larger measurement volumes may therefore be applied in this case.

Based on our study of noise sources in 3-D ADVP turbulence measurements, discussed in Hurther and Lemmin (1999), we found noise characteristics which indicate that even for third order moment estimations from 3-D ADVP data, the signal to noise ratio remains high as long as errors related to acquisition time and bandwidth can be neglected.

4.9 Summary and conclusions

Velocity and shear stress fields obtained by high resolution 3-D Doppler velocity profiling in free surface boundary layer flows over smooth and rough beds show coherent structures extending over a large portion of the boundary layer depth that are approximately independent of bottom roughness. Structural features such as ejections, sweeps, upwellings, downdrafts, vorticity patterns and spiral eddies can be identified when compared to tracer measurements found in Grass et al. (1993). Recent studies (Kumar et al. 1998) have shown that these coherent structures can be linked to surface boils. Coherent structures therefore play an important role in the dynamics of air-water transfer processes.

Good agreement is found between these qualitative observations and a statistical analyses of our measurements, which clearly exhibit the well-known quadrant distribution in the longitudinal plane. The effect of bottom roughness in changing the balance between ejections and sweep is important only below 0.2h. The quadrant decomposition of the transverse covariance term, which has not been estimated before, is found to be almost uniform over the four quadrants. This confirms our initial qualitative observations from figures. It also indicates that the organization of the flow in ejection and sweep events is essentially limited to the vertical plane defined by the mean flow direction.

The approximation of the conditional probability densities of the covariance terms $\varepsilon_1 = u'w' / \overline{u'w'}$ and $\varepsilon_2 = v'w' / \overline{v'w'}$ by a third order Gram-Charlier expansion appears to be sufficient for thresholds $H_i < 10$. Above that value, the third order cumulant discard model deviates from the observations. This suggests that the processes of shear stress generation and turbulent energy production in the boundary layer are highly intermittent.

Based on our measurements of the statistical properties of the covariance terms for different flow conditions, we have validated the wall similarity concept. We found a constant value of 0.3 for the normalized vertical flux of turbulent kinetic energy over a range of depths exceeding the equilibrium flow region, independent of the flow conditions investigated here. This agrees with the value found by López and Garcia (1999) for a different range of bottom roughness.

A different approximation for the turbulent kinetic energy flux, valid in the observed equilibrium flow depth range, is developed in Eq. (4.8). It depends on the longitudinal fluctuating velocity component only, which considerably simplifies the theoretical expression of the turbulent kinetic energy flux.

The existence of wall similarity in highly turbulent boundary layers offers a new method of determining the mean bed friction velocity. This method is better adapted to field measurements than previous methods because the measurements can be taken at a single level far from the bed over an extended depth range where the gradient of the mean flow profile is weak. In particular, this avoids the difficulty of needing to know the precise bed reference level, a difficulty that has introduced large errors in classical calculations based on profile measurements. Here we have shown that this concept is valid at the center of shallow, uniform open-channel flows at high Reynolds number where the boundary layer is two-dimensional in the mean. Under oceanic conditions, effects such as rotation and stratification may cause modifications. Recently we have studied the structure and the dynamics of secondary currents in uniform flow over rough beds by taking closely spaced 3-D ADVP profiles across a channel cross-section. It was demonstrated that in the mean the wall similarity concepts still holds despite the presence of secondary currents. In order to determine the range of validity of the method presented here, field investigations are needed.

This study has demonstrated the potential of a high-resolution 3-D acoustic Doppler velocity profiler in turbulent boundary layer flow. It is ideally suited for such studies because it can profile the total depth in one sweep. This is particularly important in boundary layer field studies where flow conditions often change rapidly and point by point measurements will fail to provide the details desired to understand the high frequency dynamics of the boundary layer. As we have shown recently, this approach can be extended to measure sediment flux (Shen and Lemmin, 1999), which will make it possible to carry out studies similar to the one presented here in sediment-laden flows (Hurther and Lemmin, 2000). New insight into sediment transport dynamics can be expected from measurements with this instrument.

4.10 References

Antonia, R. A. and Atkinson, J. D. (1973): High-order moments of Reynolds shear stress fluctuations in a turbulent boundary layer. J. Fluid Mech. 58(3): 581-593.

Graf, W. H. and Altinakar, M. (1998): Fluvial Hydraulics, Wiley & Sons Ltd. 681 pp.

Grass, A. J. (1971): Structural features of turbulent flow over smooth and rough boundaries. J. Fluid Mech. 50(2): 233-255.

Grass, A. J., Stuart, R. J. and Mansour-Tehrani, M. (1993): Common vortical structure of turbulent flows over smooth and rough boundaries. AIAA Journal 31(5): 837-847.

Hurther, D. and Lemmin, U. (1998): A constant beamwidth transducer for 3-D acoustic Doppler profile measurements in open-channel flows. Meas. Sci. Technol. 9(10): 1706-1714.

Hurther, D. and Lemmin, U. (1999): A correction method for turbulence measurements with a 3-D Acoustic Doppler Velocity Profiler. J. Atmos. Oceanic Technol (in press).

Hurther, D. and Lemmin, U. (2000): Particle transport capacity of coherent structures in suspensions flows. Submitted to Experiments in Fluids

Kline, S.J., Reynolds, W. C., Schraub, F.A. and Rundstadler, P.W. (1967): The structure of turbulent boundary layers. J. Fluid Mech. 30: 741-773

Kumar, S., Gupta, R. and Banerjee, S. (1998): An experimental investigation of the characteristics of the free surface turbulence in channel flow. Phys. Fluids 10(2): 437-456.

Lhermitte, R. and Serafin, R. (1984): Pulse-to-pulse coherent Doppler sonar signal processing techniques. J. Atmos. Oceanic Technol. 1: 293-308.

Lhermitte, R. and Lemmin, U. (1994): Open-channel flow and turbulence measurement by high-resolution Doppler sonar. J. Atmos. Oceanic Technol. 11: 1295-1308.

Lemmin, U., Hurther, D. and Shen, C. (1999): A high resolution constant beam width pulse-to-pulse coherent 3-D acoustic Doppler profiling current meter for use in laboratory and environmental studies. Proc. IEEE sixth conf. on current measurements, San Diego, CA, IEEE Oceanic Engineering Society, 216-220.

López, F. and Garcia, M. H. (1999): Wall similarity in turbulent open-channel flow. Journal of Engineering Mechanics 125(7): 789-796.

Lu, S. S. and Willmarth, W. W. (1973): Measurements of the structure of the Reynolds stress in a turbulent boundary layer. J. Fluid Mech. 60: 481-511.

Nagano,Y. and Tagawa, M. (1995): Coherent motions and heat transfer in a wall turbulent shear flow. J. Fluid Mech. 305: 127-157

Nakagawa, H. and Nezu, I. (1977): Prediction of the contribution to the Reynolds stress from bursting events in open-channel flows. J. Fluid Mech. 80(1): 99-128.

Nezu, I. and Nakagawa, H. (1993): Turbulence in open-channel flows. AIHR Monograph series, Balkema. 281 pp

Pinkel, R. (1979): Observations of non-linear motion in the open sea using a range-gated Doppler sonar. J. Phys. Oceanogr. 9: 675-680.

Raupach, M. R. (1981): Conditional statistics of Reynolds stress in rough wall and smooth wall turbulent boundary layers. J. Fluid Mech. 108: 363-382.

Robinson, S. K., Kline, S. J. and Spalart, P.R. (1988): Quasi-coherent structures in the turbulent boundary layer: Part II. Verification and new information from a numerically simulated flat-plate layer. Near-wall turbulence, Zoran Zaric memorial conference, Dubrovnik, Croatia, 218-247.

Rolland, T. and Lemmin, U. (1997): A two-component acoustic velocity profiler for use in turbulent open-channel flow. J. Hydr. Res. 33(4): 545-561.

Shen, C. and Lemmin, U. (1997): Ultrasonic scattering in highly turbulent clear water flow. Ultrasonics 35: 57-64.

Shen, C. and Lemmin, U. (1999): Application of an acoustic particle flux profiler in particle-laden, open-channel flow. J. Hydr. Res. **37**(3): 407-419.

CHAPTER 5

PARTICLE TRANSPORT CAPACITY OF COHERENT STRUCTURES IN SUSPENSION FLOW

Submitted to Exper. in Fluids. (in review)

5.1 Abstract

The particle entrainment ability of coherent flow structures is investigated by comparing higher order statistical properties of shear stress and of turbulent mass fluxes in suspension, open-channel flow under capacity charge conditions. The quadrant repartitions of these quantities as a function of the corresponding threshold levels are estimated. A higher order cumulant discarded probability density distribution is used to calculate the theoretical quadrant dynamics. Good agreement between the third order model and the experimental results is found for all investigated quantities in the wall and intermediate flow regions. In the free surface domain, the increase of intermittency of the momentum and mass transport processes leads to small discrepancies between the model and the experimental results. The quadrant distributions of the relative horizontal and vertical mass fluxes are dominated by the same two quadrants as the shear stress. Ascendent mass flux events are found to correlate with ejections over the entire water depth.

A dynamical equilibrium between the shear stress production term and the turbulent energy dissipation term is found in the intermediate flow region where the value of the normalized vertical flux of turbulent kinetic energy in suspension flow corresponds well with the one observed in clear water flows. This points towards a universality of a wall similarity in highly turbulent boundary layers.

The suspended particle transport capacity of coherent structures is directly quantified from the estimation of the conditionally sampled terms of the particle diffusion equation. Coherent structures of a burst cycle are found to be important contributors in the mass transport mechanism under highly turbulent flow conditions in open-channel flows.

5.2 Introduction

In recent years, the dynamics of coherent structures in open-channel flow have been studied in great detail in order to understand their generation mechanism and their role in different turbulence related processes such as mixing, transport or gas transfer at the air-water interface. A large number of the investigations have been concerned with the quantification of shear stress dynamics in boundary layers over smooth and rough beds. They have revealed the presence of dominant turbulence generating events identified as ejections and sweeps. These events which have been well documented are chacaterized as highly intermittent with large amplitudes and short time scales. However, no consensus has been found yet concerning the scaling laws of these structures. Models are based on inner region, outer region or mixed flow quantities and most rely on some empirical assumptions.

Several studies have tried to determine the link between these coherent flow structures and particle transport in different turbulent flows. Particles are found to respond to different forces in suspension transport and in bed-load transport. Bed-load transport may arise from pressure fluctuations at the bed while shear stress fluctuations drive the particle movement in suspension flows. Soulsby et al. (1994) observed in a tidal current that the vertical sand flux is dominated by the dynamics of the large scale turbulent structures and that the damping of the turbulent kinetic energy is due to the presence of the suspension. Garcia et al. (1995) showed in their open-channel flow study over smooth and transitionally rough beds that ejections are responsible for particle entrainment into suspension even if the particles are completely immersed in the viscous sublayer. They concluded that the dynamics of ejections are not affected by the roughness elements confirming a previous result given by Grass (1971). While the last two papers have examined the importance of ejections in lifting up particles into suspension, the studies of Heathershaw and Thorne (1985), Hogg et al. (1995), Séchet and LeGuennec (1999), investigated the role of sweeps in the event-driven bedload transport of open-channel flows and tidal flows.

The results of these studies confirm the importance of instantaneous shear stresses and their effects near the bed when particle suspension transport in highly turbulent boundary layers is considered. Assessing particle transport only from mean shear stresses obviously lacks the insight into the underlying physical processes.

The aim of the present study is to provide quantitative information on the role of coherent structures in the particle transport mechanism. For this purpose, an extention of the statistical approach used by Nakagawa and Nezu (1977) (hereinafter abbreviated as NN77) for the investigation of the shear stress statistics to mass fluxes is proposed. In a previous clear water, open-channel flow study, we have applied this statistical model to determine the theoretical values of the quadrant dynamics for covariance terms $u'w'/\overline{u'w'}$ and $v'w'/\overline{v'w'}$ using instantaneous 3-D velocity profile measurements (Hurther and Lemmin 1999). The model results were in good agreement with experimental results obtained with the quadrant threshold technique developed by Lu and Willmarth (1973). From the theoretical expressions of the probability density functions, the relevant cumulants for the quadrant repartition were obtained.

Here, this conditional statistical model will be applied to the shear stresses, and to the horizontal and vertical mass fluxes in order to calculate their relative quadrant repartition in the corresponding planes. By Comparing the statistical properties of shear stresses and mass fluxes for specific quadrants, the particle entrainment by ejections, sweeps, inward and outward interactions can be evaluated. Using these statistical parameters we will investigate the validity of the wall similarity concept in highly turbulent suspension flow and compare the present results with those in clear water flows discussed in Hurther and Lemmin (1999).

Conditional sampling will then be applied to the terms of the advection-diffusion equation in order to quantify the transport capacity of coherent structures. Thus, combined with flow visualization, the contribution to the transport in the particle concentration profile will be estimated as a function of the threshold level. This is usually considered as the parameter delimiting coherent structures in the flow field.

5.3 Experimental details

The data which will be analyzed here were obtained by Cellino (1998) in a laboratory study on suspension flow. The experiments were carried out in a recirculating tilting open-channel, 16.8m long, and 0.6m wide. The channel bed was rough with a mean roughness of 4.8mm. Special care was taken to ensure steady and uniform flow conditions.

The acoustic particle flux profiler (APFP; Shen and Lemmin 1997) was employed to measure quasi-instantaneous particle flux profiles with a sampling frequency of 25 Hz and a record length of 180s. This is a versatile tool for simultaneously measuring the profiles of the instantaneous velocity and the concentration over the entire water depth of a suspension flow. The APFP instrument was located 13m from the entrance at the centerline of the channel where turbulence is well developed.

Fig. 3.12 is an example of an APFP measurement sequence used in the present work. It shows the instantaneous iso-contourlines of the conditionally sampled shear stress patterns (see section 3.4.4. for the conditional sampling technique) over the whole water depth and the corresponding instantaneous vertical particle flux (drawn in grayscales). The instantaneous horizontal particle fluxes which are not shown will be treated in the same way in order to quantify the shear stress entrainment capacity and contribution in the particle suspension transport mechanism.

The hydraulic parameters given in Table 5.1 Hydraulic parameters for experiment characterize a highly turbulent subcritical flow of depth h=12cm with a bed friction velocity of 3.9cm/s. Quartz-like particles of d_{50}=135 μm and specific density of 2.65 were gradually added to the flow until a layer of particles, remaining stable during the experiments, appeared on the bed of the channel completely covering the bottom roughness. No more particles were added from this moment onward because the capacity charge equilibrium condition was reached. In that way the maximum suspension transport capacity of the flow is achieved. Any further supply of particles will only increase the thickness of the deposition layer on the bed. The reference concentration C_a was measured by a suction device under isokinetical conditions at the water depth z/h=0.05 (Cellino 1998).

Q (m^3/s)	h (cm)	U (cm/s)	u_* (cm/s)	S ($\times 10^{-3}$)	Re_h ($\times 10^3$)	Fr_h	k_s^+	d_{50} (mm)	ρ_S (kg/m^3)	w_0 (mm/s)	C_a (kg/m^3)
0.057	12	0.792	3.9	1	271.2	0.7	6.8	0.135	2650	12	39.33

Table 5.1 Hydraulic parameters for experiment

5.4 Theoretical aspects

In this section we briefly present the theoretical expressions of the probability density functions used to calculate the quadrant contributions of the three investigated quantities.

We define the following variables: u', w', c' are the zero mean fluctuating longitudinal, and vertical velocity and concentration components, respectively. $\hat{u}$, $\hat{w}$, $\hat{c}$ are equal to $u'/\sqrt{\overline{u'^2}}$, $w'/\sqrt{\overline{w'^2}}$, $c'/\sqrt{\overline{c'^2}}$. We shall quantify the contributions of the relative shear stress for the covariance term $\varepsilon_1 = u'w'/\overline{u'w'}$ and the contribution of the relative mass fluxes for $\varepsilon_2 = c'u'/\overline{c'u'}$ and $\varepsilon_3 = c'w'/\overline{c'w'}$. Fig. 5.1 shows the orientation of the quadrants in the respective planes. Three joint probability density functions $p_1(\hat{u},\hat{w})$, $p_2(\hat{c},\hat{u})$ and $p_3(\hat{c},\hat{w})$ given as the inverse Fourier transforms of the characteristic functions $\phi_1(\hat{u},\hat{w})$, $\phi_2(\hat{c},\hat{u})$ and $\phi_3(\hat{c},\hat{w})$ respectively, can be expressed as functions of the moment and cumulant generating functions in which $m_{1,jk} = \overline{\hat{u}^j\hat{w}^k}$, $m_{2,jk} = \overline{\hat{c}^j\hat{u}^k}$ and $m_{3,jk} = \overline{\hat{c}^j\hat{w}^k}$ denote the moments of $(j+k)^{th}$ order and $k_{1,jk}$, $k_{2,jk}$ and $k_{3,jk}$ correspond to the cumulants of $(j+k)^{th}$ order. By limitting these cumulant expansion series to an order of three, NN77 determined the conditionally sampled probability densities of covariance events ε_1 over the four quadrants from a high order cumulant discard Gram-Charlier probability density function. The mathematical manipulation is described in detail in NN77. The following general equations are given:

$$
\begin{array}{llll}
p_{i,2}(\varepsilon_i) = p_{iN}(\varepsilon_i) + \varphi_i^-(\varepsilon_i) & p_{i,4}(\varepsilon_i) = p_{iN}(\varepsilon_i) - \varphi_i^-(\varepsilon_i) & (\varepsilon_i > 0) & i = 1,2 \\
p_{i,1}(\varepsilon_i) = p_{iN}(\varepsilon_i) + \varphi_i^+(\varepsilon_i) & p_{i,3}(\varepsilon_i) = p_{iN}(\varepsilon_i) - \varphi_i^+(\varepsilon_i) & (\varepsilon_i < 0) &
\end{array}
\quad (5.1)
$$

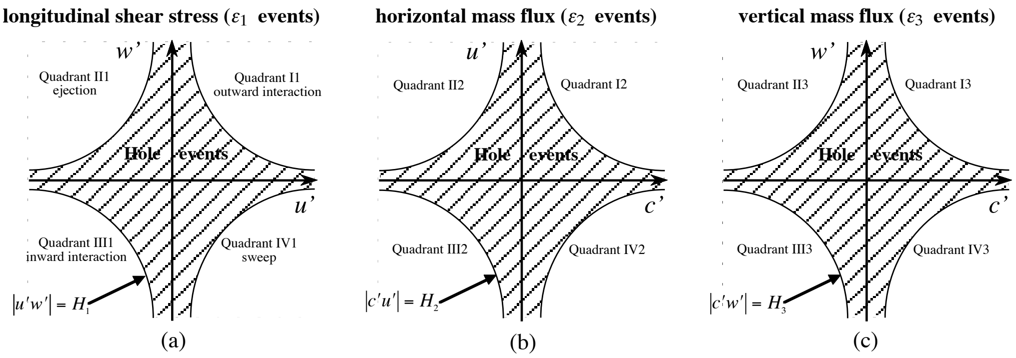

Fig. 5.1 Division of events. (a) shear stress, (b) horizontal mass flux and (c) vertical mass flux

where the index q in $p_{i,q}$ denotes the quadrant index (1 to 4) in the i^{th} plane with planes 1, 2 and 3 corresponding to the (u',w'), (c',u') and (c',w') planes, respectively. The probability density $p_{iN}(\varepsilon_i)$ is directly developed from the corresponding bivariate normal distribution (second order function). The non-conditionally sampled probability function of shear stress is $p_i(\varepsilon_i) = p_{i,1}(\varepsilon_i) + p_{i,2}(\varepsilon_i) + p_{i,3}(\varepsilon_i) + p_{i,4}(\varepsilon_i) = 2p_{iN}$ with $i = 1,2,3$ and:

$$
\begin{cases}
p_{iN}(\varepsilon_i) = \dfrac{r_i}{2\pi}\exp(r_i t_i)\dfrac{K_0(|t_i|)}{(1-r_i^2)^{1/2}} \\
\varphi_i^+(\varepsilon_i) = \dfrac{r_i}{2\pi}\exp(r_i t_i)K_{1/2}(|t_i|)\dfrac{|t_i|^{1/2}}{(1-r_i^2)}\left[(1+r_i)\left(\dfrac{S_i^+}{3}+D_i^+\right)|t_i| - \left(\dfrac{2-r_i}{3}S_i^+ + D_i^+\right)\right] \\
\varphi_i^-(\varepsilon_i) = \dfrac{r_i}{2\pi}\exp(r_i t_i)K_{1/2}(|t_i|)\dfrac{|t_i|^{1/2}}{(1+r_i^2)}\left[(1-r_i)\left(\dfrac{S_i^-}{3}+D_i^-\right)|t_i| - \left(\dfrac{2+r_i}{3}S_i^- + D_i^-\right)\right] \\
t_i = \dfrac{r_i\varepsilon_i}{(1-r_i^2)} \quad ; \quad S_i^\pm = \dfrac{1}{2}(k_{i,03} \pm k_{i,30}) \quad ; \quad D_i^\pm = \dfrac{1}{2}(k_{i,21} \pm k_{i,12})
\end{cases}
\quad (5.2)
$$

where r_i are the corresponding correlation coefficients and $K_0(t)$ is the 0-th order modified Bessel function of the second kind.

The standart deviation, skewness and flatness factors of the ε_i terms can beapproximated by :

$$\sigma_i = \sqrt{\overline{\left(\varepsilon_i - \overline{\varepsilon_i}\right)^2}} = \frac{1}{m_{i,11}}\sqrt{m_{i,22} - m_{i,11}^2}$$

$$S_{\varepsilon_i} = \frac{\overline{\left(\varepsilon_i - \overline{\varepsilon_i}\right)^3}}{\sigma_i^3} = \frac{1}{\left(m_{i,22} - m_{i,11}^2\right)^{3/2}}[m_{i,30}m_{i,03} + 9m_{i,12}m_{i,21} + 3(m_{i,31} + m_{i,13}) - 2m_{i,11}(5m_{i,11}^2 - 3m_{i,22} + 9)] \tag{5.3}$$

$$F_{\varepsilon_i} = \frac{\overline{\left(\varepsilon_i - \overline{\varepsilon_i}\right)^4}}{\sigma_i^2} = \frac{1}{\left(m_{i,22} - m_{i,11}^2\right)^2}\{m_{i,40} + m_{i,04} + 16m_{i,31}m_{i,13} + 24(m_{i,21}m_{i,03} + m_{i,12}m_{i,30}) + 18\left[m_{i,22}^2 + 2(m_{i,21}^2 + m_{i,12}^2)\right] - 30m_{i,11}^2m_{i,22}^2 - 3\left(m_{i,11}^4 + 24m_{i,11}^2 + 6\right) - 12r_i(m_{i,31} + m_{i,13} - 9m_{i,21}m_{i,12} - m_{i,30}m_{i,03})\}$$

From Eq. (5.1) we will calculate the first order moment of each conditional probability density distribution as a function of the threshold level H_i. By increasing the level of H_i, progressively stronger fractional ε_i events will be selected. Their distribution over the different quadrants can be investigated using the following expressions:

$$\begin{aligned} R_{i,q}(H_i) &= \int_{H_i}^{\infty} \varepsilon_i p_{i,q}(\varepsilon_i)d\varepsilon_i \qquad H_i \geq 0 \qquad i = 1,2 \qquad q = 2,4 \\ R_{i,q}(H_i) &= \int_{-\infty}^{H_i} \varepsilon_i p_{i,q}(\varepsilon_i)d\varepsilon_i \qquad H_i \leq 0 \qquad i = 1,2 \qquad q = 1,3 \end{aligned} \tag{5.4}$$

This method is known as the u-w quadrant threshold technique (Lu and Willmarth 1973) applied in this case to the model results. The parameters $R_{i,q}$, evaluated from the probability densities will be compared to those from experimental results in order to obtain information on the quadrant distribution of the relative covariances. The time fractions $T_{i,q}$ of these conditionally sampled events are estimated by :

$$\begin{aligned} T_{i,q}(H_i) &= \int_{H_i}^{\infty} p_{i,q}(\varepsilon_i)d\varepsilon_i \qquad H_i \geq 0 \qquad i = 1,2 \qquad q = 2,4 \\ T_{i,q}(H_i) &= \int_{-\infty}^{H_i} p_{i,q}(\varepsilon_i)d\varepsilon_i \qquad H_i \leq 0 \qquad i = 1,2 \qquad q = 1,3 \end{aligned} \tag{5.5}$$

Consequently, those terms of the events having relative shear ε_i lower than the defined thresholds are called the hole event terms (Fig. 5.1). $R_{i,5}$ and $T_{i,5}$ and are given by :

$$R_{i,5}(H_i) = 1 - \sum_{q=1}^{4} R_{i,q}(H_i) \qquad T_{i,5}(H_i) = 1 - \sum_{q=1}^{4} T_{i,q}(H_i) \tag{5.6}$$

5.5 Statistical properties of shear stress and mass fluxes

5.5.1 Probability density functions, skewness and flatness factors

The lines in Fig. 5.2 represent the probability density functions $p_i(\varepsilon_i)$, evaluated for the relative shear stress, as well as the horizontal and vertical mass fluxes. As mentioned in the previous section, all variables ε_i were treated independently. This point will be further discussed later on. The symbols in Fig. 5.2 show the probability density functions of the same variables estimated from the corresponding experimental histograms. For each of them, 64 cells are taken over a range of H_i values varying from –8 to 8. The results are shown at four flow depths corresponding to the inner, intermediate and free surface flow regions.

Good agreement between the model results and the experimental results can be seen for the shear stress and the mass fluxes at all depths. The range of variation of the variables is of the same order of magnitude for all investigated relative quantities. Furthermore, only small discrepancies exist between the shape of the different probability density functions indicating indentical statistical properties for the shear stress and the mass fluxes.

This is confirmed when profiles of skewness approximated by Eq. (5.3) are compared to experimental ones (Fig. 5.3a). Again, the experimental results are fairly well described by the model results. In this case the model results are not dependent on the choice of the analytical probability density function (i.e. a Gram-Charlier distribution), but rather depend on the relations between cumulants and moments (Antonia and Atkinson 1973).

All three quantities are positively skewed with almost the same constant value of 4 (compared to a value of 0 in the case of a Gaussian distribution) over the whole water depth. Large positive values of these random variables are more frequent than negative ones. As for the shear stress dynamics, there is a dominant contribution of 2 quadrants (known as ejections and sweeps for the shear stress) compared to the remaining two. Since the mean horizontal mass flux is negative (Shen and Lemmin 1999) the two dominant quadrants are quadrants two and four, the same as for the shear stress. The mean vertical mass flux, however, is positive and therefore quadrants one and three are the main contributors. We will calculate the exact relative contribution of all quadrants for each quantity and comment on their physical meaning in the following section.

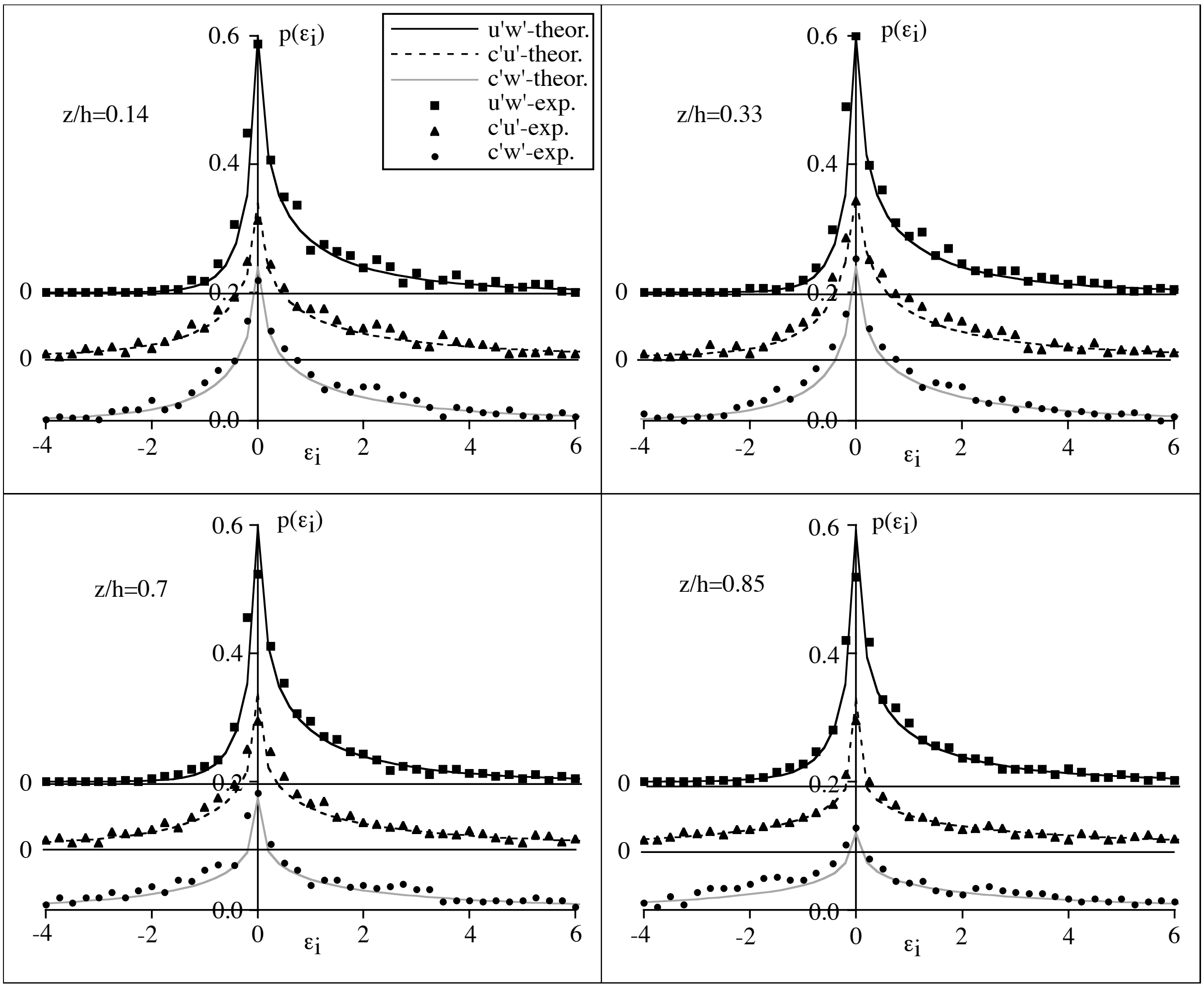

Fig. 5.2 Theoretical and experimental density probabilities of shear stress, horizontal and vertical mass fluxes at different flow depths

The flatness factors are much higher than those for a Gaussian distribution (i.e. equal to 3) (Fig. 5.3b). This emphazises the highly intermittent character of both shear stress and mass fluxes. A certain difference of the flatness factors can be distinguished for z/h<0.6 which may indicate that the mass flux events are not responding exactly to shear stress events. The detailed quadrant repartition of the relative contributions and time fractions as functions of the corresponding threshold levels discussed in the next section will clarify that observation.

It can be concluded that the non-conditionnally sampled probability density functions can well be modelled by the first terms of Eq. (5.1) which only take into account second order variables and therefore the corresponding bivariate normal distribution. This has been shown by Antonia and Atkinson (1973) who compared the second order probability density function of the shear stress to a fourth order cumulant discard Gram-Charlier probability function. The difference between the two was found to be negligible. From the results shown here the same observation is also valid for the horizontal and vertical mass flux events which occur with small values but occasionally an event with larger amplitude occurs. The importance of these high amplitude structures in the particle transport mechanism is quantified in section 5.6.

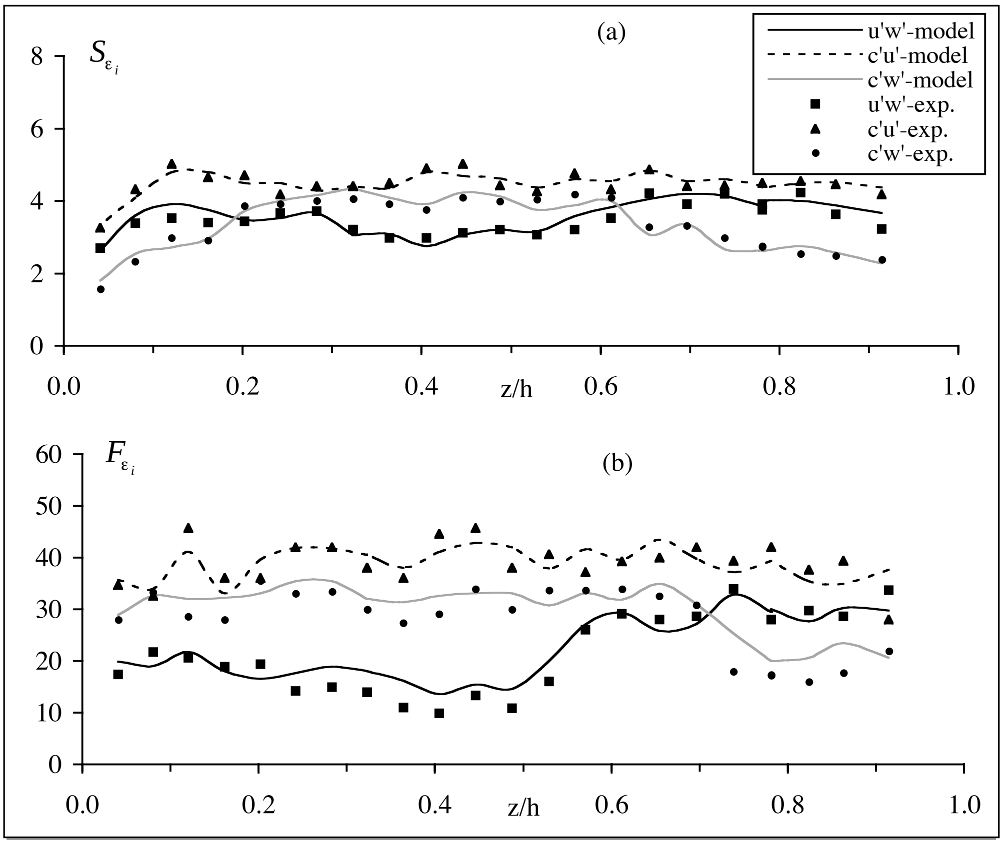

Fig. 5.3 Skewness (a) and flatness (b) profiles for the shear stress, horizontal and vertical mass fluxes

5.5.2 Quadrant contribution of shear stress and mass fluxes

The quadrant repartition introduced in section 3 was separately analyzed for each quantity. Fig. 5.4 to Fig. 5.6 show the relative magnitude of shear stress, horizontal and vertical mass fluxes, respectively, as functions of the corresponding selection criteria H_i. The theoretical (from Eq. (5.2)) and experimental results are given for three different flow depths in the wall, intermediate and free surface flow regions. The time fraction of the hole events at those three depths are also presented in each figure. The agreement between the theoretical and experimental results is good for all quantities at each depth in the inner and the intermediate flow regions. In the free surface flow region, small discrepancies are observed between the model and the experimental results. NN77 had attributed these discrepancies to the limitation of the cumulant expansion series to an order of three. This order appears to be too low in the free surface region where the process becomes more intermittent as indicated above.

The quadrant dynamics of the three investigated quantities is obviously dominated by the contribution of two quadrants. In Fig. 5.4, ejections (quadrant two) and sweeps (quadrant four) dominate, in accordance with results given in the literature. For example, the experimental contributions of quadrants two and four in Fig. 5.4 at z/h=0.85 for $H_1 = 0$ are equal to 1.1 and 0.76, respectively, which are in agreement with the values of 1 and 0.65 at z/h=0.772 given by NN77. The evolution of the curves with respect to H_1 is also found to be identical to results of Raupach (1981). They show high quadrant two and four contributions for large H_1 values while the interaction contributions (quadrants one and three) vanish earlier. This trend can be explained by the larger tails of the conditional probability density functions (not shown here) of the ejection and sweep events. It implies that these occur with higher intermittency than the interaction events.

Another well documented characteristic of the bursting phenomena is the distribution of the hole event time fraction of the relative contribution. For example in Fig. 5.4 at z/h=0.32 and $H_1 = 5$, the hole event time fraction is equal to 85%, meaning that only 15% of the events still contribute to 40% of the shear stress in quadrant two and 35% of the shear in quadrant four revealing the short lifetime and large amplitudes of the turbulence producing events. These observations are in agreement with several experimental studies (Nakagawa and Nezu 1981; Luchik and Tiederman 1987) concerning the bursting process in clear water turbulent boundary layers. Here we have demonstrated that these characteristics of shear stress dynamics in suspension flow under capacity charge condition are very similar to those in clear water flow.

From the observed probability density functions, the important contributors to the horizontal mass fluxes are identified as quadrant two and four events (Fig. 5.5). The quadrant four contribution is more important than the quadrant two contribution for any H_2 which indicates that ejections entrain more particles than sweep events. An association of quadrant four horizontal mass flux structures with ejections can be suggested. When an ejection occurs (i.e. with u'<0), it will lift up particles from a region of higher mean concentration to one of lower mean concentration. The same reasoning holds for the combination of quadrant two horizontal mass fluxes with sweeps. This hypothesis will be confirmed in the next section when the transport capacity of different event types will be estimated.

The quadrant contributions of the vertical mass fluxes are presented in Fig. 5.6. Here, quadrant three and one events are associated with ejections and sweeps, respectively. The experimental curves are fairly well described by the theoretical third order model. The order of magnitude of the relative contributions of vertical and horizontal mass fluxes versus H_2 and H_3 correspond to the relative shear stress contributions. Therefore, the general quadrant dynamics, including the hole event time fraction, of the mass fluxes and shear stress are in good agreement. This indicates the importance of the bursting process in the particle transport dynamics.

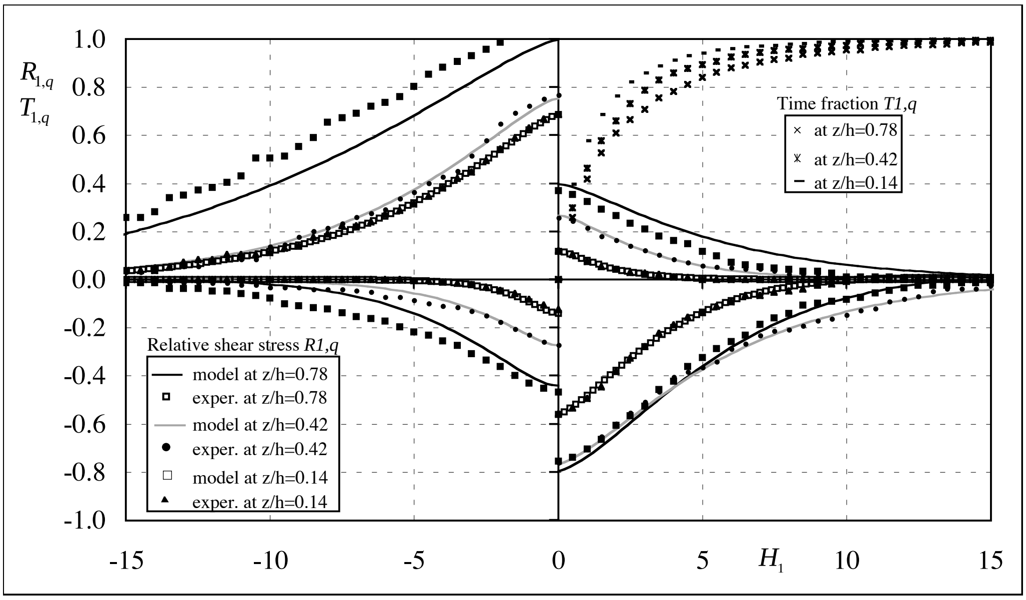

Fig. 5.4 Theoretical and experimental quadrant repartition of relative shear stress ε_1 in function of threshold criteria H_1.

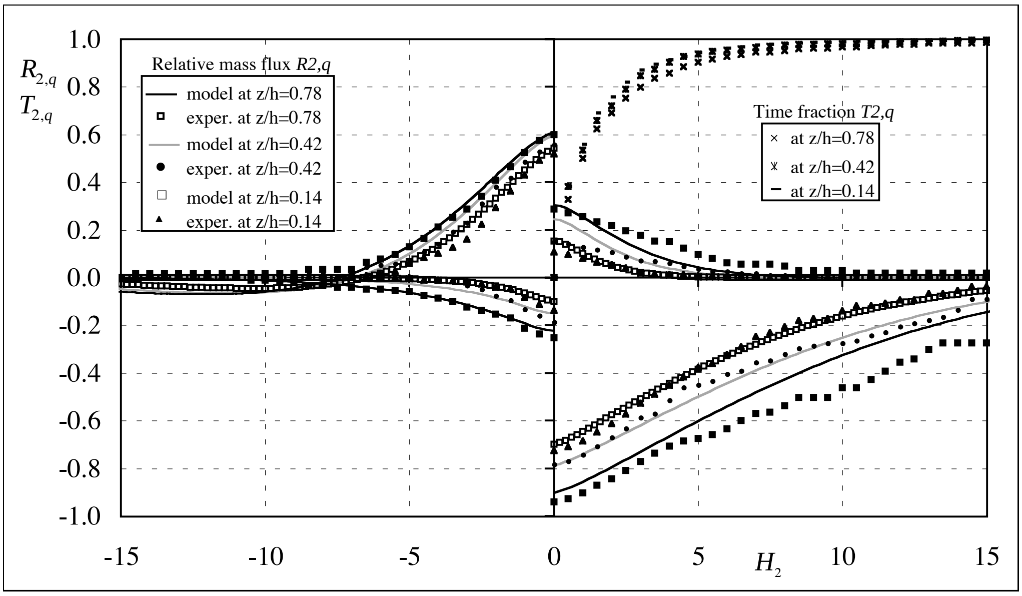

Fig. 5.5 Theoretical and experimental quadrant repartition of relative mass flux ε_2 in function of threshold criteria H_2.

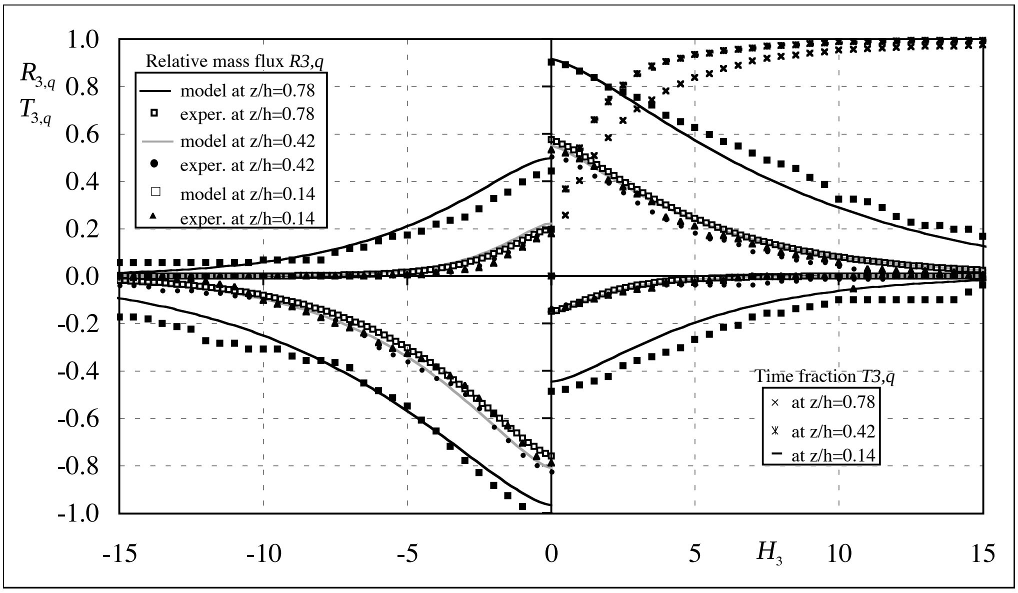

Fig. 5.6 Theoretical and experimental quadrant repartition of relative mass flux ε_3 in function of threshold criteria H_3.

5.5.3 Wall similarity concept in suspension flow

No significant differences between the shear stress dynamics in clear water and suspension flows have appeared in the results presented above. Therefore, the validity of the concept of wall similarity which is directly related to the bursting process will be investigated in suspension flows. The concept states that a dynamical equilibrium exists between the production term of turbulent kinetic energy and its dissipation rate over an extended flow region roughly corresponding to the intermediate flow domain (0.2<z/h<0.65). As a result, the vertical diffusion terms of turbulent kinetic energy and pressure fluctuations must compensate each other or be negligible in that flow region. The concept has recently been validated in clear-water, uniform open-channel flows in the region of 0.25<z/h<0.75 where the normalized (with the bed friction velocity to the power of three) flux remains constant with a value of ≅0.33, independent of the flow conditions (López and Garcia 1999; Hurther and Lemmin 1999).

The relation between the shear stress dynamics and the normalized vertical flux of turbulent kinetic energy for a uniform 2D mean flow, is given as

$$F_k = \frac{1}{2u_*^3}\overline{(u'^2 + v'^2 + w'^2)w'} = \frac{\sqrt{\overline{w'^2}}}{2u_*^3}\left(\overline{u'^2}m_{1,21} + \overline{v'^2}m^t_{1,21} + \overline{w'^2}m_{1,03}\right) \tag{5.7}$$

where $m_{i,jk}$ are the moments defined in section 3, $m^t_{1,21} = \overline{\tilde{v}^2\tilde{w}}$ is the transverse crossed third order moment and u_* is the mean bed friction velocity. The moments $m_{1,03}$, $m_{1,21}$ and $m^t_{1,21}$ measured in the suspension flow are compared with clear water flow results (Fig. 5.7) investigated in Hurther and Lemmin (1999). The hydraulic parameters of the clear water experiments are given in the figure. It can be seen that the different moments are almost identical in the domain $0.25 \le z/h \le 0.75$, independent of the flow conditions. In the present study the transverse crossed third order moment has not been measured since 2D velocity measurements were undertaken. Instead, the approximation $\overline{v'^2w'} \cong \overline{w'^3}$ (also assumed by NN77), verified previously through 3-D velocity profile measurements (Hurther and Lemmin 1999), is made here for the estimation of the normalized vertical flux of turbulent kinetic energy.

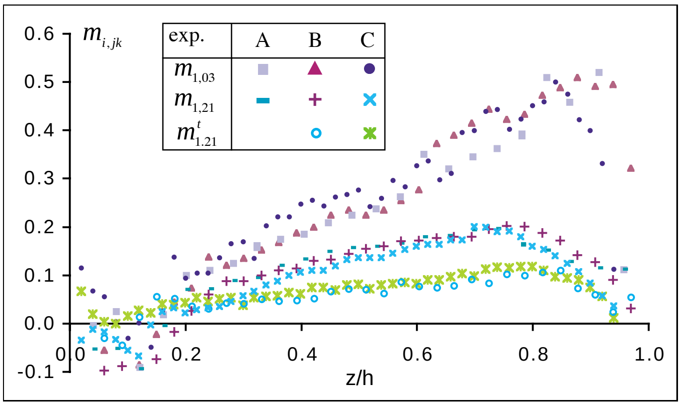

Fig. 5.7 Profiles of third order moments for different flow conditions.
Experiment A: suspension flow, Re=271000, k_s^+=7, Fr=0.73.
Experiment B: clear water flow, Re=27000, k_s^+=34, Fr=0.25.
Experiment C: clear water flow, Re=49600, k_s^+=45, Fr=0.25.
(Re: Reynolds number, k_s^+: relative roughness number, Fr: Froude number)

The energy flux for the different experiments is shown in Fig. 5.8. In the flow region $0.25 \le z/h \le 0.75$, a value of ≅0.3 is found. This confirms experimentally the existence of the wall similarity in the case of the suspension flow and points towards a universality of this concept.

This result provides for a new method to determine the bed friction velocity u_*. Methods used so far to determine u_* suffer from the problem that the reference depth of the profile had to be fixed precisely which often introduces important errors especially in flows over rough beds. Using the wall similarity concept, u_* can be determined by measurements made at a single depth far from the bed (anywhere in $0.25 \le z/h \le 0.75$) where the gradient of the mean longitudinal velocity is low and the effect of spatial averaging over the measure volume is weak. This is a great simplification combined with a gain in accuracy in the determination of u_*, particularly suited for field measurements.

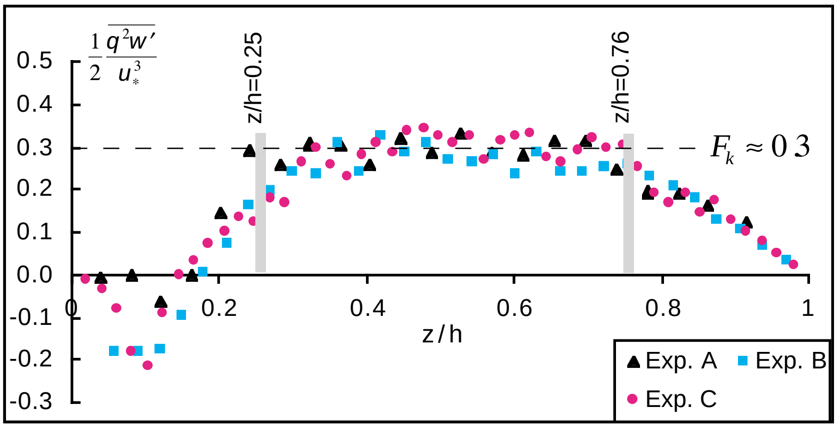

Fig. 5.8 Profile of normalized vertical flux of turbulent kinetic energy for different flow conditions (see Fig. 5.7 for legend)

5.6 Transport capacity of coherent structures

5.6.1 Method

In this section, we will evaluate the contribution of coherent structures to the concentration profile by considering the conditionally sampled diffusion equation for the particles which can be expressed in its general formulation as :

$$\frac{\partial\langle c\rangle_{H_1}}{\partial z} = \frac{1}{w_0}\left[\frac{\partial\langle cu\rangle_{H_1}}{\partial x} + \frac{\partial\langle cv\rangle_{H_1}}{\partial y} + \frac{\partial\langle cw\rangle_{H_1}}{\partial z}\right] \tag{5.8}$$

where $\langle\ \rangle_{H_1}$ denotes an averaging over the structures delimited by the selection criteria H_1. w_0 represents the mean settling velocity of the particles in pure, still, clear water. The Reynolds decomposition of the variables is not applied to avoid the ambiguous definition of the mean velocity when conditional sampling is undertaken.

The mass fluxes are measured directly and do not have to be approximated by a phenomenological law such as the Fick law. However, this approach does not take into account the dynamical interactions between the fluid and the particles. Bagnold (1966) has shown that the existence of a positive skewness of the vertical velocity fluctuation results in a mean vertical net momentum flux which balances the excess immersed weight of the particles. Third order moments in open-channel flow with various bed roughness conditions (Fig. 5.7) confirm the basic assumption of Bagnold's transport theory.

5.6.2 Coherent structure selection method and validation of the equilibrium state

The importance of the different terms in Eq. (5.8) as functions of the selection criteria H_1 will be determined in order to quantify the contribution of coherent structures to the concentration profile. The identification and selection of the flow structures is achieved with the classical instantaneous shear stress threshold technique. However, the value of H_1 defining a coherent structure depends on the selection method used and no consensus can be found in the literature about the exact value. Therefore, the shear stress threshold technique will be combined with flow visualization available from the measurement technique.

Fig. 5.9 presents a typical example of the flow over the whole flow depth taken in the middle of the channel. The fluctuating 2D velocity field $V(u',w')$ and the shear stress iso-contourlines (with H_1 equal to 4) are superimposed. The structure of the flow features delimited by the iso-contourlines is similar to that observed by Grass et al. (1993) in clear water condition. Several flow patterns such as vortex cross-sections associated with an underlying high shear layer (at t=14.2, z/h=0.225), shear layers elongated over the outer flow region (at t=15-15.5, z/h=0.175-0.85) and downwelling (layer at t=13.4, z/h=0.6-0.9) can be observed. The present observations give support to the existence of common flow features in both clear water and suspension turbulent open-channel flows. As seen in Fig. 5.9, the shear stress threshold selection technique accounts for coherent structures appearing instanteanously in the flow field.

The different terms of Eq. (5.8) for different values of H_1 are given in Fig. 5.10. For $H_1 = 0$, no particular flow structures are selected and the longitudinal gradient of the mean horizontal mass flux is obviously negligible compared to the vertical gradient of the mean vertical mass flux. The equilibrium between the mean ascending particle mass flux caused by the entrainment capacity of coherent structures and the deposition flux due to the effect of gravity is evident. The validity of this equilibrium state is not a priory obvious since horizontal non-uniformity could appear in the structures. However, the equilibrium condition can still be assumed for $H_1 \leq 5$. From the flow visualization (Fig. 5.9), coherent structures are clearly distinguished from the background flow field for $H_1 = 4$.

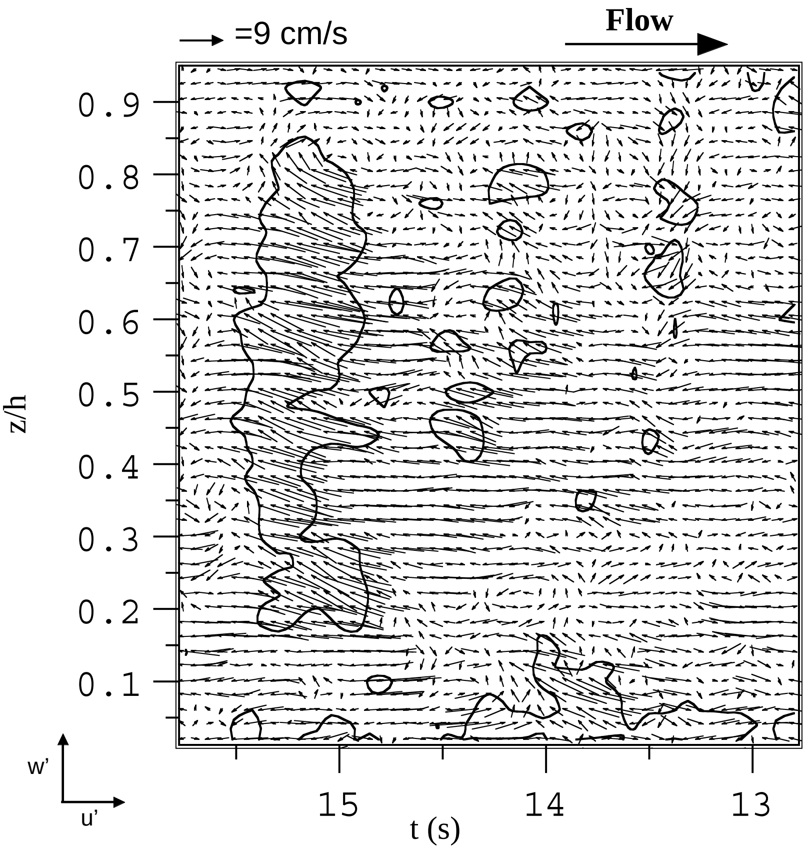

Fig. 5.9 Iso-contours of high shear patterns and fluctuating velocity field V'(u',w') at centerline of the channel.

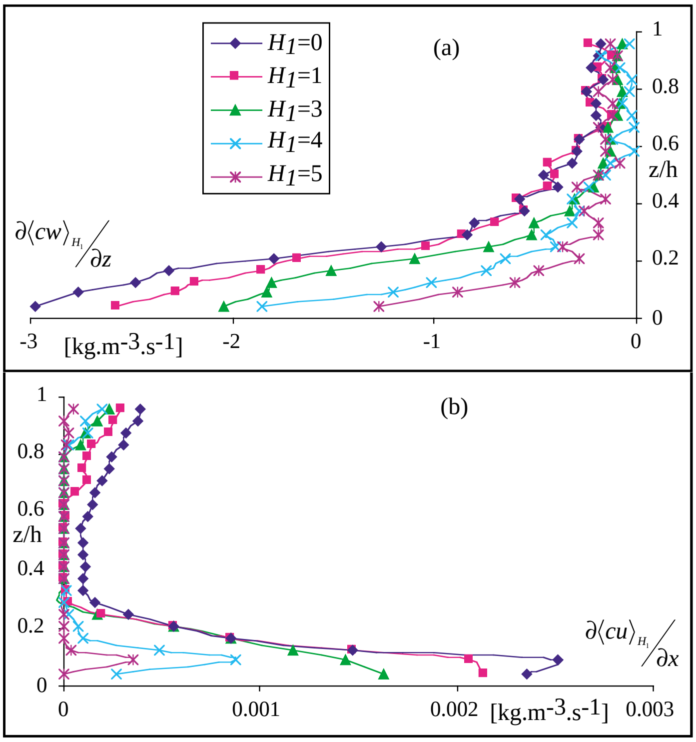

Fig. 5.10 Conditional sampled terms of the sediment diffusion equation. (a) Vertical mass flux gradient. (b) Horizontal mass flux gradient

5.6.3 Results and discussion

Fig. 5.11 shows the concentration profiles relative to the reference concentration (taken at *z/h*=0.05) for several threshold levels H_1 and the quadrant repartition diagrams of the relative vertical mass flux sampled as a function of H_1 and H_3 at z/h=0.16, z/h=0.5, z/h=0.83. From this figure, the dynamics of the relation of the instantaneous vertical mass flux to the instantaneous shear stress events can be investigated in more detail.

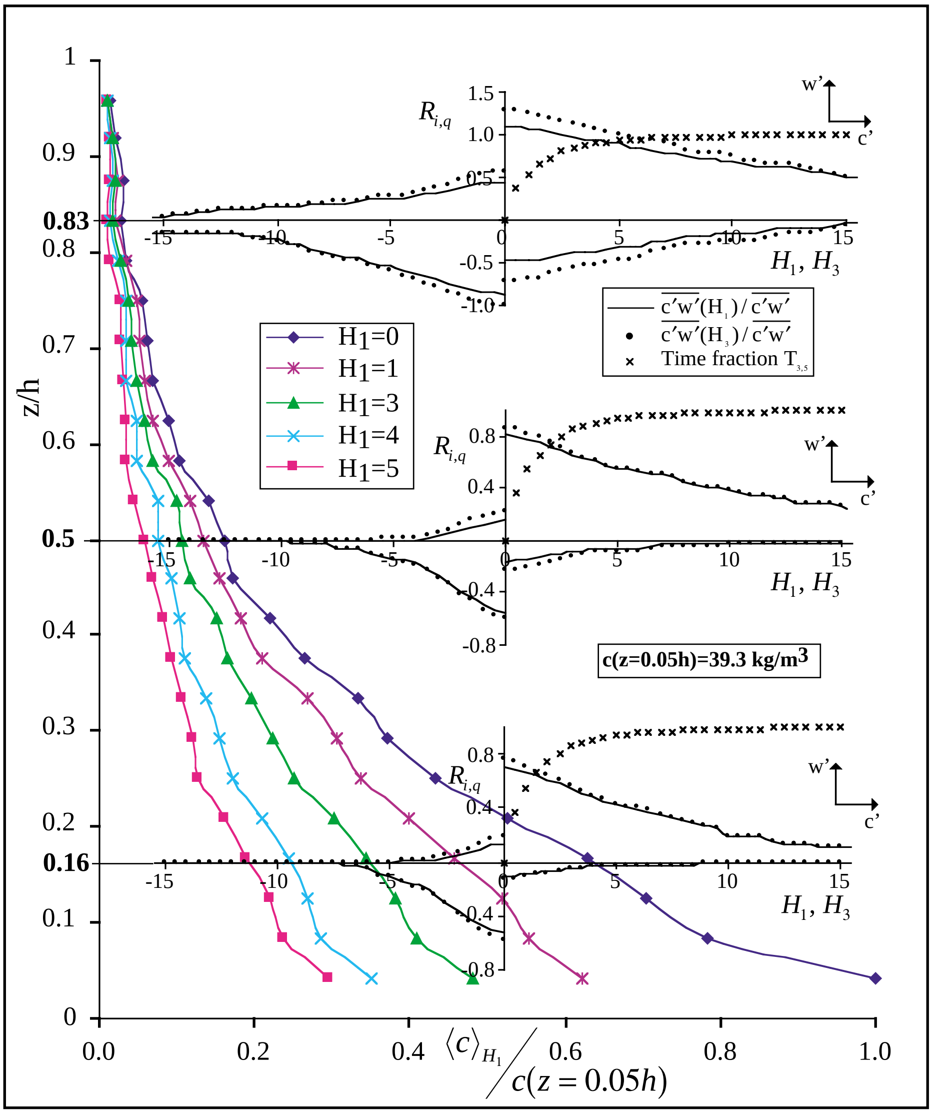

Fig. 5.11 Transport capacity in function of threshold level H_1 and quadrant distribution of c'w' in function of H_3 (dotted lines) and H_1 (solid lines) at three different depths.

Along the whole water column, the transport capacity of the coherent structures decreases proportionally with increasing H. For values of H_1=3 and H_1=5, which represent strong structures, the transport capacity of coherent structures is still equal to 49% and 31% of the total transport, respectively. Combining this information with the hole events time fraction given in the quadrant repartition diagrams, the time fraction of these coherent structures for the same two H_1 values are found to be only 30% and 10%, respectively. From this example, the importance of coherent structures in the particle suspension mechanism becomes quantitatively evident, even if their lifetime is relatively short.

In quadrant one, corresponding to ejection events (Fig. 5.6), good agreement is found between the vertical mass fluxes sampled as functions of H_1 and H_3 for all three depths. This indicates that the upward mass flux is directly correlated with ejection events for all values of H_1 and H_3 throughout the whole water column. Particle resuspension from the bed is strongly controlled by ejections even though their time fraction quickly becomes relatively small with increasing H. In Fig. 3.12, the conditionally sampled Reynolds stress superimposed on the conditional sampled vertical mass fluxes for H_1=4 has been presented in order to indicate the role of the burst process in particle transport. The quantitative results presented in Fig. 5.11 confirm the hypothesis that the contours delimiting important ejections coincide with the regions of high positive vertical mass fluxes.

In quadrant three which corresponds to sweeps, good agreement is again found for the functions of H_1 and H_3. However, at all depths but more so when approaching the channel bed, the fall-off with increasing H is more rapid than for the ejection events. Sweeps are obviously predominantly organized in low H events.

Ejections and sweeps also influence the particle flux in quadrants two and four, evident from the contributions below the solid lines in those quadrants. The contribution of interaction events of quadrants two and four is represented by the difference between the solid line and the dotted line in Fig. 5.11. It is obvious that interactions are hardly correlated with the vertical mass fluxes. Therefore, interaction events can be ignored in the particle transport and do not contribute to transport capacity curves of Fig. 5.11.

It has previously been observed by Soulsby et al. (1994) that saltating particle movement in bedload transport may arise from pressure fluctuations resulting from sweep events in the vicinity of the bed. The initial phase of particle resuspension will then be related to sweeps. Further investigations may help to understand more details of the dynamical interactions between burst processes and the particle flux through the boundary layer.

5.7 Summary and Conclusions

A third order cumulant discard Gram-Charlier probability density function has been applied to the shear stress, as well as the horizontal and vertical turbulent mass fluxes in order to quantify their quadrant dynamics. Good agreement was found between the model results and the experimental estimations in the wall and intermediate flow regions. In the free surface flow region, for all investigated quantities, the limitation of the model to the order of three leads to small discrepancies due to an increase in intermittency. On the other hand, Lagrangian simulations performed by Pan and Banerjee (1995) have demonstrated that the flow structure near the surface changes. Time-persistent free-surface patterns linked to ejections below can generate pairs of counter-rotating eddies at the water surface which might be at the origin of surface boils. This change in structure will also contribute to the observed deviation.

The shear stress quadrant dynamics correspond to results found in the literature with a clear dominance of quadrant two (ejections) and quadrant four (sweeps) events. Thus, the presence of particles in the flow, even at capacity charge, does not influence the flow dynamics on the scales of coherent structures. Instead, a quadrant repartition similar to the shear stress distribution is observed for the mass fluxes and the effect of the hole size parameter H on the mass fluxes is comparable to that of the shear stress. This shows that the mass fluxes are also strongly organized in coherent structures. The quadrant repartition obtained for the mass fluxes can be interpretated through the suspended particle entrainment capacity of ejections and sweeps.

Based on the conditionally sampled particle diffusion equation, the suspended particle transport capacity of coherent structures has been quantified. The proportion of the relative particle concentration profile (relative to the near bed reference concentration taken at $z/h=0.05$) and the time fraction were estimated as functions of the shear stress threshold level (delimiting the coherent structures in the instantaneous flow field). It has been shown quantitatively that coherent structures are important contributors to suspended particle transport. Strong structures which are only present for 30% of the time carry nearly 50% of the vertical particle flux. This indicates that particle transport is highly intermittent and that particle concentration in the water column varies strongly. Based on these results, a bursting scales dependent formulation of the near bed equilibrium concentration given by Cao (1999) has been discussed in Hurther and Lemmin (2000). The validation of the particle entrainment function in suspension flows with different particle diameters and varying Shields parameters has been investigated.

The analogy of the third order moments for suspension flows investigated here to those in clear water flows investigated previously allows to validate the wall similarity concept in highly turbulent suspension flows. This result points towards a universality of this concenpt. It provides for a simplification combined with increased accuracy in the determination of the effective wall shear velocity particularly in flows with strongly varying bottom roughness height where classical mean profile methods fail. Further investigations on the range of validity of this concept in suspension flow with different grain sizes and under field conditions will be carried out.

5.8 References

Antonia RA; Atkinson JD (1973) High-order moments of Reynolds shear stress fluctuations in a turbulent boundary layer. J Fluid Mech. 58: 581-593.

Bagnold RA (1966) An approach to the sediment transport problem from general physics. Prof. Pap. U.S. geol. Surv. 422-I: 37.

Cao Z (1999) Equilibrium near-bed concentration of suspended sediment. J Hydr. Engrg. 125: 1270-1278.

Cellino M (1998) Experimental study of suspension flow in open-channels. PhD thesis n°. Ecole Polytechnique Fédérale de Lausanne.

Garcia M; Niño Y; López F (1995). Coherent flow structures in open-channels, Leeds, U.K., (J Wiley & Sons Ltd.)

Garcia M; Parker G (1991) Entrainment of bed sediment into suspension. J Hydr. Engrg., 117: 414-435.

Grass AJ (1971) Structural features of turbulent flow over smooth and rough boundaries. J of Fluid Mech. 50: 233-255.

Grass AJ; Stuart RJ; Mansour-Tehrani M (1993) Common vortical structure of turbulent flows over smooth and rough boundaries. AIAA-31-837.

Heathershaw AD; Thorne PD (1985) Sea bed noises reveal role of turbulent bursting phenomenon in sediment transport by tidal current. Nature 316: 339-342.

Hogg AJ; Dade WB; Huppert HE; Soulsby RL (1995). Coherent flow structures in open-channels, Leeds, U.K., (J Wiley & Sons Ltd).

Hurther D; Lemmin U (1999) Shear stress statistics and wall similarity analysis in turbulent boundary layers using a high resolution 3-D ADVP. accepted for publication in IEEE J Oceanic Engrg.

Hurther D; Lemmin U (2000) Equilibrium near-bed concentration of suspended sediment. accepted for pub0lication in J Hydr. Engrg.

Kim HT; Kline SJ; Reynolds WC (1971) The production of turbulence near a smooth wall in a turbulent boundary layer. J Fluid Mech. 50: 133-160.

Kline SJ; Reynolds WC; Schraub FA; Runstadler PW (1967) The structure of turbulent boundary layers. J Fluid Mech. 30: 741-773.

López F; Garcia M (1999) Wall similarity in turbulent open-channel flow. Journal of Engineering Mechanics 125: 789-796.

Lu SS; Willmarth WW (1973) Measurements of the structure of the Reynolds stess in a turbulent boundary layer. J Fluid Mech. 60: 481-511.

Luchik TS; Tiederman WG (1987) Timescale and structure of ejection and bursts in turbulent channel flows. J Fluid Mech. 174: 529-552.

Nakagawa H; Nezu I (1977) Prediction of the contribution to the Reynolds stress from bursting events in open-channel flows. J Fluid Mech. 80: 99-128.

Nakagawa H; Nezu I (1981) Structure of space-time correlations of bursting phenomena in an open-channel flow. J Fluid Mech. 104: 1-43.

Pan Y; Banerjee S (1995) A numerical study of free surface turbulence in channel flow. Phys. Fluids 7: 1649-1664.

Raupach MR (1981) Conditional statistics of Reynolds stress in rough wall and smooth wall turbulent boundary layers. J Fluid Mech. 108: 363-382.

Séchet P; LeGuennec B (1999) Near wall turbulent structures and bedload transport. J of Hydr. Res.
Shen C; Lemmin U (1997) A two-dimensional acoustic sediment flux profiler. Meas. Sci. Technol. 8: 880-884.
Soulsby RL; Atkins R; Salkield AP (1994) Observations of the turbulent structures of a suspension of sand in a tidal current. Continental Shelf research 14: 429-435.
Van Rijn LC (1984) Sediment transport, part II: Suspended load transport. J Hydr. Engrg., 110: 1613-1641.
Zyserman JA; Fredsoe J (1994) Data analysis of bed concentration of suspended sediment. J Hydr. Engrg., 120: 1021-1042.

CHAPTER 6

EQUILIBRIUM NEAR BED CONCENTRATION OF SUSPENDED SEDIMENT

Published in Journal of Hydraulic Engineering (2001), Vol. 127, No. 5

6.1 Discussion of paper by Cao (1999) in JHE, Vol. 125, No. 12

The author proposes an expression for the equilibrium near bed concentration C_a (Eq. (3.18)) based on scales of turbulent bursts. This is a significant improvement over existing empirical formulations (VanRijn, 1984, Zyserman and Fredsoe, 1994). He gives a relation for the bed sediment entrainment function E in which the outer-scale law is used for the determination of the normalized turbulent bursting period. However, as pointed out by the author, a direct validation of the proposed near bed sediment entrainment function was not possible because quantitative data for sediment entrainment under different particle size and hydraulic conditions is lacking. Instead, the author has undertaken a calibration to determine the bursting parameter T_B^+/A_C based on existing data.

Recently we have investigated a method to estimate the dynamics of suspended sediment transport capacity from instantaneous mass flux profile measurements by applying a conditional sampling technique (see Chapter 5). Based on the measured bursting characteristics, we will herein verify and discuss the author's expression of the near bed equilibrium concentration.

The data set used to discuss these points was obtained by Cellino (1998) in open-channel laboratory experiments using the Acoustic Particle Flux Profiler (Shen and Lemmin, 1999a). Detailed information concerning the experimental setup is given in Cellino (1998). Uniform suspension flows under capacity charge conditions were investigated as shown in Table 6.1.

The following particle entrainment flux equation is given by the author:

$$E \cong \frac{A_C}{T_B^+}\frac{C_0 d}{\theta_c}\frac{(\theta-\theta_c)U_\infty}{h} \tag{6.1}$$

In which T_B^+ is the dimensionless bursting period normalized with the velocity U_∞ at the free surface and the flow depth h. The parameter A_C corresponds to the surface fraction per unit of bed area of all bursts (discussed in section 6.2). The variables θ and θ_c represent the

Shields parameter and the critical Shields parameter for the initiation of particle motion, respectively. C_0, d and w_0 are the volumetric sediment concentration at the bed, the size of the particles (taken at 50% of the granulometric curve) and the settling velocity of the considered particles in still water, respectively.

run	Q (m^3/s)	h (cm)	U (cm/s)	u_* (cm/s)	S ($\times 10^{-3}$)	Re_h ($\times 10^3$)	Fr_h	k_S^+	d (mm)	ρ_S (kg/m^3)	v_0 (mm/s)	θ_c ($\times 10^{-2}$)	θ ($\times 10^{-1}$)	C_a (kg/m^3)	T_B^+
Q50	0.058	12	80.1	3.9	1.00	274.3	0.74	8.9	0.23	2650	21	3.5	4.07	21.31	3.4
Q55	0.060	12	83.3	4.4	1.50	285.5	0.77	10.1	0.23	2650	21	3.5	5.19	28.07	3.6
Q57	0.060	12	83.6	4.5	1.75	286.4	0.77	9.9	0.23	2650	21	3.5	5.42	24.77	3.5
Q60	0.061	12	85.0	4.9	2.00	291.1	0.78	10.3	0.23	2650	21	3.5	6.43	23.29	3.6
Q65	0.062	12	86.5	5.1	2.25	296.4	0.80	10.8	0.23	2650	21	3.5	6.97	34.36	3.7
Q70	0.057	12	86.8	5.4	2.50	297.4	0.80	11.0	0.23	2650	21	3.5	7.81	33.83	3.8

Table 6.1 Hydraulic parameters for experiments

As reported in Cao (1999), the bursting period is estimated by conditionally sampling the instantaneous velocity field with a half-value shear stress threshold as defined by Nezu and Nakagawa (1993). We will refer this sampling condition as "NN50" hereinafter.

In Eq. (3.18), the author assumes an equilibrium condition between the entrainment flux E and the deposition flux $D \cong C_a w_0$ as follows:

$$E = D \tag{6.2}$$

It is important to note that the entrainment flux E is conditionally sampled while the deposition flux D is not. As will be seen, this difference between the two terms has a number of important implications.

In writing Eq. (3.18), the author assumes that the particle flux other than the vertical is negligible. Coherent structures are observed to be three dimensional patterns (Grass, Stuart et al., 1993) in which non-uniformities can exist. This implies that turbulent mass fluxes other than the vertical one may have to be considered in the diffusion equation.

In order to quantify the suspended sediment transport capacity of the flow structures related to the bursting phenomenon, we have investigated in section 5.6.2, the order of magnitude of the different terms of the conditionally sampled sediment advection-diffusion equation. The results in Fig. 5.10 have shown that even for H_1 = 3 which corresponds to the NN50 shear stress level, the longitudinal gradient of the horizontal mass flux is obviously negligible compared to the vertical gradient of the vertical mass flux. Our measurements show that a relation between the conditionally sampled vertical turbulent mass flux and the deposition flux can be considered as a good approximation, thus, confirming the author's assumption.

However, in Eq. (3.18), the author implies that the total deposition flux at the equilibrium near bed level is caused by the conditionally sampled entrainment due to bursts which are stronger than NN50. A priori, that hypothesis is not obvious since there is no physical reason that weaker bursts should not contribute to the deposit. To justify this assumption it would be necessary to prove that the contribution of the weaker bursts is insignificant.

Therefore, the entrainment capacity of those flow structures which are delimited by the threshold level NN50 has to be quantified with respect to the total entrainment flux. In order to investigate this point we start by calculating the dependence of different relative parameters on the u'w'-threshold parameter H_1 at depth z/h=0.08 which is close to the bottom but above the author's equilibrium depth. The paramenters R1, R2 and T5 represent the mean shear stress contribution, the mean vertical mass flux, and the time fraction of the unselected flow part, respectively.

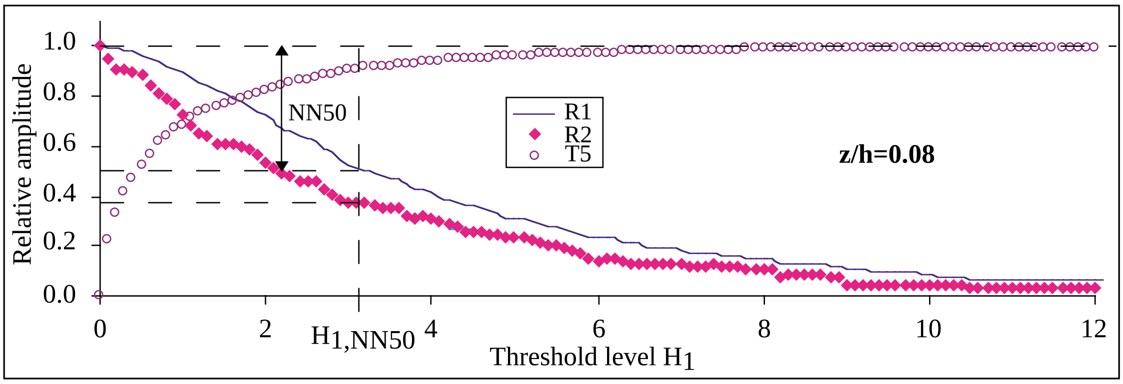

Fig. 6.1 Relative shear stress R1, relative mass flux R2 and time fraction T5 of unselected events versus threshold value H_1 for run Q50 in Table 6.1

Concerning the mean contributions of shear stress and vertical mass flux, the relative vertical mass flux R2 is found to be lower than the relative shear stress contribution R1 (Fig. 6.1). As discussed in Hurther and Lemmin (2000), this difference originates from the decorrelation between downward mass fluxes and sweeps moving towards the wall while ejection events are always highly correlated with ascendant mass flux events over the entire flow depth. This observation indicates that in the vicinity of the bottom of the flow the sediment entrainment may arise from pressure fluctuations at the bed, whereas the sediment resuspension process is highly correlated with shear stress ejection events. As indicated in Fig. 6.1, the NN50 sampling condition corresponds to a value of 3 for H_1. This is in good agreement with the results given by Nezu and Nakagawa (1993). The data in Fig. 6.1 demonstrate further that the entrainment at the near bed level, related to those bursts that obey the NN50 condition as the burst delimiting value, corresponds to only 40% of total the vertical mass flux. It is interesting to note that this 40% entrainment occurs during only 10% of the total time. This point has been discussed in the previous section 5.6.3.

In order to determine the percentage of the total entrainment at the author's near bed equilibrium depth, we calculated the concentration profiles relative to the near bed equilibrium concentration for H_1 equal to 3 corresponding to the NN50 sampling condition and for all runs (Fig. 6.2). The value of C_a was obtained from independent suction samples in iso-kinetical conditions (Shen and Lemmin, 1999b). Extrapolating our results to the near bed equilibrium depth, only about 60% of the total entrainment is found at that level independent of the hydraulic conditions.

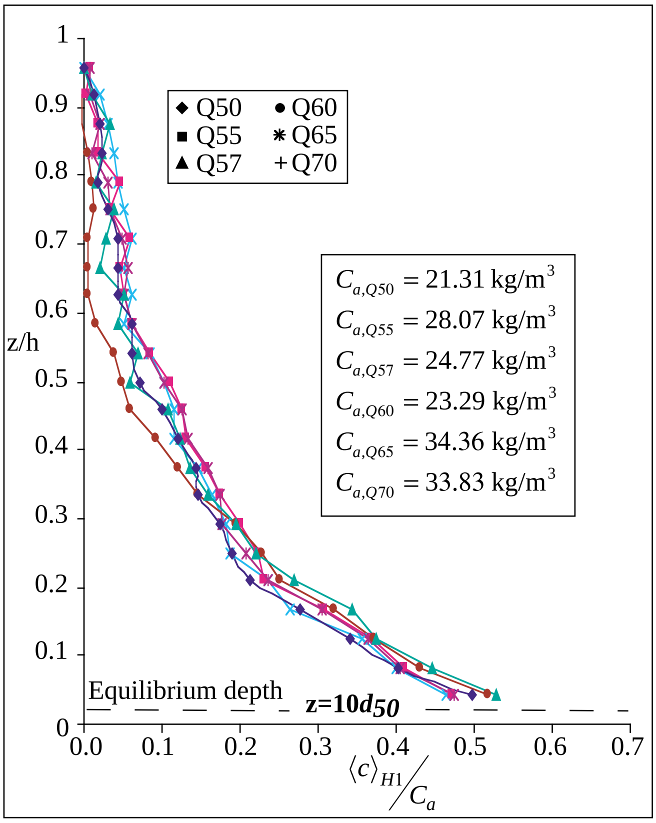

Fig. 6.2 Transport capacity of bursts sampled at the shear stress half-value threshold level H_1 = 3.

This is in contradiction to the author's assumption in Eq. (6.1). Under the NN50 sampling condition which the author imposes, our measurements discussed above show that the corresponding deposition flux accounts for only 60% of the total deposition flux. As a consequence, based on the results of our measurements, the outer-scale formulation of the volumetric near bed concentration for low sediment concentration should be corrected with a factor of 0.6 as follows :

$$0.6\,C_a \cong \frac{A_C}{T_B^+}\frac{C_0 d}{w_0\theta_c}\frac{(\theta-\theta_c)U_\infty}{h} \tag{6.3}$$

6.2 Validation of the proposed correction

As mentioned above, in the discussed paper, the parameter T_B^+/A_C has been determined through calibration. The correction factor of 0.6 which we propose here in Eq. (6.3) and which shows that the condition E = D (in Eq. (6.2)) is not correct, can only be determined through direct measurements of mass flux and the burst characteristics. Due to the wrong equilibrium assumption, the error is carried over into the author's verification procedure. Consequently, he did not observe a significant discrepancy between the results from his model based on burst scales and the results from other models.

However, in order to determine whether the proposed correction factor provides a better representation of the physical processes, we can analyse the results of the author's calibration. This results yield:

$$T_B^+/A_C = 160\left[\sqrt{\left(\rho/\rho_p - 1\right)g\,d}\cdot d/\nu\right]^{-0.8} \tag{6.4}$$

This relation is based on the calculations using Eq. (3.18) which we can compare directly to the parameter T_B^+/A_C determined with the herein proposed Eq. (6.3) for our data set.

First, the normalized bursting period T_B^+ is directly estimated from our measurements. For the results summarized in Table 6.1, a scaling on the outer flow variables was used, applying the author's method based on the NN50 condition. For all runs, we find a bursting period which varies between 3.4 and 3.8. This range is in good agreement with the experimental results previously given by Laufer and Narayanan (1971) and Jackson (1976).

As mentioned by Cao (1997), Eq. (6.3) can be written as follows :

$$0.6\,C_a \cong \frac{A_i}{T_B^+}\frac{C_0 d}{w_0}\frac{U_\infty}{h} \tag{6.5}$$

with

$$A_1 = A_C \frac{\theta - \theta_c}{\theta_c} \tag{6.6}$$

or

$$A_2 = A_C \frac{\theta}{\theta_c} \tag{6.7}$$

where A_i is the mean surface portion of the bursts per unit bed area of those bursts containing enough energy to lift up sediments from the bed (expressed by the NN50 condition). A_c is the mean surface portion of all bursts per unit bed area. Cao (1997) proposed Eqs. (6.6) and (6.7) to relate the two last mentioned parameters and found that Eq. (6.6) gives better results (i.e. the combination of Eq. (6.5) with Eq. (6.6) results in Eq. (6.3)). If Eq. (6.7) is used instead of Eq. (6.6), the following expression is found for the mean near bed equilibrium concentration :

$$0.6 C_a \cong \frac{A_C}{T_B^+} \frac{C_0 d}{w_0 h} \frac{\theta U_\infty}{\theta_c} \tag{6.8}$$

Finally, the validation of the proposed corrections can be achieved by comparing the surface portion of the bursts per unit bed area, A_C, estimated with Eqs. (3.18), (6.3) and (6.8). Considering the well accepted measurements of Kline et al. (1967) and Kim et al. (1971), Cao (1997) calculated a value of A_C roughly equal to 0.02.

Fig. 6.3 shows the values of A_C calculated with T_B^+ measured and using Eqs. (3.18), (6.3) and (6.8) for all investigated runs. It can be seen that results using Eq. (6.8) which includes the correction are in better agreement with the expected value of 0.02 while those obtained using Eq. (3.18) give a value of A_C which is significantly higher.

6.3 Summary and Conclusion

The present discussion is concerned with the formulation of the near bed equilibrium concentration C_a developed by the author considering turbulent bursts scales in the near wall flow region. We have used direct instantaneous mass flux measurements in several suspension flow conditions to verify different aspects of the author's analysis. We have shown that the conditionally sampled vertical entrainment flux is by far the dominant contributor to entrainment fluxes, in agreement with the author's assumption.

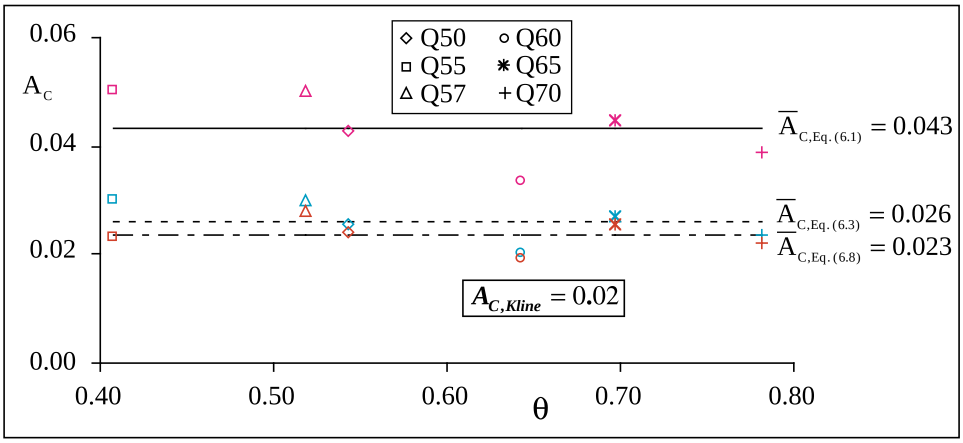

Fig. 6.3 Comparison of surface portion per unit bed area of the nursts versus Shields parameter at the equilibrium depth, calculated with Cao's (Eq. (3.18)) model and the herein corrected models (Eq. (6.3) and Eq. ((6.8))).

However, when the sampling condition NN50 is applied to the vertical entrainment fluxes, the resulting entrainment flux is not in equilibrium with the total deposition flux as assumed in the author's Eq. (6.2).

Therefore we propose to introduce a correction factor in his near bed equilibrium concentration formulation. Finally, the validity of our proposed correction has been checked by calculating the burst surface portion values for one particle size but for different hydraulic conditions. The corrected predictions are found to be in very good agreement with results given in the literature.

An important point in this context is whether the correction we propose is universal. Here we have only worked with one particle size and with different hydraulic conditions. The author's analysis indicates that the parameter T_B^+/A_C is a strong function of particle size, particularly for small size particles. However, his Fig. 3.11a shows low scatter between the experimental results and the fitted curve based on Eq. (6.4). From this observation one may expect that the value of the correction factor will not vary too much. Obviously our data do not fit onto the curve in Fig. 3.11a. Therefore, Eq. (6.4) will also have to be modified in order to take into account the correction once more data for other particle sizes are available.

6.4 References

Cellino, M. (1998). Experimental study of suspension flow in open-channels. Civil engineering. Lausanne, Ecole Polytechnique Fédérale de Lausanne.

Grass, A. J., Stuart, R. J., and Mansour-Tehrani, M. (1993). "Common vortical structure of turbulent flows over smooth and rough boundaries." AIAA Journal 31(5), 837-847.

Hurther, D. and Lemmin, U. (2000). "Particle transport capacity of coherent structures in suspension flows." submitted to Exp. in Fluids.

Kim, H. T., Kline, S. J. and Reynolds, W. C. (1971). “The production of turbulence near a smooth wall in a turbulent boundary layer.” J. Fluid Mech. 50, 133-160.

Kline, S. J., Reynolds, W. C., Schraub, F.A., and Runstadler, P. W. (1967). “The structure of turbulent boundary layers.” J. Fluid Mech. 30(4), 741-773.

Laufer, J. and Narayanan, M. A. B. (1971). “Mean period of the turbulent production mechanism in a boundary layer.” Phys. of Fluids 14, 82-183.

PART II

INSTRUMENTATION

CHAPTER 7

A 3-D ACOUSTIC DOPPLER VELOCITY PROFILER FOR TURBULENT FLOW

7.1 Introduction

The main objective of this chapter is to explain an ultrasomic technique and the development of the instrument capable of measuring the instantaneous three-dimensional velocity profile at flow scales involved in the turbulent mechanism. Particular attention has been given to its non-intrusive operation mode to minimize flow perturbations. In the first instance, this system has been adapted for the investigation of free-surface flows in laboratory as well as field conditions (river and lake studies).

7.2 The principle of pulse-to-pulse coherent ultrasonic Doppler velocity profiler

7.2.1 The Doppler effect

An incident ultrasonic wave of direction $\vec{e}_i$ (unity vector) and wave-number vector $\vec{K}_i = (2\pi/\lambda_0)\,\vec{e}_i$ is generated by a fixed emitter E (see Fig. 7.1) where λ_0 is the wavelength of the incident wave in the considered propagation medium. The wave is scattered by a moving acoustical target of velocity $\vec{V}$. The Doppler effect at the fixed receiver R is the time variation of the phase shift (i.e. frequency or pulsation) between the incident and the scattered wave. This frequency is proportional to the target's velocity as follows:

$$\omega_D = \frac{d}{dt}\vec{K}_B \cdot \vec{r}(t) = \vec{K}_B \cdot \vec{V}(t) \tag{7.1}$$

where ω_D is the Doppler pulsation, $\vec{r} = x\,\vec{i} + y\,\vec{j}$ denotes the target's position vector and $\vec{K}_B = \vec{K}_S - \vec{K}_i$ is the Bragg wavenumber. $\vec{K}_S = 2\pi\vec{e}_S/(\lambda_0 + \lambda')$ is the wavenumber vector of the scattered signal with $\vec{e}_S$ being the unity vector in the receiver's direction. $\lambda' = (\vec{V}\cdot\vec{e}_S)/\lambda_0$ is the wavelength deviation due to the target's velocity. Assuming that $(\vec{V}\cdot\vec{e}_S) << c$, yields:

$$\omega_D = \frac{2\pi f_0}{c}(\vec{e}_S - \vec{e}_i)\cdot\vec{V} \tag{7.2}$$

where f_0 denotes the frequency of the incident wave. With $\vec{e}_i(0,-1)$ and $\vec{e}_S(\sin\alpha, \cos\alpha)$ as shown in Fig. 7.1, we obtain $\vec{e}_S - \vec{e}_i(\sin\alpha, 1+\cos\alpha)$ and subsequently:

$$\vec{K}_S - \vec{K}_i = \frac{2\pi f_0}{c}(\vec{e}_S - \vec{e}_i) = \frac{2\pi f_0}{c}\, 2\cos\left(\frac{\alpha}{2}\right)\vec{e}_B \tag{7.3}$$

Finally, the Doppler frequency at R results in:

$$f_D = \frac{2f_0}{c}\cos\left(\frac{\alpha}{2}\right)\vec{V}\cdot\vec{e}_B \tag{7.4}$$

where $\vec{e}_B(\sin\alpha/2, \cos\alpha/2)$ is the unity vector of the Bragg vector and α the angle between the incident and the scattered wave in the receiver's direction.

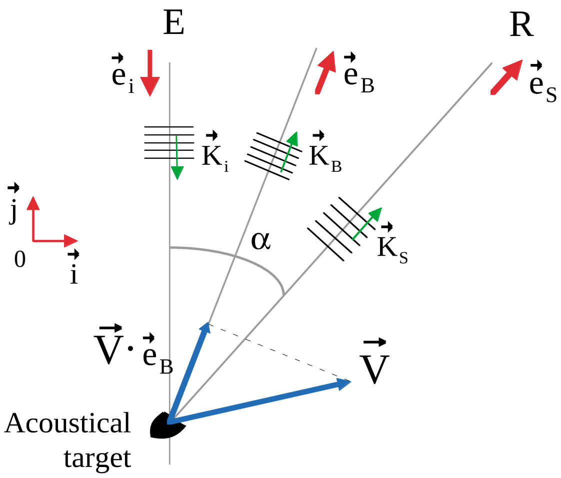

Fig. 7.1 Doppler effect in static configuration

The following definitions are valid:

- Backscattering is concerned with angle values of $\alpha \in [-\pi/2, \pi/2]$. Forward scattering means that $\alpha \in [-\pi, -\pi/2[\cup]\pi/2, \pi[$.
- A bistatic configuration is defined by $\alpha \neq 0$ with fixed emitter and receiver position in the Cartesian coordinate system.
- When $\alpha = 0$, the configuration is called monostatic. The ultrasonic source is thus used as receiver as well.

7.2.2 The velocity profiling characteristics

Monostatic configuration

The profiling ability of a pulse-to-pulse coherent Acoustic Doppler Velocity Profiler (ADVP) is explained for monostatic configuration in Fig. 7.2. Although this configuration has not been applied in the our measurements, it allows a better general understanding of the measuring principle than the multistatic configuration. An ultrasonic burst of carrier frequency f_0 =1 MHz and timelength t_e =4 μs is generated and repeated by the emitter TRA at a Pulse Repetition Frequency PRF. The direction of the incident pulses is defined by the direction of the incident unit vector $\vec{e}_i$. It corresponds to the propagation direction of the compression wave produced by the piezo-electrical sensor TRA working as a piston. The transducer is placed in a transducer chamber filled with water to ensure that the first measuring point in the flow field is located in the far field of the sensor. Thus, effects of the acoustical intensity fluctuation on the backscattered signal present in the near field of piezo-electrical transducer, can be neglected. Furthermore, this solution permits non-intrusive flow measurements. Between two consecutive pulses, the transducer TRA receives the backscattered acoustic signal diffused by the acoustical targets present in the insonified water column. The type of acoustical targets will be discussed in section 7.2.3. As shown in the time series of Fig. 7.2, the pulsed operation mode allows to determine the distance d_j between the emitter and the targets which is equal to $ct_j/2$. t_j is the total flight-time of the pulse scattered at location j in the profile. The corresponding Doppler frequency $f_{Dj} = (2\pi f_0/c)\vec{V}_j \cdot \vec{e}_B$ is obtained from Eq. (7.4) taking $\alpha = 0$ and $\vec{e}_B = \vec{e}_s$ for a monostatic configuration. An example is given in Fig. 7.2 for two depths z_1 and z_2 in the flow. The Doppler signal at one depth is reconstructed by extracting each Doppler sample from the signal backscattered after a single pulse. The red and blue signals represent the reconstructed Doppler signals at the two-different flow depths. Subsequently, the frequencies of the Doppler signals at each depth are estimated. The frequency estimation algorithm is described in section 7.4.2. It may be noted that the frequency of the Doppler signal at depth z_2 is higher than the one at z_1 with respect to the mean velocity profile in a uniform open-channel flow.

The maximal spatial resolution in the direction of the incident wave is equal to $ct_e/2 \approx 3$ mm for our settings. The size x_{-6dB} of the sample volume in the direction normal to the incident direction is determined by the -6 dB value of the normalized directivity function of the emitter. Fig. 7.2 shows the approximated cylindrical shape of the sample volume and its corresponding value. In our case a phase array emitter is employed which produces an ultrasonic beam with constant width over the entire investigated flow depth. Chapter 8 is devoted to the description of this novel transducer. The constant x_{-6dB} value is equal to 7 mm.

The temporal resolution is dependent on the repetition frequency PRF which, as shown in Fig. 7.2, represents the sampling frequency of the local Doppler signal. As will be shown in section 7.4.2, the instantaneous ultrasonic scattering process occuring in the sample volume is random, implying that time averaging over a certain number of pulses is necessary in order to reach a second order stationarity. The minimum number of pulses is Npp = 32. The corresponding sampling frequency results in PRF / NPP= 31.25 Hz for PRF = 1 KHz. The maximal velocity resolution of the measuring technique is function of the smallest sampling frequency shift equal to 1 Hz in the present case. Converting this frequency into a velocity with Eq. (7.4), leads to a value of ≅1 mm/s. An important limitation of pulsed ADVs is the depth-velocity ambiguity (see snapshot in Fig. 7.2). In all our open-channel flow investigations, the total flow depth has to be covered between two pulses in order to obtain a quasi-instantaneous velocity profile over the entire height of the turbulent boundary layer. In this situation, the maximal sampling frequency PRF is limited by the investigated flow depth, the following velocity-depth ambiguity relation is valid:

$$\left.\begin{aligned} \vec{V}_{max}\cdot\vec{e}_i &= \frac{c\cdot PRF}{4f_0} \\ PRF &= \frac{c}{2d_{max}} \end{aligned}\right\} V_{B\,max} = \vec{V}_{max}\cdot\vec{e}_i = \frac{c^2}{8d_{max}\,f_0} \tag{7.5}$$

For our settings, typical values of the range-velocity ambiguity are equal to 0.3.

Multistatic configuration

The multistatic configuration of the 3-D-ADVP is represented in Fig. 7.3. It is composed of one emitter TRA and four large angle receivers TRB-TRE placed symmetrically around TRA. Large angle receiver means that the opening angle delimiting the high-sensitivity domain of the receiver is large. This allows to receive the backscattered signal from each insonified location j when the high-sensitivity domain is matched to the the total depth of the investigated flow as shown in Fig. 7.3. Similar to the monostatic configuration, TRA sends a pulsed burst of time duration t_e at a repetition frequency PRF towards the channel bed. The direction of the incident wave is vertical. Between two bursts, the four large angle sensors receive the ultrasonic signal backscattered by the acoustical targets found in the water column.

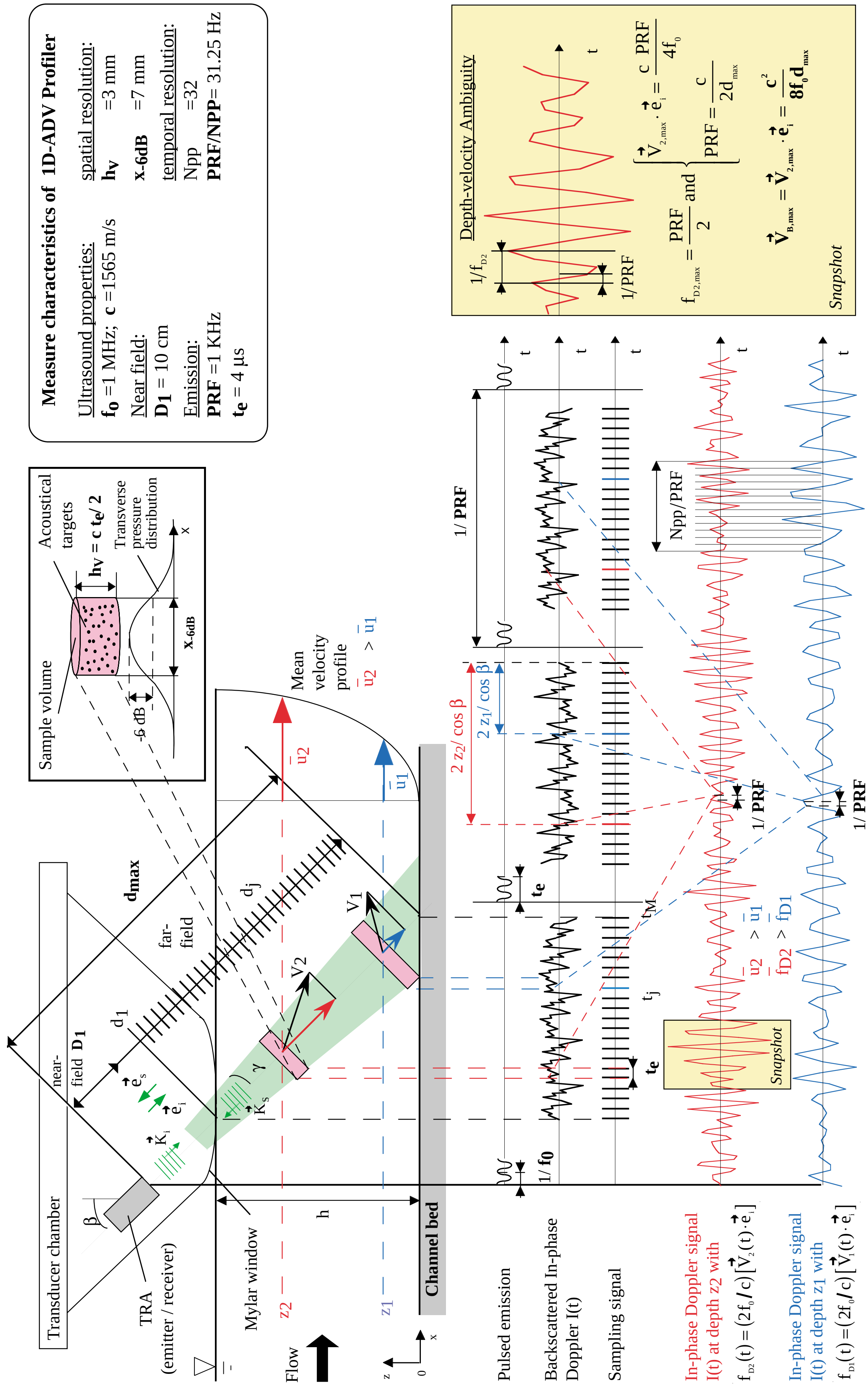

Fig. 7.2 Principle of the monostatic 1D-Acoustic Doppler Velocity Profiler

The system is divided into one tristatic subsystem located in the longitudinal flow section (TRA, TRB, TRC) and a second one (TRA, TRD, TRE) oriented in the transverse flow plane. Each tristatic subsystem contains two bistatic configurations (represented in Fig. 7.1) composed by the emitter TRA and the corresponding receiver. Since the quasi-local instantaneous backscattered signal is received simultaneously in four different directions, the following four Doppler signals and related radial velocity components can be estimated for each sample volume Rj (j=1…M). For each of the two multistatic subsystems, the two local Doppler frequencies ($f_{D1,j}$ and $f_{D2,j}$ for the longitudinal system, $f_{D3,j}$ and $f_{D4,j}$ for the transverse system) are:

$$
\begin{aligned}
f_{D1,j} &= \frac{2f_0}{c}\cos(\alpha_{1,j}/2)\,\vec{V}_j\cdot\vec{e}_{B1,j} \qquad & f_{D3,j} &= \frac{2f_0}{c}\cos(\alpha_{3,j}/2)\,\vec{V}_j\cdot\vec{e}_{B3,j} \\
f_{D2,j} &= \frac{2f_0}{c}\cos(\alpha_{2,j}/2)\,\vec{V}_j\cdot\vec{e}_{B2,j} \qquad & f_{D4,j} &= \frac{2f_0}{c}\cos(\alpha_{4,j}/2)\,\vec{V}_j\cdot\vec{e}_{B4,j}
\end{aligned}
\tag{7.6}
$$

Since the receivers are placed symmetrically around the emitter, we have $\alpha_{1,j} = \alpha_{2,j} = \alpha_{3,j} = \alpha_{4,j} = \alpha_j$.

For each bistatic system, the determination of the distance d_j between the emitter and the sample volume j is obtained by applying a triangulation method. The index i indicating the adressed subsystem is omitted since the geometry is identical for each i. The reference plane is located at the surface of the emitter TRA, the incident wave number vector being normal to the reference plane (see Fig. 7.3). The variables d_j, d_{rj} and D_0 are the distances between TRA / Rj, TRC / Rj and TRA-TRC, respectively. The variables e, α_j and r_j are the angles between the reference plane and the emitters axis, the Doppler angle at location j and the angle between the unity vector $\vec{e}_{S,j}$ and the TRA-TRC line, respectively. We will only consider backscattering configurations (i.e. $\alpha \in [-\pi/2, \pi/2]$) with $D_0 \cos e \geq d_j$. The flight time t_j of a single burst between the emitter and the receiver is equal to:

$$
ct_j = d_{rj} + d_j \tag{7.7}
$$

The following geometrical relations are valid in the triangle TRA-TRC-Rj:

$$\begin{cases} D_0^2 = d_{rj}^2 + d_j^2 - 2d_j d_{rj} \cos\alpha_j \\ \dfrac{d_{rj}}{\sin e} = \dfrac{d_j}{\sin r_j} = \dfrac{D_0}{\sin\alpha_j} \\ e + r_j + \alpha_j = \pi \end{cases} \tag{7.8}$$

Introducing the squared Eq. (7.7) into the first relation of Eq. (7.8) and using the second one, yields:

$$ct_j = \left[D_0^2 + 2d_j\left(d_{rj} + \sqrt{d_{rj}^2 - D_0^2 \sin^2 e}\right)\right]^{1/2} \tag{7.9}$$

$$d_j = \frac{d_{rj}}{\sin e} \sin\left[\pi - \arcsin\left(D_0 \sin e / d_{rj}\right) - e\right] \tag{7.10}$$

Since D_0, e are constants and ct_j is fixed, the distance d_{rj} can be calculated by resolving Eq. (7.9) by iteration. The desired distance d_j is extracted from Eq. (7.7). Rolland (1994) has shown that D_0 has to be chosen in such a way that a minimal Doppler angle α_M = 15° is ensured at the channel bed. This condition is necessary to provide a sufficient SNR (signal-to-noise ratio) for the Doppler signal produced at R_M.

Since the distances d_j do not vary linearly as function of the time t_j, the spatial resolution h_v is not constant as function of d_j. Fig. 7.4 is evaluated from Eq. (7.9) for a typical bistatic configuration with D_0 =12 cm and e = 90°. It can be seen that the spatial resolution decreases with the distance d_j. The relative difference in resolution between the nearest and furthest sample volume of a profile, is equal to 16% for the experiments conducted in the laboratory flumes. For sample volumes far from the emitter, the spatial resolution h_v (see Fig. 7.3) tends asymptotically towards a value of 3 mm.

The temporal and velocity resolutions are identical to those valid for the monostatic configuration described in the previous section.

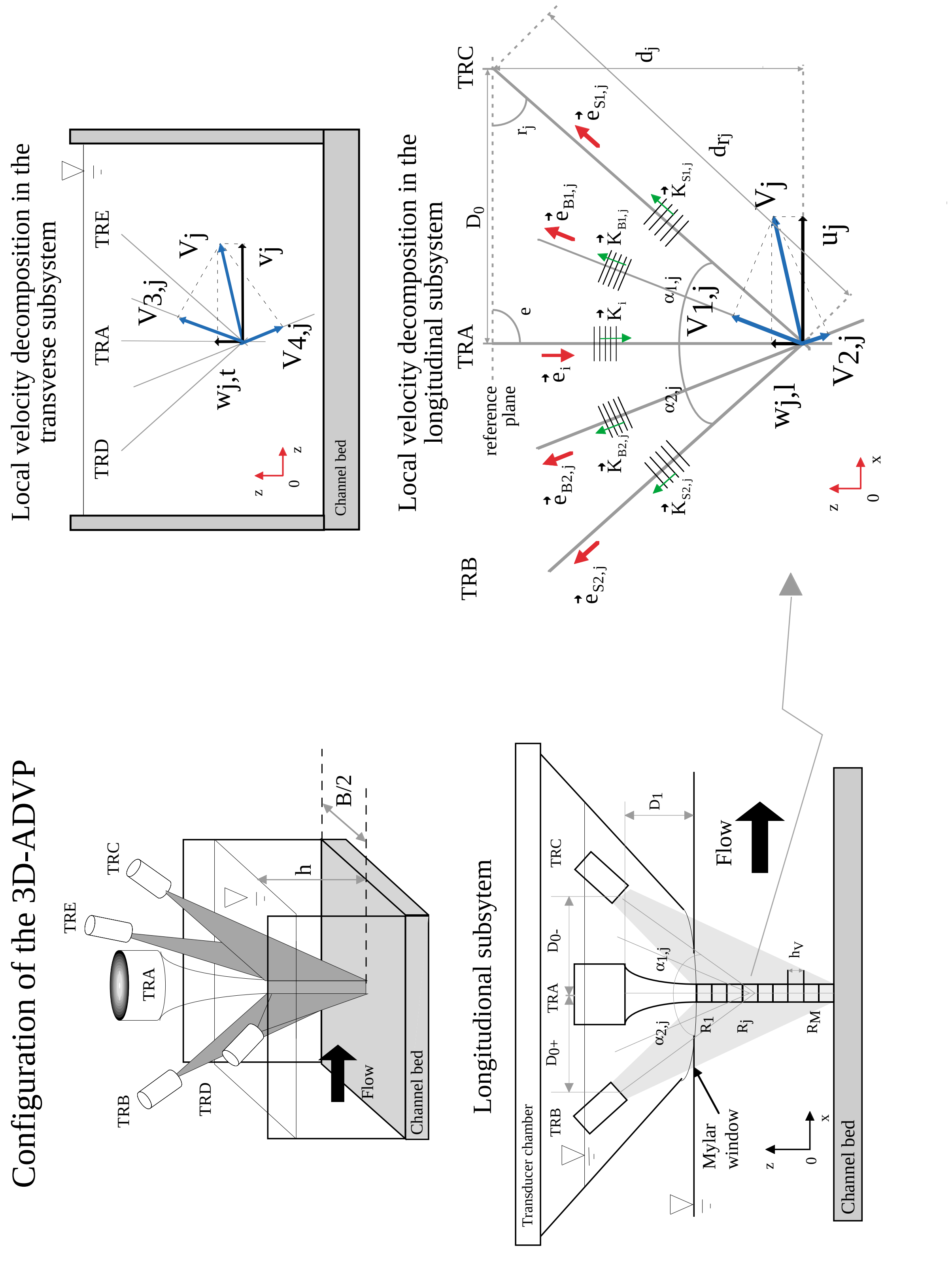

Fig. 7.3 Principle of the 3-D-ADVP

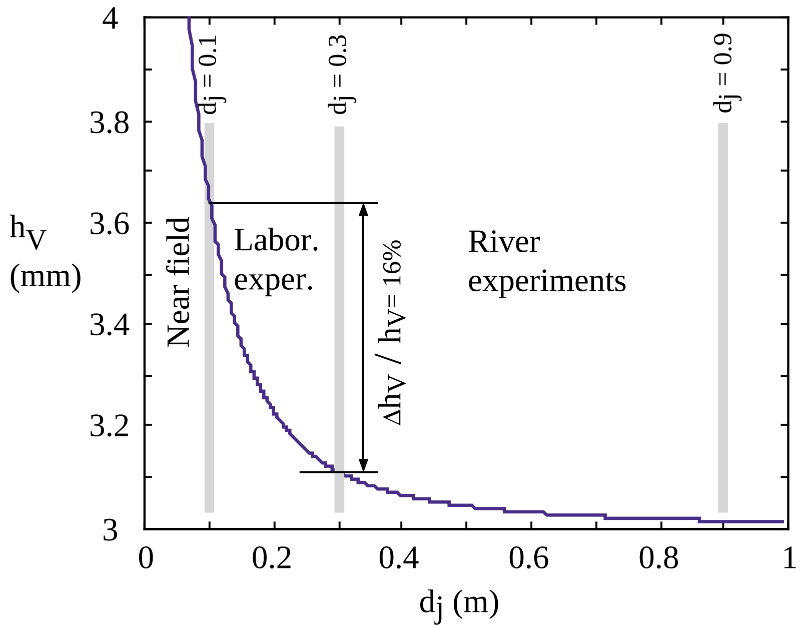

Fig. 7.4 Spatial resolution h_v, for a bistatic configuration with D_0 =12 cm and e = 90°, in function of the distance d_j between the emitter TRA and the sample volume Rj.

The combination of Eq. (7.6) and Eq. (7.7) leads to the following depth-velocity amibiguity relation for a bistatic configuration of the transducers:

$$d_{j\max} V_{Bj\max} = \frac{c}{4\ f_0\ \cos(\alpha_j/2)} \left(c - D_0\ \mathrm{PRF} \frac{\sin e}{\sin \alpha_j} \right) \tag{7.11}$$

In our conditions the value is around 0.4 which is close to the value obtained with a monostatic configuration. This is not surprising since the distances D_0 of the bistatic systems are small.

7.2.3 Ultrasonic scattering in turbulent clear water flows

The measuring principle of the 3-D-ADVP is based on the mecanism of ultrasonic backscattering in turbulent flows. It is essential to identify the scattering source in order to evaluate their tracing ability of the flow and to interpret the Doppler data to the flow turbulence. A detailed analysis of these processes has been realized by Shen (1997). We will briefly summarize the main results of this study.

It is important to mention that all experiments were conducted under clear water conditions, have been conducted without any flow seeding. In this cases, turbulence induced scattering sources from different microstructures can be suggested:

- Turbulent velocity microstructures.
- Temperature microstructures.
- Concentration microstructures of fine particles.
- Concentration microstructures of fine air bubbles contained in normal tap water.

In order to determine whether one or several of these microstructures are responsible for the observed ultrasonic backscattering a theoretical formulation of the scattering cross-section adapted to the suggested microstructures is needed. Quantitative estimations based on the theoretical relation are compared to the values of the scattering cross-section measured directly in the turbulent channel flow. A supplementary experiment is carried out under controlled condition where the contribution to the scattering cross-section from each possible microstructure can be estimated independently. A comparison of the values with those measured in the flow is undertaken.

The scattering cross section $\eta(\varsigma)$ at the angle ς is defined as the mean power P_S scattered per solid angle by an insonified volume R_M on which a plane wave of mean power P_i incidents. The following relation is valid:

$$\eta(\varsigma) = P_S / (4\pi\, R_M P_i) \tag{7.12}$$

where the angle $\varsigma = \pi - \alpha$ and α is the Doppler angle. The sample volume index j is omitted in this section. The Bragg condition imposes that the mean size l_s of the scattering structures is equal to $l_s(\varsigma) = \lambda / [2\sin(\varsigma/2)]$ where λ is the wavelength of the incident wave. In these flow conditions, Goodman (1990) has expressed the total sonar scattering cross-section as the sum of the scattering cross-section of the additive and the velocity microstructures, as follows:

$$\eta(\varsigma) = \eta_n(\varsigma) + \eta_u(\varsigma) = 2\pi\, K'^4 \Omega_n(K) + \left(K'/\bar{c}^2\right) S(K) \cos^2(\varsigma) \cos^2(\varsigma/2) \tag{7.13}$$

where K', K, $\Omega_n(K)$, $\bar{c}$, $S(K)$ are the sonar wavenumber $K' = 2\pi/\lambda$, the Bragg wavenumber $K = 2K' \sin(\varsigma/2)$, the spatial spectrum of refraction index $n = c'/\bar{c}$, with $\bar{c}$ corresponding to the mean ultrasound speed and the energy spectrum of the velocity field, respectively.

Shen and Lemmin (1997) have demonstrated that in highly turbulent, uniform open-channel flows the contribution of velocity microstructures to scattering cross-section for a bistatic sonar, is of the order of magnitude $O(10^{-12})$. This value is negligible compared to the experimental value $O(10^{-4})$ obtained from direct measurements in the laboratory flume. Consequently, since the hydraulic parameters of the flows investigated in this thesis are identical to those in Shen and Lemmin (1997) (i.e. the Reynolds, Froude, relative roughness numbers and the mean bed friction velocity are of same order of magnitude), it can be deduced that velocity structures are not responsible for the ultrasonic scattering in our flow situations.

The term $\eta_n(\varsigma)$ of Eq. (7.13) has been approximated for the case of temperature, particle or fine air bubble concentration microstructures. They are equal to $\eta_{1\max} = 1.5 \times 10^{-10}\,\mathrm{m}^{-1}$, $\eta_{2\max} = 5.2 \times 10^{-14}\,\mathrm{m}^{-1}$ and $\eta_{1\max} = 2.9 \times 10^{-4}\,\mathrm{m}^{-1}$, respectively. Only for the case of air bubble microstructures, is the scattering cross-section value in agreement with the value of $3.1 \times 10^{-4}\,\mathrm{m}^{-1}$ measured during the experiments.

An additional experiment has been performed by Shen and Lemmin (1997) to validate this result. It consisted in measuring the backscattering cross-section of the same sonar configuration in a grid-stirred tank filled with normal tap water and degassed water. The stirring frequency f_g and amplitude of the grid permits to control and to characterize the generated turbulence. Three different turbulence conditions were produced for the case of degassed and tap water: (a) with f_g =0 Hz, (b) with f_g =1 Hz and (c) f_g =4 Hz. Case (c) denotes turbulence conditions similar to those of open-channel flow. It was observed that: in the case of degassed water, very small scattering cross-sections relative to the value observed in open-channel flows have been measured independently of the turbulence situation. This confirms the previous theoretical approximation that turbulence driven temperature microstructures cannot be considered as the acoustical targets in the conducted flume experiments. Furthermore, in case (a) with normal tap water, at low turbulence levels and with water containing fine air bubbles at low concentration and radii less than 50 μm, the measured scattering cross-section is again very low compared to the value found in the flume experiment. Consequently, ultrasonic scattering originating from individual air bubbles can also be excluded. Only in case (c) in turbulence conditions similar to flume, a value of $2.29 \times 10^{-4}\,\mathrm{m}^{-1}$ close to the flume value of $3.1 \times 10^{-4}\,\mathrm{m}^{-1}$ has been measured. From these results, the acoustical targets found in our clear water conditions are turbulence induced air bubble microstructures which have a mean size of 750 μm. Subsequently, these structures appear to be ideal flow tracers since they are able to follow the turbulent fluid motion without any inertial lag.

7.3 Geometrical velocity reconstruction

The multistatic configuration represented in Fig. 7.3 allows the simultaneous measurement of the four radial velocity components $V_{i,j} = \vec{V}_{i,j} \cdot \vec{e}_{Bi,j}$ given in Eq. (7.6). As described in section 7.2.2, the longitudinal and transverse subsystems are treated independently and are placed symmetrically around the emitter TRA, thus $\alpha_{1,j} = \alpha_{2,j} = \alpha_{3,j} = \alpha_{4,j} = \alpha_j$. The longitudinal, transverse and vertical velocities are reconstructed as follows, for the longitudinal subsystem:

$$\begin{bmatrix} 2^{-1}\sin^{-1}(\alpha_j/2) & -2^{-1}\sin^{-1}(\alpha_j/2) \\ 2^{-1}\cos^{-1}(\alpha_j/2) & 2^{-1}\cos^{-1}(\alpha_j/2) \end{bmatrix} \begin{bmatrix} V_{1,j} \\ V_{2,j} \end{bmatrix} = \begin{bmatrix} u_j \\ w_{l,j} \end{bmatrix} \tag{7.14}$$

The subscript l in $w_{l,j}$ means that it is calculated from the longitudinal radial velocity components. From the transverse subsystem we obtain:

$$\begin{bmatrix} 2^{-1}\sin^{-1}(\alpha_j/2) & -2^{-1}\sin^{-1}(\alpha_j/2) \\ 2^{-1}\cos^{-1}(\alpha_j/2) & 2^{-1}\cos^{-1}(\alpha_j/2) \end{bmatrix} \begin{bmatrix} V_{3,j} \\ V_{4,j} \end{bmatrix} = \begin{bmatrix} v_j \\ w_{t,j} \end{bmatrix} \tag{7.15}$$

The redundancy of the simultaneous and independent measurement of the vertical velocity component in the longitudinal and vertical subsystems (Eq. (7.14) and Eq. (7.15)) permits to apply a Doppler signal correction method for turbulence parameters. This method is developed in section Chapter 9.

7.4 Signal treatment

7.4.1 Analogue and digital signal pre-treatment

The system represented in Fig. 7.5 is composed of the central unit of the 3-D-ADVP and the personal computer used as master computer for the configuration and the control of the data acquisition.

The analogue emission

Five identical emitters (emitter 0-4) generate the power signals (TRA0-TRA4) which supply the five concentric annular piezo-electrical transducer included in the phase array emitter

TRA (see Fig. 8.2; the transducer is described in Chapter 8). Each emitter unit is composed of a control unit labeled push and pull which generates the TTL-signals. They are needed to connect and disconnect, respectively, the high voltage produced at the power unit output. For this purpose, the control unit has the two signals P0 and PRF as inputs (see Fig. 7.5). The push signal results from the multiplication of these two signals. The pull signal corresponds to the inverted push signal. These two signals are connected to the base inputs of two ultra-fast high voltage transistors mounted in serie into the push-pull amplifier. The transistor connected to the push signal switches the power unit ouput to transducer TRA during the high level periods of the push-signal. The transistor connected to the pull signal puts the ground on the transducer's output during the high-level periods of the pull signals as shown in Fig. 7.6. A supplementary transistor controlled by the PRF-signal is placed in paralel on the pull transistor to ensure a 50 Ω output impedance at 1 MHz during the emission period. The emitter's output is therefore adapted to the transducer's impedance. The mean power of the emitter circuitry is about 100 W and is able to deliver a maximum constant high voltage of 180 V during the emission period. Consequently, the amplitude of the five signals TR0-TR4 can vary according to the setting of the power unit output amplitude.

The analogue acquisition

The analogue acquisition is composed of four demodulators. The backscattered signal received by the large angle receivers (TRB-TRE) are the inputs of the demodulators, each of them being linked to one receiver. In the first stage of each analogue acquisition, the signal is amplified by a factor of 1000 (≅ 63 dB) without any frequency band restriction. This performance is obtained by the use of a high speed instrumentation amplifier with balanced differential inputs. It enables a high gain while preserving a large bandwidth (equal to 3 MHz in our case).

The second stage of the acquisition is concerned with the coherent quadrature demodulation of the backscattered signals.

The input signal of the coherent quadrature demodulator is expressed as $a(t) = A\cos\left[2\pi\left(f_0 + f_D\right)t\right]$. The reference signal is considered as a complex signal with its real part equal to the signal P0(t) and the imaginary part is equal to P90(t), thus $ref(t) = P0(t) + j\,P90(t) = B\exp\left(j2\pi f_0 t\right)$.

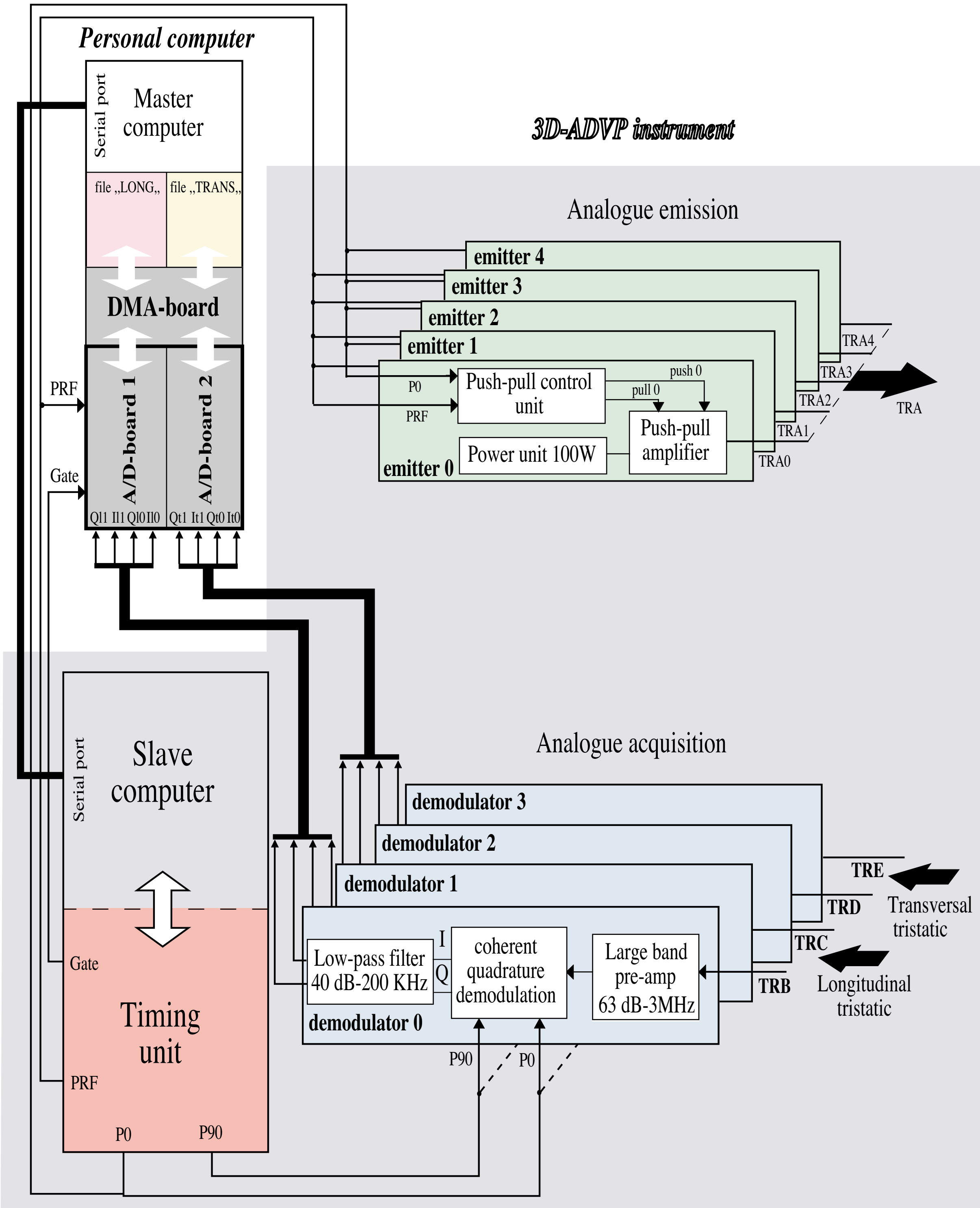

Fig. 7.5 Blockdiagram of the signal pre-treatment.

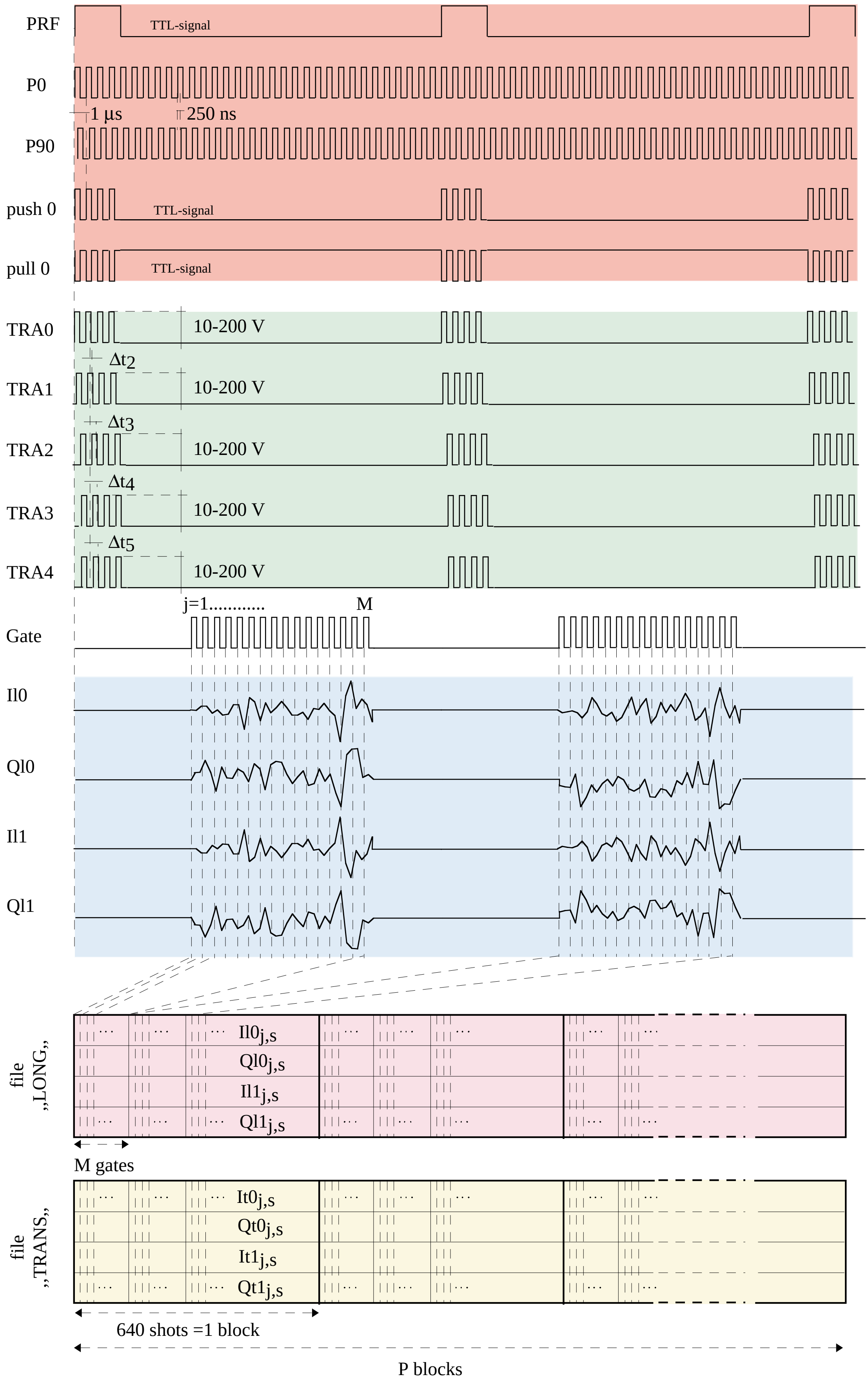

Fig. 7.6 Time-diagrams of the system.

The coherent demodulation consists of an analogue multiplication of the reference signal with the input signal. The demodulator's output yields:

$$\mathrm{ref}(t) \times a(t) = C\left\{\exp\left(j2\pi f_D t\right) - \exp\left[j2\pi\left(2f_0 + f_D\right)t\right]\right\} \tag{7.16}$$

The signal contains a high frequency component which is subsequently filtered out by the low-pass filter located behind the demodulator (see Fig. 7.5). The low frequency Doppler signal is composed of its analogue inphase and quadrature phase signals available at the outputs of analogue acquisition boards. The demodulation of the inphase and quadrature parts is necessary to determine the sign of the Doppler shift f_D and the sign of its corresponding proportional radial velocity component given by Eq. (7.4). The low-pass filter is a second order (-40 dB/ decade) Tschebycheff filter with a cut-off frequency at -3 dB equal to 200 KHz, ensuring an attenuation of -80 dB of the high frequency term in Eq. (7.16) since f_0 =1MHz.

The data arrangement

Four large angle receivers are used in the multistatic configuration of the 3-D-ADVP. Thus, eight Doppler signals must be digitized and stored in data files before the digital treatment. The analogue / digital conversion is divided into two parallel systems including the conversion and the writing of the data on the storage disc. The first one uses the A/D-board 1 to convert the four signals Il0, Ql0, Il1, Ql1, coming from the TRB and TRC receivers, respectively. These two sensors compose the longitudinal tristatic subsystem of the ADVP (see Fig. 7.3). The second one uses the A/D-board 2 to convert the signals It0, Qt0, It1, Qt1, corresponding to the inphase and quadrature phase signals of the transverse subsystem. The conversion of all Doppler signals must be done at the same moment on all eight channels. Therefore, simultaneous sampling is achieved on the four channels of each A/D-board under the control of the two TTL-signals PRF and Gate (see Fig. 7.6). The internal bus of the master computer must be able to handle each pulse with a minimal time duration of 4 μs. To obtain the maximum spatial resolution equal to 3 mm in the monostatic configuration, the time spacing between the two gates must be equal to 4 μs. Since each converted word has a width of 16 bits, writing in the data files must be completed at a rate of 12 Mbits/s. To ensure this data flux, data are digitized in binary format. The arrangement of the samples in each file, are shown in Fig. 7.5. P blocks are stored in each file. One block represents a 2D array of length equal to 640 pulses of M gates and a width of 4 channels. The data transfer from the A/D-boards to the file uses the DMA-card to access directly the circular buffer of the computer before the writing in the files. Normally, 600s of data are acquired for one measurement which results in two files roughly equal to 300 Mbytes each. External storage disks are usually required.

The master and slave computers

The master computer is used to setup the ADVP by sending the configuration file to the slave computer through its serial port (RS 232). The slave computer controls the timing unit which generates the TTL-signals PRF, Gate, P0 and P90, needed for the measuring process described above.

7.4.2 The pulse-pair algorithm

As described in the previous section, the data pre-treatment stage provide the digitized in-phase and quadrature-phase Doppler signals in two separate files corresponding to the signals of the longitudinal and transverse tristatic subsystems (see Fig. 7.3). The complex Doppler signal for each radial velocity component i at depth j, can be written as $D_{i,j}(t) = C_{i,j} \exp\left[j\, \vec{K}_{Bi,j} \cdot \vec{r}(t)\right]$. The signal $D_{i,j}(t)$ is a highly simplified model of the "true" complex Doppler signal. Effects of spatial averaging and transit time in the sample volume j are not considered here (see Garbini 1982 for details). The frequencies of the four complex Doppler signals have to be evaluated in order to calculate the radial velocity components given by Eq. (7.4). Subsequently, the geometrical reconstruction of the desired longitudinal, transverse and the two vertical quasi-instantaneous velocities is achieved by applying Eq. (7.14) and Eq. (7.15). The pulse-pair algorithm is of particular interest since it allows the estimation of quasi-instantaneous frequencies for a stationary random process (Lhermitte and Serafin 1984). The frequency estimation of the Doppler signals is independent of the component i as well as the depth index j. We will therefore omit the indexes i and j in the following equations. By definition, the auto-correlation function of a random stationary signal has the following properties (Miller and Rochwarger 1972) :

- The amplitude $A_{corr}(\chi)$ of the complex auto-correlation function $\Psi_t(\chi) = \frac{1}{T}\int_0^T D(t)D(t-\chi)dt = A_{corr}(\chi)\exp\left[j\,\varphi(\chi)\right]$ is even.

- The amplitude of the complex auto-correlation function has its maximum at $\chi = 0$, where the variable $\chi = 0$ correponds to the time delay.

- The phase is equal to zero $\varphi(\chi) = 0$ at $\chi = 0$.

The theorem of Wiener-Khintchine (see Bendat and Piersol 1971) yields that the auto-correlation function is equal to inverse Fourier transform of the power spectral density:

$$\Psi_t(\chi) = \int_{-\infty}^{+\infty} S(f)\exp[j\,2\pi f\,\chi]\,df \tag{7.17}$$

The moments of the power spectral density function can be expressed as function of the auto-correlation function as follows:

$$m_k = \int_{-\infty}^{+\infty} f^k S(f)\,df = (2\pi j)^{-k}\frac{d^k}{d\chi^k}\Psi_t(\chi)\bigg|_{\chi=0} \tag{7.18}$$

Since $d^k\Psi_t(\chi)/d\chi^k = \int_{-\infty}^{+\infty}(2\pi j f)^k S(f)\exp[j\,2\pi f\,\chi]\,df$.

Using the properties of the complex auto-correlation function $\Psi_t(\chi) = A_{corr}(\chi)\exp[j\,\varphi(\chi)]$, the first moment of the power spectral density is equal to the mean frequency $\bar{f}_D$ of the corresponding Doppler signal D(t):

$$\bar{f}_D = \int_{-\infty}^{+\infty} f\,S(f)\,df = (2\pi j)^{-1}\frac{d}{d\chi}\Psi_t(\chi)\bigg|_{\chi=0} = (2\pi)^{-1}\frac{d}{d\chi}\varphi(\chi)\bigg|_{\chi=0} \tag{7.19}$$

where the function $\varphi(\chi)$ is the phase of the complex auto-correlation function. If the time derivative in Eq. (7.19) is approximated with a finite difference method, we obtain:

$$\bar{f}_D = (2\pi j)^{-1}\frac{d}{d\chi}\Psi_t(\chi)\bigg|_{\chi=0} = (2\pi\,T_{PRF})^{-1}\left[\varphi(T_{PRF}) - \varphi(0)\right] = (2\pi\,T_{PRF})^{-1}\varphi(T_{PRF}) \tag{7.20}$$

T_{PRF} represents the period of the PRF signal (see Fig. 7.6). As shown previously, the frequency of PRF corresponds to the sampling frequency of the Doppler signal D(t). Thus, the time sampled auto-correlation function $\Psi_t(T_{PRF})$ yields:

$$\hat{\Psi}_t(T_{PRF}) = \frac{1}{N_{pp}}\sum_{s=1}^{N_{pp}-1}\left[I_s\,I_{s+1} + Q_s Q_{s+1} + j(Q_s\,I_{s+1} + I_s Q_{s+1})\right] \tag{7.21}$$

where the auto-correlation function has been estimated over N_{pp} time samples (the symbol ^ denotes a mean over N_{pp} time samples). The variables I_s and Q_s are the inphase and quadrature-phase samples at time index s stored in the corresponding files named LONG and TRANS in Fig. 7.5. The channel, depth and bistatic indexes have been omitted for simplicity of the notation. If the number of pulse-pairs is high enough to ensure a second order stationarity, i.e. that the variance of the Doppler signal D(t) evaluated over N_{pp} samples is independent of time, the local measurement process is randomly stationary. If the time interval N_{pp} x T_{PRF} is small compared to a characteristic time scale of the investigated turbulent flow, the Doppler frequency $\hat{\bar{f}}_d$ can be considered as quasi-instantaneous and is equal to:

$$\begin{aligned}\hat{\bar{f}}_d &= \left(2\pi T_{PRF}\right)^{-1} \arctan\left\{\mathrm{Re}\left[\hat{\varphi}(T_{PRF})\right] / \mathrm{Im}\left[\hat{\varphi}(T_{PRF})\right]\right\} \\ &= \left(2\pi T_{PRF}\right)^{-1} \arctan\left[\left(\sum_{s=1}^{N_{pp}-1} Q_s I_{s+1} + I_s Q_{s+1}\right) \Big/ \left(\sum_{s=1}^{N_{pp}-1} I_s I_{s+1} + Q_s Q_{s+1}\right)\right]\end{aligned} \tag{7.22}$$

It is obvious that the number N_{pp} should be as small as possible so that the time resolution of the quasi-instantaneous velocity estimation allows the resolution of turbulent scales. Rolland (1994) has tested the performance of the pulse-pair frequency estimator in turbulence conditions similar to those presented herein. He obtained a minimal number N_{pp} =25 to ensure a second order stationarity with a signal to noise ratio SNR ≈ 20 dB. Under these conditions, the Nyquist frequency of the velocity field is equal to PRF / (2 N_{pp})= 1 KHz / (2x 25) =20 Hz. This frequency is high enough to investigate the inertial sub-range of the turbulent velocity field in the studied open-channel flows. Compared to a LDA, the Nyquist frequency of the 3-D-ADVP is lower by a factor roughly equal to 2. Compared to a PIV, the frequency is higher by a factor of 1.5-2.5. The pulse-pair algorithm is simple to implement and provides a quasi-instantaneous velocity information which is an outstanding advantage compared to the commonly used FFT algorithm.

7.4.3 The phase coding method

Phase coding is necessary to isolate echoes resulting from the present pulse from those resulting from previously transmitted pulses. These echoes are called first trip echoes and are usually added to second and third trip echoes which disturb the pulse-to-pulse demodulation and can thus lead to an erroneous Doppler frequency estimation. The n^{th} emitted pulse E_n can be written as:

$$E_n(t) = E\cos(2\pi f_0 t + \varphi_{cn}) \tag{7.23}$$

where E is the amplitude, f_0 is the carrier frequency and φ_{cn} is the coded phase for the n^{th} pulse. A shape function equal to the signal PRF represented in Fig. 7.6 should be multiplied by the signal E_n to reproduce the true emitter signal. Since it has no influence on the description of the phase coding method, we neglect that term.

The backscattered signal received from location j for the radial component i (see Fig. 7.3) is expressed as:

$$\begin{aligned} R_n(t) &= R\cos[2\pi f_0 t + \varphi_{Dn}(t) + \varphi_{cn}] + \sum_{m=0}^{n-1} C\cos[2\pi f_0 t + \varphi_{Dm}(t) + \varphi_{cm}] \\ \text{with} \quad \varphi_{Dn}(t) &= \vec{K}_{Bi,j} \cdot \vec{r}_j(t) \end{aligned} \tag{7.24}$$

where the indexes i and j are deliberately omitted in the first line. The amplitudes R and C of the two terms on the right hand side are arbitrary. The equation on the second line is deduced from Eq. (7.1). The second term of the equation on the top line represents the contribution of the 0^{th} to the $(n-1)^{th}$ previous pulses corresponding to the multiple trip echoes mentioned before. φ_{cm} is the coded phase of the m^{th} pulse. Applying the coherent pulse-to-pulse demodulation defined in section 7.4.1, to the signal $R_n(t)$ yields:

$$R_n(t) = R\exp[\varphi_{dn}(t)] + \sum_{m=0}^{n-1} C\exp[\varphi_{cn} - \varphi_{dm}(t) - \varphi_{cm}] \tag{7.25}$$

If the backscattered signal would be ideal (i.e. no contribution from the pulses previous to the n^{th}), the second term on the right hand side would be equal to zero and the Doppler pulsation could be extracted directly by evaluating the time derivative of the phase $\varphi_{Dn}(t)$ of the first term (using the pulse-pair estimator). If no phase coding is imposed and multiple trip echoes are present, the second term on the right hand side reduces to $\sum_{m=0}^{n-1} C\exp[\varphi_{Dm}(t)]$. This term induces an additional frequency peak (since the phase $\varphi_{Dm}(t)$ is timevariant) in the spectrum of the signal $R_n(t)$ which affects the calculation of the desired Doppler frequency f_{Dn}.

The aim of the phase coding is to destroy the phase coherence of the second term on the right hand side of Eq. (7.25). Therefore, a coded phase is generated randomly varying from one pulse to the next. Consequently the term $\sum_{m=0}^{n-1} C\exp[\varphi_{cn} - \varphi_{Dm}(t) - \varphi_{cm}]$ becomes a white noise with a flat power spectrum. In other words, the power contained in the peak induced by $\sum_{m=0}^{n-1} C \exp[\varphi_{Dm}(t)]$ is redistributed over the resolved frequency band. Unfortunately, the SNR of the signal $R_n(t)$ is reduced. The pulse-pair algorithm is based on a moment determination from the auto-correlation function and is insensitive to white noise. Therefore, the Doppler frequency $f_D = (2\pi)^{-1} d\varphi_{Dn}(t)/dt$ is evaluated correctly using the random phase coding method.

This method can be applied to the quasi-instantaneous estimation of the Doppler frequencies as long as the probability that $\varphi_{cn+1} - \varphi_{cn} = 0$ (i.e. the difference of the coded phase between pulse n+1 and n) is low enough to ensure a sufficient redistribution over the frequency band of the energy contained in the undesired frequeny peak. The time derivative of the last condition induces a frequency equal to zero. Thus the phase coherence of the undesired signal $\sum_{m=0}^{n-1} C \exp[\varphi_{cn} - \varphi_{Dm}(t) - \varphi_{cm}]$ is not destroyed.

The pseudo-random sequence used in the ADVP produces a phase equal to 0 or $\pi / 2$ randomly superimposed on the emitter signal. A probability $P(\varphi_{cn+1} - \varphi_{cn} = 0) = 33\%$ over N_{pp} = 32 pulses is reached which implies that 66% of the power contained in the undesired frequency peak is redistributed uniformly over the frequency band.

7.4.4 De-aliasing methods of the Doppler signal

The presence of fixed echoes in the Doppler signal due to ultrasonic scattering at the water-bed and water- air interfaces leads to the major restrictions of sonar applications in open-channel flows. Although the phase coding presented in section 7.4.3 is highly efficient when it is combined with the pulse-pair algorithm, the amplitude of the fixed echoes can be too important to be decorrelated sufficiently over N_{pp} pulses. In these cases, the time intervall between two consecutive pulses may be increased until the fixed echoes are. This reduces the PRF and the corresponding unambiguous Doppler frequency range in which the frequency estimation is not aliased. The challenge is thus to find solutions to velocity aliasing problems. Two-different methods are presented in this section.

De-aliasing based on flow direction knowledge

The unambiguous Doppler-phase range of the ADVP is equal to $]-\pi\,;\pi[$, corresponding to a Doppler frequency range of $]-PRF/2\,; PRF/2[$. When the Doppler frequency f_D is smaller or exceeds the value of -PRF / 2 or PRF / 2, respectively, the estimated frequency is aliased and results in f_D+PRF or f_D-PRF, respectively. In these cases the phase of the "true" Doppler signal is less than $-\pi$ or greater than $+\pi$, respectively. This situation can be detected by analyzing the sign of the term $\mathrm{Re}\left[\hat{\varphi}\left(T_{PRF}\right)\right]$ in Eq. (7.22). Consequently, when the direction of the flow is known (i.e. the sign of the term $\mathrm{Re}\left[\hat{\varphi}\left(T_{PRF}\right)\right]$), the estimated aliased Doppler frequency can be corrected by subtracting or adding from it the frequency PRF, respectively. With this method the frequency range of unambiguity is extended from $\left]-PRF/2\,;PRF/2\right[$ to $\left]-PRF\,;PRF\right[$. The mean flow direction of the open-channel flows studied herein is known. This method is therefore an efficient solution to aliasing problems. However, the Doppler frequencies should never exceed the range $\left]-PRF\,;PRF\right[$.

De-aliasing using dual PRF

To overcome the limitations of the previously described de-aliasing method (where the flow direction has to be known), the following solution has been proposed by Lhermitte (1999). Consider a Doppler signal with frequency f_D sampled at PRF1 and PRF2. From Eq. (7.20) we deduce the corresponding estimated Doppler frequencies $f_{D1}=\left(2\pi T_{PRF1}\right)^{-1}\varphi\left(T_{PRF1}\right)$ and $f_{D2}=\left(2\pi T_{PRF2}\right)^{-1}\varphi\left(T_{PRF2}\right)$, respectively. The ratio between the sampling frequencies is PRF1 / PRF2= n / m, with n > m. The normalized difference $\Delta f_D=\left(f_{D1}-f_{D2}\right)/f_{D1}$ is shown in Fig. 7.7 for $n=4$ and $m=3$. This difference is only due to discretization differences originating from the different sampling frequencies PRF1 and PRF2. In the stippled area of Fig. 7.7, the steps of the normalized difference Δf_D are not repeated twice so that it can be used to determine the ambiguity order in the area $\left]-3PRF/2\,;3PRF/2\right[$. Table 7.1 gives the values of the frequencies to be added to f_{D1} and f_{D2} as function of the normalized difference value Δf_d. Compared to the de-aliasing methodology described in the previous section, a gain of 200% range width is permitted by the dual PRF sampling method without any requirement on the flow direction.

The limitation of this method results from the minimum value $\Delta f_{D\min}=PRF1\,(n-m)/(2\,n)$ which has to be much larger than the standard deviation of the f_{D1} and f_{D2} estimations. This condition is respected when it is applied to mean velocities. When applied to quasi-instantaneous velocity estimations, the pulses at PRF1 and PRF2 should be as close as possible in order to reduce the effect of the velocity fluctuation due to turbulence between the two pulses. A solution to that problem (which has not been tested in this thesis) consists in alternating sequentially the PRF between PRF1 and PRF2 after each two pulses. For our commonly used ADVP settings (i.e. PRF = 1 KHz, PRF1 ≈ 300 Hz, n = 5, m = 4) we obtain $\Delta f_{D\min}=0.1\,PRF1\approx 33\,\mathrm{Hz}$ which is roughly 20 times higher than the standard deviation of the mean Doppler estimation. Although this method has not been employed in our straight open-channel flow applications where the mean flow direction is known, it is well suited for velocity measurements in non-channelized currents or curved channels where the flow direction is hard to predict.

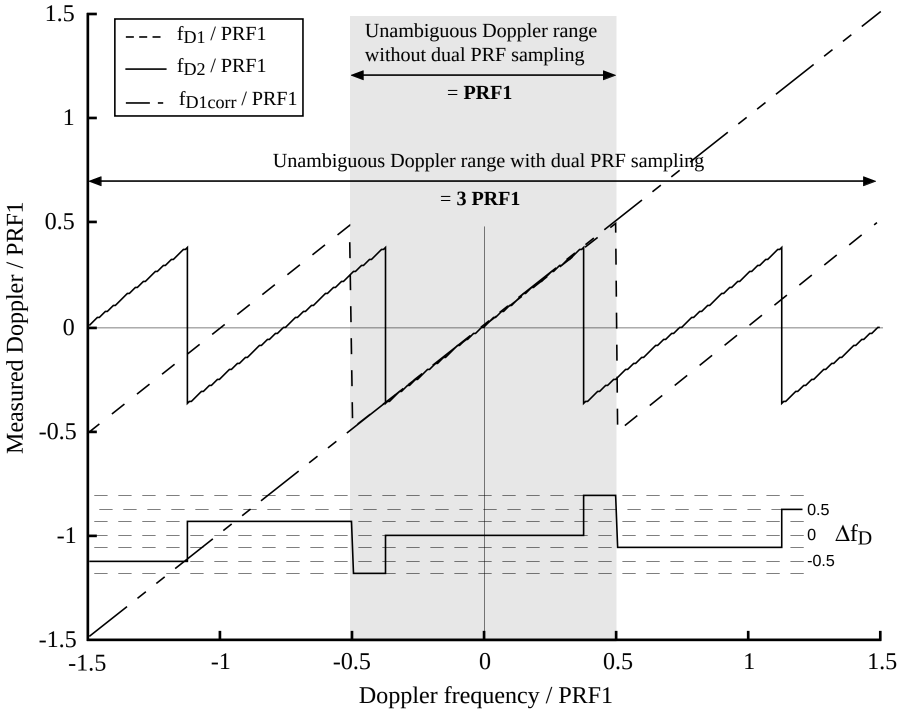

Fig. 7.7 Estimated Doppler frequencies $f_{D1} = (2\pi T_{PRF1})^{-1}\varphi(T_{PRF1})$ and $f_{D2} = (2\pi T_{PRF2})^{-1}\varphi(T_{PRF2})$ in function of the Doppler frequency f_D. Frequency difference $\Delta f_D = (f_{D1} - f_{D2})/f_{D1}$ in function of the Doppler frequency f_D.

Δf_D	Add to f_{D1}	Add to f_{D2}
0.75	0	+ PRF2
0.5	+ PRF1	+ 2 PRF2
0.25	- PRF1	- PRF2
0	0	0
-0.25	+ PRF1	+ PRF2
-0.5	- PRF1	-2 PRF2
-0.75	0	- PRF2

Table 7.1 Correction values of the estimated Doppler frequencies f_{D1} and f_{D2} in function of the normalized difference value $\Delta f_D = (f_{D1} - f_{D2})/f_{D1}$.

7.4.5 The focused phase array emitter

This section is refered to Chapter 8

7.4.6 Doppler noise reconstruction

This section is refered to Chapter 9

7.5 A Realization of the instrument

7.5.1 Hardware and software

Fig. 7.8 shows the blockdiagram of the instrument. The macintosh computer and the central unit are the two hardware components of the system which have been described in section 7.4.1. It has been pointed out that profiles of instantaneous Doppler information are needed on 4 pairs of channels (i.e. the in-phase and quadrature-phase Doppler signals of the four radial velocity components) to estimate the quasi-instantaneous velocity profiles. For that purpose, the two parallel working acquisition boards must be able to simultaneously sample the eight analogue Doppler signals and to transfer the digitized signals at a rate of 250 KHz to the computer memory for the arrangement and the storage. The rate of 250 KHz is due to the minimal time duration of 4µs of the emission pulse. In that case, the maximal spatial resolution is achieved by setting a time width between each gate (see Fig. 7.6) equal to 4 µs which results in a 250 KHz data transfer rate. The National Instruments Acquisition card NB-A2000 allows a 1 MHz transfer rate on one channel and 1 MHz / 4=250 KHz maximal transfer rate on four channels (sampling is still executed simultaneously on the four channels).

The first step of the digital signal treatment of the data stored in the files "LONG" and "TRANS" (containing the measurements of the longitudinal and the transverse tristatic subsystems shown in Fig. 7.3, respectively) is done with a Fortran 90 (Absoft software) programme. This part concerns the digital data-arrangement for the implementation of the triangulation method presented in section 7.2.2. Eq. (7.10) is therefore solved in order to calculate the distances between the emitter and the sample volume R_j. Subsequently, the de-aliasing methods are applied or not (see section 7.4.4) as function of the user settings. In the next step, the quasi-instantaneous Doppler frequency estimation is given by the pulse-pair algorithm in Eq. (7.22). The corresponding radial velocity profiles result from Eq. (7.4) and finally the longitudinal, transverse and vertical velocity components are evaluated from Eq. (7.14) and Eq. (7.15).

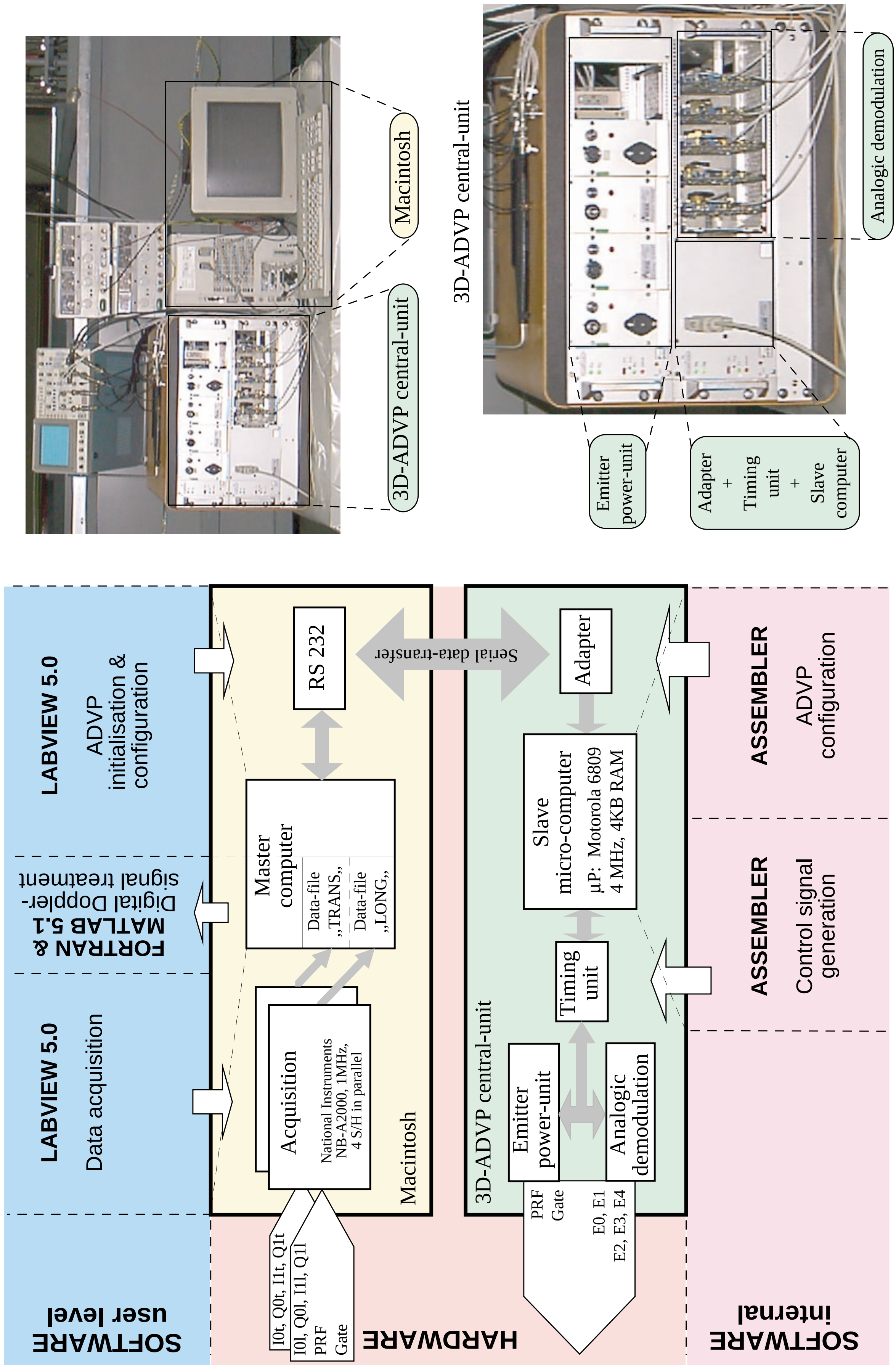

Fig. 7.8 Hardware and software of the 3-D-ADVP.

Five output files are generated by the fortran programme. They provide the local Doppler angle for each measurement point in the profile, the mean longitudinale, tranverse and vertical velocity profiles, the quasi-instantaneous longitudinal, transverse and vertical velocity profiles, the velocity variances profiles of the three velocity components and the time averaged covariance profiles $\overline{u'w'}$ and $\overline{v'w'}$.

Further digital signal treatment of the instantaneous velocity field is done with Matlab routines. Examples for the data visualization are given in Fig. 3.5, Fig. 4.1 and Fig. 5.9 as well as the conditional sampling results presented in Fig. 4.2, Fig. 4.3, Fig. 5.4, Fig. 5.5, Fig. 5.6, Fig. 5.10, Fig. 6.1.

The internal software is written in Assembler for the Motorola 6809 micro-processor. One program interprets the configuration information transferred via the RS 232 interface. The second one generates the logical signals necessary for the timing-unit in order to produce the TTL-signal. The generation of the pseudo-random phase coding sequence is ensured by an assembler routine.

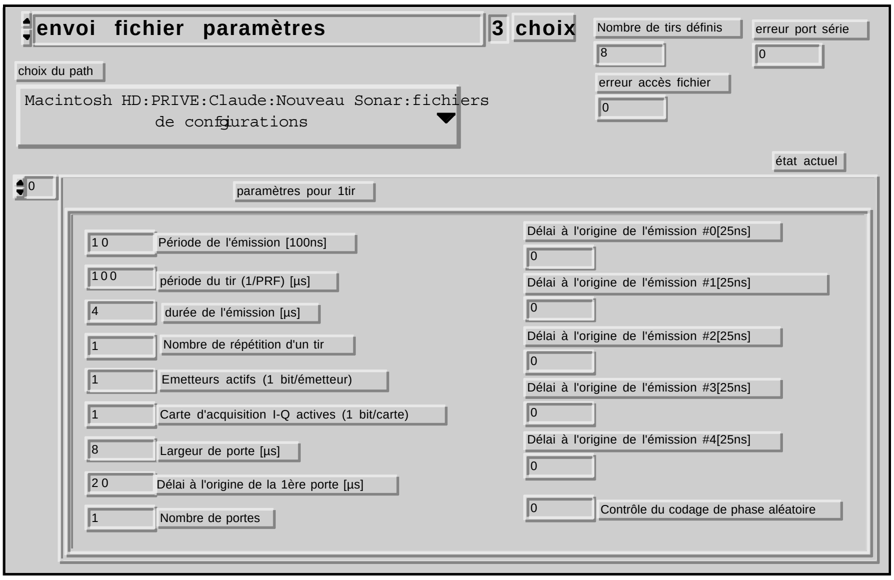

Fig. 7.9 Configuration possibilities of the instrument.

The configuration possibilities of the instrument are illustrated by the front panel of the Labview subroutine shown in Fig. 7.9. This program generates a configuration file which is transferred via the serial RS 232 interface to the slave computer. Eight pulses with different characteristics can be setup. They are repeated sequentially until a command is sent to the ADVP. The list of parameters defined for each pulse are given in Table 7.2. The large number of setting parameters permits a high flexibility of the configuration. For example, the parameters PRF, emitter frequency, number of gates, width of gates, phase coding control can be changed alternatively from one pulse to the next or can be repeated during a certain number of pulses with identical values (by defining the value of the parameter called number of repetitions of one pulse in Fig. 7.9) before accepting the configuration of the following pulse.

Fig. 7.10 represents several possibilities offered by the data acquisition software programmed in Labview. The first front panel allows to choose between three different types of outputs presented in the front panels listed below. The front panel named "fichier" directly transfers the eight digitized Doppler signals to the files "LONG" and "TRANS". The instantaneous size and time length of the files are available.

Variable name in Fig. 7.9	Function	Résolution	Min. value	Max. value
Période de l'émission	Period of the emitted burst	100 ns	3	63
Période du tir (1/PRF)	Period of the PRF	1 µs	100	8191
Durée de l'émission	Time length of the pulse	1 µs	1	63
Nombre de répétition d'un tir	Number of repetition of one pulse	1	0	255
Emetteurs actifs	Number of activated emitters	1	0	31
Cartes d'acquisition I-Q	Number of activated acquisition boards	1	0	31
Largeur de porte	Gate time-width	1 µs	2	63
Délai à l'origine	Time delay of the first gate from the emission	1 µs	20	8191
Nombre de portes	Number of gates	1	1	255
Délai à l'origine emission E0	Time-shift from the emission for emitter E0	25 ns	0	63
Délai à l'origine emission E1	Time-shift from the emission for emitter E1	25 ns	0	63
Délai à l'origine emission E2	Time-shift from the emission for emitter E2	25 ns	0	63
Délai à l'origine emission E3	Time-shift from the emission for emitter E3	25 ns	0	63
Délai à l'origine emission E4	Time-shift from the emission for emitter E4	25 ns	0	63
Contrôle codage de phase	Activation of phase coding	-	0	1

Table 7.2 Characteristics of configuration parameters.

The second type of output (shown in the third front panel) provides the on-line calculated, normalized Doppler spectrum. This information is used to check the signal quality before writing it to the files. The SNR at each depth in the profile can be verified by selecting the adequate gate number (in the Fig. 7.10 a SNR equal to 25 dB is observed). Furthermore, the presence of fixed echoes can be detected if two frequency peaks are seen in the spectrum. The third type of output is called "I(t), Q(t) Doppler". It re-arranges the acquired signal in order to visualize the time-evolution of the local Doppler signal. Consequently, a visual check of the number of acoustical targets can be undertaken. All three output types are executed in on-line mode during the acquisition.

7.5.2 Laboratory and field deployable instrument

Installation in flumes

The first picture in Fig. 7.11 shows the installation of 3-D-ADVP in a laboratory flume (Blanckaert 2001). The transducer chamber has been adapted to allow 3-D velocity profile measurements over the entire cross-section as well as very near to the banks. The ADVP is well suited for the investigation of the secondary currents shown in Fig. 7.12. These currents are induced by the turbulence anisotropy near to the outer bank (secondary currents of Prandtl's second kind, Nezu and Nakagawa 1993) where the bank erosion process occurs (Hurther and Lemmin 2000).

The inside of the transducer chamber is presented in the second picture. The central phase array and the large angle receivers described in section 7.2.2 can be recognized. At the bottom of the chamber, the mylar window is at the interface between the water surface of the channel flow and the water contained in the transducer chamber. Mylar is used because its acoustical impedance is extremely low, it resists to important normal loads and it is particularly smooth. The low acoustical impedance avoids to produce important ultrasonic scattering at the interface. Usually, the two points nearest to the water surface are weakly perturbated by the presence of the mylar.

In the flow conditions investigated herein, this maximal height corresponds to 3 % of the water depth and therefore the measurement system is considered as non-intrusive.

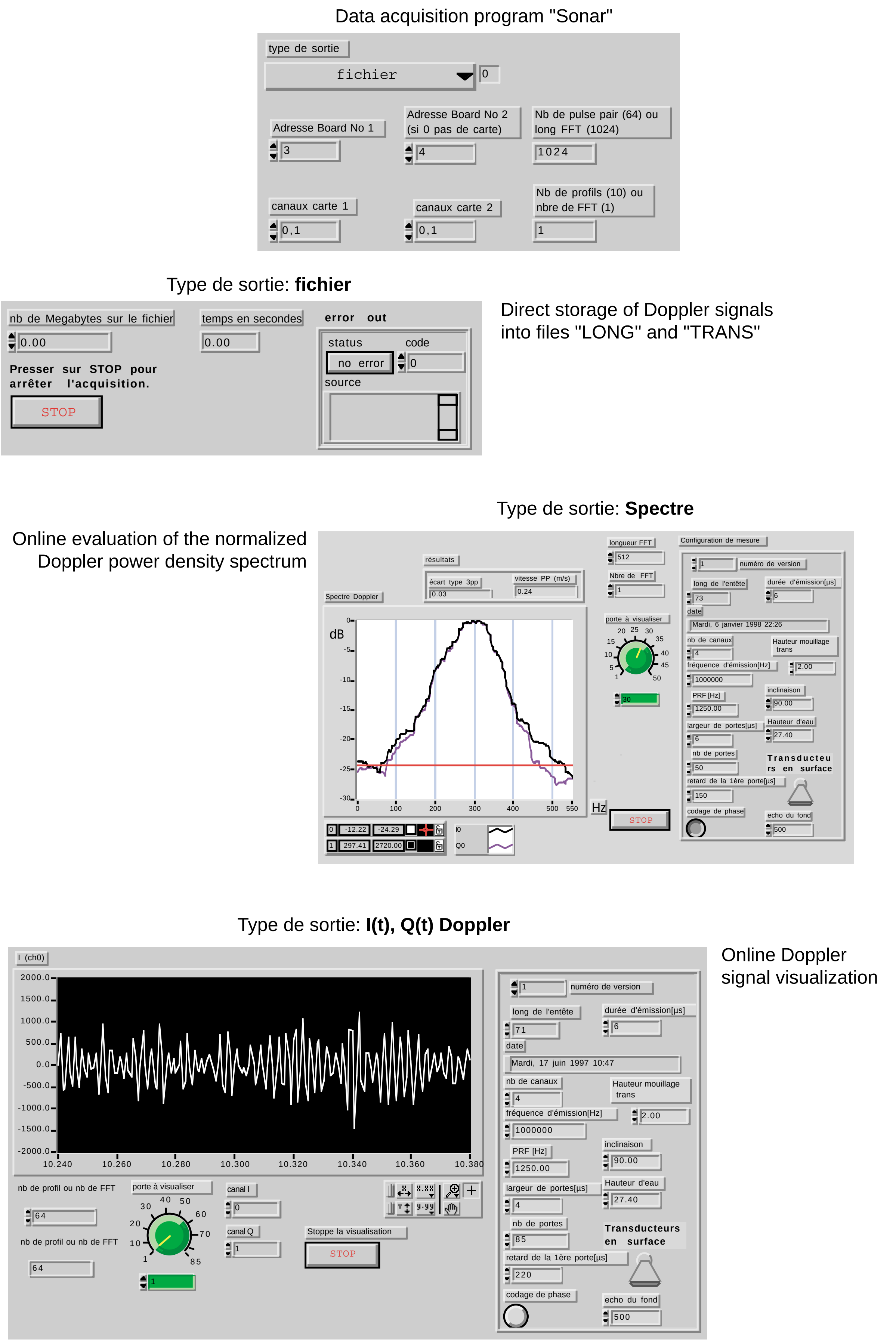

Fig. 7.10 Data-acquisition and on-line data control during the measurements .

River measurements

It is apparent from the literature that very few field measurements in natural river have actually been made. This is mainly due to the lack of suitable high resolution instrumentation. For this purpose, we decided to conceive a field deployable 3-D-ADVP and to carry out river measurements in different conditions.

The four last pictures in Fig. 7.11 illustrate the in situ installation of the ADVP for measurements over an entire cross-section of two shallow water rivers (less than 1 m water depth). As can be seen, the transducer chamber has been mounted on a metallic telescopic structure of maximal width equal to 20 m or has been clamped underneath a bridge in order to cover the total river width. These measurements will be used for a future study on transport and mixing in rivers. Unique cross-section distribution of the following parameters will be evaluated directly:

- The mean values of the three velocity components
- The velocity variances and the shear stresses.
- The profiles of the turbulent mixing coefficients.
- The structure of secondary currents.
- The dynamics of coherent structures and their relation to bottom shear stress.

Due to its capability to take instantaneous velocity profiles of all three velocity components with resolution of turbulence scales, this instrument will serve as a unique and powerful tool to advance the understanding of some aspects of river hydrodynamics.

3D-ADVP IN LABORATORY FLUMES

Transducer chamber with emitter and receivers

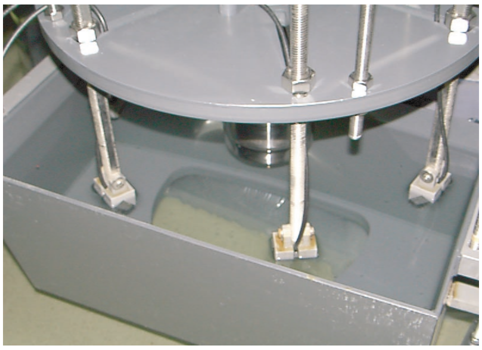

Measurements in curved channel (Blanckaert 2001)

3D-ADVP IN RIVERS

Metallic structure for cross-section measurement

3D-ADVP measurements in river Arnon (Hurther and Lemmin 2000)

3D-ADVP measurements in river Mèbre (Hurther and Lemmin 1999)

Field deployable 3D-ADVP

Fig. 7.11 Laboratory and field measurements.

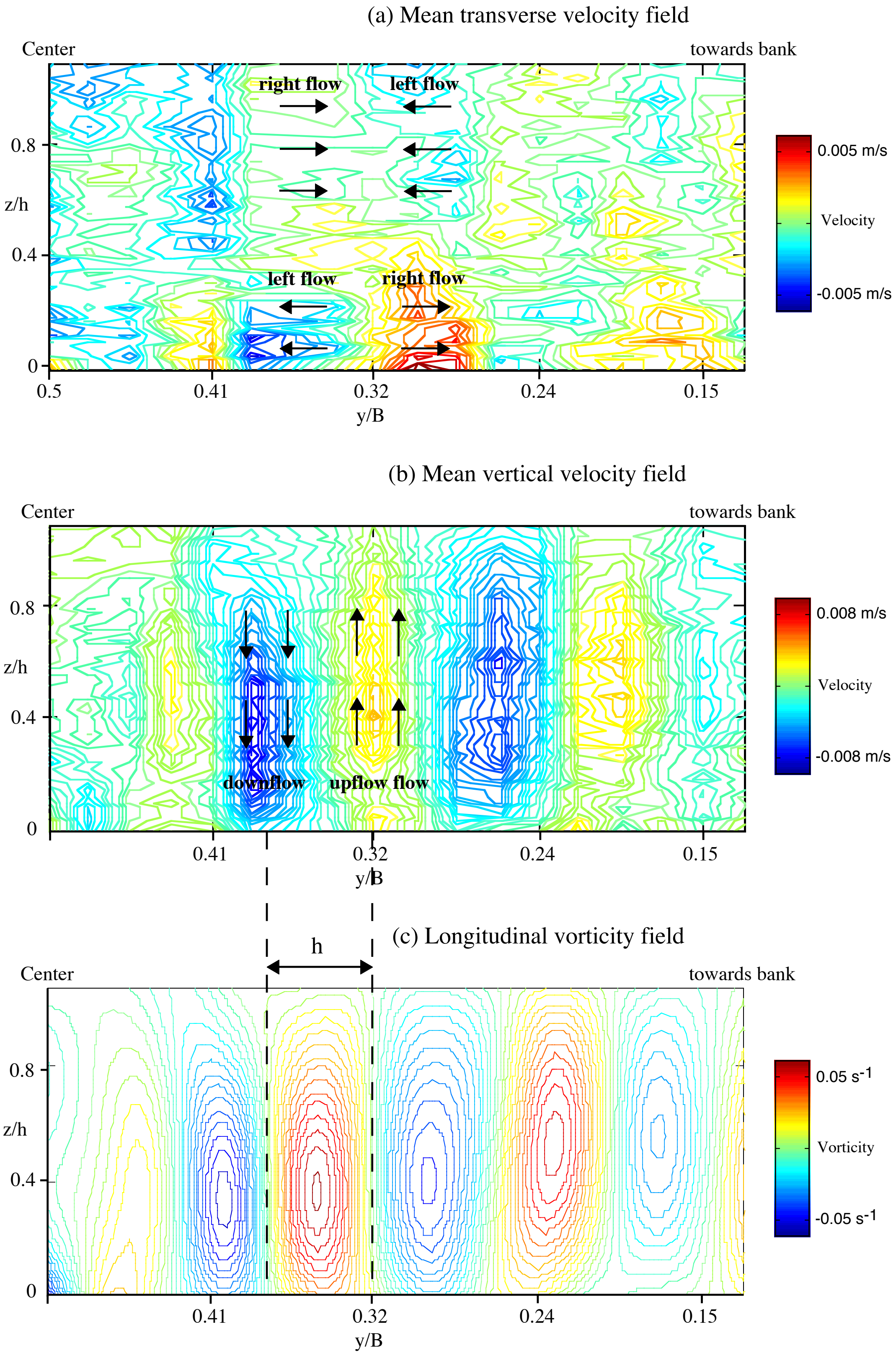

Fig. 7.12 3-D ADVP measurements of secondary currents in a half cross section of a straight open-channel flow. (a) Iso-contours of mean transverse velocit. (b) Iso-contours of mean vertical velocity. (c) Iso-contours of streamwise vorticity $\Omega_x = 1/2\left(\partial\bar{w}/\partial y - \partial\bar{v}/\partial z\right)$.

7.6 Conclusions

This chapter was devoted to the description of the working principle and the realization of the 3-D-ADVP instrument. This device has been used for the study of the hydrodynamical processes undertaken in the first part of this thesis. Quasi-instantaneous profiles of the three-dimensional velocity field can be measured simultaneously over the entire height of the turbulent boundary layer. The space, time and velocity resolutions have been discussed and evaluated. They are found to be high enough to allow quantitative estimations of turbulence related parameters in open-channel flows. An important number of high technology solutions are used to overcome some of the limitations inherent to the measuring principle. They are concerned with the use of a phase array emitter, phase coding of the emitter pulse, pulse-pair algorithm, single and dual PRF de-aliasing and Doppler noise reconstruction and extraction. A simplified version of the device could be considered for industrial applications. A further particularity of the instrument is its flexibility. It may be installed for measurements in laboratory conditions (straight, curved, compound channels, flow around a cylinder to study scour hole development) as well as field measurements in rivers or lakes.

7.7 References

Bendat, J. S. and Piersol, A. G. (1971): Random data: analysis and measurement procedures. Wiley-Interscience, New-York.

Blanckaert, K. (2001): Bend-Flow Simulation Using 2D Depth-Averaged Model. Discussion in J. Hydraulic Eng., 1127(2), 167-170.

Garbini, J. L., Forster, F. K. and Jorgensen J. E. (1982): Measurement of fluid turbulence based on pulsed ultrasound techniques. Part 1. Analysis. J. Fluid Mech. 118: 445-470.

Hurther, D. and Lemmin U. (2000): A field study of transport and mixing in rivers using a 3-D ADVP. Swiss National Science Fundation. Annual report of grant Numbered 2100.50739.97.

Lhermitte, R. and Serafin, R. (1984): Pulse-to-pulse coherent Doppler signal processing techniques. J. Atmos. Oceanic Technol., 1(4), 293-308.

Lhermitte, R. (1999): Tidal flow velocity and turbulence measurements. Internal publication of the Rosenstiel School of Marine and Atmospheric Science, University of Miamy, USA.

Miller, K. and Rochwarger, M. (1972): A covariance approach to spectral moment approximation. IEEE Trans., IT-18(5).

Nezu, I. and Nakagawa, H. (1993): Turbulence in open-channel flows. AIHR Monograph series. Balkema.

Rolland, T. (1994): Développement d'une instrumentation Doppler ultrasonore adaptée à l'étude hydraulique de la turbulence dans les canaux. PhD dissertation No 1281, Swiss Federal Institute of Technology, Lausanne.

Shen, C. (1997): An acoustic instantaneous praticle flux profiler for turbulent flow. PhD dissertation No 1630, Swiss Federal Institute of Technology, Lausanne.

Shen, C. and Lemmin, U. (1997): Ultrasonic scattering in highly turbulent clear water flow. Ultrasonics 35, 57-64.

CHAPTER 8

A CONSTANT-BEAM-WIDTH TRANSDUCER FOR 3-D ACOUSTIC DOPPLER PROFILE MEASUREMENTS IN OPEN-CHANNEL FLOWS

Published in Measurement Science and Technology (1998), Vol. 9 No. 10, pp. 1706-1714.

8.1 Abstract

An ultrasonic constant beamwidth transducer system is described which is capable of generating an extended focal zone by electronically focusing the beam over the desired water depth range. Beam directivity measurements show that the higher beam directivity and the reduction in side lobe level lead to an increase of the signal to noise ration by up to 15dB compared to a plane disc transducer. It also allows to significantly reduce undesirable spectral broadening effects which in the case of plane disc transducers lower the final resolution and interfere with the correct data interpretation.

Using the focalized transducer, simultaneous 3-D velocity component profile measurements over the whole water depth are carried out in uniform, open-channel flow and reveal the presence of coherent structures. In the transversal direction, a stationary secondary current composed of two stationary vortices is observed. Compared with a plane disc transducer system, the focalized system increases the resolution by up to 50%.

8.2 Introduction

Acoustic Doppler sonars are increasingly being used in fluid mechanics and hydraulics to investigate such turbulence parameters as turbulence intensities, turbulence scales, Reynolds stress, and turbulence energy dissipation rate. Instruments of this type which are not sensitive to water quality, have been used to analyze flows in open-channels (Lhermitte and Lemmin 1994; Song, and Graf, 1996), lakes and rivers under turbulent flow conditions. More recently, acoustic systems called multistatic ADVP (Acoustic Doppler Velocity Profiler) (Rolland 1994) have been developed, allowing accurate measurements of instantaneous profiles of several velocity components, the study of coherent structures and of secondary currents in multidimensional open-channel flows.

At present, a narrow beam plane-disc transducer, working in piston mode, is typically used as a sound emitter in these instruments. This transducer has the disadvantage that the beam widens with distance from the transducer. Three factors can be identified which reduce the accuracy of the measurements with this system. All of them are directly related to the non-zero opening angle of the emitter acoustic beam. These are: (1) the Doppler ambiguity process, which is related to the transit time of acoustic targets across the measurement volume, (2) the spatial averaging of the velocity field weighted by the sample volume directivity function, and (3) the generation of non-plane wave fronts by the emitter. The Doppler ambiguity process generates a broadening of the turbulence spectrum. The spatial averaging causes an attenuation of higher spectral components limiting the resolution of small scale eddies. The phase distortion of the emitted wave is related to the transducer characteristics.

In order to reduce negative effects of the plane-disc transducer, we investigate the sound beam generation by an annular concave phase array transducer which is not only focused at one fixed point but over the entire measurement depth. This focusing will narrow the beam size and reduce the additional variance due to the non-planeness of the wave. We will identify and quantify the contributions to spectral broadening for the focused transducer and for a plane-disc transducer.

Using the focused transducer, a new configuration of a tristatic sonar will be presented which allows to measure the instantaneous three-dimensional velocity profile over an extended water column. Experimental results in open-channel flow obtained with the system will show its capability to improve the resolution of coherent structures and secondary currents.

8.3 Determination of spectral broadening effects

Turbulence provides the main contribution to spectral width in a 1-D acoustic Doppler spectrum. However, there are additional variance sources unrelated to the velocity field which will cause spectral broadening and will affect the turbulence interpretation in some spectral regions. The total variance can be written as $\sigma^2_{tot} = \sigma^2_{turbulence} + \sigma^2_{ambiguity} + \sigma^2_{phase}$ where $\sigma^2_{ambiguity}$ and σ^2_{phase} represent respectively the variance generated by the Doppler ambiguity process and the variance due to the phase distortion of the transmitted acoustic wave. As mentioned above the spatial averaging process will affect the higher frequency domain of the spectrum. This artifact is not expressed as an additional variance in the Doppler spectrum but appears as an ensemble average of the velocities of all scatterers present in the sample volume, weighted by the directivity function of the emitter. The smaller the size of the sample volume, the less consequence this inherent physical process will have on the measurements. These aspects (Doppler ambiguity and spatial average) were treated by many authors in the field of meteorological radars (Doviak and Zrnic 1993) and it can be shown that the Doppler ambiguity contribution to the total Doppler spectrum is approximated by:

$$\begin{cases} S_{ambiguity}(f) = const. \cdot \exp\left[\dfrac{-f^2}{2 \cdot \sigma^2_{ambiguity}}\right] \\ \\ \sigma^2_{ambiguity} = \dfrac{1}{4}\left(\dfrac{1}{t_x^2} + \dfrac{1}{t_y^2} + \dfrac{1}{t_z^2}\right) + \dfrac{1}{4\pi^2}\left(K_B \overline{\Delta V_r}\right)^2 \end{cases} \tag{8.1}$$

where t_I corresponds to the sample volume transit-times of scatterers in x, y, z-directions, $\vec{K}_B$ is the Bragg wavenumber (where $\vec{K}_B = \vec{K}_s - \vec{K}_i$ with $\vec{K}_s$ the scattered wave vector and $\vec{K}_i$ the incident wave vector) and $\overline{\Delta V_r}$ represents the mean spatially averaged radial-velocity deviation (see definition in Chapter 1). The variable const. is a device dependant constant.

For our conditions the expression of $\sigma^2_{ambiguity}$ can be simplified into:

$$\sigma^2_{ambiguity} = \frac{1}{4t_x^2} \qquad \text{with} \qquad t_x^2 = \left(\frac{\bar{u}}{x_{-3dB}}\right)^2 \tag{8.2}$$

where x_{-3-DB} is the width of the normalized directivity function $H_{norm}(x_{-3-DB})$ at -3 dB point distance from beam axis, $\bar{u}$ represents the mean longitudinal velocity of the flow. Eq (8.2) reveals that only the emitter beam transit time of the scatterers in x-direction , i.e. the direction of mean flow, creates a significant amplitude modulation of the backscattered Doppler signal (assuming a nearly Gaussian shape of the transversale directivity function). Sample volume transit times, in all other directions can be considered as infinitly long.

The term $\overline{\Delta V_r}$ of Eq. (8.1) is the ambiguity induced by the spatial averaging process which increases with turbulence intensity but can be neglected as long as the sample volume size is sufficiently small to avoid large spatial averaging of the spectrum. In acoustic Doppler velocity applications this last effect represents typically 1 to 5 % of the total ambiguity and thus is not considered here.

The term σ^2_{phase} is related to the opening angle of the emitter main beam and the mean radial velocity component of the scatterers inside this lobe weighted by the sample volume directivity function. By making accurate directivity measurements of the transducer we will estimate this angle and evaluate the σ^2_{phase} term by following expression:

$$\sigma^2_{phase} = (\overline{u_x} / x_{-3dB})^2 \cdot \sin^2\gamma \tag{8.3}$$

γ corresponds to the opening half angle of the -3 dB main lobe.

The two parameters ($H_{norm}(x_{-3\text{-}dB})$ and α) needed to quantify the contributions to spectral width by ambiguity and phase distortion variances can be evaluated directly from measurements of backscatter intensity caused by an acoustical test target moving edge-to-edge across the beam of the transducer in a reservoir filled with water which is at rest and free of any turbulence (Fig. 8.1). In this case, the undesired variance terms can be calculated as given above by determining the -3 dB and -6 dB beam widths from these measurements and assuming (reasonably) that the mean velocity of the target through the beam is constant.

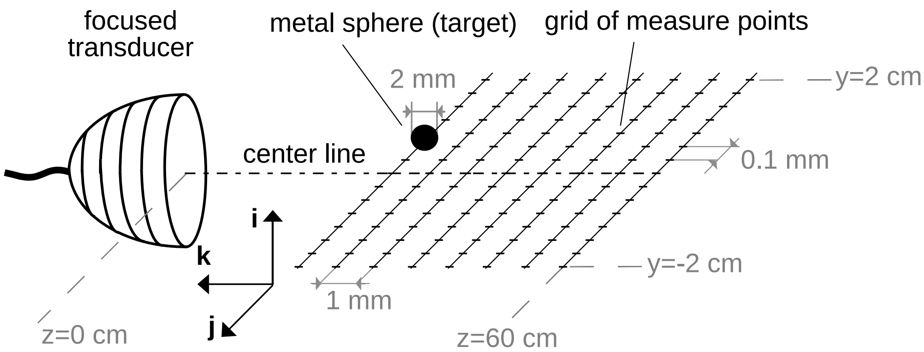

Fig. 8.1 Experimental set-up for beam size measurements.

8.4 The phase array transducer system

The annular concave phase-array transducer has been designed to produce an acoustical beam with a nearly zero degree opening angle γ and a constant directivity function over the entire water column (Arditi et al. 1981). To achieve this, the transducer is composed of several concentric rings. Its cup form produces an initial mechanical focusing similar to an acoustic lens. The radius of curvature is chosen to be approximately one half of the total range of interest (Fig. 8.2). In our case the maximum investigated depth has been fixed to Z_{max} = 60 cm. Thus the curvature radius is taken as R $=Z_{max}$ / 2 = 30 cm.

Additional focusing is provided by electrically controlling the time delay of the sound pulse emission between the different rings. To concentrate the beam at a distance Z_{foc} from the transducer face, the time delay between sound pulses emitted from the j^{-th} ring and the central element is given by:

$$\Delta t_j = \frac{a_j^2\left(\frac{1}{R} - \frac{1}{Z_{foc}}\right)}{2c} \tag{8.4}$$

where c is the speed of the acoustic wave in the medium. This equation is valid if the maximum radius a_N satisfies the following condition:

$$\left(\frac{a_N}{Z_{foc}}\right)^2 << 1 \tag{8.5}$$

a_j represents the mean ring radius with an internal radius a_{j1} and an external radius a_{j2}:

$$a_j = \sqrt{\frac{a_{j1}^2 + a_{j2}^2}{2}} \tag{8.6}$$

The present transducer is composed of one central element and four concentric rings around it. With this transducer, a constant beam width over the entire depth range Z_{max} can only be produced by splitting Z_{max} into four different working zones along the beam axis (Fig. 8.2a). Only one zone is focused at a time. The geometrical characteristics of the transducer, and the time delays between pulses emitted from the different rings and the central element which are needed for the beam focusing in each of these zones are summarized in Table 8.1.

Zone	Z (mm) Min/max	Z_{foc} (mm)	N° of Used Elements	External radius a_N (mm)	Δt_1 (ns)	Δt_2 (ns)	Δt_3 (ns)	Δt_4 (ns)	Δt_5 (ns)
1	100 / 150	116.6	1	12.2	0	NC	NC	NC	NC
2	150 / 250	183.3	1 & 2	22.5	186	0	NC	NC	NC
3	250 / 400	300.0	1 to 3	34.0	0	0	0	NC	NC
4	400 / 600	466.7	1 to 5	50.0	0	105	302	567	835

Table 8.1 Parameters of the focused transducer (NC means Not Connected).

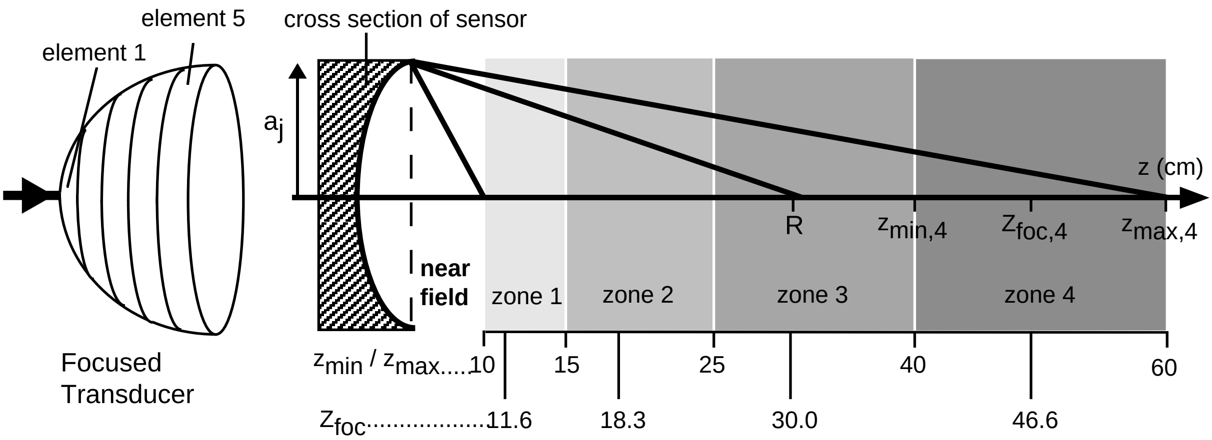

(a)

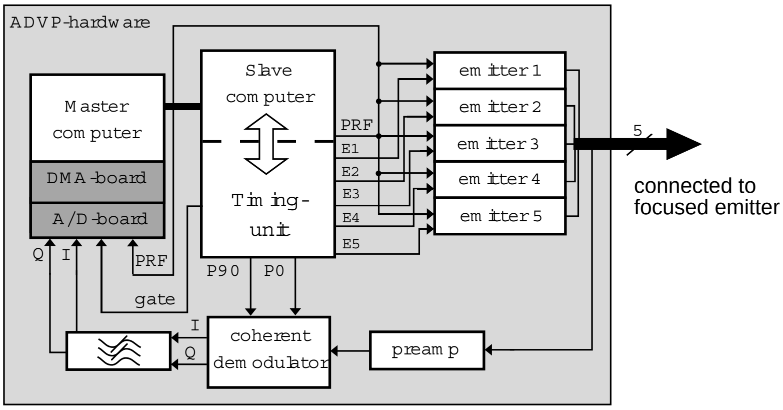

(b)

Fig. 8.2 (a) The curved concentric annular phase array transducer and the four focusing zones, (b) the beam focusing electronics.

The hardware for beam focusing of the ADVP is shown in Fig. 8.2b. Each ring element of the transducer is supplied with a sound pulse generated by a separate high power emitter circuit which is controlled by the timing unit through the following two-digital signals: Firstly, the PRF (Pulse Repetition Frequency) signal ensures a high impedance entrance of the preamplifier to avoid signal saturation during the emission period. Secondly, the signals E0 to E5 directly command the push-pull circuit of each emitter. These signals are phase shifted, as indicated in Table 8.1, in order to focus the beam over the desired zone. Only the central element 1 works as the receiver of the backscattered signal from the test target in all measurements. The received signal is then amplified, demodulated in a phase coherent way and low-pass filtered to obtain the inphase and the quadrature part of the Doppler signal. These signals are digitized and stored in the master computer for further treatment.

8.5 Acoustic beam size measurements

In order to evaluate the focusing efficiency, the acoustic field measured for the new annular curved phase array transducer is compared with that of a plane-disc transducer under the same conditions. The directivity measurements of both transducers are realized in the monostatic mode where the transducer is used as a transmitter of the incident wave and as a receiver. For the beam width measurements, the chosen target is a metal sphere with a given value for the parameter $ka = (2\pi/\lambda) \cdot a$ where k is the wave number of the transmitted wave, a the radius of the sphere (2 mm) and λ the wavelength. Since the backscattered intensity varies strongly with that parameter, an accurate measure of the beam size can be obtained. The resultant – 6 dB acoustic fields of the two transducers are shown in Fig. 8.3. The positive effect of the focusing system over the whole measurement range is obvious. All along the beam, the opening angle γ remains nearly zero. This will practically eliminate any contribution of the variance σ^2_{phase} for the focused transducer. For the plane-disc transducer, an opening angle $\gamma = 1.8°$ was measured. For a horizontal velocity of 30 cm/s (i.e. perpendicular to the emitter axis), this will result in $\sigma^2_{phase} = 0.62\ cm^2s^{-2}$. This value is close to the one given by Lhermitte and Lemmin (1994) for a similar transducer.

To estimate $\sigma^2_{ambiguity}$, the methodology presented in section 2 was applied. For the same velocity as above, the variance due to the amplitude modulation is approximately equal to $0.36\ cm^2s^{-2}$ for the plane-disc transducer and equal to $0.55\ cm^2s^{-2}$ for the focused transducer. The latter value is greater due to the strong reduction in volume size for the focused beam. This reduction increases the directivity function variance which is proportional to the square of the inverse transit time.

However, the advantage is that this variance remains constant over the whole measuring range and since σ^2_{phase} is irrelevant, the total undesired variance of the phase array transducer is decreased to 45% of the plane disc contributions. For the focalized transducer, velocity variance estimations all along the beam axis can be corrected by the same constant value. This is not possible for the plane-disc transducer because the variance varies greatly with distance along the beam (from $0.024\ cm^2s^{-2}$ to $0.55\ cm^2s^{-2}$) and no efficient adjustment can be realized.

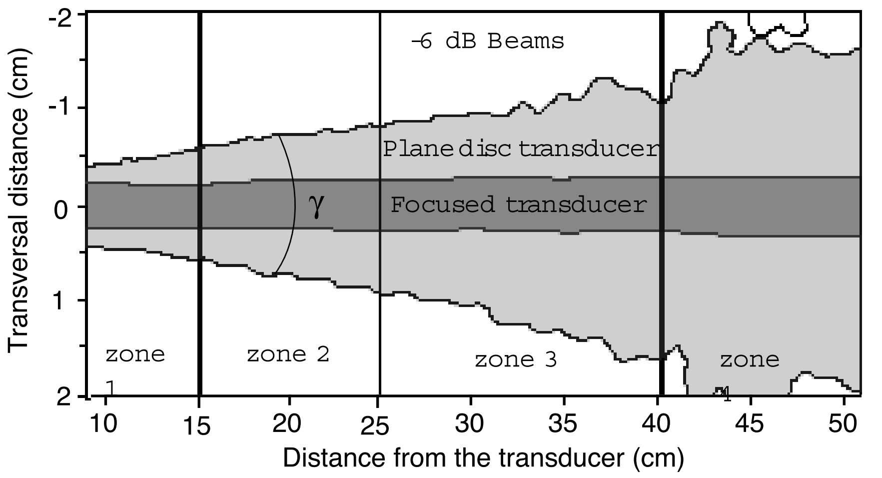

Fig. 8.3 – 6 dB acoustic beams of the plane-disc transducer and the focused transducer.

A further advantage of the phase array emitter is the considerable increase of the backscattered signal amplitude. This is evident when comparing the normalized backscattered intensity on the main axis of the two transducers (Fig. 8.4). For the focalized transducer, the signal increases from one zone to the next due to the increasing number of ring elements used (Table 8.1). For the plane-disc transducer, the well-known farfield attenuation along the beam axis is observed. In zone 4, this leads to an improvement of 15 dB for the main lobe signal amplitude of the focalized transducer. No attenuation compensation amplification is needed with the new transducer.

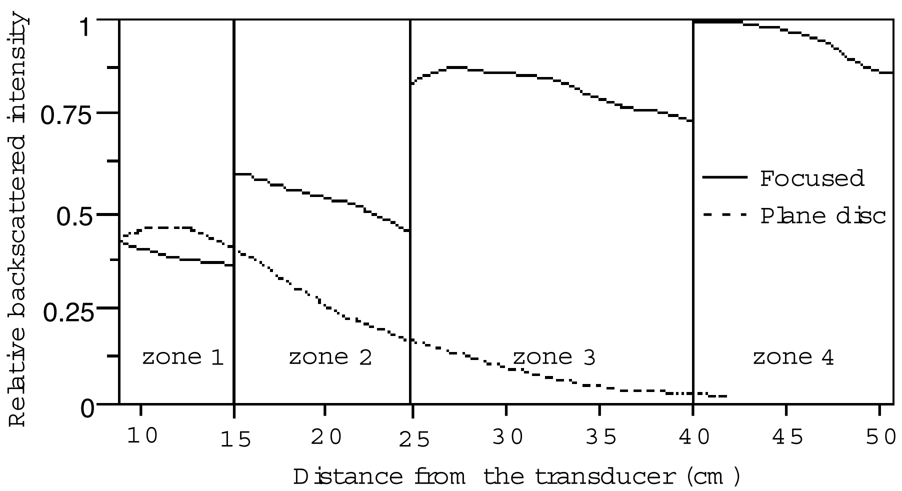

Fig. 8.4 Normalized backscattered intensity distribution on the main axis.

8.6 Configuration of the 3-D Acoustic Doppler Velocity Profiler system (ADVP)

The 3-D ADVP is composed of the 1 MHz focused emitter (TRA) discussed above which is installed vertically in the center and four 1 MHz large angle receivers placed symmetrically around it (see Fig. 7.3). The latter are used to measure the four velocity components in the tilted directions, TRB, TRC, TRD, and TRE. For the data analysis, the system is split into two tristatic subsystems. The first one is oriented in the longitudinal plane (TRA, TRB, TRC) of the flow, and measures the vertical and longitudinal instantaneous velocity profiles over the whole water depth. The second one is oriented in the transversal direction (TRA, TRD, TRE) of the flow, and allows to measure the vertical and transversal instantaneous velocity profiles. The redundancy in the vertical velocity information is used to verify the symmetry of the receiver positions (distances D_{0+} and D_{0-} in Fig. 7.3).

The vertical position of the focused emitter in the transducer housing has been adapted to the water depth. Zone 4 has been selected to cover the entire water depth in the open-channel flow which in the present application is equal to 20 cm. In order to generate the desired narrow beam with a nearly zero opening angle, all five concentric annular rings of transducer TRA must be excited by the phase shifted electrical signals defined in Table 8.1 for zone 4.

8.7 A laboratory application

The experiments were carried out in uniform flow in a laboratory open-channel (29m long, 2.45m wide) with a sand bed (mean grain size 2 mm). The ADVP is installed in a downstream section where turbulent flow is well developed. The transducer chamber is separated from the flow in the channel by a Mylar window which is adjusted to provide contact at the surface of the channel flow and to minimize the disturbance of the channel flow.

In the first experiment, data were taken in the center of the open-channel with a resolution of 10 Hz. In order to investigate the dynamics of coherent flow structures, the two components of the Reynolds stress tensor, the longitudinal u'w' covariance term and the transversal v'w' covariance term, were extracted. The importance of coherent structures in generating intermittent regions of high u'w' was already shown previously under different flow conditions (Shen and Lemmin 1997). The data were then filtered for four different velocity quadrants where quadrant 1 represents events with $u'>0$ and $w'>0$, quadrant 2 those events with $u'<0$ and $w'>0$, etc.

The time evolution of the two components of the Reynolds stress tensor over a 30 s period is given in Fig. 8.5. Events of coherent flow structures are evident in this figure as bands of high covariance extending over most of the water column height. For the u'w' term in Fig. 8.5a, fewer events are found in quadrant 1 and quadrant 3 than in quadrants 2 and 4 which confirms previous observations. The v'w' term, measured for the first time, is of the same order of magnitude as the u'w' term but varies at a higher frequency (Fig. 8.5b). The v'w' term also shows a more uniform distribution over all four quadrants. This corresponds to theoretical predictions which indicate that the coherent structures in the longitudinal direction require mass compensation in the transversal direction (Nezu and Nakagawa 1993). The organized behaviour of the flow is again apparent in Fig. 8.6 where the 2-D longitudinal fluctuating velocity field V'(u'(t),w'(t)) of the same data set is presented for a 3 s period. Regions of high velocity are always found to be oriented in quadrants 2 and 4. Low velocity regions vary more randomly in direction.

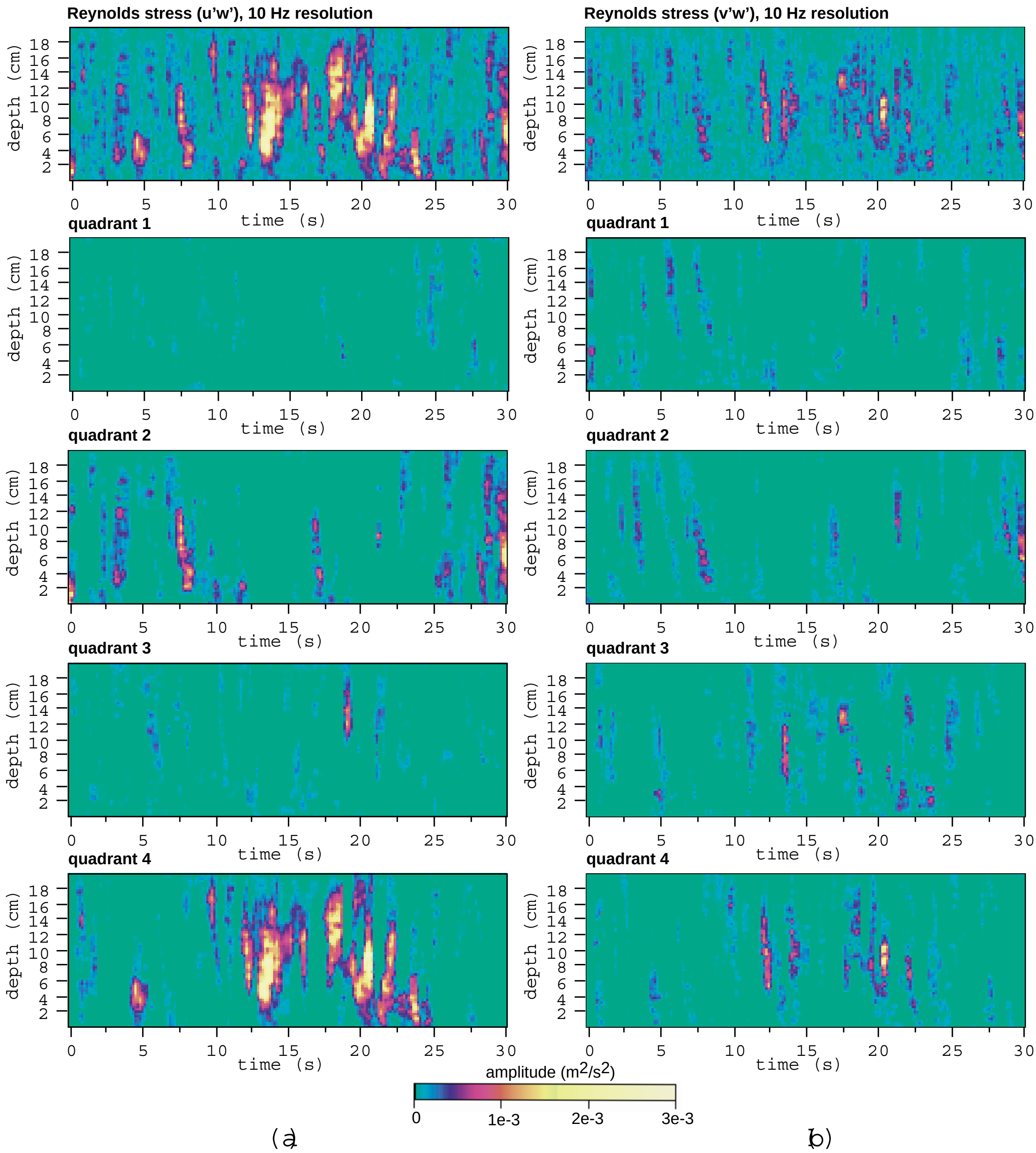

Fig. 8.5 (a) Time series of covariance term u'w' with quadrant selection, (b) Time series of covariance term v'w' with quadrant selection.

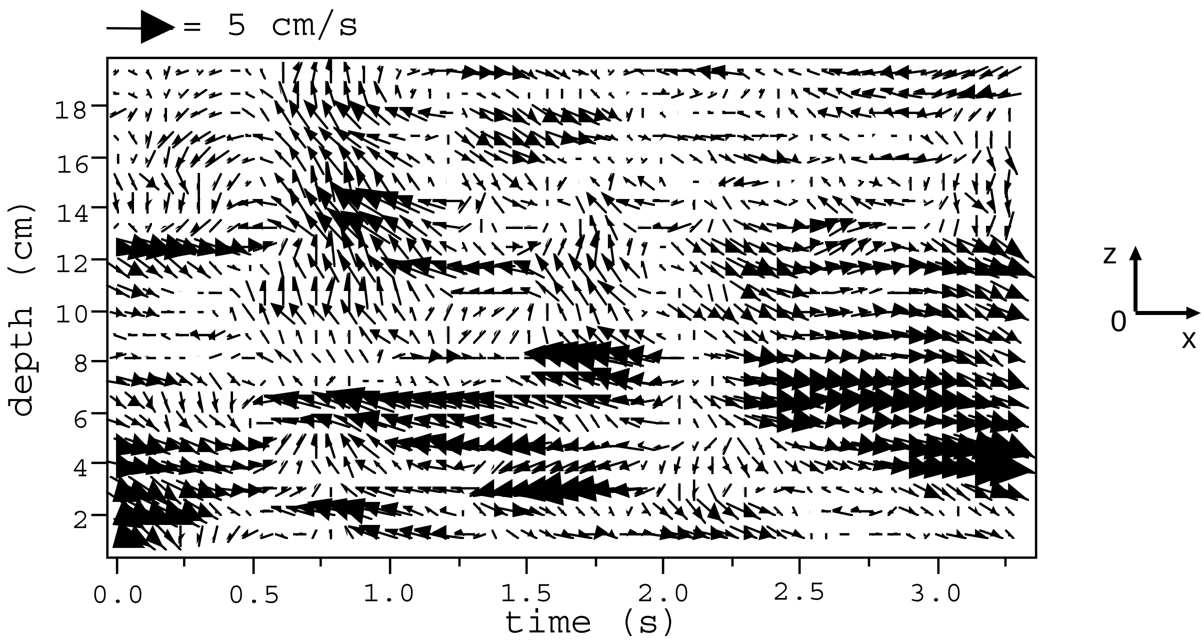

Fig. 8.6 Time series of 2-D fluctuating velocityvector $\vec{V}'(u'(z,t), w'(z,t))$ with 10 Hz resolution.

In a second experiment in the same channel, the velocity field in a transversal plane of the channel was investigated. Considering that the flow is symmetrical with respect to the center of the channel, measurements were only made in one half-plane. For this purpose, a sequence of ADVP-profiles was taken at 16 equally spaced positions between the center of the channel and a sidewall. In each position, a full 3-D velocity profile was recorded. From these data, profiles of the mean 2-D velocity vector $\vec{\mathbf{V}}(\overline{v};\overline{w})$ were extracted for each position and assembled for the transversal half-plane (Fig. 8.7). The data reveal the presence of two stationary counterclockwise turning vortices, rotating at a very low velocity. Their axes are aligned with the channel axis. Good agreement is found between the vortex dimensions and the velocity magnitude observed here and those predicted by numerical simulation for a flow field in a channel with an aspect ratio of B/h equal to 13 (Naot and Rodi 1982; Nezu and Nakagawa 1993), where B is the width of the channel and h the water depth. For our observations, we find B/h=12.

The above examples demonstrate the high spatial and temporal resolution that is possible due to the improvements in the S/N ratio obtained with the focused transducer. Compared to previous measurements with a plane-disc transducer both resolutions have been improved by 50%. Details of hydraulic aspects of the data presented here will be discussed elsewhere.

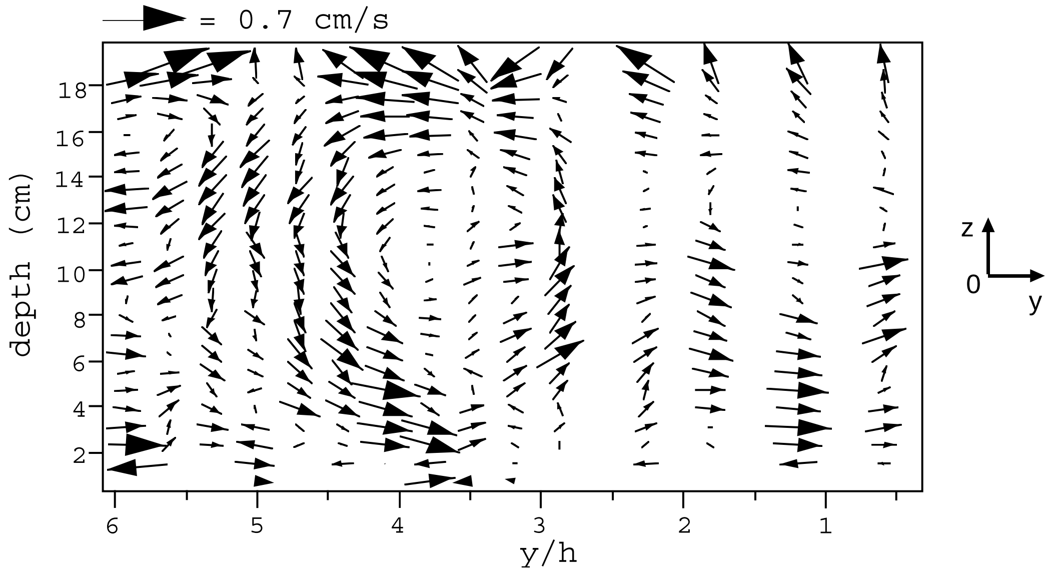

Fig. 8.7 Mean 2-D velocity vector $\vec{V}(\overline{v};\overline{w})$ across one half cross section of the channel. The channel axis is at y/h=0.

8.8 Conclusions

A novel 3-D acoustic Doppler velocity profiler using a focused emitter has been developed to measure the instantaneous 3-D velocity profile over the whole investigated water column. The acoustic beam size measurements of the focused transducer show an important decrease of the lateral size of the sample volume at long distances. A nearly zero opening angle over a depth range of 60 cm indicates that the proposed electrical beam focusing works well. The focusing provides for cleaner signals. The resultant improvement in the S/N ratio allows for a significant increase in the spatial and temporal resolution of the velocity measurements (about 50%) compared to a system with a standard plane-disc transducer.

Experiments carried out in open-channel flow show that coherent structures, secondary currents in transversal direction to the flow and turbulence parameters in the inertial subrange can be properly resolved and that measurements are not affected by water quality. Ejection and sweep events can be analyzed quantitatively in great detail with the present system. Therefore this system permits new approaches in experimental investigations advancing the understanding of complex hydrodynamic processes. Recently, a 3-D ADVP system based on the one described here has been developed for field measurements in shallow rivers.

8.9 References

Arditi, M. et al. (1981) Transient fields in concave annular arrays. Ultrasonic Imaging 3 37-61.

Doviak, R. and Zrnic, D. (1993) Doppler radar and weather observations. Academic Press, Inc.

Lemmin, U. and Rolland, T. (1997) Acoustic velocity profiler for laboratory and field studies. J. Hydraulic Eng. (ASCE) 123 1089-1098.

Lhermitte, R. and Lemmin, U. (1994) Open-channel flow and turbulence measurement by high-resolution Doppler sonar. JAOTech. 11(5) 1295-1308.

Naot, D. and Rodi W. (1982) Calculation of secondary currents in channel flow. J. Hydraulic Div. (ASCE) 108 948-968.

Nezu, I. and Nakagawa, H. (1993) Turbulence in open-channel flows. IAHR Monograph series (Rotterdam: Balkema).

Rolland, T. (1994) Développement d'une instrumentation Doppler ultrasonore adaptée à l'étude hydraulique de la turbulence dans les canaux. PhD dissertation No 1281, Swiss Federal Institute of Technology, Lausanne.

Shen, C. and Lemmin, U. (1997) A two-dimensional acoustic sediment flux profiler. Meas. Sci. Technol. 8 880-884.

Song, T. and Graf, W. H. (1996) Velocity and turbulence distribution in unsteady open-channels flows. JHE 122 141-154.

CHAPTER 9

A CORRECTION METHOD FOR TURBULENCE MEASUREMENTS WITH A 3-D ACOUSTIC DOPPLER VELOCITY PROFILER

Published in Journal of Atmospheric and Oceanic Technology (2001), Vol. 18 No. 3, pp. 446-458

9.1 Abstract

A correction method of mean turbulence measurements from a 3-D Acoustic Doppler Velocity Profiler is proposed. This method does not require any hypothesis on the flow characteristics nor does it depend on device dependent parameters. It is based on a noise spectrum reconstruction from cross-spectra evaluations of two independent and simultaneous measurements of the same vertical velocity component over the whole water depth. The noise spectra and the noise variances are calculated and removed for the three fluctuating velocity components measured in turbulent open-channel flow. The uncorrected turbulence spectra show the flat high frequency regions typical for noise effects. This effect is more pronounced for the horizontal velocity components. The corrected turbulence spectra show a –5/3 slope over the whole inertial subrange delimited by the frequency band of the device.

The corrected profiles of turbulence intensities, turbulent kinetic energy, shear stress, turbulent energy balance equation terms such as the production, transport and dissipation, are compared to the uncorrected data, different semi-theoretical formula and other measurements from the literature.

Combined with the use of a phase array emitter, the proposed correction method allows measurements with a relative error under 10% in the outer flow region. The corrected inner flow region measurements are still affected by errors which may originate from spatial averaging effects within the sample volume due to the high local velocity gradient or the lack of validity of the universal laws concerning turbulence quantities over a rough bed.

9.2 Introduction

Over the past decades, high resolution multistatic ultrasonic velocity profilers working with coherent demodulation of the backscattered Doppler phase have found an increasing interest in the fields of fluid dynamics, physical oceanography and more recently, sediment transport and river hydrodynamics. They have shown their advantage particularly in field applications where the presence of particulate matter often does not allow measurements by other techniques.

In all turbulent flows the accuracy and the identification of noise sources are of great importance. In this respect, the mean flow can be treated separately from the turbulent component. When classical hydraulic mean flow characteristics are estimated from high resolution sonar data, the accuracy of the measurements is typically better than 4% (Rolland (1994); Lemmin and Rolland (1997)) confirming their high reliability. The remaining error is mainly due to the accuracy of positioning the sensors.

Noise effects are of particular importance if turbulence measurements are evaluated because they are directly based on the fluctuating quasi-instantaneous velocity field estimation. In that case several mechanisms inherent to the measurement technique may reduce the accuracy. Several authors, Garbini et al. (1982), Lhermitte and Lemmin (1994), Voulgaris and Trowbridge (1998), have worked on the theoretical and experimental identification of the noise sources affecting the turbulence measurements with ultrasonic Doppler velocity profilers.

These undesired physical processes can be classified as follows: (1) the Doppler ambiguity process which is characterized by the amplitude modulation of the backscattered signal related to the transit time of the acoustical targets through the measurement volume. (2) The spatial averaging of the instantaneous velocity field (a large number of targets are present instantaneously) which is taken over the sample volume weighted by the directivity function of the emitter. (3) The effect of the mean flow shear stress present within the sample volume. (4) The phase distortion effect of the emitted front wave. (5) The effect of those turbulent scales which are of the same order of magnitude or smaller than the sample volume's transverse size. (6) The electronic circuitry's sampling errors linked to the A/D-conversion.

Except for the spatial averaging process (2), all other noise sources enter as additional variance terms in the measured fluctuating velocities variances and therefore are statistically independent. Due to the geometrical configuration of the sensors these noise variances have different values dependent on which component (longitudinal, vertical or transverse) is measured. This relates to different weighting factors for the total noise variance common to all components, as will be shown later.

Correction methods for the mean turbulence measurements expressed as additional variances broadly fall into two-different categories:

9.2.1 Indirect correction method

This method is most frequently used (Lhermitte and Lemmin (1994), Zedel et al. (1996)). The different noise variance terms are estimated as a function of the sample volume’s distance from the sensors (processes (1), (3), (4), (5) above). They are added together to form the total noise variance, and a factor is applied to each component to remove the corresponding term from the measured variance. Three main disadvantages can be identified:

The evaluation of the different noise variances is based on assumptions about specific flow conditions. Variance (3) is calculated by assuming the logarithmic distribution of the mean longitudinal velocity profile. Variance (5) requires the knowledge of the turbulence dissipation rate (Cabrera et al. (1987)), often computed from expressions valid for isotropic turbulence.

The transverse size of the sample volume has to be known (Voulgaris and Trowbridge (1998)) to calculate variances (1), (4) and (5). It can either be estimated from acoustical beam approximations or be measured directly (Lhermitte and Lemmin (1994)). The noise term related to (6) also has to be evaluated from additional measurements (Zedel et al. (1996)) because an expression for the phase resolution uncertainty can not be established.

No direct correction of the turbulence power spectral density is possible even if the noise variances are evaluated correctly.

9.2.2 Correction method based on two point cross-correlation

This method, proposed by Garbini et al. (1982) assumes that the noise signals (variances (1), (3), (4), (5)) between two points in the velocity profile are uncorrelated. It should be noted that Garbini et al. (1982) used a monostatic ADVP (Acoustic Doppler Velocity Profiler), where one transducer serves as emitter and receiver. In that case the cross-correlation has to be applied to two spatially separated volumes in the velocity profile to ensure that the noise processes are uncorrelated.

The advantage is that it can directly be applied to measured data and does not require any prediction as does the indirect correction method. The disadvantage is that the target population in the two sample volumes, to which the cross-correlation is applied, has to be different to ensure the decorrelation. The existence of overlapping regions between two consecutive volumes in the profiles which have to be inclined with respect to the flow direction, limits the decorrelation of the noise part. The method is applied to two volumes separated by one measuring volume, which decreases the noise but in turn also attenuates the desired velocity signal. Our experience has shown that this method cannot be used with multistatic Doppler systems.

In the present paper, a correction method is presented to reduce the effects of variances (1), (3), (4), (5), (6). The main contribution to noise reduction presented here concerns a direct treatment of the data similar the one proposed by Garbini et al. (1982). The essential difference is that it can be used with a multistatic 3-D-ADVP sensor configuration. We will discuss the efficiency of the method as function of the flow depth in boundary layer applications such as open-channel flow where the improvement can be compared against the exsisting universal laws.

9.3 Description of the 3-D-ADVP

9.3.1 General principle

The 3-D ADVP is composed of the 1 MHz focused phase array emitter (TRA), discussed in Chapter 8. The effects of process (2) and variance (4) cited in the introduction can be significantly reduced due to the use of this transducer.

Four 1 MHz large angle receivers are placed symmetrically around the emitter (see Fig. 7.3). They are used to obtain the velocity components in the tilted directions, TRB, TRC, TRD, and TRE. For the data analysis, the system is divided into two independently working multistatic subsystems (each multistatic system is composed of two bistatic configurations). The first subsytem is oriented in the longitudinal plane (TRA, TRB, TRC) of the flow, and measures the vertical and longitudinal instantaneous velocity profiles over the whole water depth. The second one is oriented in the transverse direction (TRA, TRD, TRE) of the flow, and allows to measure simultaneously with the longitudinal plane the vertical and transverse instantaneous velocity profiles.

The 3-D velocity vector components are shown in Fig. 7.4. The Doppler frequency corresponding to each sample volume R_j (j=1…M) is calculated using the pulse-pair algorithm (Lemmin and Rolland (1997)). For each of the two multistatic subsystems, the two local Doppler frequencies ($f_{D1,j}$ and $f_{D2,j}$ for the longitudinal system, $f_{D3,j}$ and $f_{D4,j}$ for the transverse system) are:

$$f_{D1,j} = \frac{2f_0}{c}\cos(\alpha_{1,j}/2)\cdot V_{1,j} \qquad f_{D3,j} = \frac{2f_0}{c}\cos(\alpha_{3,j}/2)\cdot V_{3,j}$$
$$f_{D2,j} = \frac{2f_0}{c}\cos(\alpha_{2,j}/2)\cdot V_{2,j} \qquad f_{D4,j} = \frac{2f_0}{c}\cos(\alpha_{4,j}/2)\cdot V_{4,j} \tag{9.1}$$

where $V_{i,j}$, are the projections of the local instantaneous velocity $\mathbf{V}_j$ on the Bragg wave number vectors $\mathbf{K}_{Bi,j}$ with i=1…4 and j=1…M. From these Doppler frequencies we can determine the longitudinal, transverse and two vertical components of the quasi-instantaneous velocity vector over the whole insonified water column as

$$u_j = \frac{c}{2f_0 \sin\alpha_{1,j}}\left[f_{D1,j} - f_{D2,j}\right] \qquad v_j = \frac{c}{2f_0 \sin\alpha_{3,j}}\left[f_{D3,j} - f_{D4,j}\right]$$
$$w_{j,t} = \frac{c}{2f_0(1+\cos\alpha_{3,j})}\left[f_{D3,j} + f_{D4,j}\right] \qquad w_{j,l} = \frac{c}{2f_0(1+\cos\alpha_{1,j})}\left[f_{D1,j} + f_{D2,j}\right] \tag{9.2}$$

where l denotes the longitudinal tristatic subsystem and t the transverse one. f_0 is the emitted sound wave frequency and c the speed of sound for our water condition. It is noted that two independent estimates of the vertical velocity are obtained simultaneously with this system.

The temporal resolution is fixed by PRF and by the number N_{pp} of consecutive samples needed to estimate a quasi-instantaneous velocity by the pulse-pair algorithm. The corresponding Nyquist frequency is $PRF/2/N_{pp}$ (in our case equal to 666.67 / 2 / 16) ≅ 20.84 Hz).

9.3.2 Expression of mean turbulence characteristics in terms of geometrical configuration and noise

The measured mean turbulent characteristics which can be expressed as function of the multistatic configuration (subscript i) and as a function of the measurement position (subscript j) can be written as the sum of the true quantity and the noise contribution. The measured fluctuations of the radial velocities can be composed as:

$$\left\langle V'_{i,j}\right\rangle(t) = \left\langle \tilde{V}'_{i,j}\right\rangle(t) + \left\langle n_{i,j}\right\rangle(t) \tag{9.3}$$

All terms are quasi-instantaneous quantities. The fluctuating quantities are noted by a prime. < > indicates spatial averaging weighted by the transducer's directivity function. The tilde denotes the true flow quantities. The term $n_{i,j}(t)$ is the instantaneous noise signal for component i at location j.

As suggested by Lohrmann et al. (1995), the following assumptions are made concerning the noise signal:

- the noise signal has a flat power spectral density over the investigated frequency band PRF / 2 / Npp (white noise)
- it is unbiased
- it is statistically independent of the velocity fluctuations
- it is uncorrelated between the different radial components i.

The validity of these assumptions will be demonstrated as part of the verification of the method.

Variances:

The variance of the radial velocity components is given by:

$$\overline{\left\langle V_{i,j}'^2 \right\rangle} = \overline{\left\langle \tilde{V}_{i,j}'^2 \right\rangle} + \left\langle \sigma_{i,j}^2 \right\rangle \tag{9.4}$$

where the second term of the right member of Eq (9.4) is the variance of the noise signal.

The velocity variances can then be written as:

$$\begin{cases} \overline{\left\langle u_j'^2 \right\rangle} = \dfrac{1}{4\sin^2(\alpha_j/2)}\left(\overline{\left\langle V_{1,j}'^2 \right\rangle} + \overline{\left\langle V_{2,j}'^2 \right\rangle} - 2\overline{\left\langle V_{1,j}' \right\rangle\left\langle V_{2,j}' \right\rangle}\right) = \overline{\left\langle \tilde{u}_j'^2 \right\rangle} + \dfrac{1}{2\sin^2(\alpha_j/2)}\left\langle \sigma_j^2 \right\rangle \\ \overline{\left\langle v_j'^2 \right\rangle} = \dfrac{1}{4\sin^2(\alpha_j/2)}\left(\overline{\left\langle V_{3,j}'^2 \right\rangle} + \overline{\left\langle V_{4,j}'^2 \right\rangle} - 2\overline{\left\langle V_{3,j}' \right\rangle\left\langle V_{4,j}' \right\rangle}\right) = \overline{\left\langle \tilde{v}_j'^2 \right\rangle} + \dfrac{1}{2\sin^2(\alpha_j/2)}\left\langle \sigma_j^2 \right\rangle \\ \overline{\left\langle w_{j,1}'^2 \right\rangle} = \dfrac{1}{4\cos^2(\alpha_j/2)}\left(\overline{\left\langle V_{1,j}'^2 \right\rangle} + \overline{\left\langle V_{2,j}'^2 \right\rangle} + 2\overline{\left\langle V_{1,j}' \right\rangle\left\langle V_{2,j}' \right\rangle}\right) = \overline{\left\langle \tilde{w}_j'^2 \right\rangle} + \dfrac{1}{2\cos^2(\alpha_j/2)}\left\langle \sigma_j^2 \right\rangle \end{cases} \tag{9.5}$$

to obtain:

$$\begin{cases} \overline{\langle u_j'^2 \rangle} = \overline{\langle \tilde{u}_j'^2 \rangle} + a_j \langle \sigma_j^2 \rangle \\ \overline{\langle v_j'^2 \rangle} = \overline{\langle \tilde{v}_j'^2 \rangle} + a_j \langle \sigma_j^2 \rangle \\ \overline{\langle w_{j,1}'^2 \rangle} = \overline{\langle \tilde{w}_j'^2 \rangle} + b_j \langle \sigma_j^2 \rangle \end{cases} \tag{9.6}$$

assuming that $\alpha_{1,j} = \alpha_{2,j} = \alpha_{3,j} = \alpha_{4,j} = \alpha_j$ and $\langle \sigma_{i,j}^2 \rangle = \langle \sigma_j^2 \rangle$. This implies that the receiver transducers are identical and ideal. This hypothesis will be verified in section 9.6.1 The coefficients a_j and b_j are related to the geometrical configuration of the 3-D-ADVP (represented in Fig. 7.3; Table 9.1).

z/h [-]	dj [cm]	αj [°]	aj [-]	bj [-]	aj+bj/2 [-]
0.97	22.9300	24.4172	11.1806	0.5234	11.4423
0.94	23.2550	24.1324	11.4421	0.5228	11.7035
0.90	23.5850	23.8543	11.7065	0.5223	11.9676
0.87	23.9100	23.5827	11.9737	0.5218	12.2346
0.84	24.2300	23.3175	12.2437	0.5213	12.5044
0.81	24.5550	23.0540	12.5213	0.5208	12.7817
0.78	24.8800	22.8008	12.7972	0.5203	13.0573
0.75	25.2050	22.5491	13.0806	0.5199	13.3405
0.71	25.5300	22.3072	13.3622	0.5194	13.6219
0.68	25.8500	22.3072	13.3622	0.5194	13.6219
0.65	26.1750	22.0665	13.6515	0.5190	13.9110
0.62	26.4950	21.8312	13.9438	0.5186	14.2031
0.59	26.8200	21.6047	14.2341	0.5182	14.4932
0.56	27.1400	21.3793	14.5323	0.5178	14.7912
0.53	27.4600	21.1587	14.8334	0.5174	15.0921
0.50	27.7850	20.9426	15.1375	0.5171	15.3960
0.46	28.1050	20.7311	15.4445	0.5167	15.7029
0.43	28.4250	20.5239	15.7545	0.5164	16.0127
0.40	28.7450	20.3209	16.0675	0.5161	16.3255
0.37	29.0650	20.1219	16.3834	0.5157	16.6413
0.34	29.3850	19.9269	16.7024	0.5154	16.9601
0.31	29.7050	19.7357	17.0242	0.5151	17.2818
0.28	30.0250	19.5483	17.3491	0.5148	17.6065
0.25	30.3450	19.3644	17.6769	0.5146	17.9341
0.22	30.6650	19.1840	18.0076	0.5143	18.2648
0.18	30.9850	19.0041	18.3470	0.5140	18.6040
0.15	31.3050	18.8305	18.6837	0.5137	18.9406
0.12	31.6250	18.6601	19.0234	0.5135	19.2802
0.09	31.9400	18.4901	19.3719	0.5132	19.6285
0.06	32.2600	18.3258	19.7176	0.5130	19.9741
0.03	32.5800	18.1646	20.0662	0.5128	20.3226

Table 9.1 Constants depending on the geometrical configuration. The first three columns are the normalized water depth, the distance from the emitter and the Doppler angle, respectively. The last three columns are the noise weighting factors for the vertical, horizontal turbulence variances and for the turbulence kinetic energy, respectively

In Table 9.1, the variables d_j and α_j represent the distances of the measurement point j from the emitter and the Doppler angle at measurement point j, respectively. The horizontal velocity components are much more affected by noise (due to the geometrical configuration) than the vertical component. Furthermore, the weighting factors for the vertical component are nearly independent of the location j, while the factors affecting the variances of the horizontal components change strongly.

Kinetic energy:

The kinetic energy can be expressed as:

$$\left\langle K_j \right\rangle = \left\langle \tilde{K}_j \right\rangle + (a_j + b_j/2)\left\langle \sigma_j^2 \right\rangle \quad \text{with} \quad \left\langle K_j \right\rangle = 1/2\left(\overline{\left\langle u_j'^2 \right\rangle} + \overline{\left\langle v_j'^2 \right\rangle} + \overline{\left\langle w_{j,l}'^2 \right\rangle}\right) \tag{9.7}$$

Reynolds stress terms and tri-covariances:

With the same approach as outlined above, we obtain the Reynolds stress and tri-covariance terms entering in the turbulent energy balance equation for a 2-D mean flow:

$$\overline{\left\langle u_j' w_{j,l}' \right\rangle} = \frac{1}{2\sin(\alpha_j)}\left(\overline{\left\langle \tilde{V}_{1,j}'^2 \right\rangle} - \overline{\left\langle \tilde{V}_{2,j}'^2 \right\rangle}\right) = \overline{\left\langle u_j' w_{j,l}' \right\rangle} \tag{9.8}$$

$$\begin{cases} \overline{\left\langle u_j'^3 \right\rangle} = \dfrac{1}{8\sin^3(\alpha_j/2)}\left(\overline{\left\langle \tilde{V}_{1,j}'^3 \right\rangle} - \overline{\left\langle \tilde{V}_{2,j}'^3 \right\rangle} + 3\overline{\left\langle \tilde{V}_{1,j}'^2 \right\rangle\left\langle \tilde{V}_{2,j}' \right\rangle} - 3\overline{\left\langle \tilde{V}_{2,j}'^2 \right\rangle\left\langle \tilde{V}_{1,j}' \right\rangle}\right) = \overline{\left\langle u_j'^3 \right\rangle} \\ \overline{\left\langle v_j'^3 \right\rangle} = \dfrac{1}{8\sin^3(\alpha_j/2)}\left(\overline{\left\langle \tilde{V}_{3,j}'^3 \right\rangle} - \overline{\left\langle \tilde{V}_{4,j}'^3 \right\rangle} + 3\overline{\left\langle \tilde{V}_{3,j}'^2 \right\rangle\left\langle \tilde{V}_{4,j}' \right\rangle} - 3\overline{\left\langle \tilde{V}_{3,j}'^2 \right\rangle\left\langle \tilde{V}_{4,j}' \right\rangle}\right) = \overline{\left\langle v_j'^3 \right\rangle} \\ \overline{\left\langle w_{j,l}'^3 \right\rangle} = \dfrac{1}{8\cos^3(\alpha_j/2)}\left(\overline{\left\langle \tilde{V}_{1,j}'^3 \right\rangle} + \overline{\left\langle \tilde{V}_{2,j}'^3 \right\rangle} + 3\overline{\left\langle \tilde{V}_{1,j}'^2 \right\rangle\left\langle \tilde{V}_{2,j}' \right\rangle} + 3\overline{\left\langle \tilde{V}_{2,j}'^2 \right\rangle\left\langle \tilde{V}_{1,j}' \right\rangle}\right) = \overline{\left\langle w_{j,l}'^3 \right\rangle} \end{cases} \tag{9.9}$$

$$\begin{cases} \overline{\left\langle u_j'^2 w_{j,l}' \right\rangle} = \dfrac{1}{4\sin(\alpha_j)\sin(\alpha_j/2)}\left(\overline{\left\langle \tilde{V}_{1,j}'^3 \right\rangle} + \overline{\left\langle \tilde{V}_{2,j}'^3 \right\rangle} - \overline{\left\langle \tilde{V}_{1,j}'^2 \right\rangle\left\langle \tilde{V}_{2,j}' \right\rangle} - \overline{\left\langle \tilde{V}_{1,j}' \right\rangle\left\langle \tilde{V}_{2,j}'^2 \right\rangle}\right) = \overline{\left\langle \tilde{u}_j'^2 \tilde{w}_{j,l}' \right\rangle} \\ \overline{\left\langle v_j'^2 w_{j,t}' \right\rangle} = \dfrac{1}{4\sin(\alpha_j)\sin(\alpha_j/2)}\left(\overline{\left\langle \tilde{V}_{3,j}'^3 \right\rangle} + \overline{\left\langle \tilde{V}_{4,j}'^3 \right\rangle} - \overline{\left\langle \tilde{V}_{3,j}'^2 \right\rangle\left\langle \tilde{V}_{4,j}' \right\rangle} - \overline{\left\langle \tilde{V}_{3,j}' \right\rangle\left\langle \tilde{V}_{4,j}'^2 \right\rangle}\right) = \overline{\left\langle \tilde{v}_j'^2 \tilde{w}_{j,t}' \right\rangle} \end{cases} \tag{9.10}$$

There are no contributions from noise signals to the Reynolds stress (Eq. (9.8)) and all tri-covariances terms (Eqs. (9.9) and (9.10)). The Eqs. (9.9) and (9.10) are found by taking the skewnesses equal to zero under the white noise assumption. Therefore the probability density function of the noise is symmetrical. Only the effect of spatial averaging is still present in the measured quantities.

As Garbini et al. (1982) have shown, the ambiguity induced by the spatial averaging process can be neglected as long as the sample volume size is sufficiently small to avoid large spatial averaging in the spectrum. For non-focused piston emitters, the size of measurement volume changes along the beam axis and the averaging effect varies in rapport. The phase array emitter used here ensures a constant sample volume size over the entire ensonified water depth. Thus, variations in spatial averaging contributions will result from changes of the flow characteristic only. Effects of this process will be found most likely in the near wall region of the flow where strong gradients occurr.

9.4 Principle of correction method

The aim of the correction method is to eliminate the noise terms from the above equations. These contain the additional and undesirable variances discussed in the introduction. For the correction, use will be made of the fact that the configuration of the 3-D-ADVP provides a redundant and independent measurement of the quasi-instantaneous vertical velocity component in the longitudinal and transverse planes. All quantities in the following are considered spatially averaged over the sampling volume. Based on Eqs. (9.6) and (9.7) the vertical velocities can be rewritten including the noise signal term as:

$$\begin{cases} \langle w'_{j,l} \rangle(t) = \langle \tilde{w}'_{j,l} \rangle(t) + \langle n^*_{j,l} \rangle(t) \\ \langle w'_{j,t} \rangle(t) = \langle \tilde{w}'_{j,t} \rangle(t) + \langle n^*_{j,t} \rangle(t) \end{cases} \tag{9.11}$$

where * denotes the geometrical weighted noise signal.

The cross-correlation, $\langle R_{xy,j} \rangle$, of these two signals at location j is:

$$\begin{aligned} \langle R_{xy,j} \rangle(\tau) &= \overline{\langle w'_{j,l} \rangle(t) \cdot \langle w'_{j,t} \rangle(t+\tau)} = \overline{\langle \tilde{w}'_{j,l} \rangle(t) \cdot \langle \tilde{w}'_{j,t} \rangle(t+\tau)} + \overline{\langle \tilde{w}'_{j,l} \rangle(t) \cdot \langle n^*_{j,t} \rangle(t+\tau)} \\ &+ \overline{\langle \tilde{w}'_{j,t} \rangle(t+\tau) \cdot \langle n^*_{j,l} \rangle(t)} + \overline{\langle n^*_{j,l} \rangle(t) \cdot \langle n^*_{j,t} \rangle(t+\tau)} \end{aligned} \tag{9.12}$$

If the noise signals of the two velocity estimates are uncorrelated, we obtain:

$$\left\langle R_{xy,j}\right\rangle(\tau)=\overline{\left\langle \tilde{w}'_{j,l}\right\rangle(t)\cdot\left\langle \tilde{w}'_{j,t}\right\rangle(t+\tau)} \tag{9.13}$$

from which we can calculate the magnitude of the cross-spectrum $\left\langle S_{xy,j}\right\rangle$:

$$\left\langle S_{xy,j}\right\rangle(f)=\left|\int_{-\infty}^{+\infty}\left\langle R_{xy,j}\right\rangle(\tau)\cdot\exp(-j2\pi f\,\tau)\,d\tau\right| \tag{9.14}$$

to finally express the noise spectrum:

$$\left\langle N_j^{*}\right\rangle(f)=b_j\cdot\left\langle N_j\right\rangle(f)=\left\langle S_{xx,j}\right\rangle(f)-\left\langle S_{xy,j}\right\rangle(f)=\left\langle S_{yy,j}\right\rangle(f)-\left\langle S_{xy,j}\right\rangle(f) \tag{9.15}$$

where b_j is the geometrical weighting factor for the vertical component defined in section 9.3.2. $\left\langle S_{xx,j}\right\rangle(f)$ and $\left\langle S_{yy,j}\right\rangle(f)$ are the power spectral densities of the fluctuating vertical velocity components measured in the longitudinal and transverse plane, respectively. The power spectral density and the related noise variance which appears in Eq. (9.6), common to all measured velocity components, is then:

$$\begin{cases}\left\langle N_j\right\rangle(f)=\dfrac{1}{b_j}\left[\left\langle S_{xx,j}\right\rangle(f)-\left\langle S_{xy,j}\right\rangle(f)\right]=\dfrac{1}{b_j}\left[\left\langle S_{xx,j}\right\rangle(f)-\left\langle S_{xy,j}\right\rangle(f)\right]\\ \left\langle \sigma_j\right\rangle^2=\dfrac{1}{b_j}\displaystyle\int_{-\infty}^{+\infty}\left[\left\langle S_{xx,j}\right\rangle(f)-\left\langle S_{xy,j}\right\rangle(f)\right]df=\dfrac{1}{b_j}\displaystyle\int_{-\infty}^{+\infty}\left[\left\langle S_{xx,j}\right\rangle(f)-\left\langle S_{xy,j}\right\rangle(f)\right]df\end{cases} \tag{9.16}$$

As mentioned in the following section, the spectra are estimated from timeseries of 600s in order to minimize the statistical uncertainty (less than 5% with the present device Bandwidth). It is now possible to verify the above assumptions on the noise signal if the following relations are valid:

$$\begin{cases}\overline{\left\langle w'^2_{j,l}\right\rangle}=\overline{\left\langle w'^2_{j,t}\right\rangle}\\ \left\langle S_{xy,j}\right\rangle(f)<\left\langle S_{xx,j}\right\rangle(f) \qquad \forall \quad f\\ \left\langle S_{xx,j}\right\rangle(f)=\left\langle S_{yy,j}\right\rangle(f) \qquad \forall \quad f\end{cases} \tag{9.17}$$

The first relation in Eq. (9.17) indicates that the receivers can be considered as identical due to the same noise contribution in terms of their energy. The last two relations show that the magnitude of the cross-sprectrum is lower than the power spectral densities of the vertical velocity component calculated from the longitudinal and transverse planes. Since these two spectra are identical, any difference can only originate from the uncorrelated noise signals between the two independent measurements of $\langle w' \rangle (t)$. With the geometrical relations given in section 9.3.2. it is possible to extract the noise spectrum and the corresponding variances for each velocity component for all locations j.

9.5 Experimental setup

Experiments were carried out in a laboratory open-channel (29m long, 2.45m wide, 75cm deep) under uniform flow conditions over a rough bed. The measurement section is placed 12m downstream from the entrance where turbulent flow is well developed. All velocity data presented here were taken at the center of the channel with the transducers mounted in a separate chamber above the flow as indicated in Fig. 7.3.

The experiments were conducted in clear water conditions where particles do not contribute significantly to backscattering (Shen and Lemmin (1997)). All measurements presented here are extracted from data sets acquired over 600 second intervals. The spatial and temporal resolutions are dependent of the settings of the instrument and are equal to ≅3mm and 0.024s, respectively in the present case.

The hydraulic parameters which indicate a subcritical highly turbulent flow are given in Table 9.2. The variables $u_{*,m}$ and $u_{*,S}$ represent the friction velocities obtained from linear extrapolation of the mean Reynolds stress at the wall and from the energy line slope formula for uniform flow, respectively. The relative errors (relative to $u_{*,S}$) are less than 3% which shows that uniform flow conditions are established. The roughness Reynolds number k_s^+ is evaluated from the standard roughness of the sand (d_{50}=2.1mm) and is equal to 36 which indicates an incompletely rough channel bed.

Q (m^3/s)	h (cm)	$u_{*,S}$ (cm/s)	u_{*m} (cm/s)	S ($\times 10^{-4}$)	Re_h ($\times 10^3$)	Fr_h	B/h	k_s^+	Π
0.069	10	1.71	1.66	3	28	0.28	24.5	36	0.11

Table 9.2 Hydraulic parameters

Fig. 2.1 shows results for the mean longitudinal velocity measurements. They agree well with theoretical estimations (wall-law, velocity-defect law and Coles wake function). The Π factor of Coles wake function has a value of 0.11 (Table 9.2; see Fig. 2.1d) and is obtained using the velocity defect law with κ equal to 0.4. These values are typical for uniform open-channel flow with a rough bed (Graf and Altinakar (1998)).

In the following, we will apply the noise corrections to the fluctuating components of these measurements.

9.6 Results and discussion

9.6.1 Validation of the method

Eq. (9.17) gives the relations that are needed for the evaluation of the application of the proposed method to the sonar data. Fig. 9.1 shows the variance profiles of the vertical fluctuating velocity component measured by the two independent multistatic subsystems. The relative error between the two measurements which is also shown, never exceeds a value of 1 %, except for the point nearest to the bed ($z \cong 3$mm). That high error value is due to sound scattering problems at the wall-water interface. The low error values at all other depths indicate that the first relation of Eq. (9.17) is valid and that the two subsystems can be taken as identical and close to ideal.

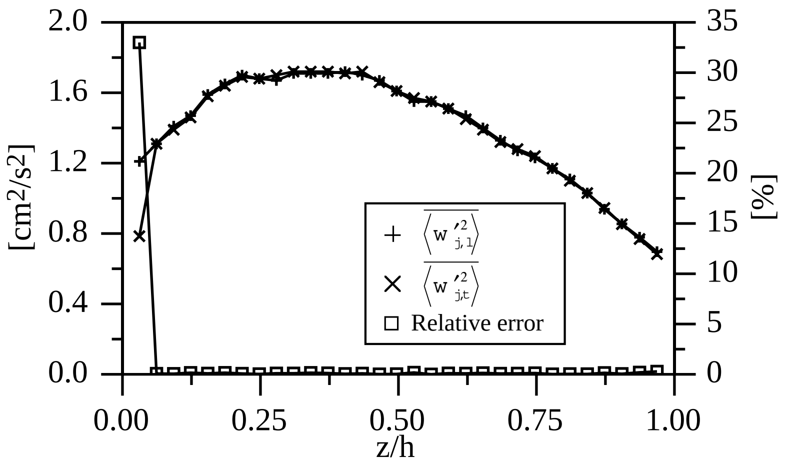

Fig. 9.1 Comparison of the two vertical velocity variances measured in the longitudinal and transverse flow sections. The squared line shows the relative error in percent.

Fig. 9.2a and Fig. 9.2b show the magnitude of the cross-spectrum $\langle S_{xy,j} \rangle$, the power spectral densities $\langle S_{yy,j} \rangle$ and $\langle S_{xx,j} \rangle$ measured simultaneously in the longitudinal and transverse planes at water depth z/h=0.4 and z/h=0.9, respectively. The last two relations of Eq. (9.17) can be considered as valid and it can be confirmed that the lower energy contained in $\langle S_{xy,j} \rangle$ is due to the attenuation of the uncorrelated signal parts between the two independent measurements of the vertical velocity fields. The difference between either of the power spectral densities and the magnitude of the cross-spectrum is identified as the noise spectrum of the vertical velocity component $\left\langle N_j^* \right\rangle$, also drawn in Fig. 9.2a and Fig. 9.2b. At each depth, the calculated cross-spectrum has been taken to evaluate the noise spectrum common to all measured components.

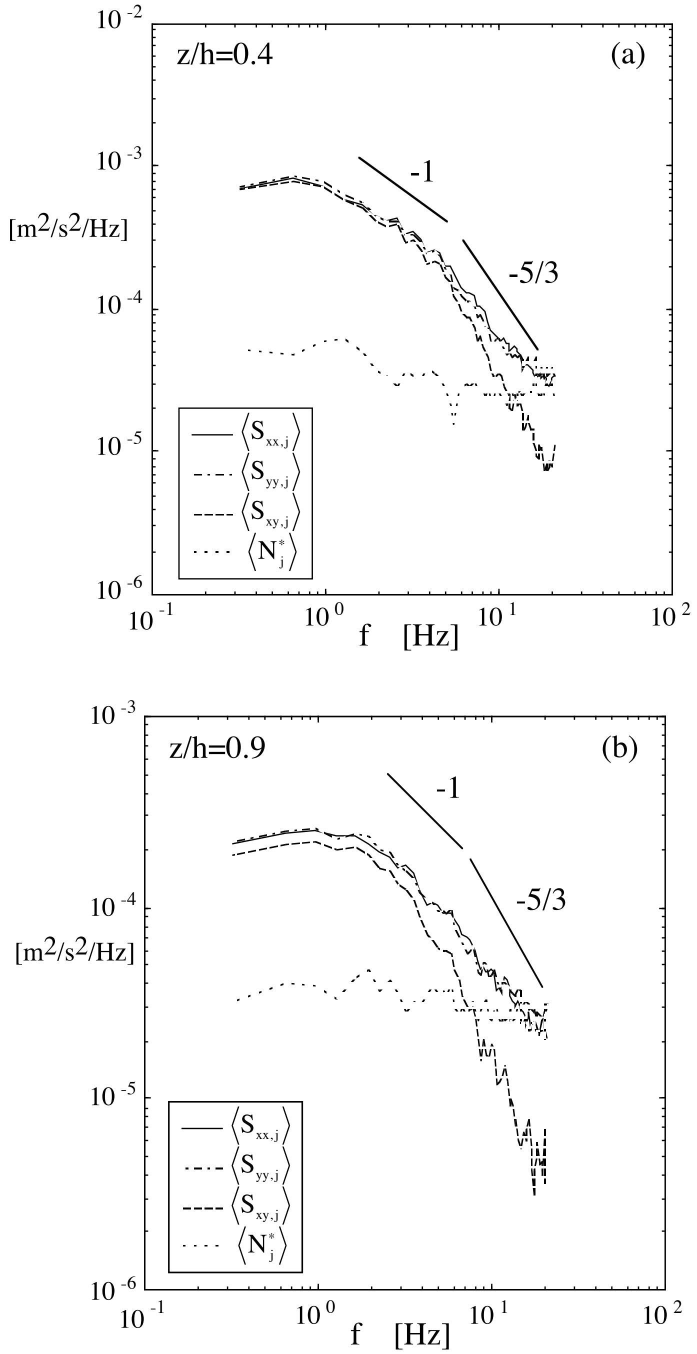

Fig. 9.2 Power spectra of vertical fluctuating velocity and corresponding noise signals. (a) At depth z/h=0.4. (b) At depth z/h=0.9. In the two figures the solid line, dashdotted line and dashed line represent the power spectra from the longitudinal, transverse and cross-correlation measurements, respectively. The dotted lines show the extracted vertical noise signals.

In Fig. 9.3 the noise spectra $\left\langle N_j \right\rangle$ for different depths are given. In all cases we observe a flat noise spectrum over the investigated frequency domain confirming the assumption of white noise. The level of the noise signal changes with depth. This trend is confirmed by the noise profile in Fig. 9.4 where its standard deviation normalized with the friction velocity has been plotted. The noise contribution increases first slowly towards the bed but increases significantly for z/h<0.15. Also shown in Fig. 9.4 is the relative difference of the standard noise deviations calculated with the cross-correlation method applied to two consecutive points (Garbini et al. (1982)) and the two independent vertical velocity field measurements, respectively. The relative difference is about 5% near the free surface and increases towards the wall where it reaches a value of 40%. The depth averaged difference is about 20%. The disadvantage of the method used by Garbini et al. (1982) is evident because it overestimates the noise part. It actually incorporates part of the uncorrelated but desired velocity signal between two consecutive points into the noise signal.

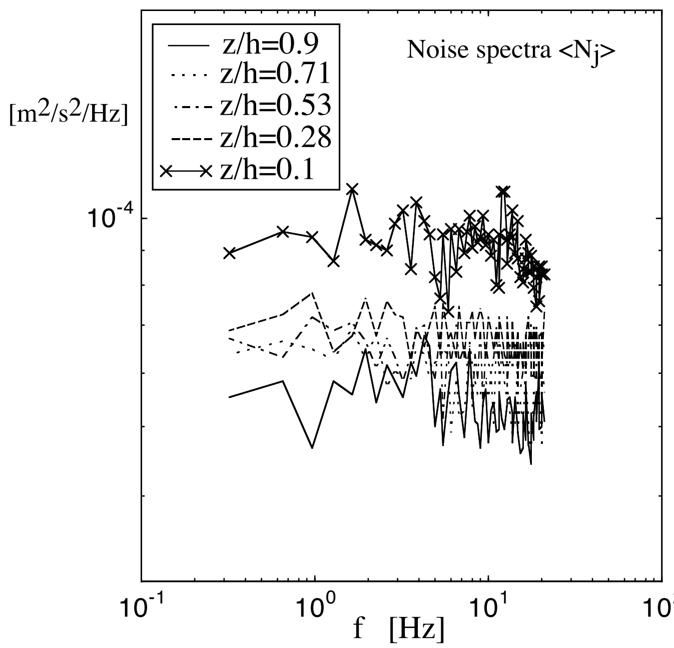

Fig. 9.3 Power spectra of noise signals at different water depths.

The same effect is also seen in Fig. 9.5 where the spectrum calculated with the two point method, called $\langle S_{j,j+1} \rangle$, is lower than the spectrum $\langle S_{xy,j} \rangle$ at depth z/h=0.4. Additionally, in the inertial subrange, the slope of $\langle S_{j,j+1} \rangle$ is weakly increased compared to that of $\langle S_{xy,j} \rangle$. Furthermore, in the range from 10 to 20 Hz the spectrum $\langle S_{j,j+1} \rangle$ becomes flat whereas the spectrum $\langle S_{xy,j} \rangle$ holds the same slope. That behaviour may originate from the overlapping of two consecutive sample volumes implying an incomplete decorrelation of the noise signals.

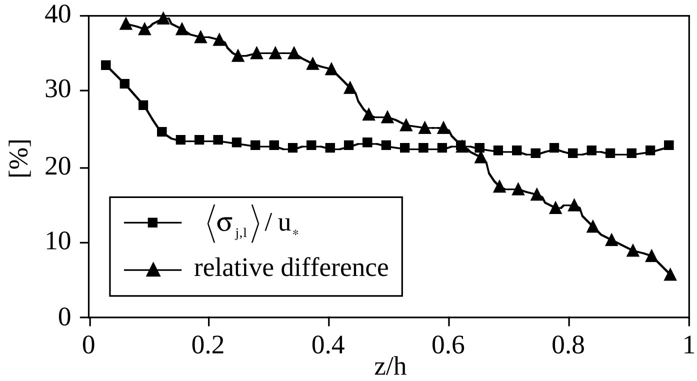

Fig. 9.4 Profile of noise standard deviation relative to the friction velocity (squares). Profile of relative difference of the standard noise deviations calculated with the cross-correlation method applied to two consecutive points (Garbini et al. 1982) and the two independent vertical velocity field measurements.

9.6.2 Results

Power spectral densities

In Fig. 9.6a and Fig. 9.6b the uncorrected and corrected power spectral densities are shown for the longitudinal and transverse fluctuating velocity components at depth z/h=0.68.

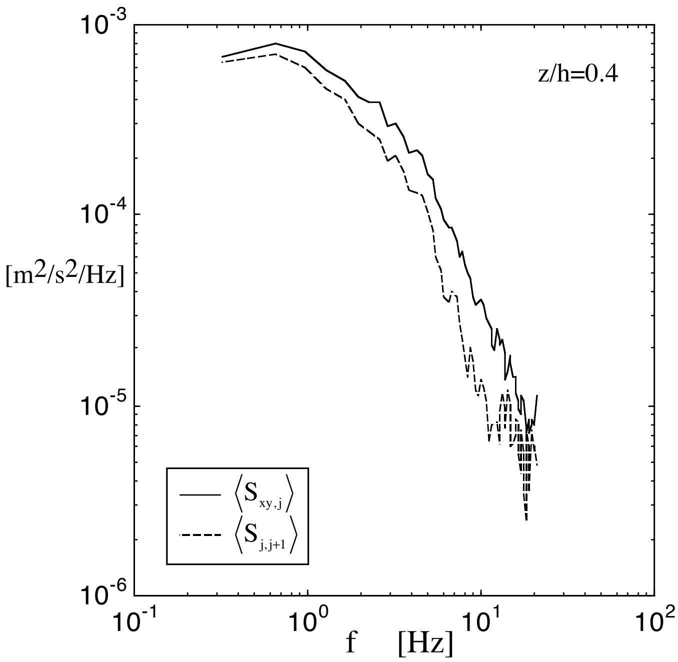

Fig. 9.5 Spectra of the vertical fluctuating velocity component at depth z/h=0.4. The solid line represents the result of the cross-correlation between the measurements in the longitudinal and transverse flow sections. The dashed line shows the result of the cross-correlation between two consecutive points as proposed by Garbini et al. (1982).

In the higher frequency domain, the characteristic flattening of the noise affected spectra can be distinguished. As mentioned above, the contribution of the noise in the longitudinal and transverse velocity components is more pronounced than for the vertical component mainly because of the larger magnitude of the weighting factors due to the geometrical configuration.

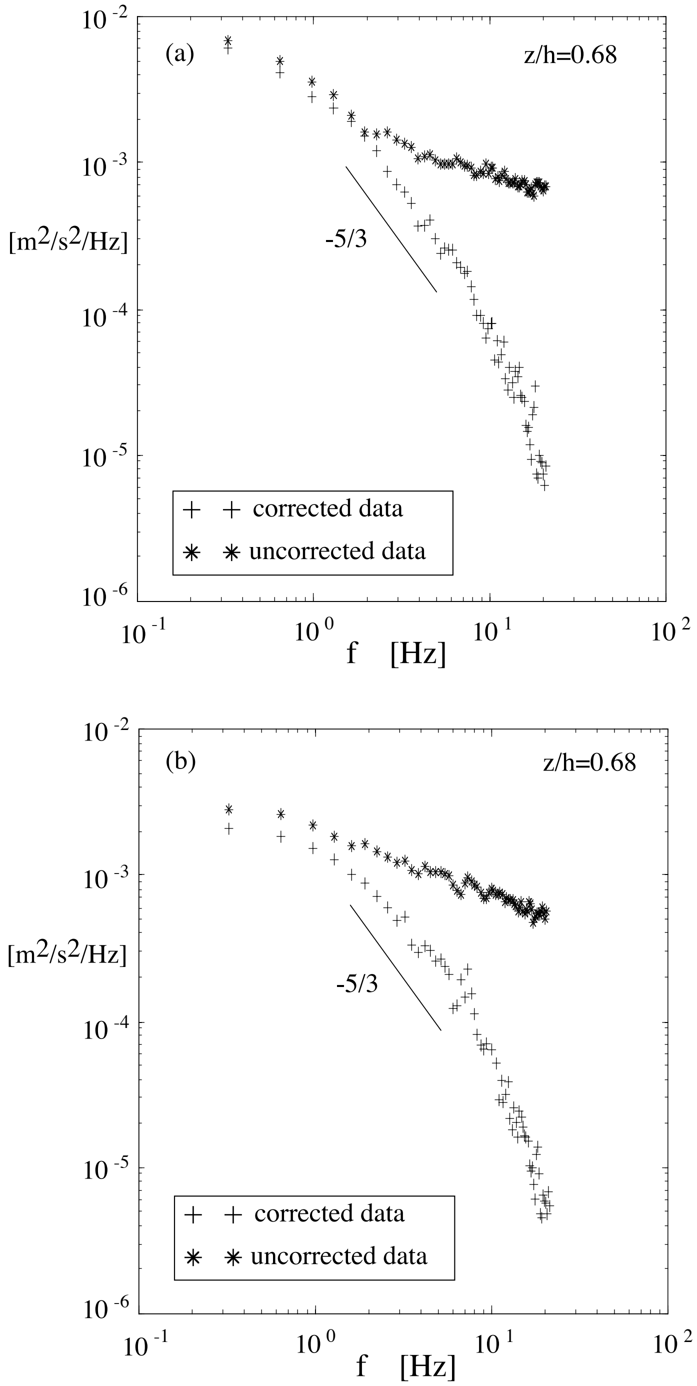

Fig. 9.6 Power spectra of uncorrected and corrected fluctuating velocities at depth z/h=0.68. (a) For the longitudinal component, (b) for the transverse component. In each figure the stars represent the uncorrected data, the crosses show the corrected data.

These factors are the same for the longitudinal and transverse components. Therefore the effect of noise attenuation on the power spectra is particularly significant for both components. The slope of –5/3 of the spectrum in the inertial subrange traced in Figs. 8a and 8b is followed by the two corrected spectra indicating an effective correction.

Turbulent intensities

Fig. 9.7 shows the uncorrected and corrected turbulent intensities for each component normalized by the friction velocity. For each depth, the corrected quantities are obtained from the integration of the corresponding corrected spectra as those presented in Fig. 9.6a and Fig. 9.6b. Also drawn in Fig. 9.7 are the semi-theoretical curves of the turbulent intensities given by Nezu and Nakagawa (1993) as:

$$\begin{cases} \sqrt{\overline{u'^2}}/u_* = 2.3\exp(-z/h) \\ \sqrt{\overline{v'^2}}/u_* = 1.63\exp(-z/h) \\ \sqrt{\overline{w'^2}}/u_* = 1.27\exp(-z/h) \end{cases} \tag{9.18}$$

Again, the difference of the uncorrected and the corrected intensities of the longitudinal and the transverse components is more significant than for the vertical component. The comparison of the corrected quantities with the curves from Eqs. (9.18) allows a certain evaluation of the efficiency of the correction method (see part 5.c. for the error analysis). For all three components the curves are in good agreement with the measurements in the flow region z/h>0.2.

In the range z/h<0.2, the vertical and longitudinal intensities deviate significantly from the theoretical curves. If the comparison of the corrected data is limited to the curves expressed by Eqs. (9.18) these deviations could be interpreted as inaccuracies of the instrument in the wall region of the flow. However, if we consider the effect of roughness on turbulence intensities which is not taken into account in Eqs. (9.18), these deviations may not necessarily be the result of measurement inaccuracies.

To investigate this point further, the corresponding curves from measurements of turbulent intensities over a rough bed with a normalized roughness value of k_s^+=85, presented by Grass (1971) using hydrogen-bubble technique, are also plotted in Fig. 9.7. It can be seen that the effect of roughness is to reduce the longitudinal turbulence intensity for z/h<0.3. The vertical intensity is less affected. It is evident that our corrected measured data are in better agreement with these curves taking into account bed roughness. The deviation of the transverse intensity is less important. A similar behaviour was also observed by Nezu and Nakagawa (1993). It confirms that the roughness strongly affects the longitudinal intensity for z/h<0.3 and less so the transverse and vertical ones.

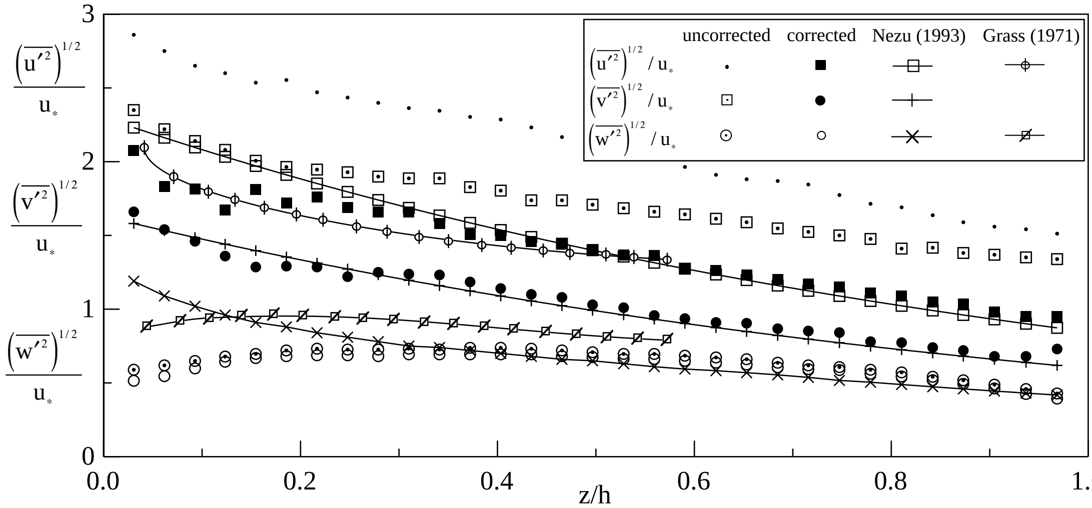

Fig. 9.7 Profiles of turbulence intensities relative to the friction velocity: from the uncorrected data, from the corrected data, from the semi-theoretical curves of Nezu and Nakagawa (1993) and from hydrogen-bubble technique measurements of Grass (1971).

Turbulence kinetic energy and shear stress profiles

In Fig. 9.8 the uncorrected, the corrected turbulence kinetic energy $K_j = 1/2(\overline{u_j'^2} + \overline{v_j'^2} + \overline{w_{j,1}'^2})$ and the mean covariance term $-2\overline{u'w'}$ are compared to the following relations:

$$K/u_*^2 = 4.78\exp(-2z/h) \qquad -2(\overline{u'w'}/u_*^2) = 2(1-z/h) \tag{9.19}$$

Again, the difference between the uncorrected and the corrected kinetic energy is important due to the sum of the geometrical weighting factors. The agreement of the corrected measurement with the semi-theoretical prediction is good for z/h>0.2. In the region z/h<0.2, the deviation becomes more pronounced (the bottom roughness effect is not taken into account in Eqs. (9.19)).

The shear stress profile also shows a deviation of the measured profile from the theoretical prediction for z/h<0.2. Since this quantity is inherently not affected by the noise signal present in the turbulent intensities (see section 9.3.2) the only remaining error source is related to the spatial averaging effect in the sample volume. However, the possible effect of bed roughness on the shear stress in this profile range is not well documented in the literature.

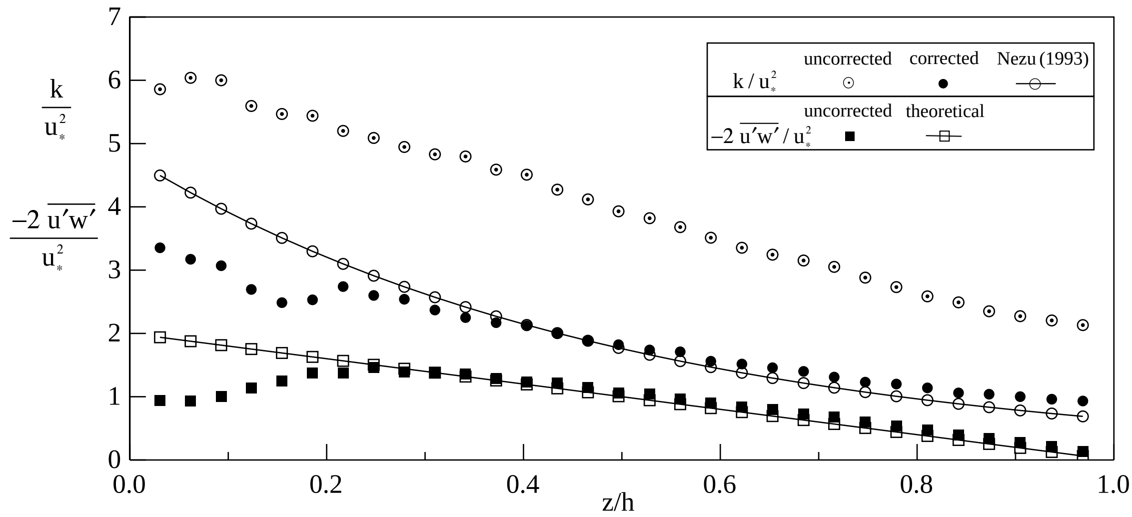

Fig. 9.8 Profiles of turbulent kinetic energy relative to the friction velocity for uncorrected data, corrected data and semi-theoretical curve of Nezu and Nakagawa (1993). Profiles of shear stress relative to the friction velocity for uncorrected data and theoretical curve.

Terms of the energy balance equation

In Fig. 9.9 the profiles of the different terms of the energy balance equation, all normalized by the term h/u_*^3, over the whole water depth are presented. The uncorrected and corrected energy dissipation rates are evaluated from the inertial subrange of the longitudinal uncorrected and corrected spectra, respectively. The following formula is used:

$$\varepsilon = \left[C^{-1} k_u^{5/3} \overline{u'^2} S_u(k_u)\right]^{3/2} \tag{9.20}$$

where C is the Kolmogoroff constant (with a value of 0.5), k_u, $S_u(k_u)$ and $\overline{u'^2}$ are the longitudinal wavenumber, the longitudinal wave-number spectrum and the longitudinal variance, respectively. It is obvious from Fig. 9.6 that the uncorrected dissipation rate is largely overestimated because the –5/3 power law is not observed in the uncorrected spectrum. In consequence, the dissipation rate calculated from the uncorrected spectrum is much higher than the one calculated from the corrected spectrum (Fig. 9.9). Good agreement is found between the corrected normalized $\varepsilon h / u_*^3$ and the expression given by Nezu and Nakagawa (1993):

$$\frac{\varepsilon h}{u_*^3} = E_1 (z/h)^{-1/2} \exp(-3z/h) \tag{9.21}$$

where the value E_1 is equal to 9.8 for a Reynolds number between 10^4 and 10^5.

Also drawn in Fig. 9.9 are the normalized production and corrected transport terms, written as:

$$\begin{cases} \dfrac{Ph}{u_*^3} = \dfrac{P_{11}h}{2u_*^3} = -\dfrac{\overline{u'w'}\,h}{u_*^3}\dfrac{\partial \bar{u}}{\partial z} \\ \\ \dfrac{Th}{u_*^3} = \dfrac{(T_{11}+T_{22}+T_{33})h}{2u_*^3} = -\dfrac{h}{2u_*^3}\dfrac{\partial}{\partial z}\overline{(u'^2+v'^2+w'^2)w'} \end{cases} \tag{9.22}$$

For z/h<0.15, the profile of the production term decreases which indicates an energy deficiency (the production is lower than the dissipation). This trend probably confirms the inaccuracies of the measurements in that region due to the spatial averaging process in the sheared velocity domain.

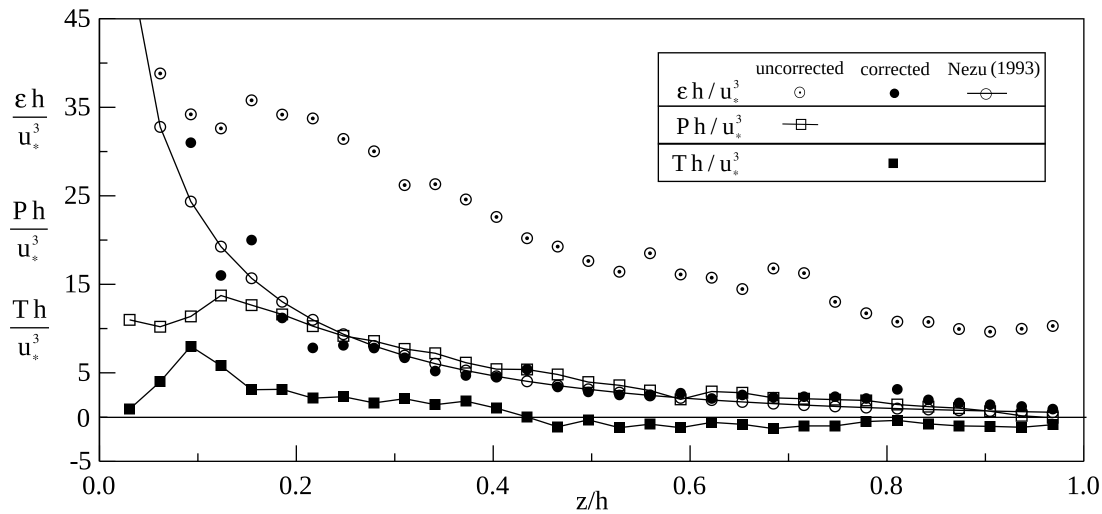

Fig. 9.9 Profiles of normalized terms of the turbulent energy balance equation: the turbulent energy dissipation term (from the corrected and uncorrected data), the production and corrected transport terms.

In the free surface flow region the dissipation is slightly higher than the production term which again is indicative for an energy deficiency. The normalized transport term is also drawn in Fig. 9.9 and is positive for z/h≤0.4 with a maximum value of 9. For z/h>0.1, the corrected results are in agreement with the measurements found in Nezu and Nakagawa (1993). For z/h<0.1, this term decreases towards the wall which again indicates a deviation from the results found in the literature.

Error analysis

Here we present a quantitative value of the relative differences of the corrected mean turbulence measurements with the above mentioned models. The profiles of relative differences are computed for the longitudinal, transverse and vertical turbulent intensities, the turbulent kinetic energy and the shear stress, noted ε_u, ε_v, ε_w, ε_K, ε_{uw}, respectively. They are calculated as follows;

$$\varepsilon_i(z/h) = \frac{\left|q_c(z/h) - q_m(z/h)\right|}{q_m(z/h)} \tag{9.23}$$

where q_c is the corrected measured quantity and q_m the quantity calculated from the model. Errors written with an overbar, $\overline{\varepsilon_i}$, are the depth averaged relative differences.

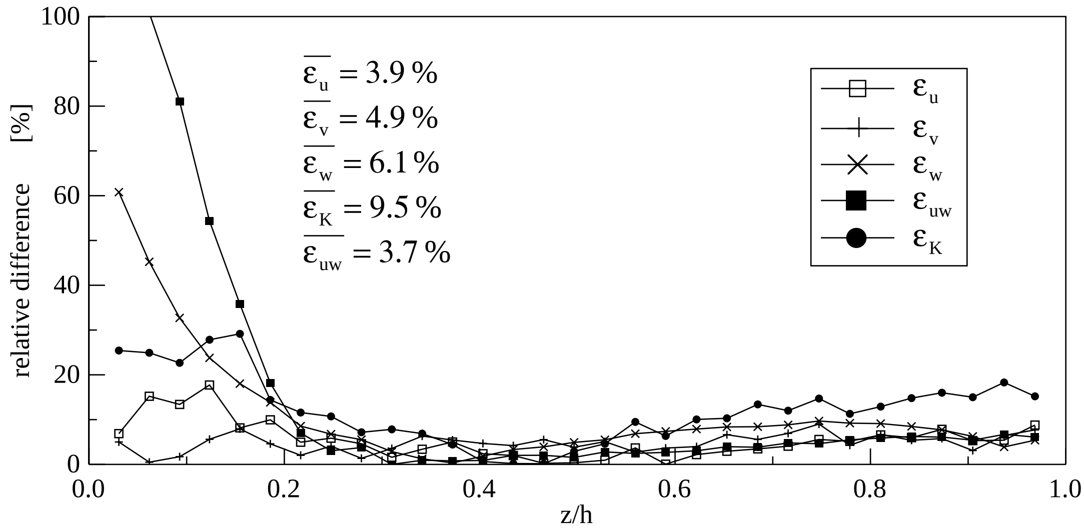

Fig. 9.10 Profiles of relative errors: for the three turbulence intensities, the turbulent kinetic energy and the shear stress. The variables written with overbars are the depth averaged quantities (for z/h>0.2).

For z/h>0.2, the depth averaged values do not exceed 10% (Fig. 9.10) (for the turbulent kinetic energy) which confirms the high accuracies of the corrected sonar measurements.

Except for the error of the transverse turbulent intensity, all other errors are significant for z/h<0.2. As mentioned before it is difficult to attribute these high values clearly to measurement inaccuracies considering that some physical process, especially the bed roughness effects, are not taken into account in the semi-theoretical models.

9.7 Conclusion

A combination of two techniques to improve the accuracy of turbulence measurements with a 3-D-ADVP is discussed.

The first concerns the use of a phase array emitter discussed in Hurther and Lemmin (1998). The following improvements have been made:

- the sample volume has a constant width (≅7mm) over a maximal distance of 60cm from the emitter

- the effect of the beam divergence (or phase distortion of the front wave), appearing as an additional noise variance in the measurements, can no more be distinguished on beam measurements

- spatial averaging effect is considerably reduced and is only dependent on flow characteristics in the vertical flow direction since the normalized emitters directivity function is no longer a function of the water depth.

The second technique used to increase the signal to noise ratio of the measurements is a direct correction method of the Doppler signal. It has been verified that the following noise signal characteristics apply to the method

- the noise has a flat spectrum independent of the flow depth

- the noise signal is uncorrelated from the velocity signal

- the noise signal is uncorrelated between the different receivers

- the receivers and the different analogue circuitries can be considered as identical

Based on these results it is possible to apply the correction method. It consists in making a redundant measurement of the instantaneous vertical velocity field with two independent working tristatic subsystems in the longitudinal and transverse flow sections. By calculating the difference between the magnitudes of the auto- and cross-spectra we rebuild the noise spectra of each velocity component by considering the specific geometrical configuration. Thereby, the following mean turbulence quantities were corrected:

- the three turbulence intensities (with a mean relative error of ≅5% in the outer flow domain)

- the turbulent kinetic energy (with a mean relative error of ≅9% in the outer flow domain)
- the turbulence spectra over the entire resolved frequency band
- the turbulent energy dissipation rate which is of particular importance if energy balances are investigated.

From quantitative comparisons of the corrected data with raw data and with results from literature, we have shown quantitatively that the corrected ADVP data are highly reliable and accurate in the flow region z/h>0.2. This result is of major importance for our further investigations concerning free surface turbulence in open-channel flow based on 3-D-ADVP velocity field measurements. Therefore the presented method has been programmed as a systematic correction method of the sonar measurements. Another advantage of the proposed technique is that it does not require assumptions about the flow characteristics. As a result the presented solution can be applied to any ADVP applications as long as the geometrical configuration permits a simultaneous redundant velocity component measurement. Voulgaris and Trowbridge (1998) have mentioned in their conclusion that the presence of high noise terms is an inescapable feature of the geometry of an ADV. This remark is valid for their case. We have shown here that with another geometrical configuration and an appropriate signal treatment the noise contribution to the mean turbulence terms can be eliminated.

Supplementary studies are needed to quantitatively evaluate the “true” accuracy of sonar measurements in the wall region of an open-channel flow. From theoretical considerations (which are difficult to validate experimentally), we allocate the remaining deviations (in the wall region) of the corrected measurements to effects of the spatial averaging since no other noise process is identified after application of the presented correction method. However, effects of bottom roughness cannot be excluded either.

9.8 References

Cabrera, R., Deines, K., Brumley, B. and Terray, E. (1987): Development of a practical coherent acoustic Doppler current profiler. Proc. Oceans'87, Canada, IEEE Oceanic Engineering Society, 93-97.

Garbini, J. L., Forster, F. K. and Jorgensen, J. E. (1982): Measurement of fluid turbulence based on pulsed ultrasound techniques. Part 1. Analysis. J. Fluid Mech., 118, 445-470.

Graf, W. H. and Altinakar, M. (1998: Fluvial Hydraulics. Wiley & Sons Ltd. 681 pp.

Grass, A. J., (1971): Structural features of turbulent flow over smooth and rough boundaries. J. Fluid Mech., 50(2), 233-255.

Hurther, D. and Lemmin, U. (1998): A constant beamwidth transducer for 3-D acoustic Doppler profile measurements in open-channel flows. Meas. Sci. Technol., 9(10), 1706-1714.

Lemmin, U. and Rolland, T. (1997): An acoustic velocity profiler for laboratory and field studies. J. Hydraul. Eng., 123, 1089-1098.

Lhermitte, R. and Lemmin, U. (1994): Open-channel flow and turbulence measurement by high-resolution Doppler sonar. J. Atmos. Oceanic Technol., 11(5), 1295-1308.

Lohrmann, Cabrera, A., R. and Kraus, N. C. (1995): Direct measurements of Reynolds stress with an acoustic Doppler velocimeter. Proc. IEEE fifth conf. on current measurements, St. Petersburg, FL, IEEE Oceanic Engineering Society, 205-210.

Nezu, I. and Nakagawa, H. (1993): Turbulence in open-channel flows. AIHR Monograph series. Balkema.

Rolland, T. (1994): Développement d'une instrumentation Doppler ultrasonore adaptée à l'étude hydraulique de la turbulence dans les canaux. PhD dissertation n°1281, Swiss Federal Institute of Technology-Lausanne.

Shen, C. and Lemmin, U. (1997): Ultrasonic scattering in highly turbulent clear water flow. Ultrasonics , 35, 57-64.

Voulgaris, G. and Trowbridge, J. H. (1998): Evaluation of the Acoustic Doppler Velocimeter (ADV) for turbulence measurements. J. Atmos. Oceanic Technol., 15, 272-289.

Zedel, L., Hay, A. E. and Lohrmann, A. (1996): Performance of a single beam pulse-topulse coherent Doppler profiler. IEEE J. Ocean Eng., 21(3), 290-297.

CHAPTER 10

SUMMARY AND CONCLUSIONS

10.1 Contributions of the thesis work

Understanding the dynamical details of transport of momentum, energy and tracers in currents is essential in assessing the impact of pollutants and their effect on water quality, at a time when high quality water is becoming progressively scarce. This thesis is a contribution to our understanding of turbulence related transport mechanism in currents and to advances in flow measurement techniques.

10.1.1 Hydrodynamical aspects

Momentum transport in clear water open-channel flows

1) Velocity and shear stress fields obtained by high resolution 3-D Doppler velocity profiling in free surface boundary layer flows in open-channels over smooth and rough beds show coherent structures extending over a large portion of the boundary layer depth that are independent of bottom roughness. Structural features such as ejections, sweeps, upwellings, downdrafts, vorticity patterns and spiral eddies can be identified when compared to tracer measurements found in Grass et al. (1993).

2) Good agreement is found between these qualitative observations and a statistical analysis of our measurements, which clearly exhibit the well-known quadrant distribution in the longitudinal plane. The effect of bottom roughness in changing the balance between ejections and sweeps is important only below 0.2h. The quadrant decomposition of the transverse covariance term, which has not been estimated before, is found to be almost uniform over the four quadrants. This confirms our initial qualitative observations from flow visualization. It also indicates that the organization of the flow in ejection and sweep events is essentially limited to the vertical plane defined by the mean flow direction.

3) The approximation of the conditional probability densities of the covariance terms $\varepsilon_1 = u'w'/\overline{u'w'}$ and $\varepsilon_2 = v'w'/\overline{v'w'}$ by a third order Gram-Charlier expansion appears to be sufficient for thresholds $H_i < 10$. Above that value, the third order cumulant discard model deviates from the observations. This suggests that the processes of shear stress generation and turbulent energy production in the boundary layer are highly intermittent.

4) Based on the measurements of the statistical properties of the covariance terms for different flow conditions, we have validated the wall similarity concept. We found a constant value of 0.3 for the normalized vertical flux of turbulent kinetic energy over a range of depths exceeding the equilibrium flow region, independent of the flow conditions investigated. This agrees with the value found by López and Garcia (1999) for a different range of bottom roughness.

5) A different approximation for the turbulent kinetic energy flux, valid in the observed equilibrium flow depth range is developed. It depends on the longitudinal fluctuating velocity component only, which considerably simplifies the theoretical expression of the turbulent kinetic energy flux.

6) The existence of wall similarity in highly turbulent boundary layers offers a new method of determining the mean bed friction velocity. This method is better adapted to field measurements than previous methods because the measurements can be taken at a single level far from the bed over an extended depth range where the gradient of the mean flow profile is weak. In particular, this avoids having to know the precise bed reference level, a difficulty that has introduced large errors in classical calculations based on profile measurements.

Suspended particle transport in open-channel flows

The particle entrainment ability of coherent flow structures is investigated by comparing higher order statistical properties of shear stress and of turbulent mass fluxes in suspension, open-channel flow under capacity charge conditions.

1) A third order cumulant discard Gram-Charlier probability density function has been applied to shear stress, as well as to horizontal and vertical turbulent mass fluxes in order to quantify their quadrant dynamics. Good agreement was found between the model results and the experimental estimations in the wall and intermediate flow regions. In the free surface flow region, for all investigated quantities, the limitation of the model to the order of three leads to small discrepancies due to an increase in intermittency.

2) The shear stress quadrant dynamics correspond to results found in the literature with a clear dominance of quadrant two (ejections) and quadrant four (sweeps) events. Thus, the presence of particles in the flow, even at capacity charge, does not influence the flow dynamics on the scales of coherent structures. Instead, a quadrant repartition similar to the shear stress distribution is observed for the mass fluxes and the effect of the hole size parameter H on the mass fluxes is comparable to that of the shear stress. This shows that the mass fluxes are also strongly organized in coherent structures. The quadrant repartition obtained for the mass

fluxes can be interpreted through the suspended particle entrainment capacity of ejections and sweeps.

3) Based on the conditionally sampled particle diffusion equation, the suspended particle transport capacity of coherent structures has been quantified. The proportion of the relative particle concentration profile (relative to the near bed reference concentration taken at z/h=0.05) and the time fraction were estimated as functions of the shear stress threshold level (delimiting the coherent structures in the instantaneous flow field). It has been shown quantitatively that coherent structures are important contributors to suspended particle transport. Strong structures which are only present for 30% of the time carry nearly 50% of the vertical particle flux. This indicates that particle transport is highly intermittent and that particle concentration in the water column strongly varies.

4) Based on these results, a bursting scale dependent formulation of the near bed equilibrium concentration has been discussed in Chapter 6. The validation of the particle entrainment function in suspension flows with one particle diameter and varying Shields parameters has been investigated.

5) We have used direct instantaneous mass flux measurements in several suspension flow conditions to verify that the conditionally sampled vertical entrainment flux is by far the dominant contributor to entrainment fluxes.

6) However, when the sampling condition NN50 is applied to the vertical entrainment fluxes, the resulting entrainment flux is not in equilibrium with the total deposition flux as assumed in the model. These results have been confirmed for all the flow conditions analysed herein. Therefore, we propose to introduce a correction factor in the near bed equilibrium concentration formulation. Finally, the validity of our proposed correction has been checked by calculating the burst surface portion values for one particle size but for different hydraulic conditions. The corrected predictions are found to be in very good agreement with results given in the literature.

10.1.2 Instrumentation

1) A novel 3-D acoustic Doppler velocity profiler using a focused emitter has been developed to measure the instantaneous 3-D velocity profile over the whole investigated water column. The instrument is conceived to undertake laboratory as well as field measurements (rivers or lakes) of which very little exist today.

Hardware and software have been modified to allow 3-D measurements with the electronically focused phase array emitter.

A combination of two techniques (presented in Chapter 8 and Chapter 9) to improve the accuracy of turbulence measurements with a 3-D-ADVP have been designed and tested.

2) The first technique concerns the use of a phase array emitter discussed in Chapter 8. The following improvements have been made:

- The sample volume has a constant width (≅7mm) over a maximal distance of 60cm from the emitter.
- The acoustic beam size measurements of the focused transducer show an important decrease of the lateral size of the sample volume at great distances. A nearly zero opening angle over a depth range of 60 cm indicates that the proposed electrical beam focusing works well. The focusing provides for cleaner signals. The resultant improvement in the SNR (signal-to-noise) ratio allows for a significant increase in the spatial and temporal resolution of the velocity measurements (about 50%) compared to a system with a standard plane-disc transducer.
- The effect of the beam divergence (or phase distortion of the front wave), appearing as an additional noise variance in the measurements, can no longer be distinguished on -6 dB beam measurements
- The spatial averaging effect is considerably reduced and is only dependent on flow characteristics in the vertical flow direction since the normalized emitters directivity function is no longer a function of the water depth.

3) The second technique used to increase the SNR ratio of the measurements is a direct correction method of the Doppler signal (see Chapter 9). It has been verified that the following noise signal characteristics apply to the method:

- The noise has a flat spectrum independent of the flow depth.
- The noise signal is uncorrelated from the velocity signal.
- The noise signal is uncorrelated between the different receivers prooving its isotropic nature.
- The receivers and the different analogue circuitries can be considered as identical.

Based on these results it is possible to apply the correction method. It consists in making a redundant measurement of the instantaneous vertical velocity field with two independent working tristatic subsystems in the longitudinal and transverse flow sections. By calculating the difference between the magnitudes of the auto- and cross-spectra we rebuild the noise spectra of each velocity component by considering the specific geometrical configuration. The following mean turbulence quantities were corrected:

- The three turbulence intensities (with a mean relative error of ≅5% in the outer flow domain).
- The turbulent kinetic energy (with a mean relative error of ≅9% in the outer flow domain).
- The turbulence spectra over the entire resolved frequency band.
- The turbulent energy dissipation rate which is of particular importance if energy balances are investigated.

From quantitative comparisons of the corrected data with raw data and with results from the literature, we have shown quantitatively that the corrected ADVP data are highly reliable and accurate in the flow region $z/h>0.2$. This result is of major importance for our further investigations concerning free surface turbulence in open-channel flow based on 3-D-ADVP velocity field measurements. Therefore the presented method has been programmed as a systematic correction method of the sonar measurements. Another advantage of the proposed technique is that it does not require assumptions about the flow characteristics. As a result the presented solution can be applied to any ADVP application as long as the geometrical configuration permits a simultaneous redundant velocity component measurement. Voulgaris and Trowbridge (1998) have mentioned in their conclusion that the presence of high noise terms is an inescapable feature of the geometry of an ADV. This remark is valid for their case. We have shown here that with another geometrical configuration and an appropriate signal treatment the noise contribution to the mean turbulence terms can be eliminated.

10.2 Further research

Hydrodynamical aspects

The results reported in Chapter 4 have demonstrated that the wall similarity concept is valid at the center of shallow, highly turbulent, uniform open-channel flows at high Reynolds numbers where the boundary layer is two-dimensional in the mean. Recently we have studied the structure and the dynamics of secondary currents in uniform flow over rough beds by taking closely spaced 3-D ADVP profiles across a channel cross-section. It was found that in the mean the wall similarity concept still holds despite the presence of secondary currents of Prandtl's second kind. In order to determine the range of validity of the method presented here, direct field investigations are needed.

The analogy of the third order velocity moments for suspension flows estimated in Chapter 5 to those in clear water flows investigated in Chapter 4 allows to validate the wall similarity concept in highly turbulent suspension flows. This result points towards a universality of this concept. It provides for a simplification combined with increased accuracy in the determination of the effective wall shear velocity particularly in flows with strongly varying bottom roughness height where classical mean profile methods fail. Further investigations on the range of validity of this concept in suspension flow with different grain sizes, varying Shields parameter and under field conditions are recommended for future work in this area.

From the correction of the particle entrainment function proposed in Chapter 6: it can be asked whether this correction can be considered as universal. Here we have only worked with one particle size and with different hydraulic conditions. It has been demonstrated by Cao (1999) that the parameter T_B^+/A_C is a strong function of particle size, particularly for small size particles. However, his Fig. 3.11a shows low scatter between the experimental results and the fitted curve based on Eq. (6.4). From this observation one may expect that the value of the correction factor not to vary much. Obviously our data do not fit onto the curve in Fig. 3.11a. Therefore, Eq. (6.4) will also have to be modified in order to take into account the correction once more data for other particle sizes are available. Further investigations are needed to determine whether the suspended sediment transport capacity of coherent flow structures in highly turbulent boundary layers is universal. In other words, is a general characterization of the flow structures transporting suspended sediments possible? As discussed in Chapter 6, such a concept can be applied to the near bed equilibrium concentration prediction in suspension flows. An extension of this approach to the concentration profile prediction would lead to a novel model for the sediment transport assessment in suspension flows based on coherent structure characteristics.

Instrumentation

This study has demonstrated the potential of a high-resolution 3-D acoustic Doppler velocity profiler in turbulent boundary layer flow. It is ideally suited for such studies because it can profile the total depth in one sweep. This is particularly important in boundary layer field studies where flow conditions often change rapidly and point by point measurements will to provide the details desired to understand the high frequency dynamics of the boundary layer. Future research could be concentrated on:

- Increase the acoustic frequency in order to decrease the sample volume size and consequently attenuate the effects of spatial averaging. The relative errors on turbulence measurements in the wall region of the boundary layer (see Fig. 9.10) could therefore be compared to the same measurements with the high-frequency sonar.

- Develop a wide band sonar capable of generating a frequency scanning over an extended range of emission frequence. Phase distinction in two-phase flows such as suspension flows could be undertaken. Very few other techniques provide this possibility today. However this can be achieved by combining the 3-D ADVP with the Acoustic Particle Flux Profiler developed by Shen (1997).

- Integrate the different analogue and digital treatment stages of the instrument in order to reduce the number of eventual error sources andincrease the flexibility for the field deployment of the instrument.

- Increase the speed of the digital signal arrangement and treatment by using at least two parallel working DSPs in order to improve the on-line processing. A direct check of the data quality during the measurement would considerably reduce the duration of the measurement procedure.

The last two points are of particular interest for the development of a commercial version of the 3-D-ADVP better adapted to environmental in-situ investigations, as well as to industrial applications.

10.3 References

Cao, Z. (1999): Equilibrium near-bed concentration of suspended sediment. J Hydr. Engrg. 125: 1270-1278.

Grass, A. J., Stuart, R. J. and Mansour-Tehrani, M. (1993): Common vortical structure of turbulent flows over smooth and rough boundaries. AIAA Journal 31(5): 837-847.

López, F. and Garcia, M. H. (1999): Wall similarity in turbulent open-channel flow. Journal of Engineering Mechanics 125(7): 789-796.

Shen, C. (1997): An acoustic instantaneous praticle flux profiler for turbulent flow. PhD dissertation No 1630, Swiss Federal Institute of Technology, Lausanne.

Voulgaris, G. and Trowbridge, J. H. (1998): Evaluation of the Acoustic Doppler Velocimeter (ADV) for turbulence measurements. J. Atmos. Oceanic Technol., 15, 272-289.

CURRICULUM VITAE

Prénom et Nom	: **David HURTHER**	Nationalité	: France
Adresse	: EPFL-DGC-LRH CH-1015 Lausanne Suisse	Etat civil	: célibataire
		N° de tél.	: (41) 21 693 2400
		e-mail	: david.hurther@epfl.ch
Né le	: 7 Septembre 1972		

FORMATION

2001 — **Docteur ès sciences** en hydrodynamique environnementale et instrumentation. *Ecole polytechnique fédérale de Lausanne*. Suisse.

1995 — **Diplôme d'études approfondies** de mécanique et ingénierie. *Université Louis Pasteur de Strasbourg.*

1995 — **Ingénieur diplômé**. Filière génie électrique. *Université des sciences appliquées de Offenburg, Allemagne*.

CERTIFICATS

1999 — Certificat en **hydraulique fluviale** (aspects environnementaux) délivré par la *European Graduate School of Hydraulics de l'AIRH*.

1997 — Certificat en **modélisation et simulation numérique des écoulements** délivré par l'*école polytechnique fédérale de Lausanne*.

1997 — Certificat en **transport de matière dans les écoulements** délivré par l'*école polytechnique fédérale de Lausanne*.

1994 — Certificat en **théorie des réseaux neurones et leurs applications en ingénierie** délivré par l'*université des sciences appliquées de Offenburg, Allemagne.*

EXPERIENCE PROFESSIONNELLE

Depuis juil. 1998 — **Assistant de recherche** au laboratoire de recherches hydrauliques à *l'école polytechnique fédérale de Lausanne, Suisse*.

Mar. 1996 à juin 1998 — **Coopérant scientifique chercheur** (service national) au laboratoire de recherches hydrauliques à l'*école polytechnique fédérale de Lausanne, Suisse.*

Oct. 1996 à fév. 1997 — Etudiant chercheur au *Groupement pour l'Evaluation des Composants en eau et Assainissement* (GEMCEA), Nancy, France.

Mar. 1994 à sept. 1994 — Stage d'élève ingénieur chez *A.N.T. Bosch Telecom, Offenburg, Allemagne*.

EXPERIENCE EN ENSEIGNEMENT

Depuis juil. 1998 — **Assistant EPFL** en mécanique des fluides (2 semestres / an) et hydraulique fluviale (1 semestre / an). *Ecole polytechnique fédérale de Lausanne, Suisse*.

Oct. 1996 à fév. 1997 — Enseignement d'un cours d'instrumentation (6 heures) au DEA de mécanique et ingénierie *Université Louis Pasteur de Strasbourg (institut de mécanique des fluides de Strasbourg, UMR CNRS 7507).*

PRIX

Mars 2001 — Lauréat du "post-doctoral scholar award in ocean science and engineering". *Woods Hole Oceanographic Institution*, Massachusetts, USA.

DIVERS

Langues bilingue (français et allemand), anglais (très bon niveau).

Informatique Langages (fortran, pascal, Turbo pascal, C/C++). Logiciels (matlab, labview).

Loisirs Sports: ski, course à pieds, tennis. Musique ancienne (baroque, classique).

PUBLICATIONS ET COMMUNICATIONS ORALES

Publications avec comité de lecture et communications orales

[1] **D. Hurther and U. Lemmin (2000)**, *Shear stress statistics and wall similarity analysis in turbulent boundary layers using a high resolution 3D ADVP*. IEEE Jounal of Oceanic Engineering 25(4): 446-457.

[2] **D. Hurther and U. Lemmin (2001),** *A correction method for turbulence measurements with a 3D acoustic Doppler velocity profiler.* Journal of Oceanic and Atmospheric Technologies 18: 446-458.

[3] **D. Hurther and U. Lemmin (2001)**, a discussion of *Equilibrium near bed concentration of suspended sediment.* Journal of Hydraulic Engineering 16(5).

[4] **D. Hurther and U. Lemmin (1998),** *A constant-beam-width transducer for 3D acoustic Doppler profile measurements in open-channel flow*. Meas. Sci. Technol. 9(10): 1706-1714.

[5] **D. Hurther and U. Lemmin (2001),** *Sediment transport capacity of coherent structures in suspension flows.* Experiments in Fluids. (in review).

[6] **D. Hurther (2001),** *Sediment transport assessment in suspension flow based on coherent structures characteristics*. Proceedings of the XXIX IAHR congress, Beijing, 17-21 September 2001, China.

[7] **D. Hurther and U. Lemmin (2000),** *A correction method for turbulence measurements with a 3D acoustic Doppler velocity profiler using a constant beam width transducer*. Proceedings of ASME 2000 Fluids Engineering Division summer meeting, Boston, 12-15 June 2000, Massachusetts, USA.

[8] **D. Hurther and U. Lemmin (1999),** *Shear stress statistics in a turbulent, open-channel flow over a rough bed*. Proceedings of the XXVIII IAHR congress, Graz, 22-27 August 1999, Austria.

[9] **U. Lemmin, D. Hurther and C. Shen (1999),** *A high resolution constant beam width pulse-to-pulse coherent 3D acoustic Doppler profiling current meter for use in laboratory and environmental studies.* Proceedings of the 6th IEEE working conference on current measurements, San Diego, 11-13 March 1999, USA.

Communications orales

[10] **D. Hurther (1998),** *A 3D acoustic Doppler profiler ans its application to velocity measurements in rivers*. ERCOFTAC, annual meeting, Lausanne, 20 February 1998, Switzerland.

[11] **D. Hurther (2000):** présentation orale des publications [1], [2], [3], [4] sur invitation dans les laboratoires suivants (séjour aux USA du 10 juin au 22 juillet 2000):

- Laboratory of environmental fluid mechanics (Prof. S. Monismith), Stanford university, Paolo Alto, USA.
- Laboratory of environmental hydraulics (Prof. H. Nepf), M.I.T., Boston, Massachusetts,USA.
- Woods Hole oceanographic Institution (Dr. E. Terray), Woods Hole, Massachusetts, USA.
- National sedimentation laboratory (Prof. S. Wang), university of Mississippi, Oxford, Mississippi, USA.
- Iowa institute of hydraulic research (Prof. J. Odgaard), university of Iowa, Iowa City, USA.